Thèse de doctorat

Charge density response of 2D polymorphs: borophene as a prototypical case

Thèse de doctorat de l'Institut Polytechnique de Paris
préparée à l'École polytechnique

École doctorale n°626 École doctorale de l'Institut Polytechnique de Paris (EDIPP)
Spécialité de doctorat : Physique

Thèse présentée et soutenue à Palaiseau, le 15 Avril 2024, par

ALAM TONALTZIN OSORIO DELGADILLO

Composition du Jury :

Giovanni ONIDA Professeur, University of Milan	Président
Sohrab ISMAIL-BEIGI Professeur, Yale University	Rapporteur
Arjan BERGER Professeur associé, Université Paul Sabatier	Rapporteur
Cecilia NOGUEZ Professeure, Universidad Nacional Autónoma de México	Examinateur
Alice RUINI Professeure associée, University of Modena and Reggio Emilia	Examinateur
Francesco SOTTILE Ingénieur de recherche, École polytechnique	Directeur de thèse
Lucia REINING Directrice de recherche CNRS, École polytechnique	Co-directeur de thèse

Acknowledgments

First of all, I want to thank my supervisors, Francesco Sottile and Lucia Reining, for their support even before the beginning of my PhD: when I still had to secure funding, when I got stuck in Belgium, and, of course, upon my arrival in Palaiseau. I am very grateful for their time, all the motivation they showed, and the effort they put into my project. Both personally and academically, working with them was without a doubt one of the best choices I could have made.

I also want to thank all the great voices I learned from on this journey: Matthieu Verstraete, who initially suggested I join the Palaiseau group under the description that the Palaiseau group was excellent and had a familial atmosphere (of course, the dinners at Lucia's place do a big part of the job). Michele Amato and Hans-Christian Weissker for their suggestions and comments about my project during the mini-soutenance, and in particular to Hansi for the interest he showed in my project and my well-being, even sharing a beer after a conference in Olerón. Lastly, I want to thank Andrea Cucca for his technical support and for all the non-technical conversations in the kitchen, some days helping me with cluster-related problems and other days on how to prepare eggplant at home.

The times in the kitchen were undoubtedly among my favorite moments: discussions about news, wine, and coffee, and birthday celebrations (even though one needs to bring their own birthday cake). These moments would not have been possible without all the amazing people from the Palaiseau group. Big thanks to everyone; you really made every day easier.

I want to give a special mention to all the friends I made along the way: Abdallah El-Sahili, with whom I shared room during conferences and summer schools, long talks, and tea during the Friday night card games. Marc Aichner, with whom I had long personal and technical talks, shared laughs, and many beers. Elisa Serrano, who helped me enormously to organize the 19th Young Researchers Meeting of the ETSF, and who, during the process, became a friend to talk about physics, movies, and books. Nathalie Saouli, who, after all these years, I got to know, and became the best friend to visit Paris with and invent stories. Vitaly Gorelov and Muhammed Gunes, both for the table tennis games and the coffee talks; I definitely developed further my passion for coffee. I could name every single one of them, remembering many highlights. Unfortunately, I cannot let the acknowledgments be the longest section of my thesis. That said, thanks to everyone I shared friendly moments with: Maram Ali, Fatema Mohamed, Laura Urquiza, Johnny Pinzon, Paula Kleij, Shalu Rani, Simone Vacondio, Jakob Wolff, Rajarshi Sinha, Georg Michelitsch, and the list goes on.

Also, thanks to all my friends from before who supported me on many occasions when I needed it: Baldo Luis Najera Santos, Parastoo Agharezaei, and Mariela Villareal; this

long (but short) journey definitely needed you. And lastly, of course, my family, who, regardless of what I do, when, and where, are there to support and advise me. It does not matter if I am on the other side of the world; I bring you with me all the time. Thank you.

Thank you, everyone.

Preface

Understanding properties of materials by theory and calculations involves two aspects that both require theoretical efforts: the general description of a given property on one side, and the materials-specific considerations on the other side. Of course, depending on the property and the material one wants to look at, different descriptions for the same object are pertinent. In the present thesis we are interested in describing a class of materials which is atomically thin. This suggests that the most pertinent description is at the atomic level. Here we focus on borophene: this refers to a family of experimental and theoretical two-dimensional (2D) materials constituted of a single atomic species: boron. Thus, among the multiple polymorphs that have been predicted and synthesized, the only difference is the atomic arrangement of atoms. Still, different polymorphs show different properties.

The most obvious question is then: how does the atomic structure affect the properties of borophene? This is the fundamental question of our work. We address it by distinguishing between what are the properties which are common for the material and what properties are specific for the polymorphs. We perform this study in two steps: First, to determine how the atomic structure affects the electronic structure, and then to determine how the electronic structure affects the properties. In particular, we focus on the dielectric properties: these have a clear connection with the electronic system, and can also be related to experimental measurements.

In this work we deal mostly with two concepts: the electronic structure of different borophene polymorphs, and the electronic polarizability. The latter is constructed from the electronic structure. With the electronic structure we explore and answer different questions: 1) what is common in the electronic structure of different borophene polymorphs?, 2) what is different?, and 3) how can the electronic structure of certain polymorphs be tuned?

Moreover, with the polarizability (and the electronic structure) we characterize primarily optical absorption. In our discussion a central topic is borophene as transparent conductor. Thus, the main questions in this regard are two: 1) how does borophene becomes transparent?, and 2) how can we tune transparency in this material? We discuss simple theoretical rules which can be useful for engineering borophene as a transparent conductor.

Finally, we deal with a last point concerning the static response. We discuss it in the context of nesting of the Fermi surface, which is, for example, of interest for superconductivity applications, and also to understand structural instabilities. Here we highlight to the possibility of using the electronic polarizability for the discussion of structural instabilities, which go beyond a mere search for nesting. The static response, despite being largely used in different contexts, for example as ingredient in many-body perturbation

theory, is a computationally challenging quantity. In this work we develop a method that allows us to approximate the static response in an efficient manner: as an explicit functional of the single-particle one-body reduced density matrix.

Contents

Contents 7

Part I

Background

Borophene

1.1 A large family of structures

Two-dimensional materials are of interest for innumerable applications: plasmonics, transparent conductors, superconductivity and energy storage, among others [1–7]. Consequently, different families of materials have emerged: these go from perovskites [8], transition metal dichalcogenides (TMDs) [9], and graphene and related materials [10–12], to a much less studied family: the ones constituted by boron-only 2D structures, called "borophene", in analogy to graphene [13]. However, contrary to graphene which refers only to the well known carbon-made hexagonal structure (with sp^2 bonds and a p_z orbital), borophene refers to many theoretical and/or experimentally found polymorphs [14], which appear as a consequence of one electron difference in the boron atom with respect to carbon[1], frustrating the perfect $sp^2 + p_z$ configuration of the graphene structure [15].

Several theoretical studies of borophene can be found in the literature, and we can classify them in two groups: 1) those which focus on finding stable polymorphs, mainly based on formation energies and phonon spectra calculations [14, 16–18]; 2) works which focus on the fundamental studies of specific properties of certain polymorphs and their possible applications: see for example Refs. [19–23] for borophene in superconductiviy, supercapacitance [24], hydrogen storage [25, 26], plamonics [27–29], and transparent conductors [30, 31]. However, despite the interest in this material only few highly studied polymorphs have been synthesized: the first realization of a borophene monolayer was achieved by Mannix *et. al.*, in 2015, obtaining the triangular buckled structure known as δ_6 on top of a silver substrate [32] (Fig. 1.1). After this, other polymorphs were synthesized by different research groups on top of metallic substrates: β_{12} and χ_3 (synthesized in 2015) [33], δ_3 (2018) [34], and the more recent α'-Bilayer (2022) [35] (Fig. 1.1). Only two structures, β_{12} and χ_3 (and intermediate phases), have been reported experimentally in their free-standing form (2019) [36].

We put special emphasis on the structures from Refs. [32–36], as they contain only few atoms per unit cell and therefore can be used (and have been used) to perform numerical studies of the properties borophene exhibits, but it is worth mentioning that more (and more complex) structures have been synthesized in the last years: superstructures with line defects [37], concentric superlattices [38], large bilayers [39], and even hydrogenated structures [40]. The latter (hydrogenation of borophenes) gives birth to a subfamily of materials known as "borophanes", which shows polymorphism similar to borophene [40], and which has recently been predicted to show semimetallicity and superconductivity [41]. This subfamily is its own world and it will not be further addressed in this work.

---

[1]The boron atom has 5 electrons: 2 are considered as core electrons (thus not expected to interact in the chemistry of borophene), and 3 as valence.
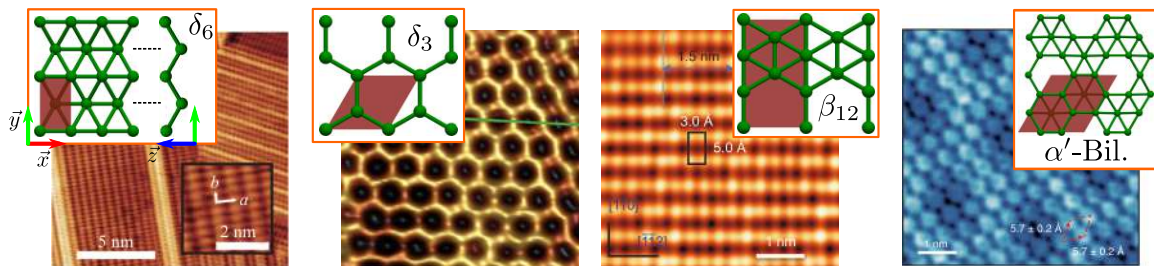
Figure 1.1: Atomic structure and scanning tunneling microscopy (STM) images of borophene δ_6, δ_3, β_{12} and α'-Bilayer (in that order). The STM topography images have been adapted from Refs. [32–35], and the shaded regions in the atomic structures correspond to the unit cells in-plane of the polymorphs.
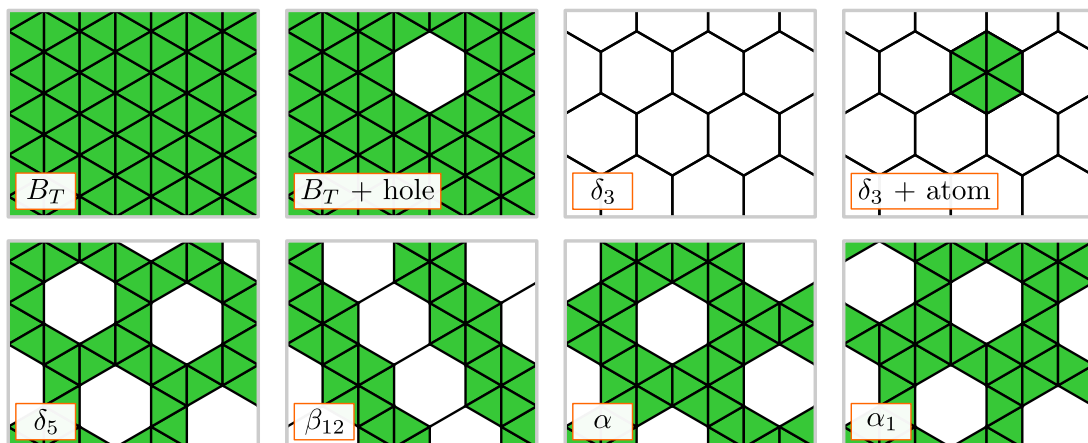
Figure 1.2: Model borophene structures, each vertex in the figures correspond to an atomic position. B_T and δ_3 (top row) can be used as parent structures of other allotropes upon the creation of holes (empty hexagons in white) and the addition of atoms (filled hexagons in green). Both mechanisms can be used conceptually to construct the children structures (lower row) from B_T or δ_3. Moreover, in an sp^2 bonding configuration in-plane (like graphene), δ_3 is electron-deficient, while the B_T lattice has an excess of electrons, thus the children structures can be seen as a competition of the two lattices, where the balance is achieved for the α structure [45].

Some relevant references concerning atomic structures, synthesis, mechanic and electronic properties can be found in Refs. [40–44].

1.2 A common parent structure

In Fig. 1.1 we show the atomic structure of borophene δ_6, δ_3, β_{12} and α'-Bilayer together with the scanning tunneling microscopy images adapted from Refs. [32–35]. Already with these polymorphs we can see that some similarities exist between flat monolayers: for instance, δ_3 and β_{12} can be described from a common model structure: a periodic array of hexagonal building units in which every vertex describes an atomic position in-plane (see δ_3 in Fig. 1.2). This model structure is equivalent to δ_3, and we can see a similar hexagonal pattern in β_{12} with the difference that some of the hexagons are filled with a boron atom in the center (Fig. 1.2). This visual comparison between δ_3 and β_{12} allows us to think of δ_3 as a "template" for β_{12}, thus we will refer to this conceptual δ_3 model structure as "parent structure" of β_{12}.

We can recreate different polymorphs from this parent structure (δ_3), for example the α monolayer (Fig. 1.2). However, the empty hexagonal building units are not always compatible with the periodicity of more complex structures (see for example δ_5 and α_1 in Fig. 1.2). Hence, it is more convenient to construct a different parent structure, one in which all hexagons are filled by a boron atom in the center: we will refer to this model system as "B_T" (see in Fig. 1.2). Thus, using B_T, we can define a second conceptual mechanism to build other polymorphs: that is, removing atoms from the full hexagonal mesh. The latter is a more convenient choice than the honeycomb structure: we can easily relate it to different polymorphs simply by removing atoms without facing a problem with the commensurability of the different unit cells. Thus, we can say that B_T is a parent structure for the other polymorphs.

Using B_T as parent structure for other polymorphs is of course a simplification, nonetheless it helps us to make the conceptual association between different allotropes to a common parent structure (B_T). Two assumption come with this model: 1) B_T is perfectly regular (all bond distances are equal), and planar, and 2) the creation of vacancies from B_T does not affect the bond lengths of the 'B_T + hole' structure. Under these assumptions, B_T acts a parent structure for other polymorphs, and thus, it is convenient to define its atomic density (number of boron atoms, N_{B_T}, per unit area, A) as:

$$\rho_{N_{B_T}} = \frac{B_T}{A} \tag{1.1}$$

Creating holes in the model system to construct other polymorphs results in a different atomic density, $\frac{N_{B_P}}{A}$, in the children structures, thus it is convenient to write a quantity that characterizes this difference. For instance, an extended practice [14–17, 45–49] is to define this change with respect to B_T as (Eq. 1.2):

$$\eta_P = \frac{\rho_{B_T} - \rho_{B_P}}{\rho_{B_T}} = \frac{N_{B_T} - N_{B_P}}{N_{B_T}} \tag{1.2}$$

where η_P describes the number of holes per unit area that exist in a given polymorph P, with respect to the triangular mesh . Taking as an example δ_3, from Fig. 1.1, in its primitive unit cell one has $N_{\delta_3} = 2$, while for the same unit cell $N_{B_T} = 3$, and therefore $\eta_{\delta_3} = {}^1\!/_3$. Moreover, we can use this parameter η_P to express the density of valence electrons in a given polymorph as (Eq. 1.3):

$$\rho_{\text{el}}^P = 3\rho_{N_{B_T}}(1 - \eta_P) \tag{1.3}$$

Using η_P as a basic descriptor of the different polymorphs is a common practice, and some general observations in borophene have been linked to this parameter: perhaps the most notorious examples are the prediction of polymorphism, with the lowest-energy configurations occurring at $\eta = {}^1\!/_9$, ${}^1\!/_8$ and ${}^2\!/_{15}$ [14], and the discussion of the electronic stability of borophene, deriving in a concept known as "self-doping" [45, 46].

1.2.1   The self-doping picture

The search of stable borophene polymorphs is an area of intense research, and the problem is tackled from different perspectives: phonon spectra [16,18,50,50,51], formation energies [14, 17, 48, 52], temperature-dependent dynamics [18, 48, 49] and electronic stability [45,
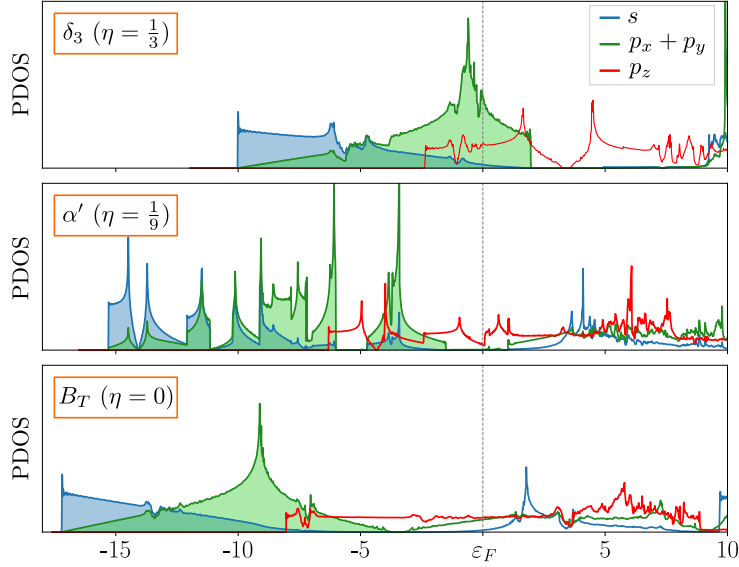
Figure 1.3: Projected density of states (PDOS) over atomic orbitals, averaged over the atoms in the unit cell (computational detail in Section 3): the three plots are in the same XY scale, and the shaded regions correspond to the bonding states in-plane according to Ref. [45]. From the bondind/antibonding definition of the states it follows that: 1) in δ_3 not all bonding states are filled hence it is electron-deficient, 2) B_T has an excess of electrons thus overfilling the in-plane states, and 3) the "optimal" filling of bonding states occurs at $\eta = 1/9$: all in-plane bonding states are full, and the antibonding ones are empty). Moreover, we highlight the resemblance between the PDOS of B_T and δ_3 supporting the self-doping picture [46], but also the difference with respect to α' showing the limitations of using a rigid electronic structure.

47]. Among the latter, we highlight the works of Tang and Ismail-Beigi, describing the lowest-energy electronic configurations of the polymorphs in terms of the bonding and antibonding character of the bonds [45, 46]: in these studies η_P plays a key-role as an indicator of stability.

From Ref. [45], bonding and antibonding in-plane states of different polymorphs are distinguished from each other by a gap in the computed density of states (see Fig. 1.3). And from this distinction, it follows that: 1) polymorphs which bonding states are not fully occupied are electron deficient (not all bonding states are full), hence electronically unstable (δ_3 in Fig. 1.3). 2) the more electronically stable configuration is that in which the bonding states in-plane are fully occupied, while the in-plane antibonding ones are empty ($\eta = 1/9$ in Fig. 1.3). 3) Polymorphs with $\eta < 1/9$ have an excess of electrons with respect to the optimal η_α configuration (B_T in Fig. 1.3).

In these observations η served as an indicator of the number of electrons for the optimal filling of the states (and its divergence from it). Moreover, it suggested that upon the addition or removal of atoms, the bonding and antibonding states in the electronic structure are not changed, but just filled differently according to the number of electrons in the system. This behavior of the electronic structure was later described also by Tang and Ismail-Beigi, in a concept known as "self-doping"[2] [46]: in this, it is proposed to look at borophene in terms of a rigid electronic structure, in which the change of the atomic structure can be simply linked to the change of the atomic density ρ_{B_P}, and therefore

---

[2]The self-doping picture was discussed based on two factors: 1) the occupation of the states, and 2) the wave functions of specific states resembling each other even among different structures.

the vacancy ratio, η_P, which in turn can be directly linked to the number of electrons (Eq. 1.3) and hence the filling of the states. In other words, the electronic structure of different polymorphs can be estimated by using a fixed borophene electronic structure (for example of the parent structure B_T), and the vacancy ratio η.

The doping mechanism is discussed on the basis of two sublattices in competition (δ_3 and B_T): one being electron-deficient (δ_3), and the other one acting as electron donor (B_T) [45]. Therefore with the use of a fixed electronic structure, and the combination of the two sublattices, self-doping provides a simple rule to relate the atomic structure with the electronic structure. Along the same line, Zhang *et al.* observed that the occupation of bonding and antibonding π orbitals (out-of-plane) can also play a role in the stability of the polymorphs [52], and more recently Qiu and co-workers [47] noted that the self-doping mechanism might occur from π-to-σ orbitals upon the creation of vacancies in the B_T structure.

It is worth pointing out that, from multiple and extensive first-principles calculations [14, 17, 48, 49, 52], η has been shown to be good indicator of the theoretical stability of borophene polymorphs (finding the lowest-energy configurations), and thus it has been largely adopted in the literature. However, the electronic occupation of the states of a freestanding isolated layer is not enough to describe the stability of a system in all circumstances. For instance, in Ref. [45] it is suggested that the electron deficient polymorph δ_3 might stabilize upon the obtention of electrons from a different source. This was later investigated by Zhu *et. al.* [51], by doping the δ_3 monolayer with 1 electron per boron atom (reaching $\eta = 1/9$). Still, imaginary frequencies in its phonon spectrum were found[3] [51].

In this work we will use η and the self-doping mechanism as a starting point for studying the electronic structure of different polymorphs. Look, for example, at the atomic orbital projected density of states (PDOS) of borophene δ_3 and B_T in Fig. 1.3: despite being different polymorphs, the PDOS look very similar, hence suggesting the similarity of their electronic structures (in line with the self-doping picture). Regarding α' in Fig. 1.3, there are some obvious differences with respect to δ_3 and B_T: overall one finds, a more complicated shape of the PDOS, and in particular a gap opening between the in-plane bonding states. We will address in Section 5 the differences of the electronic structure of the different polymorphs. For now, let us highlight that even in this more complicated situation there is a rigid shift of the electronic structure with respect to the Fermi energy: we can see this from the in-plane bonding states and also from the filling of the out-of-plane states. Hereafter we describe the set of polymorphs selected for this work.

1.3   Selected polymorphs

The selection of polymorphs for this study was based on their structural differences and relevance for the theoretical and experimental results found in literature. We included five flat monolayers: B_T, δ_3, β_{12}, α_1 and δ_5, two buckled monolayers: α' and δ_6, and the AA-stacked α'-bilayer, from Refs. [16, 18, 27, 32, 35, 53] (atomic structures in Figure 1.4). Below, we describe the unit cells of the selected polymorphs as-used in this work:

---

[3]The stabilization of δ_3 on a metallic substrate is not due to the electron transfer, but to the hybridization with the substrate [51].
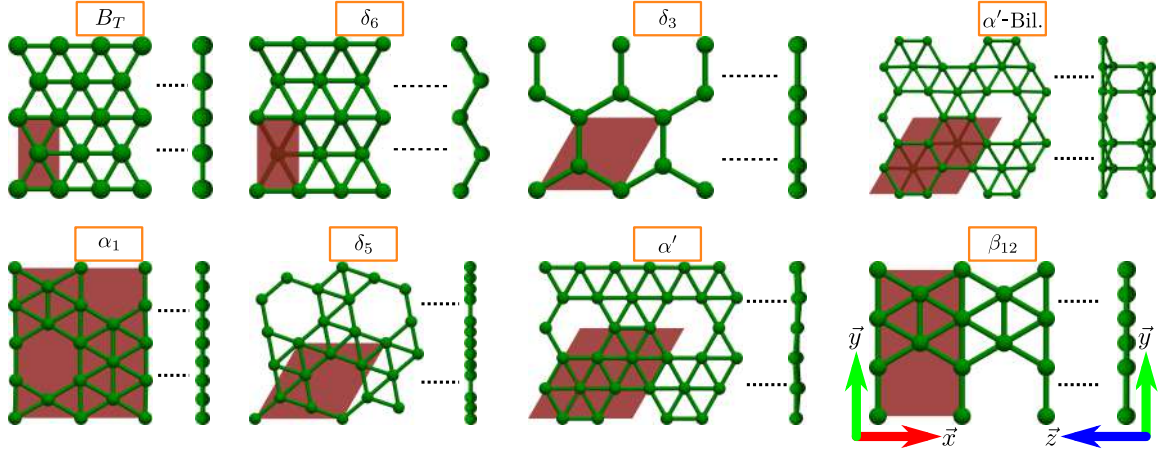
Figure 1.4: Atomic structure of borophene polymorphs. We selected a set of borophene polymorphs for our study, including flat, buckled and bilayer structures from Refs. [16,18,27,32,35,53]. As all polymorphs are two-dimensional we present their projection in the xy-plane, accompanied by a projection of the structure in the yz-plane. In our calculations we have used the unit cells highlighted in brown, unless otherwise specified.

symmetry, atomic positions (Wyckoff sites), lattice parameters, number of atoms per unit cell and vacancy ratio.

B_T: This structure is a model system, flat and regular, and we use it only for comparison with other structures. However, since this polymorph buckles upon the full optimization of the atomic positions (leading to the δ_6 structure), there are no optimal lattice parameters nor atomic positions, although some constrained calculations can be found in the literature [45,50]. We built this structure by imposing equal bond lengths choosing between the two bond distances from δ_6. We found found no significant difference among the two choices (see Appendix IV). Thus, for comparison, we simply selected the structure with bond distances 1.68 Å.

δ_3: The graphene-like structure belongs to the group of the synthesized borophene polymorphs [34]. It contains two-atoms per unit cell in a hexagonal system with symmetry $P6/mmm$ at the positions $2c$. The atomic positions and lattice parameters were obtained from Ref. [53]. In the latter reference the in-plane parameters are $a = b = 2.91$ Å, calculated with DFT-GGA using the Perdew-Wang exchange-correlation functional [54].

β_{12}: This is a popular polymorph which has been successfully synthesized and used as toy model due to its high stability and promising properties regarding transparent conductors, superconductivity and plasmonics, among others [19, 27, 31, 33, 36, 55]. It contains five atoms per unit cell in a structure with symmetry $Pmmm$, with positions $2m$, $2o$ and $1e$, the latter being in the center of the hexagonal building unit. The in-plane dimensions for this structure were obtained from the calculations of Ref. [27]: $a = 2.92$ and $b = 5.06$ Å. These parameters are in good agreement with the theoretical (GGA-PBE) and experimental parameters of β_{12} on Ag(111) from Refs. [33,55].

α_1: The theoretical research concerning the structural features of borophene, mainly based on formation energies and phonons, lead to a structure known as α_1. This structure has not gained much attention within the community. Nonetheless, recently it has been predicted to appear under low boron concentration and low temperatures [49]. This polymorph contains 14 atoms per unit cell in a structure with *Cmmm* symmetry, localized at the positions *4i*, *8p* and *2b*. The lattice parameters ($a = 5.84$, $b = 6.74$ AA) and atomic positions were obtained from Ref. [16] via DFT calculations using the exchange-correlation functionals PBE and PBE0 [56].

δ_5: Different structures have emerged as a result of the search for stable polymorphs with specific properties, among which we highlight the case of δ_5, the only polymorph here presented without any six-coordinated atom, and which has been mentioned in the literature for showing a Dirac cone at K as in graphene, although above the Fermi energy [17, 18]. The unit cell has symmetry *P6/m* with lattice parameters $a = b = 4.47$ Å, with six atoms at the sites *6j*, as obtained from Ref. [18] via DFT-GGA calculations using the PBE exchange-correlation functional.

α': In terms of formation energy and electronic stability one of the most investigated structures is the planar α polymorph [14, 15, 45, 57]. This was, however, found to be unstable and it was predicted to show a slight distortion out-of-plane. The resulting polymorph was called α' [16]. The unit cell of this polymorph has symmetry *P-3m1*, with 8 atoms at the positions *6g* and *2d*. For this case, the atomic positions and lattice parameters were optimized in the present work using DFT-GGA (PBE) [58], and the lattice parameters were found to be $a = b = 5.058$ Å, with an off-plane displacement of the two atoms by ± 0.085 Å. The optimized structure can be compared with Refs. [16,59]. In Ref. [16], $a = 5.046$ and $b = 5.044$ Å (DFT-PBE) with buckling distance of ± 0.17 Å (atomic positions optimized with PBE0 on top of the PBE-optimized lattice parameter structure), while in Ref. [59] $a = b = 5.10$ Å with the off-plane displacement of ± 0.14 Å (DFT-PBE). Despite the differences in the atomic structure the electronic structure is almost unaffected (see Appendix IV).

δ_6: Starting from the hypothetical flat triangular structure B_T, the flat configuration has been shown to be thermodynamically unstable, and it has been predicted to buckle, leading to the so-called δ_6 polymorph [50, 60]. This system has symmetry *Pmmn* and contains two atoms per unit cell at positions *2a*. The lattice parameters, in-plane, are $a = 1.62$ and $b = 2.87$ Å, with a buckling height of 0.80 Å. These were obtained from Ref. [32] (DFT-PBE) and are in good agreement with the experimental results on Ag(111) in the same reference.

α'-Bilayer: We selected this polymorph for easy comparison with the α'-monolayer. The unit cell has symmetry *P6/mmm*, and the atoms are at the positions *12n* and *4h*. For this polymorph we optimized the lattice parameters and atomic positions (for more computational details see Section 3), and we obtained $a = b = 5.70$ Å, with distances among the bottom layer and top layer of 1.80 and 3.10 Å, for the inner and outer atoms of the bilayer, in excellent agreement with the reference structure from Ref. [35] calculated with DFT-PBE, and their experimental measurements on Ag(111).

	η	Symmetry	Lattice parameters (Å)		Wyckoff sites (atomic positions)
			a	b	
B_T	—	*P6/mmm*	1.68	1.68	*1a* $(0.00, 0.00, 0.00)$
δ_3	$^1/_3$	*P6/mmm*	2.91	2.91	*2c* $(0.33, 0.66, 0.00)$
β_{12}	$^1/_6$	*Pmmm*	2.92	5.06	*2m* $(0.00, 0.83, 0.00)$ *2o* $(0.50, 0.33, 0.00)$ *1e* $(0.00, 0.50, 0.00)$
α_1	$^1/_8$	*Cmmm*	5.84	6.67	*4i* $(0.00, 0.75, 0.00)$ *8p* $(0.75, 0.12, 0.00)$ *2b* $(0.50, 0.00, 0.00)$
δ_5	$^1/_7$	*P6/m*	4.47	4.47	*6j* $(0.57, 0.72, 0.00)$
α'	$^1/_9$	*P-3m1*	5.06	5.06	*6g* $(0.33, 0.00, 0.00)$ *2d* $(0.33, 0.66, -0.00)^*$
δ_6	—	*Pmmn*	1.62	2.87	*2a* $(0.25, 0.25, -0.02)$
α'-Bil.	—	*P6/mmm*	5.70	5.70	*12n* $(0.33, 0.00, -0.07)$ *4h* $(0.33, 0.66, -0.04)$

Table 1.1: Structural parameters of selected borophene polymorphs. Here we have summarized the structural features of the different borophene polymorphs as used in this work. The atomic positions are reported in reduced coordinates (rounded to two decimals), with $c = 19.05$ Å ($c = 21.17$ Å exceptionally for the α'-Bilayer). $^*\alpha'$ has a slight out-of-plane distortion of $-0.0045c$.

We summarize the atomic structure of the different polymorphs as used in this work in Table 1.1: vacancy ratio with respect to B_T, symmetry, lattice parameters, and Wyckoff sites (atomic positions).

It is worth remarking that the literature in the search of stable polymorphs is extensive and goes far beyond the structures here presented: for instance, we can find other bilayer structures [39,61], borophene with large holes [48,49], intermixed superstructures [37,38], polymorphs with Dirac cones [18,62] and Kagome lattices [63], among others. What is interesting to notice is that in this large family of polymorphs there is only a single atomic species: boron. Thus, all the different properties that the multiple polymorphs exhibit can be related just to the different atomic structure. Therefore, borophene constitutes an excellent playground to study how the atomic structure determines the properties of the system.

In this work we focus in this fundamental question: the relation between the atomic structure with the electronic structure (Section 5), and hence with the properties of different borophene polymorphs. In particular, we focus on the dielectric properties, and more specifically optical absorption and loss function (Section 6), and the static response (Section 7).

Theoretical methods

2.1 Density functional theory

2.1.1 The many-body problem

The description of matter and its interactions require (in principle) from a full description of the problem: all internal and external forces. However, depending on the scale at which a given phenomena of our interest occurs we could address the problem differently, for instance, if we delimit the problem only to field popularly-known as "condensed matter", *i. e.*, only the interaction between nuclei and electrons, then we would be talking of the so-called "many-body problem". This is the case of our interest, and we relate the solution of the many-body problem to the determination of the eigenstates and eigenfunctions of the Schrödinger equation $\hat{\mathscr{H}}_{\mathrm{MB}}\Psi(\{\mathbf{r},\mathbf{R}\}) = E\Psi(\{\mathbf{r},\mathbf{R}\})$, with

$$\hat{\mathscr{H}}_{\mathrm{MB}} = -\sum_{I}\frac{\hbar^2}{2M_I}\nabla_{\mathbf{R}_I}^2 - \sum_{i}\frac{\hbar^2}{2m_e}\nabla_{\mathbf{r}_i}^2 + \frac{1}{2}\sum_{IJ(J\neq I)}\frac{Z_I Z_J e^2}{|\mathbf{R}_J - \mathbf{R}_J|} + \frac{1}{2}\sum_{ij(j\neq i)}\frac{e^2}{|\mathbf{r}_i - \mathbf{r}_j|} \\ -\sum_{iI}\frac{Z_I e^2}{|\mathbf{R}_I - \mathbf{r}_i|} \tag{2.1}$$

where m_e (M_I) and $\mathbf{r}_i$ ($\mathbf{R}_i$) are the mass and position of the electron i (ion I), respectively, and Z_I the atomic number of ion I.

The solution of Eq. 2.1 is, however, impossible for complex systems (both analytically and numerically) and we are forced to approximate the Hamiltonian in some way or another. A simple, but very powerful approximation is the Born-Oppenheimer (BO) approximation [64], which takes into account the fact that electronic transitions occur at much larger energy scales than the vibrational ones, such that for a given solution of the many-body problem, in presence of nuclear motion, the electronic states are unaffected[1]. This implies that upon nuclear motion the electron-nucleus term in Eq. 2.1 must remain unchanged, and thus it is common to think about the this approximation as the electrons instantaneously adjusting to the nuclear positions. An equally valid interpretation is that, for a given electronic structure, the nuclei remains immobile ("frozen"), and therefore we can neglect the contribution of the kinetic energy of the nuclei (first term in the right side of Eq. 2.1) [65].

---

[1]This is not true for metals as there can be electronic transition at almost zero energy. However in metals the electron-hole pairs carry low oscillator strength and thus they they have a very small effect on the lattice (Migdal's theorem) [65,66].

The Born-Oppenheimer approximation allows us to write the many-body wave function in the form (Eq. 2.2):

$$\Psi(\{\mathbf{r}, \mathbf{R}\}) = \psi(\{\mathbf{r}; \mathbf{R}\})\Theta(\mathbf{R}) \tag{2.2}$$

composed of a nuclear $\Theta(\mathbf{R})$, and an electronic wave function $\psi(\{\mathbf{r}; \mathbf{R}\})$ that depends parametrically on the atomic positions.

Another important approximation that help us simplify the many-body problem is to treat the atomic nuclei as classical particles, which is justified from the mass of the nuclei being large and thus their wave function highly localized [65, 67]. This latter approximation results in a very convenient description of the nuclei as point charges, such that the nucleus-nucleus term in Eq. 2.1 can then be treated by simple electrostatics, and its contribution to the energy computed apart; this known as the Madelung energy [68]. Making use of both the Born-Oppenheimer approximation and considering the atomic nuclei as classical particles we can simplify the complete many-body problem to the electronic many-body problem $\hat{\mathscr{H}}_{\mathrm{MB}}^{el}\psi(\{\mathbf{r}; \mathbf{R}\}) = E^{el}\psi(\{\mathbf{r}; \mathbf{R}\})$ with

$$\hat{\mathscr{H}}_{\mathrm{MB}}^{el} = -\frac{1}{2}\sum_i \nabla_{\mathbf{r}_i}^2 + \frac{1}{2}\sum_{ij(j\neq i)} \frac{1}{|\mathbf{r}_i - \mathbf{r}_j|} - \sum_{iI} \frac{Z_I}{|\mathbf{R}_I - \mathbf{r}_i|} \tag{2.3}$$

Unfortunately these two approximations are not enough to tackle the many-body problem in condensed matter (as in Eq. 2.3), and this is simply because in an usual situation there are more electrons than nuclei concerned in the problem. Thus, even with the approximations described above we still need to account for all interactions between electrons. Naturally, a different description of the problem is necessary. For the following section (for historical reasons) we will rename the terms in Eq. 2.3, respectively, as $\hat{\mathscr{H}}_{\mathrm{MB}}^{el} = \hat{\mathscr{T}} + \hat{\mathscr{U}}_{ee} + \hat{\mathscr{V}}$, where $\hat{\mathscr{T}}$ and $\hat{\mathscr{U}}_{ee}$ are the kinetic and potential energy operators describing the electron-electron interactions, and $\hat{\mathscr{V}}$ is the potential energy operator describing the interaction between the classical nuclei and the electrons (commonly referred to as the external potential).

2.1.2 The electron density as a variable

In 1964 W. Kohn and P. Hohenberg proposed a different perspective into this problem for the ground state of a system: instead of solving the many-body Shrödinger equation which necessarily requires from the explicit knowledge of the many-body wave-function, they proposed to look at the electron density [69]. Thus, they developed a different formulation of the many-body problem based solely in this single three-dimensional quantity. They proved what is famously known today as "the Hohenberg and Kohn theorems":

- The external potential V (to within a constant) is a unique functional of the ground state electron density n_0, and hence, the ground state many-body wave function Ψ_0 is also a unique functional of n_0.

$$\Psi_0 = \Psi_0[n_0] \tag{2.4}$$

- Since the ground state many-body wave function is a unique functional of the ground state electron density, also the kinetic term (T) and the electron-electron potential

(U_{ee}) of Eq. 2.3, and thus $F[n_0]$ (Eq. 2.5) is a universal functional of the ground state electron density,

$$F[n_0] = T[n_0] + U_{ee}[n_0] \qquad (2.5)$$

These theorems have an important implication: that, upon the selection of the correct (ground state) electron density, we can obtain the ground state total energy for a given external potential. Thus, we can search for the ground state simply via minimization of the energy by varying the electron density in Eq. 2.6,

$$E[n] = F[n] + \int V(\mathbf{r})n(\mathbf{r})\mathrm{d}\mathbf{r} \qquad (2.6)$$

The latter equation (Eq. 2.6) works as an analogy to the electronic many-body Schödinger equation, but instead of needing from the many-body wave function it requires from the (much simpler) electronic density. In principle this is a huge simplification of the problem, but in practice the challenge of the density functional formalism resides on the fact that we do not know the many-body electron density, and even if we knew it, we do not know the universal functional $F[n]$ [65, 69], so the computability of the ground state and its observables remains unsolved. The complication relies on the many-body nature of the problem, in particular in a property known as correlation.

Correlation and exchange

In the density functional theory, as with the many-body Schrödinger equation, we have exponentially increasing number of electron-electron interactions with respect to the number of electrons in the system (given by $\hat{\mathcal{U}}_{ee}$) [70]. For simplicity we can think about this problem in classical terms in which all electrons are point charges: we observe from Eq. 2.3 that the dynamics of one of these single particles depends on each of all the others to a lower or higher extent, depending on the distance to each of them by simple electrostatics. This is in fact a first approximation to the problem, and it is known in the literature as the Hartree potential (Eq. 2.7) [65, 67, 70, 71]:

$$\hat{\mathcal{V}}_H = \frac{1}{2} \sum_{ij(j \neq i)} \frac{n(\mathbf{r}_i)n(\mathbf{r}_j)}{|\mathbf{r}_i - \mathbf{r}_j|} \qquad (2.7)$$

This approximation assumes that the electric field of each of the charges remains static regardless of the multiple interactions, however in a more realistic situation the electric field "adjusts" to the medium, or in other words, it is screened by the medium [65, 69]. This screening effect modifies not only the potential energy, but it also has an effect on the kinetic term. We refer to this phenomenon inherent of the many-body problem as correlation[2].

In the density functional theory a term that appears together with correlation is exchange, but contrary to correlation, exchange cannot be understood classically. Exchange is an effect of Pauli's exclusion principle that states that that two fermions cannot be in

---

[2]Correlation in the electronic many-body problem is field of intense research for which multiple approximations exist, from the simpler ones neglecting correlation (Hartree or Hartree-Fock), to the more refined ones such as GW [71–73].

the same state. Thus, two electrons cannot share the same position unless they have different spin; this translates as their many-body wave function being antisymmetric [72,74], and as it occurred with correlation, as a correction of the energy which can also be related to a screening effect [65,75].

2.1.3 The Kohn-Sham equations

Addressing the complexity of the many-body problem in the density functional formalism, in 1965 W. Kohn and L. Sham proposed to rewrite the universal functional $F[n]$ into a more practical form, mapping the real system of interacting electrons onto a set of fictitious non-interacting particles giving the same ground state density as its interacting counterpart ($\rho = n_0$) [76]. Using this fictitious system of non-interacting particles $\phi_i(\mathbf{r})$, we can write the density of the non-interacting system $\rho = \sum_i |\phi(\mathbf{r})_i|^2$, and with it a new set of equations known as the Kohn-Sham (KS) equations (Eq. 2.8) [65,67]:

$$\left[-\frac{1}{2}\nabla^2_{\mathbf{r}_i} + V_{KS}([\rho], \mathbf{r}) \right] \phi_i(\mathbf{r}) = \varepsilon_i \phi_i(\mathbf{r}) \tag{2.8}$$

with

$$V_{KS}([\rho], \mathbf{r}) = V(\mathbf{r}) + V_H([\rho], \mathbf{r}) + V_{xc}([\rho], \mathbf{r}) \tag{2.9}$$

These equations are very similar to the original electronic many-body problem (Eq. 2.3), but there are some subtleties to highlight: 1) the Hartree potential (unscreened by definition, Eq. 2.7) plays the main role as the potential energy, 2) the kinetic energy of a non-interacting particle does not depend on all the intricate interactions with other particles and it is therefore simply $T_i = \frac{1}{2}\langle\phi_i|\nabla^2|\phi_i\rangle$ and 3) as these two latter quantities are not enough to recover the full information of the many-body system, a new extra term appears accounting for the missing terms: exchange and correlation, V_{xc}. We can write the universal functional in terms of the non-interacting system as (Eq. 2.10):

$$F[\rho] = T[\rho] + U_H[\rho] + E_{xc}[\rho] \tag{2.10}$$

Comparing Equations 2.5 and 2.10 we can notice the simplification of the problem from the interacting case to the non-interacting one, but we can also point out the complexity of the exchange-correlation functional as it is becomes "all what we cannot easily define from the electronic many-body problem". We know however that upon the correct choice of the density we can find the ground state variationally [69], thus we can use the variational principle to write the exchange-correlation potential as $V_{xc}([\rho], \mathbf{r}) = {\delta E_{xc}[\rho]}/{\delta n(\mathbf{r})}$[3].

The search for the ground state

Using Eqs. 2.8 and 2.9 (and under the supposition that we know an approximation for V_{xc}) we still face a challenge: we need to find the ground state density of the non-interacting system such that it is equal (or approximate) to the real many-body density ($\rho = n_0$). In practice this is solved self-consistently in a cycle known as the self-consistent field (SCF):

---

[3]This of course goes back to the main challenge: knowing the true many-body density, however different approximation for V_{xc} have proven to reproduce properties of the real systems such as the local density approximation [76,77], or the Perdew-Burke-Ernzerhof (PBE) exchange-correlation functional [58]

- From a given external potential $V(\mathbf{r})$, we take an initial guess to construct a test non-interacting density, ρ_{in}.

- We use this density to build the KS potential (Eq. 2.9) and solve the KS equations (Eq. 2.8). This step gives us a set of non-interacting orbitals $\phi_i(\mathbf{r})$, from which we construct a new density ρ_{out}.

- Then we compare ρ_{in} with ρ_{out}, and if they are equal (or approximate within a given threshold) the cycle is stopped as convergence has been reached, and thus we have obtained the ground state related to the given external potential.

- If the ground state was not reached then ρ_{out} is modified and re-fed into the SCF cycle.

- The cycle stops when the ground state is reached.

The SCF cycle takes advantage of the Hohenberg and Kohn theorems and the Kohn-Sham equations to through an iterative process find the ground state non-interacting density that resembles the most the many-body electron density. This cycle is the basis of any density functional theory calculation, and there is a lot of work in the literature on, for example, how to make efficient modifications of the output density before being reintroduced into the KS potential [78–80]. These details however lie out of the scope of this work, and in particular out of the scope of this section in which we aimed to introduce the basic concepts of the density functional theory. Some relevant approximations concerning the computational details related to our DFT calculations are discussed in Section 3.

2.2 Time-dependent density functional theory

Density functional theory (DFT) is a time-independent theory that describes the ground state of a system, but sometimes we are interested on the evolution of the system due to a time-dependent perturbation, for example to describe electronic excitations, for which we need to reformulate the problem. Naively, we could think of solving the time-dependent Schrödinger equation $\hat{\mathscr{H}}(\{\mathbf{r}\}, t)\Psi(\{\mathbf{r}\}, t) = i\hbar\frac{\partial}{\partial t}\Psi(\{\mathbf{r}\}, t)$, but we would immediately encounter the same problem as before due to electronic correlation. Naturally, we would have to recast the problem in a similar form as within the DFT. The time-dependent extension of the DFT was formulated by Runge and Gross in 1984, and it is known today as the Time-dependent density functional theory (TDDFT). Similarly to the DFT, the TDDFT relies on two theorems:

- Two densities $n(\mathbf{r}, t)$ and $n'(\mathbf{r}, t)$ evolving from the same initial state $\Psi(\{\mathbf{r}\}, t = 0)$, due to two different time-dependent external potentials $V(\mathbf{r}, t)$ and $V'(\mathbf{r}, t)$ (Taylor expandable) eventually differ if the potentials differ from more of a time-dependent-only constant $c(t)$. As in the first HK theorem, this implies a one-to-one correspondence between the potentials and the electronic densities. Therefore, in the TDDFT as in the DFT, the potentials are unique functionals of the density, and so the wave functions are also unique functionals of the density.

$$\Psi(t) = \Psi([n], t) \tag{2.11}$$

- For a time-dependent external potential the total energy is not conserved as it is also a time-dependent quantity, thus the use of the variational principle to find the wave functions as in the DFT is excluded. However, in analogy to the energy, we can use the quantum-mechanical action functional (Eq. 2.12), which derivative to respect to a many-body wave function vanishes at the true many-body wave function. Thus, we can solve the time-dependent problem by finding stationary solutions of the action.

$$A[n] = \int_0^{t_1} \mathrm{d}t \, \langle \Psi[n] | \, \mathrm{i}\frac{\partial}{\partial t} - \hat{\mathscr{H}}(t) \, | \Psi[n] \rangle \tag{2.12}$$

2.2.1 Time-dependent Kohn-Sham equations

Similarly as for DFT from the Hohenberg-Kohn theorems, TDDFT from Runge-Gross requires to be approximated, as we do not know nor the initial many-body electron density nor the functionals. Thus, it is convenient to recast the many-body problem onto a set of non-interacting particles yielding the density $\rho(t) = \sum_i |\phi_i(\mathbf{r}, t)|^2$, and consequently the time-dependent version of the Kohn-Sham equations, analogously to Eqs. 2.8 and 2.9:

$$\left[-\frac{1}{2}\nabla_{\mathbf{r}_i}^2 + V_{KS}([\rho], \mathbf{r}, t) \right] \phi_i(\mathbf{r}, t) = \mathrm{i}\frac{\partial}{\partial t}\phi_i(\mathbf{r}, t) \tag{2.13}$$

with

$$V_{KS}([\rho], \mathbf{r}, t) = V(\mathbf{r}, t) + V_H([\rho], \mathbf{r}, t) + V_{xc}([\rho], \mathbf{r}, t) \tag{2.14}$$

The time-dependent Kohn-Sham potential (Eq. 2.14) contains similar ingredients as the time-independent case: the time-evolution of the Hartree, exchange-correlation and external potentials. It is worth pointing out that the external potential, in the static case, we had associated it only with the electron-ion interaction (Eq. 2.3), but now besides the electron-ion interaction, it must also contain the external time-dependent perturbation for which the TDDFT formalism was built. Moreover, this external perturbation we would like to link it to a certain physical phenomena, and in that regard it results more convenient to resort to linear response theory.

2.2.2 Linear response theory

We now assume that the external time-dependent perturbation is small, such that we can approximate the time-evolution of the density perturbatively: to first order $n(\mathbf{r}, t) \approx n(\mathbf{r}) + \delta n(\mathbf{r}, t)$, where the first term in the right describes the static density (ground state, n_0), and the second one the "induced density" by means of a time-dependent perturbation $\delta V(\mathbf{r}', t')$. Moreover, in linear response we can write the induced density using a response function χ describing the response of the electronic system to the external time-dependent perturbation. The linear-response induced density reads (Eq. 2.15):

$$\delta n(\mathbf{r}, t) = \int dt' \int d\mathbf{r}' \chi(\mathbf{r}, \mathbf{r}', t - t') \delta V(\mathbf{r}', t') \tag{2.15}$$

and characterizes the change of the electronic density at point $\mathbf{r}$ and at time t, by a perturbation at point $\mathbf{r}'$ and time t'. This function aims to describe how the complete density "reacts" to an external perturbation, and because the reaction cannot occur prior to the perturbation, then $t > t'$ (this condition is known as causality: $\chi = 0$ for $t < t'$).

Notice that in Eq. 2.15 we are still using the notation of the many-body electron density that we have used in the DFT and TDDFT (n). This is because, besides the linear approximation, we have not defined $\chi(\mathbf{r}, \mathbf{r}', t - t')$, meaning that, in principle, we can make any approximation for this quantity (or use the many-body response function if we knew it) and use it in Eq. 2.15 to compute the linear density response. χ is known as the polarizability, and particularly in the TDDFT framework as the density-density response function. Although we are free to choose any approximation, it results convenient to use the Kohn-Sham scheme of non-interacting particles, in which the KS density-density response function in real-space and frequency domain[4] reads:

$$\chi_{KS}(\mathbf{r}, \mathbf{r}', \omega) = \sum_{nn'} \frac{(f_{n'} - f_n)\phi_{n'}^*(\mathbf{r})\phi_n(\mathbf{r})\phi_n^*(\mathbf{r}')\phi_{n'}(\mathbf{r}')}{\omega - (\varepsilon_n - \varepsilon_{n'}) + i\eta} \tag{2.16}$$

where n and n' are electronic states, and f_n the electronic occupation number of state n. η is just an infinitesimal number such that the χ_{KS} does not diverges when $\omega = (\varepsilon_n - \varepsilon_{n'})$, i. e., for an electronic excitation between states n and n'. We refer to the Kohn-Sham density-density response function in Eq. 2.16 as χ_{KS}, but it is also common to find it referred to as χ^0, and as the "independent-particles" approximation (IPA).

The Dyson equation

Ideally, we would like to go beyond the IPA, for example, to describe collective electronic phenomena such as plasmons. For this, we can look back to Eq. 2.16: the linear response induced density should be the same regardless of the level of approximation we use, thus we can write $\delta n_{MB}(\mathbf{r}, t) = \delta n_{KS}(\mathbf{r}, t)$, with both induced densities taking the form of Eq. 2.16, one many-body and the other one Kohn-Sham. Taking the integrands of Eq. 2.16 many-body and Kohn-Sham, we can write an expression for χ_{MB}:

$$\begin{aligned} \chi_{MB} = \chi_{KS}\frac{\delta V}{\delta V} &= \chi_{KS}\frac{\delta V + \delta V_H + \delta V_{xc}}{\delta V} \\ &= \chi_{KS}\left(1 + \frac{\delta V_H}{\delta V} + \frac{\delta V_{xc}}{\delta V}\right) \end{aligned} \tag{2.17}$$

and, because V_H and V_{xc} are functionals of the density, we can use the chain rule $\frac{\delta V_H}{\delta V} = \frac{\delta V_H}{\delta n}\frac{\delta n}{\delta V}$, from where we can recognize $\frac{\delta n}{\delta V} = \chi_{MB}$, so:

$$\chi_{MB} = \chi_{KS} + \left(\frac{\delta V_H}{\delta n} + \frac{\delta V_{xc}}{\delta n}\right)\chi_{MB} \tag{2.18}$$

---

[4]We prefer frequency domain over time domain because it gives us an straightforward representation of the polarizability in a pole structure (see Eq. 2.16) that we can relate to electronic excitations.

moreover, the functional derivative of the Hartree potential with respect to the density is simply the coulomb potential. Thus, we can write a final expression that allow us to obtain χ_{MB} in terms of the Kohn-Sham response function, the Coulomb potential and the functional derivative of the exchange-correlation potential with respect to the density (we replace this term by f_{xc}), all in the form of a Dyson equation (Eq. 2.19):

$$\chi_{MB} = \chi_{KS} + (V_c + f_{xc})\,\chi_{MB} \tag{2.19}$$

Equation 2.19 is the protagonist of the linear response theory, and simply by looking at its ingredients we can realize that it is analogous to the Kohn-Sham equations in the DFT and TDDFT: in Eq. 2.19, as in the Kohn-Sham equations, we have separated the terms that we know how to calculate from the one term that we do not know: the one containing the information on exchange and correlation. In the linear response theory this term is referred to as the "exchange-correlation kernel". As for V_{xc}, different approximations exist in the literature for f_{xc}, and the selection of either one or another relies on the spectroscopic quantities that one wants to describe. In the following section we introduce two relevant quantities used this work: absorption and electron energy loss.

2.3 The polarizability as a main ingredient

The advantage of computing the response with Eq. 2.19 lies in the starting point: the Kohn-Sham polarizability, which is straightforwardly defined from the one-particle orbitals $\phi_i(\mathbf{r})$ and their eigenvalues ε_i (Eq. 2.16). Thus, in principle, we can track the response of a system all the way down to the wave functions, or to the mixing of the orbitals with the Coulomb potential and the exchange correlation kernel. Therefore, we can understand and approximate the different macroscopic quantities that can be measured experimentally, for example, absorbance, reflectance and loss function. Below, we define the main quantities used in this work, for simplicity for extended systems, in the reciprocal space. We start by rewriting Eq. 2.16:

$$\chi^0_{\mathbf{G}\mathbf{G}'}(\mathbf{q},\omega) = \sum_{nn'}(f_{n'} - f_n)\frac{\tilde{\rho}_{n'n}(\mathbf{q}+\mathbf{G})\tilde{\rho}^*_{n'n}(\mathbf{q}+\mathbf{G}')}{\omega - (\varepsilon_n - \varepsilon_{n'}) + \mathrm{i}\eta} \tag{2.20}$$

with $\tilde{\rho}_{n'n}(\mathbf{q}+\mathbf{G}) \equiv \langle n', \mathbf{k}' | e^{\mathrm{i}(\mathbf{q}+\mathbf{G})\cdot\mathbf{r}} | n, \mathbf{k} \rangle$. As we said earlier, Eq. 2.20 quantifies the response of a system to a time-dependent perturbation: Eq. 2.20 is the one-particle (Kohn-Sham) case, but the fully interacting polarizability can be obtained by solving the Dyson equation with the Coulomb potential and the exchange-correlation kernel (Eq. 2.19).

Upon the response of the system the latter induces a change in the potential which can be measured in linear response (similarly to Eq. 2.15) with the inverse microscopic dielectric function, ϵ^{-1}. This change in the total potential is also referred to as "screening" [81], and it relates to the fully interacting polarizability as:

$$\epsilon^{-1}_{\mathbf{G}\mathbf{G}'}(\mathbf{q},\omega) = \delta_{\mathbf{G}\mathbf{G}'} + v_c\chi_{\mathbf{G}\mathbf{G}'}(\mathbf{q},\omega) \tag{2.21}$$

with v_c the Coulomb potential, $v_c = \frac{4\pi}{|\mathbf{q}+\mathbf{G}|^2}$. Eq. 2.21 is tightly linked to experimental quantities via the macroscopic dielectric function ϵ_M [82,83]:

$$\epsilon_M(\omega) = \lim_{\mathbf{q}\to 0} \frac{1}{\left[\epsilon_{\mathbf{G}\mathbf{G}'}^{-1}(\mathbf{q},\omega)\right]_{\mathbf{G}=\mathbf{G}'=0}} \tag{2.22}$$

from where optical absorption and the loss function can be obtained as:

$$\text{Absorption} = \text{Im}\left(\epsilon_M\right)$$
$$\text{Loss function} = -\text{Im}\left(\frac{1}{\epsilon_M}\right) \tag{2.23}$$

Moreover, it is convenient to relate these quantities to an auxiliary polarizability, $\bar{\chi}$ [70, 84, 85]:

$$\epsilon_M(\mathbf{q},\omega) = 1 - v_c\bar{\chi}_{\mathbf{G}=\mathbf{G}'=0}(\mathbf{q},\omega) \tag{2.24}$$

which satisfies the Dyson equation $\bar{\chi} = \chi^0 + \chi^0\bar{v}\bar{\chi}$, where the auxiliary Coulomb potential $\bar{v} = v_c$ for $\mathbf{G} \neq 0$, and $\bar{v} = 0$ for $\mathbf{G} = 0$. In this sense, we can obtain an expression for ϵ_M with and without the mixing of the off-diagonal elements of the polarizability, *i. e.*, with and without crystal local field effects. For instance, for $\mathbf{G} = 0$, then $\bar{v} = 0$ and $\bar{\chi} = \chi^0$, consequently:

$$\epsilon_M^{NLF}(\mathbf{q},\omega) = 1 - v_c\chi_{00}^0(\mathbf{q},\omega) \tag{2.25}$$

We use Eq. 2.25 to compute properties without crystal local fields: this equation has a clear connection the Kohn-Sham polarizability, and its imaginary part with optical absorption (Eq. 2.23): we refer to this as the independent particles approximation (IPA).

On the other hand the local field effects are evaluated implicitly through the solution of the Dyson equation (Eq. 2.19), for example in the context of the random phase approximation (RPA) with $f_{xc} = 0$:

$$\chi = \chi^0 + \chi^0 v_c\chi \tag{2.26}$$

and with the definition of the macroscopic dielectric function via Eq. 2.22 and 2.23. This different choice with respect to Eq. 2.24 is preferred because it inherently contains the long range term of the Coulomb potential ($\mathbf{G} = 0$), which is of importance for extended systems [85, 86].

In the context of absorption along this work we refer to "without local field effects" to the IPA, hence Eq. 2.25, and "with local field effects" to the RPA with off-diagonal elements (Eq. 2.21). Note however that on solving the Dyson equation for χ (Eq. 2.19) we can also neglect the off-diagonal terms and include only the long range component: this is interesting for testing purposes, to identify whether a given effect comes from an specific element or another, in that case we refer to χ^{NLF}.

Experimental quantities in 2D systems

The equations presented above are formulated for periodic systems in the three spacial directions, but in 2D systems we are interested only on periodic systems "in-plane" that do not repeat out of plane as in a layered material. Nonetheless in practice it is common to threat 2D materials in 3D periodic codes by simply increasing the distance between layers far enough that they do not interact with each other (usually called the "supercell

approach"). This is an standard practice and in general yields good results upon the expense of large unit cells.

In terms of the optical properties however, in particular because of the long-range component of the Coulomb potential, the "replicas" of the 2D system can give spurious effects [87], and so different approaches have been developed that allow to threat separately the in-plane and out-of-plane components [87,88]. Nonetheless, different treatments yield differences in the out-of-plane response due to the ambiguity on the definition of the out-of-plane dimension: this is referred to as the "L_{mat} problem" in Ref. [88]; however, this is simply a consequence of the model, and thus the difference should not be reflected in experimental quantities. In that regard, in the supercell approach, absorbance is usually reported as: $Absorbance = \frac{\omega}{c}L_{mat}\mathrm{Im}\epsilon_\parallel$ with ω the energy of the photon, c the speed of light, L_{mat} the out-of-plane dimension of the simulation supercell, and $\epsilon_\parallel$ the in-plane component of the macroscopic dielectric function of an isotropic 2D system (see for example Ref. [31, 89]).

This ambiguity has been formally addressed in Refs. [88, 90], yielding the following expressions for the reflectance and transmittance coefficients of 2D isotropic systems (from Ref. [88]):

$$r_{pp} = \frac{i\sin\left(\kappa_p\right)\left[1 - 1/\epsilon_\perp \sin^2(\theta) - \epsilon_\parallel \cos^2(\theta)\right]}{2\sqrt{\epsilon_\parallel}\sqrt{1 - \left[1/\epsilon_\perp \sin^2(\theta)\right]}\cos\left(\kappa_p\right)\cos(\theta) - i\sin\left(\kappa_p\right)\left[1 - 1/\epsilon_\perp \sin^2(\theta) + \epsilon_\parallel \cos^2(\theta)\right]} \tag{2.27}$$

$$t_{pp} = \frac{2\sqrt{\epsilon_\parallel}\sqrt{1 - \left[1/\epsilon_\perp \sin^2(\theta)\right]}\cos(\theta)}{2\sqrt{\epsilon_\parallel}\sqrt{1 - \left[1/\epsilon_\perp \sin^2(\theta)\right]}\cos\left(\kappa_p\right)\cos(\theta) - i\sin\left(\kappa_p\right)\left[\left[1 - 1/\epsilon_\perp \sin^2(\theta)\right] + \epsilon_\parallel \cos^2(\theta)\right]} \tag{2.28}$$

with

$$\kappa_p = \frac{\omega}{c}L_{\mathrm{mat}}\sqrt{\varepsilon_\parallel}\sqrt{1 - \left[1/\varepsilon_\perp \sin^2(\theta)\right]} \tag{2.29}$$

and where θ is the angle of the incident light beam with respect to the out-of-plane component, and $\epsilon_\perp$ and $\epsilon_\perp$ the in-plane and out-of-plane component of the macroscopic dielectric function (complex). Both, r_{pp} and t_{pp} are complex quantities, thus $Reflectance = |r_{pp}|^2$ and $Transmittance = |t_{pp}|^2$, moreover $Absorbance$ is calculated indirectly as:

$$Absorbance = 1 - |r_{pp}|^2 - |t_{pp}|^2 \tag{2.30}$$

In this work we make the link between the absorption calculated by first principles and the experimental quantities using Eqs. 2.25, 2.28, 2.29, 2.30 with $\theta = 0$.

Computational parameters

The exchange-correlation term   The use of the electronic density as a variable does not imply any approximation thus, DFT by itself is not an approximated method. However, there is no universal solution for the exchange and correlation term, and therefore an approximation is required. The two mainly used are the Local Density Approximation (LDA) and the Generalized Gradient Approximation (GGA): in LDA the electron-electron interaction is locally treated as in an homogeneous gas for each point of the non-homogeneous electronic density of the system [91], while in GGA the variations of the electronic density in the vicinity of the point are considered through the inclusion of a gradient term [91].

Computational implementation   Strictly speaking, DFT requires the integration of its parameters over all the space. However, this is not an approach that can be done computationally. Hence, due to the computational limitations, other approximations need to be implemented. The main examples for crystalline solids are the use of atomic pseudopotentials, the plane-wave cutoff energy and the sampling points of the Brillouin zone.

Atomic pseudopotentials   Conventionally, as only the electrons in the outer shells participate actively in the bonding, the contribution of the electrons in inner shells can be neglected (this is not true for all cases). Thus, it is possible to approximate the actual atomic potentials by the so-called pseudopotentials, by just taking into account the outer electrons and adding them to a global potential created by the nucleus and the "frozen core" electrons.

There are different ways to approximate an atomic potential, being the use of norm-conserving pseudopotentials one of the most popular methods. In this, despite the modification of the potential at the core, the valence states of the pseudopotential are equal to the valence states of the atom, and the norm for each of these states is set to be equal to those of the real case [91].

Sampling of the Brillouin Zone   In a system where the atoms are periodically arranged it is possible to take advantage of this concept to solve the many body-problem. To do so, the electronic wave function, $\psi_{n\boldsymbol{k}}(\boldsymbol{r})$, can be related to a periodic wave function $u_{n\boldsymbol{k}}(\boldsymbol{r})$ that takes into account the periodicity of the system, $\boldsymbol{R}$, such that the condition $u_{n\boldsymbol{k}}(\boldsymbol{r}) = u_{n\boldsymbol{k}}(\boldsymbol{r} + \boldsymbol{R})$ is satisfied. This is achieved by adopting $\psi_{n\boldsymbol{k}}(\boldsymbol{r})$ in the Block-form (Eq. 3.1),

$$\psi_{n\boldsymbol{k}}(\boldsymbol{r}) = \frac{1}{\sqrt{N\Omega_0}} u_{n\boldsymbol{k}}(\boldsymbol{r}) e^{i\boldsymbol{k}\cdot\boldsymbol{r}} \tag{3.1}$$

where N stands for number of units cells in the crystal (within the simulation cell), and Ω_0 for their volume. Even under this definition, the calculation of the electronic density, for example, requires an infinite set of calculations over the complete BZ (Eq. 3.2, where s stands for the occupation of the states and the factor 2π is only due to the convention of the reciprocal space):

$$n(\boldsymbol{r}) = \frac{1}{(2\pi)^3} \int_{BZ} s \sum_n u_{n\boldsymbol{k}}^{\star}(\boldsymbol{r}) u_{n\boldsymbol{k}}(\boldsymbol{r}) d\boldsymbol{k} \tag{3.2}$$

However this integration is not computationally feasible, thus different approximations have been proposed considering only a limited number of $\boldsymbol{k}$-points in the BZ. For example, the method proposed by Monkhorst and Pack, to efficiently capture the information in a $l \times l \times l$ $\boldsymbol{k}$-points mesh [91].

Cutoff Energy From Eq. 3.1 it is clear that, for a periodic solid, only the description within the BZ is necessary, and outer points are recovered due to the phase-factor $e^{i\boldsymbol{k}\cdot\boldsymbol{r}}$. This definition is specially convenient for the use of plane waves as the basis set, as this behavior naturally arises from the Bloch theorem. In this context, it is possible to rewrite Eq. 3.1 as a expansion of plane waves (Eq. 3.3):

$$\psi_{n\boldsymbol{k}}(\boldsymbol{r}) = \frac{1}{\sqrt{N\Omega_0}} \sum_{\boldsymbol{G}} u_{n\boldsymbol{k}}(\boldsymbol{G}) e^{i(\boldsymbol{k}+\boldsymbol{G})\cdot\boldsymbol{r}} \tag{3.3}$$

where $\boldsymbol{G}$ defines the periodicity of the system in the reciprocal space. In practical terms, the cutoff energy approximation consists in cutting of Eq. 3.3 to a limited number of plane waves according to a given parameter E_{cut}, such that $\frac{1}{2}|\boldsymbol{k}+\boldsymbol{G}| \leq E_{cut}$. This parameter is the so-called cutoff energy.

3.1 Computational details

We have used the atomic structures for polymorphs δ_6, δ_3, β_{12}, α_1 and δ_5 as obtained from Refs. [16, 18, 27, 32, 35, 53] without any further optimization. Instead, as we aimed to compare α'-Monolayer with α'-Bilayer, these polymorphs were obtained through full relaxation of the atomic positions (within a threshold on the maximal force of 0.01 eV/Å), starting out from the bilayer structure in Ref. [35]. The relaxation of the structures was performed using the optimized norm-conserving Vandervilt pseudopotentials (ONCVPSP 3.2.3.1), evaluating the exchange-correlation potential within the generalized gradient approximation (GGA) using the Perdew-Burke-Ernherhof (PBE) functional [58, 92]. The model system B_T has been manually created taking a bond distance of 1.68 Å, based on the shortest bond in δ_6. The symmetry of the polymorphs was determined using FINDSYM [93, 94].

	No. Bands	No. Plane waves	No. $\mathbf{G}$'s	No. $\mathbf{k}$-points
δ_6	50	997	59	361
δ_3	50	2981	99	6144
β_{12}	60	1995	99	4096
δ_5	70	1497	69	1296
α_1	80	2995	97	480
α'	60	1477	60	3456
Bil.	70	1995	99	3456

Table 3.1: Converged parameters for absorption spectra of borophene polymorphs, as implemented in DP. The number of $\mathbf{G}$'s refers to the calculation of local fields under the RPA approximation.

Other calculations (ground state and band structure) were performed employing the Hartwigsen-Goedecker-Hutter (HGH) pseudopotential within the local density approximation (LDA) [76,95], finding minimal differences with respect to those of the GGA-PBE (here only LDA results are included). In the framework of the DFT we have used the Abinit package [69,91], and we have converged the ground state with respect to the total energy within a threshold of 0.5 meV/atom. We have converged the interlayer vacuum distance to 19.05 Å (21.17 Å exceptionally for α'-bilayer). For all polymorphs we have used a cutoff energy of 75 Hartree (~ 2041 eV) and the $\mathbf{k}$-meshes for the self-consistent calculation of the KS density for δ_6, δ_3, β_{12}, α_1, δ_5, α' and α'-bilayer are, respectively: $38 \times 38 \times 1$, $40 \times 40 \times 1$, $32 \times 32 \times 1$, $28 \times 28 \times 1$, $30 \times 30 \times 1$, $34 \times 34 \times 1$ and $40 \times 40 \times 1$ [96]. All polymorphs here presented are metallic and we have used 0.01 Hartree to simulate the electronic temperature.

The absorption spectra and static response were calculated by means of the TDDFT with the DP code [97,98], within the independent-particles (IPA) and the random phase approximations (RPA) [70]. We have converged the absorption spectra of each polymorph up to 30 eV with respect to number of bands, plane waves to describe the wave functions, sampling of the BZ, and reciprocal lattice vectors $\mathbf{G}$ to account for the crystal local fields. Here we only show the results up to 15 eV, where the continuum-like behavior is already more predominant. The converged parameters are summarized in Table 3.1. Similar parameters were used for the calculation of the static response. Other computational parameters used in this work for specific cases are mentioned in the text.

Part II

Developments and Results

The confined 3D HEG

4.1 The self-doping picture and the HEG

We described in Section 1 the self-doping mechanism proposed in Ref. [46] to understand the electronic structure of different borophene polymorphs from a rigid electronic structure. We illustrated this concept pointing out to the similarities between the projected density of states (PDOS) of borophene δ_3, α' and B_T in Fig. 1.3: in particular, the shifting of the in-plane bonding states and the out-of-plane states with respect to the Fermi Energy (see Fig. 1.3). However, it is evident that the electronic structures are not simply shifted but that other changes occur, for example the opening of the gap between the bonding states of α'. The latter is a limitation of self-doping and we will discuss it in detail in Section 5.

For now, we want to profit from the self-doping idea, as it captures the information of the position of the Fermi level with respect to the in-plane and out of plane states (Fig. 1.3). However, from the differences of the electronic structures, we are left to an ambiguous choice of the starting point: should we use the electronic structure of B_T, δ_3, α' or of other polymorph as the starting point?. In order to get rid of this ambiguity we selected a universal model: the homogeneous electron gas (HEG)[1].

Of course fundamental differences exist between the HEG and borophene. One of them is the dimensionality: in borophene, in spite of being a so-called "two-dimensional" material, the electron density (mostly localized in-plane) extends along the out-of-plane direction exponentially decaying with the distance from the atomic plane, while for the HEG the electron density is homogeneously distributed over the unit cell, formally delimited within one, two or three dimensions. Thus, there is no fundamental reason why we should use either the 2D or 3D HEG for its comparison with with borophene. We computed the band structure of the model system B_T in its primitive unit cell, and compare it with both, the 2D and the 3D HEG with the same number of electrons $n_{el}^{B_T} = n_{el}^{3DHEG} = n_{el}^{2DHEG} = 3$ (Fig. 4.1): for the 2D case we used the unit cell defined by the in-plane lattice parameters of B_T ($a = b = 1.68$ Å), while for the 3D case we used the same unit cell as for the B_T calculation ($a = b = 1.68$, $c = 19$ Å).

For comparison with the B_T band structure (calculated only in-plane along K $\rightarrow$ $\Gamma \rightarrow$ M $\rightarrow$ K), we included in Fig. 4.1 only $\mathbf{k}$'s in-plane. However, notice that the 3D HEG is also dispersive out-of-plane: this explains the significantly lower position of the Fermi energy with respect to the 2D HEG, as the states out-of-plane are also occupied. Moreover, for the 3D HEG band structures in Fig. 4.1 we did not include $\mathbf{G}$-vectors out-of-plane: this point is relevant as the $\mathbf{G}$'s out-of-plane fold back within the BZ and

---

[1]It should be noted that B_T was compared to the HEG in a previous work [60], however this comparison was not further developed.
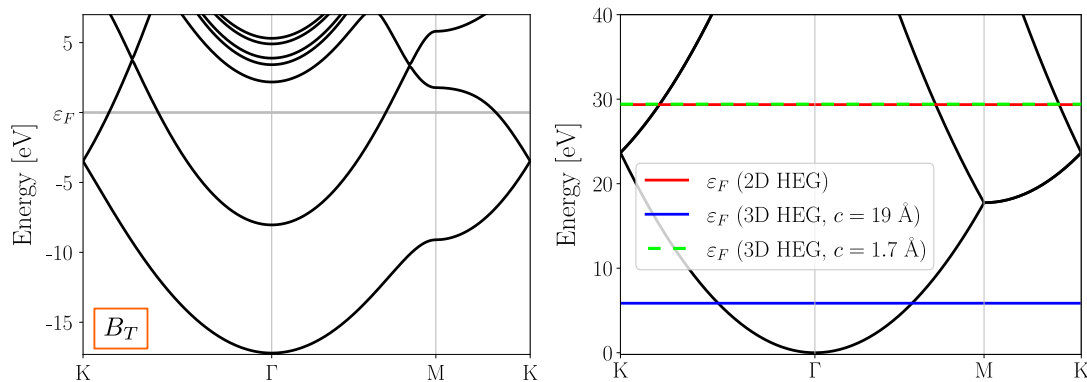
Figure 4.1: (Left) Electronic structure of model system B_T calculated with DFT. (Right) Homogeneous electron gas band folded within the same BZ as for the B_T calculation. For the HEG three Fermi energies are shown: for the 2D case (same unit cell as the in-plane dimension of B_T), and for the 3D case (same unit cell as the DFT calculation, $c = 19$ Å), and changing the out-of-plane dimension to $c = 1.7$ Å to fit the Fermi energy of the 2D case.

thus different "replicas" of the band structure should appear in Fig. 4.1 for the 3D HEG. In fact, in the selected energy window these replicas are only present for the 3D HEG with $c = 19$ AA. For the case of the 3D HEG with $c = 1.7$ AA the replicas appear much higher in energy.

Despite the fundamental differences, we highlight the qualitative resemblance between the band structure of the borophene polymorph and the 2D HEG, in particular, the relative position of the bands with respect to the Fermi energy (ε_F^{2DHEG}). The 3D HEG fails to describe the relative position of the Fermi level, because of localization of the density in-plane in the 2D monolayer, in contrast with the homogeneous electron density distribution of the HEG. However, if we confine the 3D HEG in the out-of-plane direction, in order to describe an isolated slab (as borophene within the supercell), it is possible to displace the Fermi energy of the 3D HEG to a higher position: for instance, with $c = 1.7$ Å, $\varepsilon_F^{3DHEG} = \varepsilon_F^{2DHEG}$.

4.2   A confined 3D model

We can take inspiration from the 3D HEG with $c = 1.7$ Å and its resemblance with the 2D HEG. Now we want to define a three-dimensional model that maintains the 2D HEG-like behavior of the system in-plane, but also that includes the extension of the density out-of-plane. We propose to split the Hamiltonian and wave functions of the problem, and therefore the eigenvalues, into in-plane ($\parallel$) and out-of-plane ($\perp$) components as in Eq. 4.1:

$$(\hat{\mathscr{H}}_{\parallel} + \hat{\mathscr{H}}_{\perp})\phi_{\parallel}(\mathbf{r}_{\parallel})\phi_{\perp}(\mathbf{r}_{\perp}) = (\varepsilon_{\parallel} + \varepsilon_{\perp})\phi_{\parallel}(\mathbf{r}_{\parallel})\phi_{\perp}(\mathbf{r}_{\perp}) \tag{4.1}$$

Notice that from this separation of terms (Eq. 4.1) the problem in-plane is two-dimensional, while the problem out-of-plane is one-dimensional. For the description of the problem in-plane we select the 2D HEG. For the out-of-plane component we must make the observation from Fig. 4.1 that the dispersion of the second lowest band in B_T ($j = 2$) is parallel to the lowest band ($j = 1$) simply shifted upwards in energy. This in agreement

with the sum of eigenvalues in Eq. 4.1, and so we can use a simple model from quantum mechanics text books: a 1D "particle in a box" with eigenvalues:

$$\varepsilon_\perp = \frac{\pi^2 j^2}{2c^2} \tag{4.2}$$

where j is the index of the state, and c the depth of the box.

In this way we can write the eigenvalues of Eq. 4.1, and hence the band structure of the confined model (Box), in a similar form as:

$$\varepsilon^{Box} = \frac{1}{2}\left[|\mathbf{k}_\parallel - \mathbf{G}_\parallel|^2 + \left(\frac{\pi j}{c}\right)^2 \right] \tag{4.3}$$

The Box model is not dispersive out-of-plane. It only contains $\mathbf{k}$-vectors in plane, and the out-of-plane components are simple "replicas" of the former. Moreover, notice that in the Box model, the "particle in a box" part of the problem (Eq. 4.2) $j = 0$ yields the unphysical result $\varepsilon_\perp = 0$ (and $\phi_\perp(\mathbf{r}_\perp) = 0$). Therefore j must take only integer numbers $j > 0$. In the DFT-calculated band structure for B_T (Fig. 4.1, left) we can recognize two parabolic bands crossing crossing at Γ below the Fermi energy. Making the analogy to the Box model of Eq. 4.3, these states correspond to $j = 1$ and $j = 2$. Thus, it is appropriate to evaluate the Box model of Eq. 4.3 as two 2D HEG (for $j = 1$ and $j = 2$, respectively) such that the total number of electrons in the box, n_{el}, is $n_{el} = n_{el}^{j=1} + n_{el}^{j=2}$. In this form,

$$n_{el} = \frac{A}{\pi}\left[2\varepsilon_F - \frac{5\pi^2}{2c^2} \right] \tag{4.4}$$

where A is the area of the unit cell in-plane and c the depth of the box. Moreover, from Eq. 4.4, the depth of the box in the Box model can be obtained as:

$$c = \frac{\pi\sqrt{5A}}{\sqrt{4A\varepsilon_F - 2\pi n_{el}}} \tag{4.5}$$

Eq. 4.5 yields the depth of the box for constructing the band structure using the Box model of Eq. 4.3 as a function of the Fermi energy. However, it is also convenient to construct the model based on the energy difference among the two states $j = 1$ and $j = 2$. Then, using Eq. 4.2 we can define this energy difference as: $\varepsilon_{\tilde{\mathbf{G}}_\perp} = \varepsilon_\perp^{j=2} - \varepsilon_\perp^{j=1} = \frac{3\pi^2}{2c^2}$ so that:

$$c = \pi\sqrt{\frac{3}{2\varepsilon_{\tilde{\mathbf{G}}_\perp}}} \tag{4.6}$$

We plotted in Fig. 4.2 the band structure of B_T and the Box model fixing the energy difference $\varepsilon_{\tilde{\mathbf{G}}_\perp}$ from the DFT calculation, and fixing the Fermi energy with the DFT-calculated band width. Qualitatively, the band structures of Fig. 4.1 are comparable. Hence, the Box model gives us a simple approximation of the electronic band structure of B_T provided that we know its band width or the difference in energy between $j = 1$ and $j = 2$.

We must emphasize the qualitative aspect of the Box model: while it gives a general idea of the band structure, it fails to describe some details of the band structure. For
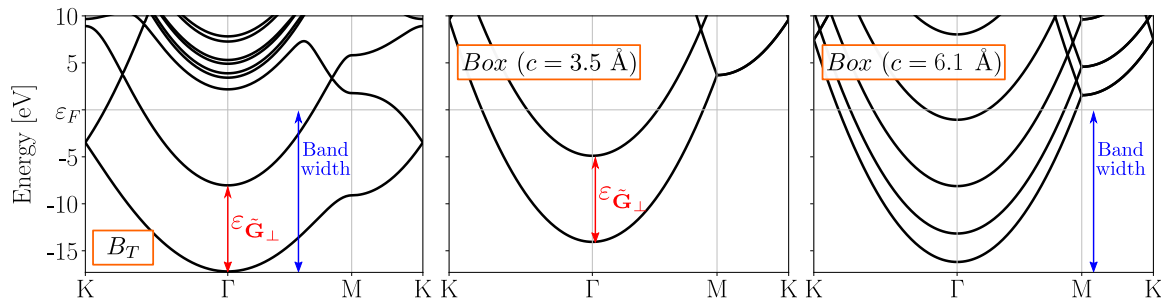
Figure 4.2: B_T electronic structure: DFT-calculated (left), *Box* model with fixed energy difference between $j = 1$ and $j = 2$, $\varepsilon_{\tilde{\mathbf{G}}_\perp}$ (center), and *Box* model with fixed ε_F (right).

example, from Fig. 4.2, it is clear that it lacks the splitting of the bands at M (in Fig. 4.2 the lowest band along M $\to$ K is doubly degenerated): this is a direct consequence of using the 2D HEG to describe the in-plane part of the problem. Moreover, the *Box* model also overestimates the dispersion of the bands, and consequently, the bands crossing at K are not occupied while in B_T they appear below the Fermi level.

4.2.1 The wave function and the density distribution

We have focused the discussion of the *Box* model only on the band structure (Eq. 4.3), but it is interesting to look as well at the wave functions in Eq. 4.1: in-plane, the system behaves as a 2D HEG, thus $\phi_\parallel(\mathbf{r}_\parallel) = C_\parallel e^{i(\mathbf{k}_\parallel + \mathbf{G}_\parallel)\cdot\mathbf{r}_\parallel}$. Out of plane, the system adopts the solutions of the particle in a box ($C_\parallel$ and $C_\perp$ are just normalization coefficients):

$$\phi_\perp(\mathbf{r}_\perp) = C_\perp \sin\left(\frac{\pi j |\mathbf{r}_\perp|}{c}\right) \tag{4.7}$$

where the cases of $j = 1$ and $j = 2$ are of our particular interest, as they are the ones playing a role in the density of B_T (Fig. 4.2).

In the *Box* model the wave functions out-of-plane vanish outside the box walls. In quantum mechanics text books the walls are described using an infinite potential; in our model we can think about this confinement as an effect of the Coulomb potential produced by the atomic plane[2]. Moreover, to preserve the symmetry of the potential well, the atomic plane must be situated at mid-distance of the box depth, *i. e.*, at $c/2$ (schematic representation in Fig. 4.3).

Positioning the atomic plane within the box gives another interesting interpretation, this time regarding the wave functions (Eq. 4.7) and the density: $|\phi_\perp^{j=1}|^2$ has its maximum at $c/2$, that is, at the position of the atomic plane (in-plane). While $\phi_\perp^{j=2}$ has a node at $c/2$, and so $|\phi_\perp^{j=2}|^2$ in-plane is zero, and the maxima of $|\phi_\perp^{j=2}|^2$ occur out-of-plane at $c/4$ and $3c/4$ (this is schematically represented in Fig. 4.3). Interestingly, $\phi_\perp^{j=1}$ describes a state mostly localized in-plane, while for $\phi_\perp^{j=2}$ the density extends out-of-plane but vanishes in-plane (like an atomic p_z orbital). This interpretation of the states is in agreement with the orbital-resolved electronic structure of B_T shown in Fig. 4.3. Thus the *Box* model not only gives an approximation to the electronic band structure of B_T, but also to the density distribution of the states.

---

[2]The Coulomb potential, v_c, acts as a potential well with infinite effective walls near the atomic plane: the bands described by Eq. 4.3 are bound states of v_c.
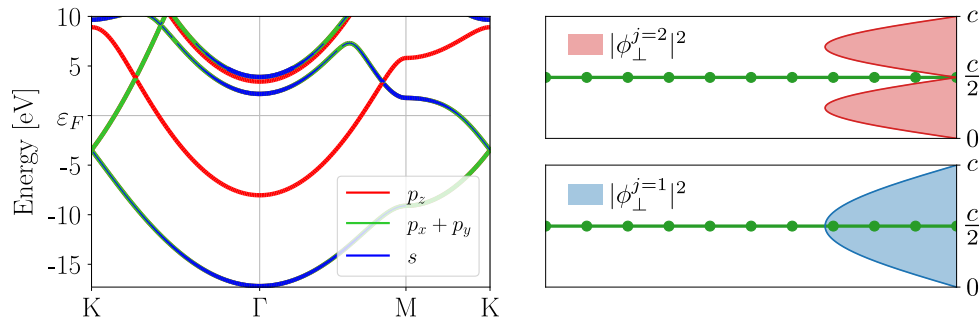
Figure 4.3: (Left) B_T band structure projected onto atomic orbitals: the total charge is normalized so that all bands have equal linewidth. (Right) Schematic representation of the position of the monolayer within the box of depth c, and density distribution of the "particle in a box" eigenstates with $j = 1$ and $j = 2$. In the model, as in the DFT calculation, we can identify the lowest state ($j = 1$) as in-plane and the "replica" ($j = 2$) as out-of-plane.

4.2.2 Borophene polymorphs and the confined model

Let us look now to other polymorphs similarly to Fig. 4.2. For instance, the opposite case of B_T: δ_3 ($\eta = 1/3$), and the intermediate non-hexagonal situation: β_{12} ($\eta = 1/6$). Compared to the primitive unit cell of B_T these structures are larger, and the folding of the bands make it difficult to find $j = 1$ (in-plane) and $j = 2$ (out-of-plane) visually in the same way as before. Nonetheless we can take advantage of the orbital-resolved electronic structures to define $\varepsilon_{\tilde{\mathbf{G}}_\perp}$ as the energy difference between the lowest in-plane state and the lowest p_z state[3]. We plotted in Fig. 4.4 the DFT-calculated and the *Box* model electronic structures of borophene δ_3 and β_{12}.

From Fig. 4.4 we can observe that the band structure of the *Box* model qualitatively resemble the DFT-calculated band structure of borophene δ_3 and β_{12} (particularly by fixing $\varepsilon_{\tilde{\mathbf{G}}_\perp}$). Thus, despite the "holes" in the atomic structure of these polymorphs (with respect to B_T) we can still relate the band dispersion of the children structures to those of the *Box* model.

Note that in borophene δ_3 the choice of calculating c from $\varepsilon_{\tilde{\mathbf{G}}_\perp}$ (Eq. 4.6) or from the band width (Eq. 4.5) has a strong impact on the relative position of the bands. This occurs because this structure is the furthest from the 2D HEG + "particle in a box" model. This is not surprising considering that δ_3 is the structure with the most holes, and hence the 2D HEG overestimates the density in-plane. Regardless of this difference, fixing $\varepsilon_{\tilde{\mathbf{G}}_\perp}$ gives a good approximation to the position of the in-plane and out-of-plane states within the electronic structure, as well as for the Fermi energy.

4.2.3 Limitations of the *Box* model

Using our confined 3D HEG model is a very computationally inexpensive idea that can be used for understanding the electronic band structure of the different borophene polymorphs. However, it needs to be taken with caution, as despite the qualitative similarities that exist with the DFT-calculated band structures, other characteristics might signifi-

---

[3]The lowest points of both bands are at Γ, so $\varepsilon_{\tilde{\mathbf{G}}_\perp}$ is the energy difference between the two bands at this $\mathbf{k}$-point.
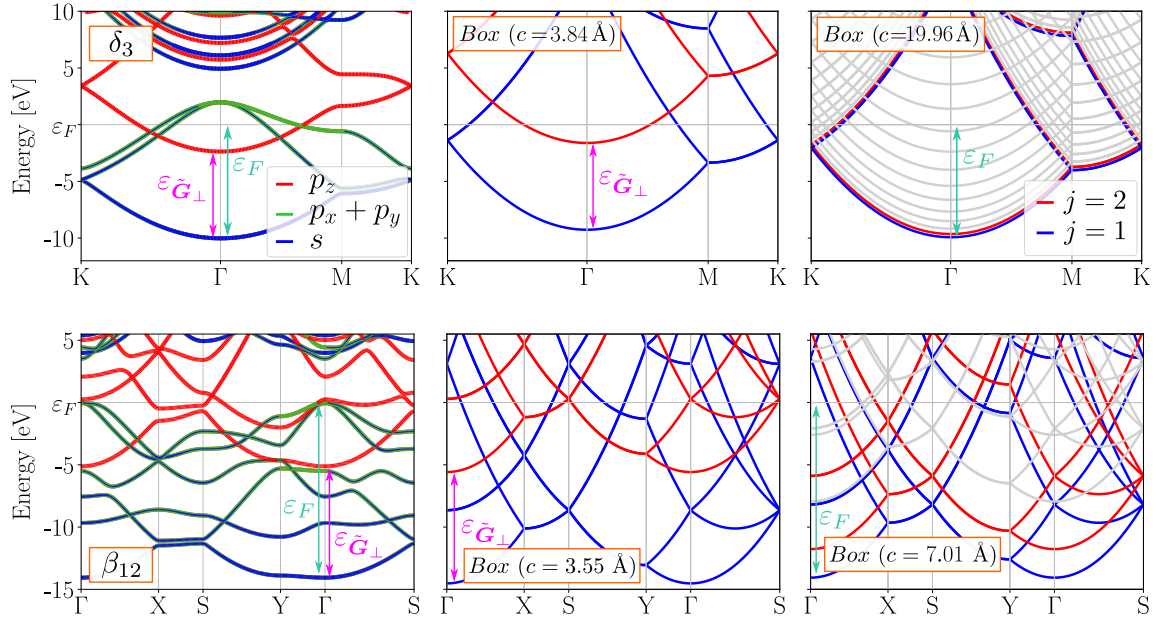
Figure 4.4: Normalized orbital-resolved electronic structure of borophene δ_3 and β_{12}, and band structures calculated with the *Box* model at fixed $\varepsilon_{\tilde{\mathbf{G}}_\perp}$ (center), and band width (right). The states in gray in the right column correspond to $j > 2$.

cantly differ. For example, let us look to the wave function of the lowest state $j = 1$ and $j = 2$. In the DFT case the wave functions are written as a sum of plane waves:

$$\phi_{\mathbf{k}}^j(\mathbf{r}) = \sum_{\mathbf{G}} C_{\mathbf{k}}^j(\mathbf{G}) e^{i(\mathbf{k}+\mathbf{G})\cdot\mathbf{r}} \tag{4.8}$$

while in the *Box* model for the description of the problem in-plane a single plane wave is necessary ($\mathbf{G}_s$):

$$\phi_{\mathbf{k}}^{\text{Box}}(\mathbf{r}) = \sum_{\mathbf{G}} \delta(\mathbf{G} - \mathbf{G}_s) e^{i(\mathbf{k}+\mathbf{G})\mathbf{r}} = e^{i(\mathbf{k}+\mathbf{G}_s)\mathbf{r}} \tag{4.9}$$

Thus, the wave functions are not necessarily equivalent. However, if in the DFT-calculated wave function (Eq. 4.8) exist a $\mathbf{G}$-vector, $\mathbf{G}_s$, such that $|C_{\mathbf{k}}^j(\mathbf{G}_s)| >> |C_{\mathbf{k}}^j(\mathbf{G})|$ for all the other $\mathbf{G}$'s, then we could approximate the plane waves wave function of that state as:

$$\phi_{\mathbf{k}}^j(\mathbf{r}) \approx C_{\mathbf{k}}^j(\mathbf{G}_s) e^{i(\mathbf{k}+\mathbf{G}_s)\cdot\mathbf{r}} \tag{4.10}$$

therefore, proportionally to Eq. 4.9.

In order to determine whether this behavior occurs in borophene at the level of the wave function, we selected a simple case: B_T along $\Gamma \to M$[4], for which we obtained the KS wave functions as a sum of plane waves (Eq. 4.8), and we computed $|C_{\mathbf{k}}^j(\mathbf{G})|$ for different $\mathbf{k}$'s, and $\mathbf{G}$'s (Fig. 4.5): for both cases ($j = 1$ and $j = 2$), the $\mathbf{G}$ components out-of-plane

---

[4]We selected the path $\Gamma \to M$ here only for representation, but $K \to \Gamma$ follows the same trend: the further from Γ, the less 2D HEG-like. In agreement with the same trend, along $M \to K$ the 2D HEG-like behavior of the wave function is completely lost, and different $|C_{\mathbf{k}}^j(\mathbf{G})|$'s share similar contributions as the highest one.
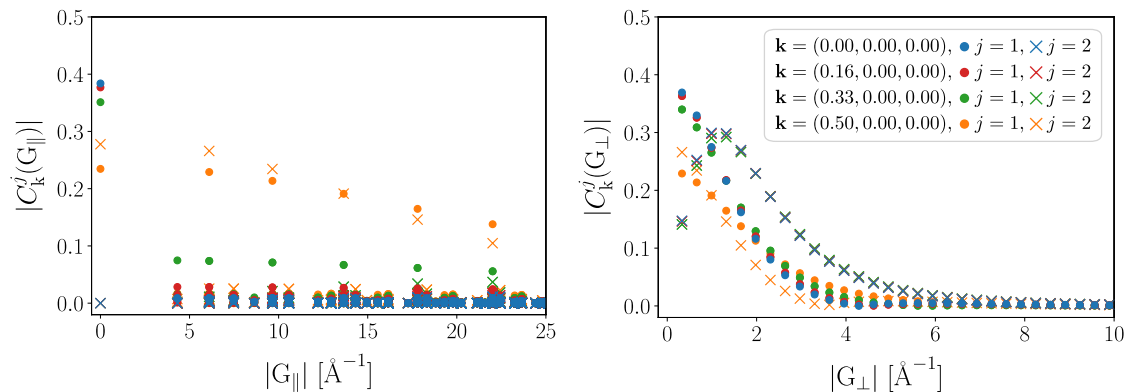
Figure 4.5: Plane waves wave function coefficients of borophene δ_3 computed at different **k**-points: components in-plane (left), and out-of-plane (right). Only for the components in-plane, near Γ and for $j = 1$ the wave function is HEG-like, that is, a coefficient $|C_{\mathbf{k}}^{j}(\mathbf{G})|$ exists that is much larger than the other coefficients.

($\mathbf{G}_\perp$), require from more than one plane wave: this is simply due to the localization of the electronic density near the atomic plane.

Only for the in-plane part ($\mathbf{G}_\parallel$), there is a major contribution of $|C_{\mathbf{k}}^{j}(\mathbf{G})|$ coming from $\mathbf{G} = (0,0,0)$, but only for the lowest state ($j = 1$) and close to Γ. As we move away from the zone-center this approximation breaks. Thus, despite the HEG-like dispersion of the electronic bands of borophene, the *Box* model is not enough to capture the full information of the system.

4.3   Conclusions

In this Section we showed that the electronic band structure of borophene B_T resembles the band structure of the 2D HEG within the same in-plane unit cell configuration. We took advantage of this resemblance and developed a model based on the 2D HEG and the 1D "particle in a box" to better approximate the band structure of different borophene polymorphs. Then, we showed that our model qualitatively describes the band structure of borophene B_T, δ_3, and β_{12}, and it distinguishes between in-plane and out-of-plane states. Of course, the *Box* model is limited to a qualitative description of the band structure: as we showed, it fails to describe more complex quantities like the DFT-calculated wave functions.

The *Box* model gives an straightforward strategy to approximate the band structure of borophene polymorphs without any expensive calculation. This can be useful, for example, as a guide for understanding the electronic structures of large unit cells: the *Box* model is independent of the atomic structure, thus provided that one knows the vacancy ration η of a polymorph, and the energy difference $\varepsilon_{\tilde{\mathbf{G}}_\perp}$ (or the band width) it is possible to approximate the folding of the bands of the polymorph in any unit cell configuration.

Electronic structures

In this chapter we aim to understand what is the role of the atomic structure on the electronic structure of the different borophene polymorphs. These polymorphs have repeatedly been reported as metallic due to the multiple electronic bands crossing the Fermi energy [16–18, 32–35, 45, 55]. As in the literature, we have obtained such behavior in our calculations (Fig. 5.1), and overall we have found good agreement between our results using the LDA and results reported in the literature and using different functionals [16, 18, 21, 27, 32, 33, 35, 51, 99, 100]. Only for α_1, we have found a rigid shift of the band structure (upwards) by 1 eV with respect to Ref. [16]. The origin of this discrepancy is unclear as our calculations are consistent with the number of electrons and the electronic temperature. We proceed with the discussion of the results only making use of our own calculations.

In order to understand the changes of the electronic structure from polymorph to polymorph we separated them into three different groups, each of them relative to a conceptual "engineering mechanism" with respect to a parent structure: 1) via creation of defects; either creating vacancies from B_T ($\overset{\circ}{\rightarrow}$), or adding interstitial atoms into the hexagonal sites of δ_3 ($\overset{\bullet}{\rightarrow}$), 2) out-of-plane distortion (buckling, $\overset{\triangle}{\rightarrow}$) as in α' and δ_6, and 3) the addition of a second layer on top of a monolayer (comparison between α' and α'-Bilayer).

5.1 Flat monolayers

5.1.1 Electronic structures in commensurable unit cells

We can relate all flat monolayers among themselves simply via addition or removal of atoms from a common "parent" structure (see for example, Refs. [14, 17, 18, 45, 46, 48, 49]). However, employing this engineering mechanism requires the adjustment of the unit cell, leading to different primitive unit cells for different polymorphs. This change of the unit cell upon the creation of defects causes the "periodic defects" not to have an intuitive effect on the electronic structure of borophene. So, despite of the similar atomic building units, the polymorphs are studied independently of each other. Regardless of the difficulty comparing different polymorphs, some attempts have been made to understand them as a group: for example with respect to symmetry [18], bond nature [47], and occupation of the states [46]. The undeniable similarities among different results of different polymorphs take us to investigate in-depth how some features of the polymorphs change with the defects, and how others stay similar. We start from the electronic band structure.

We selected two representative cases: the creation of β_{12} upon the addition of atoms into δ_3, which we denote as ($\delta_3 \overset{\bullet}{\longrightarrow} \beta_{12}$), and the creation of δ_5 from the removal of atoms
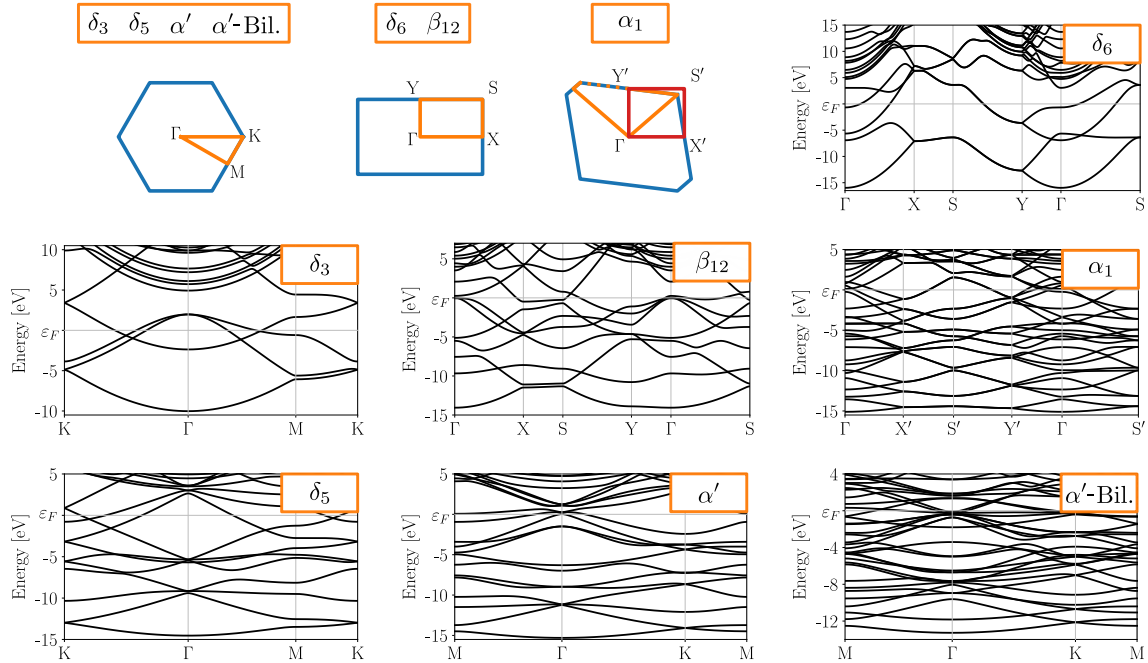
Figure 5.1: Brillouin zones (BZs) and electronic band structure of the borophene polymorphs selected in this work. All the polymorphs here presented are metallic and our calculated band structure are in good agreement with previously reported results [16, 18, 21, 27, 32, 33, 35, 51, 99, 100]. Referring to α_1, of symmetry $Cmmm$, the band structure is not computed along the high symmetry paths of the BZ, but along a non-conventional path including the **k**-points used in Ref. [16] to facilitate comparison. We have highlighted the two lowest states in the α' structure to illustrate their similarity with the two sets of bonding- and antibonding-like states of the α'-Bilayer.

from B_T ($B_T \xrightarrow{\circ} \delta_5$). In order to compare each pair in a clear manner, we propose to build a supercell commensurable to both structures of the pair. With this choice it is easy to observe the changes of the electronic structure from polymorph to polymorph. However, depending on the parent and child structures, this comparison can easily grow in complexity and hide features of the electronic structure due to the folding of the bands into the Brillouin zone. For this reason we stick for the moment to the simple cases ($\delta_3 \xrightarrow{\bullet} \beta_{12}$) and ($B_T \xrightarrow{\circ} \delta_5$). Later on we will comment on more complex situations.

How to build commensurable unit cells?

There are different ways (not necessarily equivalent) in which we can construct the commensurable unit cells. For instance, for our selected cases ($\delta_3 \xrightarrow{\bullet} \beta_{12}$) and ($B_T \xrightarrow{\circ} \delta_5$), we could create the two children structures (β_{12} and δ_5) simply by removing atoms from the model systems B_T, or by adding atoms into δ_6, but we could also start from the atomic positions of β_{12} and δ_5, and removing and adding atoms, respectively, to construct the parent structures δ_3 and B_T. Both B_T and δ_3, as used in this work, are perfectly regular with all their interatomic distances the same. However, in δ_5 and β_{12} some distances are longer than others, making the children and parent structures inequivalent among the two different choices of commensurable cells.

To show that the selection of the commensurable unit cell does not have any important effect on the overall picture of the electronic structure we selected the case ($B_T \xrightarrow{\circ} \delta_5$).
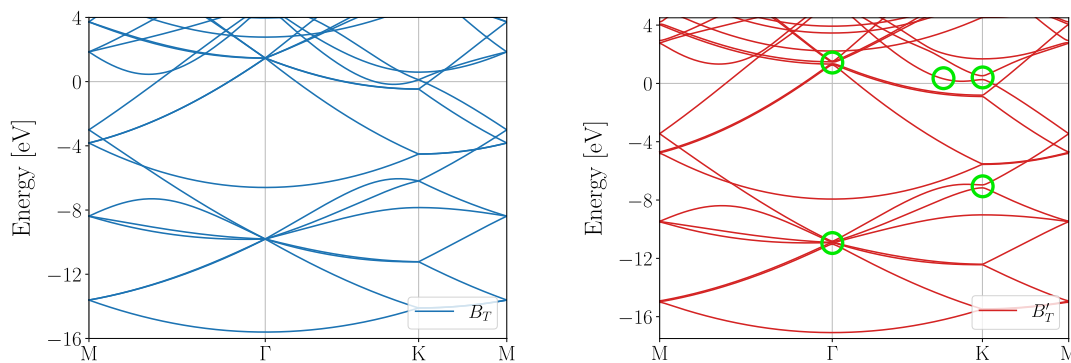
Figure 5.2: Electronic band structure of model systems B_T and B'_T (B_T constructed from the atomic positions of δ_5). Overall the band structure between the two configuration is maintained. Some differences appear due to the varying bonding distances in B'_T: in particular, the breaking of degeneracies at Γ and K, and an additional crossing of the Fermi energy.

We know from the construction of B_T that the band width of the electronic structure changes with the interatomic distance (Appendix IV), but we also know that despite this difference, the electronic bands maintain their overall structure, and that no degeneracies are broken. This allows us to compare other (also regular) polymorphs directly with B_T. However, in the case of δ_5 not all interatomic distances are equal, and we could expect this to have an effect in the electronic structure. To verify whether this affects our choice of the parent and children structures we computed the band structure of B_T (perfectly regular), and of another B_T-like structure based on the atomic positions of δ_5[1], which we refer momentaneously as B'_T (Figure 5.2).

Besides an expected change of band width, we observe a weak breaking of some degeneracies in the band structure of B'_T with respect to B_T. Nonetheless, despite these minor differences, the overall characteristics of the folding of the bands remain similar in both structures. Thus, we continue our comparison among the parent and children structures using B'_T and δ'_3, the latter constructed from the β_{12} structure. From the similarities, we could have used B_T and B'_T interchangeably. For simplicity, from now on we refer to B'_T and δ'_3 simply as B_T and δ_3, respectively.

Different atomic structures, similar electronic structures

We computed the electronic bands of the commensurable structures ($B_T \xrightarrow{\circ} \delta_5$) and ($\delta_3 \xrightarrow{\bullet} \beta_{12}$), and we show them in Fig. 5.3. We start by pointing out the obvious: the electronic structures are not the same, and therefore either adding or removing atoms from a parent structure leads to a change of the electronic states. Qualitatively speaking, however, we can point to some similarities between the parent and the children structures: for example, the similar-looking dispersion of the lowest state ($j = 1$), and the overall resemblance of the B_T and δ_5 band structures, and of the δ_3 and β_{12}, respectively.

Within this qualitative description of the band structure, we can guide the attention near the Fermi energy (ε_F): for the two cases, ($B_T \xrightarrow{\circ} \delta_5$) and ($\delta_3 \xrightarrow{\bullet} \beta_{12}$), the disper-

---

[1]To construct a B_T-like structure from δ_5 we simply took the atomic position of the latter and added the missing atom to complete the triangular mesh. The interstitial atom was introduced in the center of mass defined by the surrounding atoms.
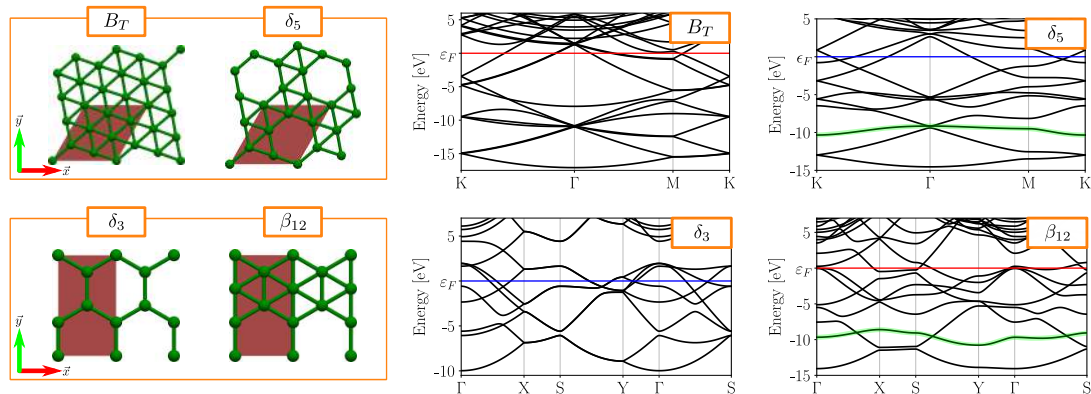
Figure 5.3: Commensurable unit cells of (B_T and δ_5) and (δ_3 and β_{12}), and electronic structures calculated in these unit cells configurations. We remark the qualitative resemblance of the band structure within each pair.

sion of the bands is, roughly speaking, maintained between the parent and the children structures, and the bands seem to only be shifted along the energy axis. This "rigid shift" view of the band structure is in agreement with the number of available electrons in each unit cell ($n_{el}{}^{B_T} = 21$, $n_{el}{}^{\delta_5} = 18$, $n_{el}{}^{\delta_3} = 12$, $n_{el}{}^{\beta_{12}} = 15$). So, in view of the similarities between the parent and children structures, it is pertinent to ask if it is possible to relate different borophene polymorphs to a fixed "reference" electronic structure (for example B_T or δ_3), as within the self-doping idea [46].

5.1.2   Self-doping and beyond

We have seen that the *Box* model gives a general idea of the electronic band structure for different borophene polymorphs, but it fails to describe the wave functions of the same polymorphs. Now, we aim at investigating the self-doping picture only among borophene structures. In this regard, all what we have described so far is the overall resemblance of the electronic bands between two parent and children structures, but now we compare the wave functions of different states, $\phi_{\mathbf{k}}^j(\mathbf{r})$, via the so-called partial partial density, *i. e.*, $|\phi_{\mathbf{k}}^j(\mathbf{r})|^2$ (we refer to the partial density of a given polymorph, B, as $B_{\mathbf{k}}^j$, where B $= B_T$, δ_6, δ_3, α_1, α', δ_5, β_{12}, α'-Bil). .

For this comparison, beyond the overall resemblance of the electronic structures among the polymorphs (Fig. 5.3), we need to look closely to the changes: for instance, via creation of vacancies ($B_T \xrightarrow{\circ} \delta_5$), we recognize that some degeneracies are broken with respect to the electronic structure of B_T. As a consequence, low-dispersive states appear[2] (see the highlighted $\delta_5^{j=3}$ state in Fig. 5.3). Note that low-dispersive states within the electronic structure indicate the localization of the partial charge, a feature not originally present in the parent B_T structure. So, to investigate the wave function of these states we plotted their partial density in commensurable unit cells at $\mathbf{k} = (0.10, 0.00, 0.00)$ (Fig. 5.4, left panel). Two situations can be recognized: 1) similar-looking states between the

---

[2]We need to be careful about the origin of these states: of course, by removing atoms from the parent structure (therefore electrons from the system) no extra states can be added to the electronic structure. Thus, the low-dispersive states must emerge from the previously existing states. For example, interference of the wave function has been evoked to explain this phenomenon (Ref. [101].
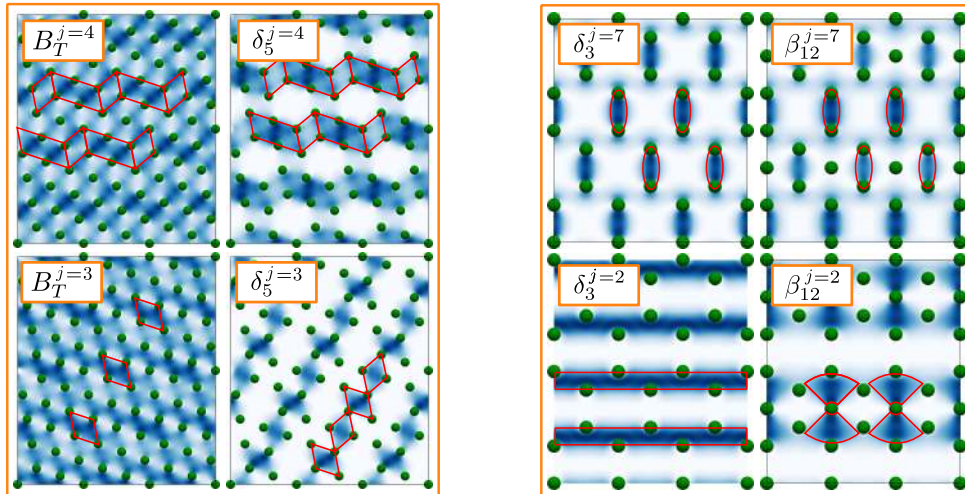
Figure 5.4: Partial densities of ($B_T \xrightarrow{\circ} \delta_5$) and ($\delta_3 \xrightarrow{\bullet} \beta_{12}$) at $\mathbf{k} = (0.10, 0.00, 0.00)$ and $(0.12, 0.00, 0.00)$, respectively, comparing similar-looking and defect states. Upon the projection of the partial density in-plane, after the introduction or removal of atoms two situations appear: there are states which maintain a similar partial density distribution ($B_T^{n=4} \xrightarrow{\circ} \delta_5^{n=4}$), ($\delta_3^{n=7} \xrightarrow{\bullet} \beta_{12}^{n=7}$), and others which completely change in space ($B_T^{n=3} \xrightarrow{\circ} \delta_5^{n=3}$), ($\delta_3^{n=2} \xrightarrow{\bullet} \beta_{12}^{n=2}$). We refer to the latter case as defect-like states. They show up in the electronic band structure as the low-dispersive bands.

parent and child structures ($B_T^{j=4} \leftrightarrow \delta_5^{j=4}$), and polymorph-specific states ($\delta_5^{j=3}$). We refer to the latter as "defect-like" states. Both cases are clearer in the next example, but already at this point we can draw attention to the observation that even at the level of the wave function, upon the creation of defects, some states in the child structure stay similar to those of the parent one, while others are specific of the polymorphs.

Via addition of atoms into the interstitial sites of δ_3, the picture is similar. We now compare ($\delta_3 \xrightarrow{\bullet} \beta_{12}$ highlighted in Fig. 5.3), from where we can also recognize the appearance of a low-dispersive state at low energies ($\beta_{12}^{j=2}$), and once again, the similar states between the parent and the child structures. We plotted in Figure 5.4 (right panel) the partial density of relatable states ($\delta_3^{j=7} \leftrightarrow \beta_{12}^{j=7}$), as well as the partial density of a β_{12} defect-like state. In this example ($\delta_3 \xrightarrow{\bullet} \beta_{12}$), the differences and similarities between the partial charge of the electronic states are even clearer than in the previous case ($B_T \xrightarrow{\circ} \delta_5$) and the conclusions are the same: some electronic states from the parent polymorph can be recognized from the electronic structure of the child one, but others are unique features of the specific atomic structure (*i.e.*, of the defects introduced into the parent structure).

Our results for the partial density show that taking the next step beyond the self-doping idea is necessary, as the self-doping picture is only adequate for some states, while others are significantly different from those of the parent structure. We can find polymorph-specific (or defect-like states) in other structures like α_1 and α': an example for each of these structures is shown in Fig. 5.5 (notice that these defect-like states are also accompanied by a low-dispersive band in the electronic structure).
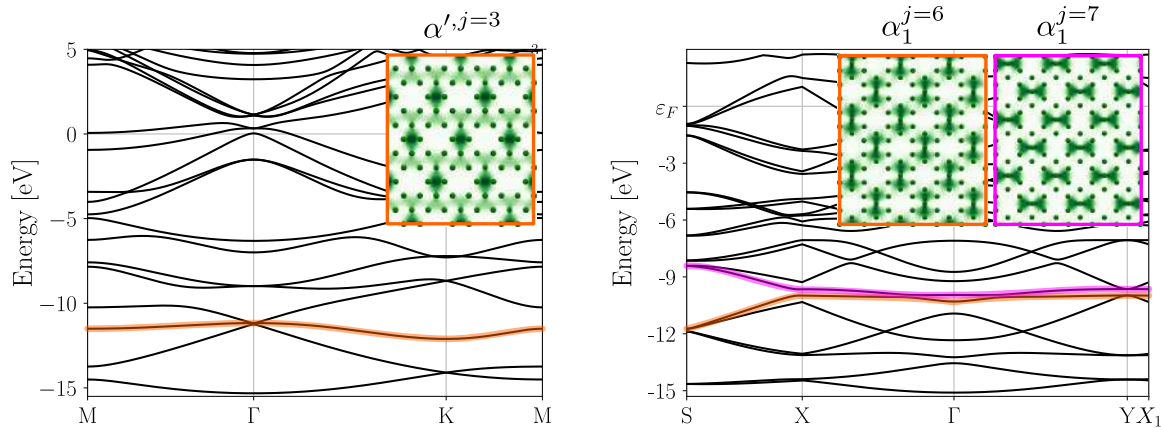
Figure 5.5: Electronic band structure of α' and α_1 highlighting the low-dispersive defect-like states $\alpha'^{,j=3}$, and $\alpha_1^{j=6}$ and $\alpha_1^{j=7}$. For each case we have added the partial density in-plane (insets), showing the localization of the partial charge.

Defect-like states in larger structures

Above, we have used small examples to show the appearance of defect-like states in borophene, but multiple other structures can be found in the literature. So now, we want to investigate whether such defect-like states appear also in more complex situations. For this, we briefly focus on a structure in particular: α_1 with a big hole, inspired by the work of Park *et. al.* [49]. In this reference, the authors observed (via DFT + kinetic Monte Carlo simulations) that liquid borophene (with vacancy ratio $\eta > 1/8$), under cooling, crystallizes as α_1, creating large holes within the structure. These holes seem to have a maximal size and are protected by a double boron chain [49]. For our example we created a smaller structure following this configuration: an α_1 supercell with a large hole protected by a double boron chain with $\eta = 21/144$, which we refer to as α_1^H. We computed its ground state using a $12 \times 10 \times 1$ **k**-mesh and 75 Hartree for the cutoff energy. The calculated lowest bands of α_1^H and α_1-commensurable with α_1^H are shown in Figure 5.6.

We highlight three aspects of the electronic structure of α_1^H: 1) compared to α_1, the electronic band width is larger (-15.76 eV instead of -15.10 eV), 2) all the computed bands are low dispersive, in particular the lowest four from which $\alpha_1^{H,j=4}$ stands out for this characteristic, and 3) starting from $\alpha_1^{H,j=5}$ (15.04 eV at Γ) the states of α_1 lie within a similar energy range and show a similar shape as those of α_1^H. So, to exemplify the appearance of low-dispersive defect-like states due to the large hole, we plotted the partial density of α_1^H with $j = 3, 4, 5$, together with $\alpha_1^{j=1}$ at **k** $= (0.0, 0.0, 0.0)$ in Figure 5.6.

Broadly speaking, $\alpha_1^{H,j=5}$ resembles $\alpha_1^{j=1}$, which reminds us the existence of common electronic states between the parent and child structures. On the other hand, the flat band $\alpha_1^{H,j=4}$ localizes the partial density in the atomically denser zones next to the defect, and also the lowest states $\alpha_1^{H,j=1}$, $\alpha_1^{H,j=2}$ and $\alpha_1^{H,j=3}$ are found in different sites around the large hole ($\alpha_1^{H,j=1}$ and $\alpha_1^{H,j=3}$ overlap in the same zone). Thus, with this simple example we have shown that the appearance of flat bands is not restricted to the simpler monolayers, and that even in the large holes situation, we can associate the low-dispersive states to the creation of defects from a parent structure.
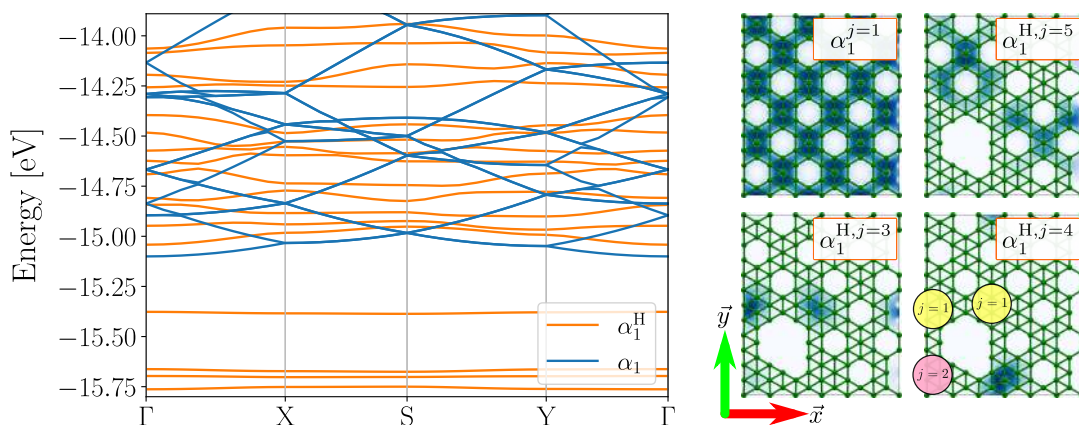
Figure 5.6: (Left) Lowest energy region of the calculated band structures of α_1 and α_1^{H}. Upon the creation of a large hole in the atomic structure, low-dispersive (flat bands) appear in the band spectra, among which $\alpha_1^{\mathrm{H},j=4}$ stands out for this characteristic. (Right) Partial density plots (in-plane) of the low states $\alpha_1^{j=1}$, $\alpha_1^{\mathrm{H},j=3}$, $\alpha_1^{\mathrm{H},j=3}$ and $\alpha_1^{\mathrm{H},j=4}$ at Γ: the partial density of $\alpha_1^{\mathrm{H},j=5}$ resembles that of $\alpha_1^{j=1}$. However, upon the creation of the large hole, localized states appear around this hole ($\alpha_1^{\mathrm{H},j}$ with $j = 1$, 2, 3 and 4); we only show $j = 3$ and $j = 4$, but $j = 1$ and $j = 2$ also localize around the hole in the labeled zones.

5.2   Buckled monolayers

5.2.1   Electronic structure

In the previous section we commented on the effect of adding interstitial atoms, and the creation of vacancies in borophene (*i. e.*, the creation of defect-like states). Another interesting situation, frequently found in the ground state of theoretical structures, is the buckling of the monolayers [16–18]. We denote the effect of buckling with respect to a parent structure with ($\xrightarrow{\wedge}$), with $\wedge$ being the buckling height measured from the lowest (in-plane) to the highest atomic position along the out-of-plane direction ($\vec{z}$ in Figure 1.4). Specifically, we will investigate the effect of the transitions ($\alpha \xrightarrow{\wedge} \alpha'$) and ($B_T \xrightarrow{\wedge} \delta_6$) which, from the literature, both buckle along the direction of an imaginary phonon mode of the parent structure [16, 50, 60]. For our comparison we induced the minimal required deformation in the parent structures to obtain the children ones: in other words, for ($\alpha \xrightarrow{\wedge} \alpha'$) we simply moved the atoms in the $2d$ sites[3] along the out-of-plane direction, while for ($B_T \xrightarrow{\wedge} \delta_6$) we performed two steps: 1) applying the in-plane deformation of the B_T lattice to break the hexagonal symmetry, and 2) the out-of-plane displacement of the atoms to finally obtain the buckled structure.

We show in Fig. 5.7 that the breaking of the hexagonal symmetry has almost no effect on the electronic structure of this system. Thus, it is more interesting to look at the changes due to the buckling height. Now we focus only on the off-plane displacement of the atoms. For both pairs ($\alpha \xrightarrow{\wedge} \alpha'$) and ($B_T \xrightarrow{\wedge} \delta_6$), we constructed different structures with different heights and computed their band structures. In general, we observed that even a minimal off-plane deformations can lead to an abrupt change of the electronic bands: in ($\alpha \xrightarrow{\wedge} \alpha'$) this is seen around the Fermi energy at Γ (see bands **U** and **V** in
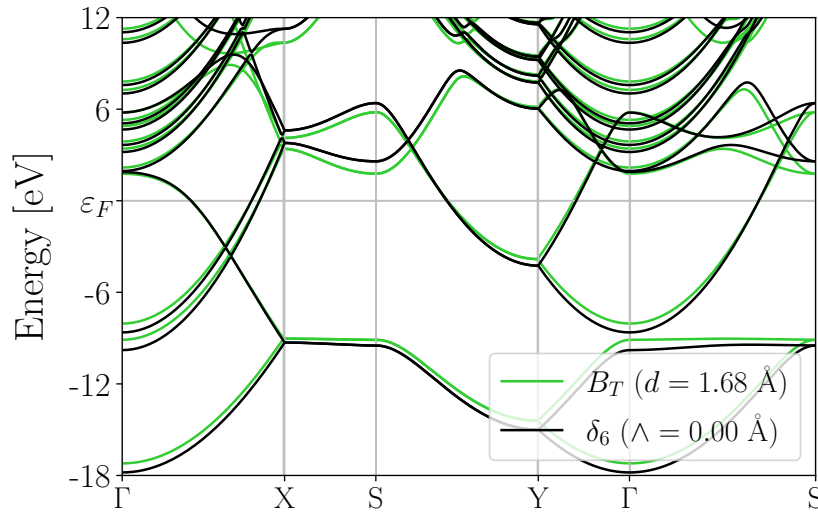
---

[3]Wyckoff positions.

Figure 5.7: Electronic structure of model system B_T (perfectly regular and planar) with hexagonal symmetry, and unbuckled δ_6 (with tetragonal symmetry). Despite the in-plane distortion, the electronic structures are nearly identical.
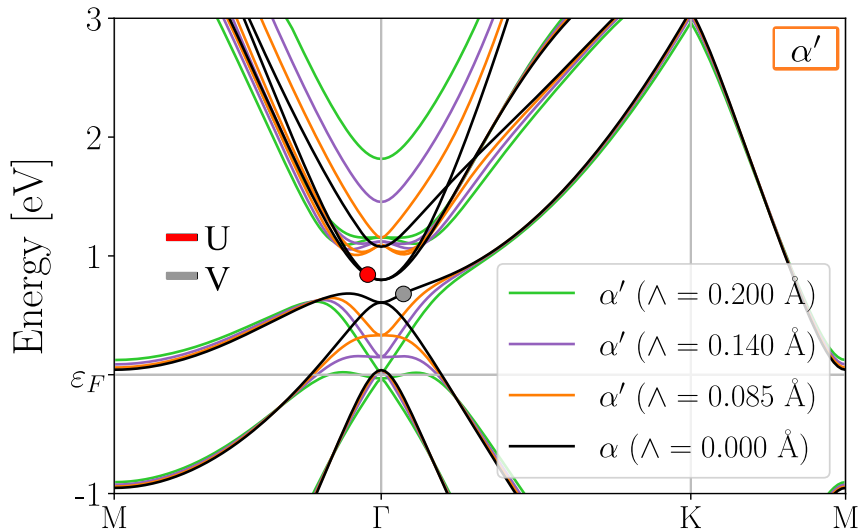

Figure 5.8: Electronic band structure of α' at different buckling heights. The loss of the perfectly planar geometry changes the shape of the bands at Γ right above the Fermi energy, and the increasing buckling distance promotes the evolution of the lower bands ($\mathbf{V}$) towards the Fermi energy. $\mathbf{U}$ and $\mathbf{V}$ are labels for the bands.

Fig. 5.8). In $(B_T \xrightarrow{\wedge} \delta_6)$, as an avoided crossing along $\Gamma \to X$ (see bands $\mathbf{A}$ and $\mathbf{B}$ in Fig. 5.9).

In both monolayers, buckling results in a different shape of the electronic band structure (energy shifts and breaking of degeneracies), but contrary to the creation of defects in the flat monolayers, these changes do not reflect as the appearance of low-dispersive bands. These small changes can also be identified from the partial density, in particular we remark from $(\alpha \xrightarrow{\wedge} \alpha')$ the redistribution of charge that follows the out-of-plane distortion (Fig. 5.10): see for example $(\alpha^{j=14} \leftrightarrow \alpha'^{,j=13})$ corresponding to the α-$\mathbf{U}$ band[4]:

---

[4]We change the indices from $\alpha^{j=14}$ to $\alpha'^{,j=13}$ due to the occurring band inversion upon buckling.
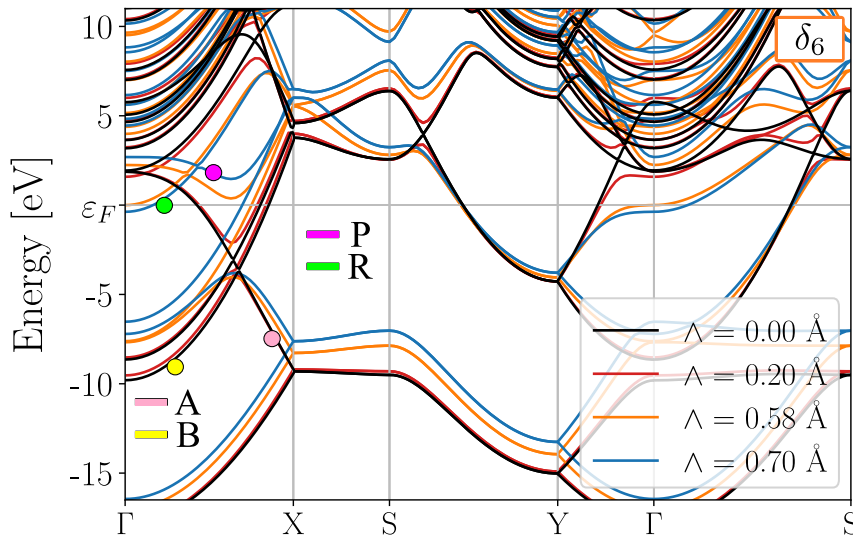
Figure 5.9: Band structure of borophene δ_6 at different buckling heights. Upon buckling, the bands **A** and **B** break their degeneracy around $3/4$ of $\Gamma \to$ X, which results in the **P** band. This "new" band moves smoothly above ε_F with increasing buckling distance, while **R** (already present in the unbuckled structure) moves downwards crossing the Fermi energy. **A**, **B**, **P**, and **R** are labels for the bands.

the charge initially in-plane (green) is dragged out-of-plane upwards and downwards (blue and red, respectively) where it redistributes. However, even upon buckling some states resemble those of the unbuckled parent structure, for example ($\alpha^{j=13} \leftrightarrow \alpha'^{,j=15}$), corresponding to the α-**V** band. Similar situations can be found for ($B_T \xrightarrow{\wedge} \delta_6$): out-of-plane dragging of the partial density ($B_T^{j=3} \leftrightarrow \delta_6^{j=2}$) and similar-looking states between the flat and buckled configurations ($B_T^{j=4} \leftrightarrow \delta_6^{j=5}$)[5].

5.2.2   Exotic properties upon buckling

Borophene α' as a semimetal   Varying the buckling distance in δ_6 and α' leads to a smooth evolution of the electronic structure. In α' the major change comes from the bands crossing at Γ slightly above the Fermi energy: these bands go down in energy with increasing buckling height, and at $\wedge \approx 0.2$ Å the monolayer adopts a nearly perfect semimetal behavior (Fig. 5.11). This unusual situation in the electronic structure is referred to in the literature as "new fermion" [102], and similar situations occur in bulk CoSi and RhSi [103]. Contrary to the latter examples where the fermion is triple-degenerate, in our calculations only the lower bands ($j = 11$ and $j = 12$) are degenerate. In fact, we can track these bands back to the states moving downwards upon the increasing buckling height (Fig. 5.8), which we had previously associated with the **U**-band of the flat α configuration. We show in Figure 5.11 the partial density of $\alpha'^{,j=11+12}$ (degenerate) and $\alpha'^{,j=13}$ at the Γ point.

Complementary to this section it is worth pointing out that the search of exotic properties in borophene, in particular the search for Dirac cones, has lead to some interesting structures, but to our knowledge only few of them are able to isolate the semimetal behav-

---

[5]There is a difference of meaning of "in-plane" for B_T and δ_6: while B_T is flat and then in-plane means "in the atomic plane", in δ_6 there is not a single atomic plane but two (from the buckling), so for this structure we refer to "in-plane" as the mid-plane perpendicular to $\vec{z}$ defined by the atomic positions.
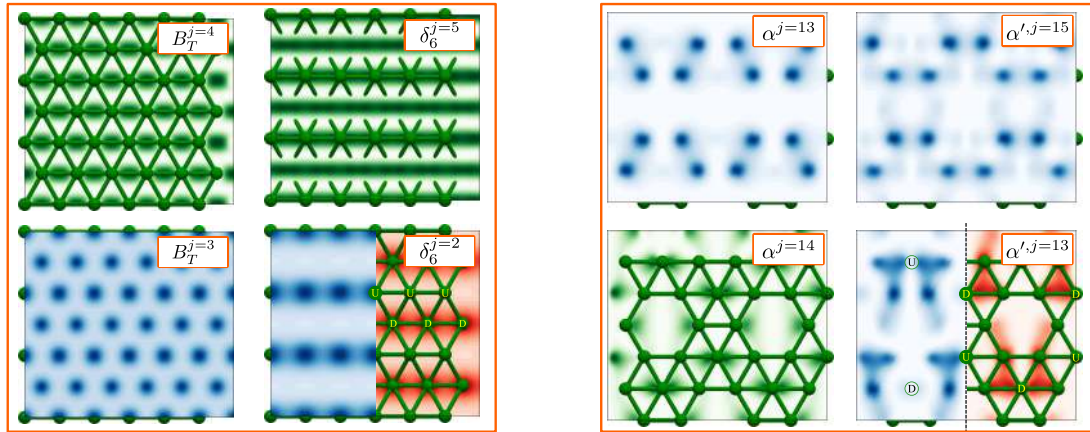
Figure 5.10: Change of the partial density upon buckling: $(B_T \xrightarrow{\wedge} \delta_6)$ at $\mathbf{k} = (0.05, 0, 0)$ and $(\alpha \xrightarrow{\wedge} \alpha')$ at $\mathbf{k} = (0.05, 0.03, 0)$. We color-coded three different planes parallel to the xy-plane: in the mid-position of the atoms (green), over the upper atoms (blue), and below the lower atoms (red); for the two latter cases we distanced the plane ± 0.4 Å, approximately where the local maxima reside (for the flat structures we only show the upper plane as the lower is symmetric with respect to the atomic positions). As it happens with the flat monolayers, for the buckled structures some states maintain the characteristics of those of the parent polymorphs, while others follow the out-of-plane deformation.
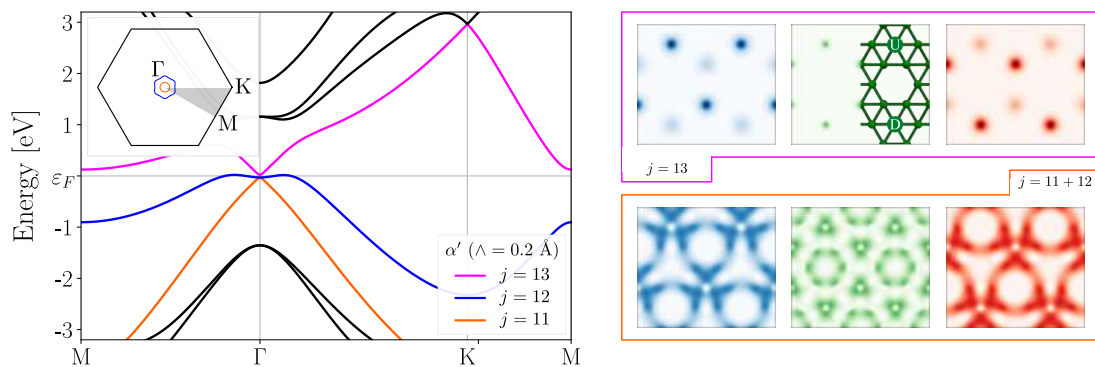

Figure 5.11: (Left) Electronic structure of α' with $\wedge = 0.2$ Å, inset: Fermi surface. (Right) Partial density at Γ of $\alpha'^{,j=11+12}$ (degenerate) and $\alpha'^{,j=13}$. As for Fig. 5.10, the different cuts of the partial density are in-plane (green), and above and below the atomic plane by 0.4 Å.

ior in their ground state: for instance borophene-$P6/mmm$ [104], $Pmmn$ [62], χ-h_1 [18], and α' as reported by Wu *et. al.* ($a = 5.046$, $b = 5.044$, $\wedge = 0.17$ Å) [16]. Despite the different ground state for α' in Ref. [16] with respect to our calculation, we have shown that it is possible to reach the semimetal state via buckling of the structure. Finally, we also want to highlight the shape of the Fermi surface of the specific configuration with $\wedge = 0.2$Å (Fig. 5.11, inset), as upon buckling $\alpha'^{,j=12}$ leads to parallel regions perpendicular to $\Gamma \to K$, leading to nesting of the Fermi surface that could be an indicator of superconductivity (this is explored in Ref. [22]).

Borophene δ_6 as a superconductor Regarding the δ_6 polymorph, the smooth evolution of the band structure has two effects: 1) a small decrease of the band width with increasing buckling height, and 2) the change of the bands crossing the Fermi energy (Fig. 5.9). From the latter point we remark the change along the $\Gamma \to X$ direction (and near Γ along $\Gamma \to Y$ and $\Gamma \to S$): one band (labeled as **P** in Fig. 5.9) moves upwards to
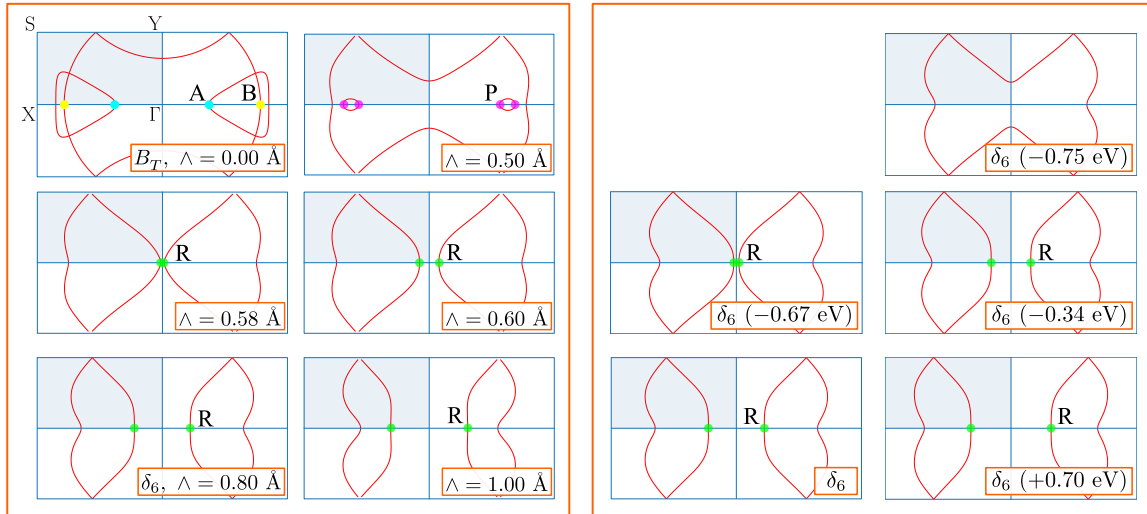
Figure 5.12: (Left) upon buckling, the continuous evolution of bands **P** and **R** change completely the shape of the Fermi surface (same labels as in Fig. 5.9). This gives rise to, for example, small "pockets" at $\wedge = 0.50$ Å (given by **P**). At $\wedge \approx 0.58$ Å, **R** starts crossing the Fermi energy and moves away from Γ at increasing buckling height giving the quasi-parallel parts of the Fermi surface observed in δ_6 ($\wedge = 0.80$ Å). (Right) Hole(electron)-doping in the rigid-shift model has a similar effect on the electronic band structure of this polymorph as decreasing (increasing) its buckling height.

the conduction states with increasing buckling height avoiding the crossing of the Fermi energy at $\wedge \approx 0.50$ Å, while another (**R**) moves downwards and crosses the Fermi energy at $\wedge \approx 0.58$ Å. As the buckling height increases, the **R** band moves deeper down in the band structure, crossing at a larger **k**-vector.

At first glance the changes described above for $(B_T \overset{\wedge}{\longrightarrow} \delta_6)$ might not seem very astonishing. However, from the perspective of the Fermi surface (see Figure 5.12), the band **A** crossing the Fermi energy near Γ in B_T behaves very differently from **R** in δ_6: in the former, the band crossing along $\Gamma \to$ X leads to a quasi-parabolic shape of the Fermi surface, while in the latter the corresponding parts of the Fermi surface extends quasi-parallel to the $\Gamma \to$ Y direction. This quasi-parallel region has been identified as the cause of a Kohn anomaly in δ_6 due to nesting of the Fermi surface, and therefore as the probable origin of high electron-phonon coupling at the corresponding **q** [19, 23]. From the nesting contribution to the electron-phonon coupling constant [19, 105], these differences between **A** and **R** could lead to significantly different behaviors between B_T and δ_6 despite the overall similitude among their electronic band structure.

Varying the buckling distance in δ_6 has a strong impact in the shape of the Fermi surface (Fig. 5.12, left). For instance, we remark two effects: 1) the tuning of the nesting vector (distance between the **R** points), which increases as the buckling distance is increased, and 2) the change of curvature of the quasi-parallel regions, straightening as the buckling height is increased. We also noticed that adding or removing electrons from δ_6 (using a rigid-band model) has similar effect as changing the buckling height concerning to both the tuning of the nesting vector and the curvature of the bands (Fig. 5.12, right). Both situations are only related to changing the relative position of the δ_6-**R** band with respect to the Fermi energy.

The change of the Fermi surface with respect to buckling and carrier doping might serve as an indicator for potential superconductivity. However, only a full electron-phonon
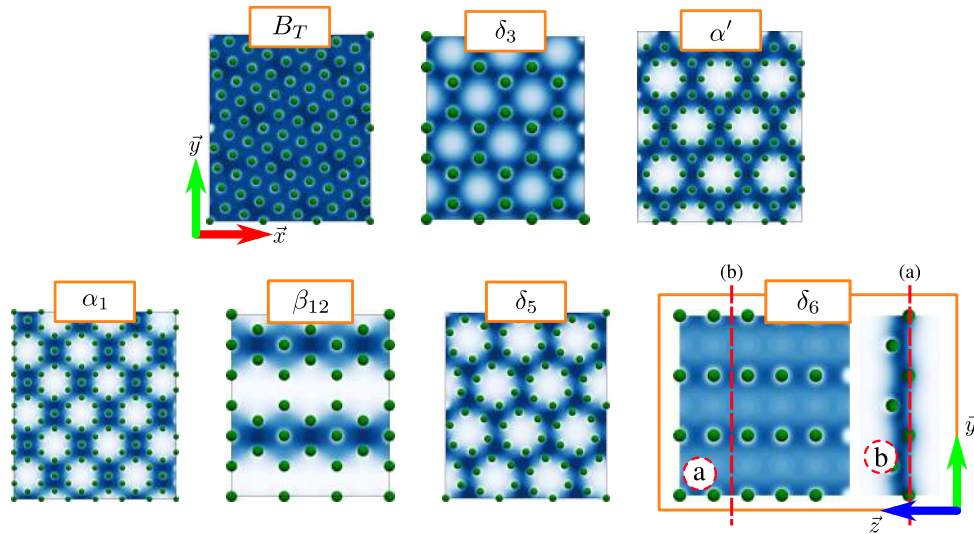
Figure 5.13: Partial density of the lowest state ($j = 1$) for each of the selected polymorphs. The plots here presented have been computed at $\mathbf{k}$, in reduced coordinates, $(0.10, 0.00, 0.00)$, $(0.10, 0.00, 0.00)$, $(0.12, 0.00, 0.00)$, $(0.12, 0.00, 0.00)$, $(0.05, 0.00, 0.00)$, $(0.05, 0.03, 0.00)$, $(0.05, 0.03, 0.00)$, $(0.09, 0.00, 0.00)$, and $(0.05, 0.00, 0.00)$ for δ_5, B_T commensurable with δ_5, β_{12}, δ_3 commensurable with β_{12}, δ_6, α', α'-Bil., and α_1, respectively.

coupling calculation can allow one to draw final conclusions. For instance, Xiao $et.$ al, studied the effect of strain and carrier-doping in this polymorph, and found hole-doping to be beneficial towards superconductivity, while electron-doping had the opposite effect [23].

5.3 α'-bilayer

Lastly, we discuss the α'-bilayer (AA-stacked α'-bilayer) as compared to the α' monolayer. The monolayer, in turn, is slightly distorted in the out-of-plane direction, alternating the displacement off-plane of the 6-coordinated atoms (Fig. 1.4). In the bilayer this distortion has a preferential direction: towards the second monolayer, covalently bonding with its 6-coordinated atoms [35].

In the discussion of the flat monolayers we did not mention the out-of-plane states, because they were not directly relevant to the effect of the defects on the electronic structure. For instance, in the flat monolayers the lowest out-of-plane states simply mirror the partial density of the lowest in-plane state ($j = 1$ for all polymorphs in Fig. 5.13) but below and above the monolayer (as for the out-of-plane p_z atomic orbital), with local maximums on top and below each atom. In the flat monolayers this is the expected behavior, as the out-of-plane states do not interact with anything else. In the bilayer however, the interaction exists and it is responsible for dragging the 6-coordinated atoms towards the central plane of the structure [35].

Compared to the monolayer, the bilayer states show states of bonding and antibonding character built from the states of the two stacked monolayers: Fig. 5.14 shows the bonding and antibonding states of the bilayer, highlighted in Figure 5.15 (only α'-Bil^j with $j = 1$ and $j = 2$), similar to $\alpha'^{,j=1}$ at $\mathbf{k} = (0.05, 0.03, 0.00)$ (Fig. 5.13). Overall, besides the doubling of the states, the shape of the bands is maintained and even the
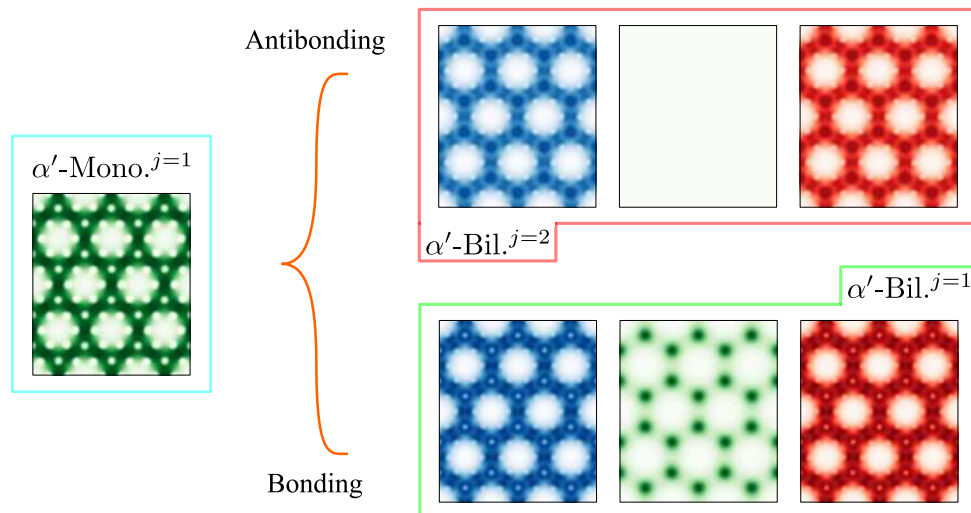
Figure 5.14: Partial density of the two lowest states of the α'-Bilayer, highlighted in green and red in Fig. 5.15. These states are similar in shape to the lowest state of the monolayer (highlighted in blue in Fig. 5.15) but showing bonding and antibonding nature. For representation, the blue partial density plots correspond to the mid-plane of the upper layer, the red plot to the lower layer, and the green plots to the mid out-of-plane position of the complete structures. One can see the similar partial densities between states of the α'-Monolayer and the upper and lower layers in the α'-Bilayer. The main difference occurs in the mid (green) plane, through the localization of the density in the bond between the two layers, showing the "bonding" (α'-Bil.$^{j=1}$) and "antibonding" (α'-Bil.$^{j=2}$) character of the states.
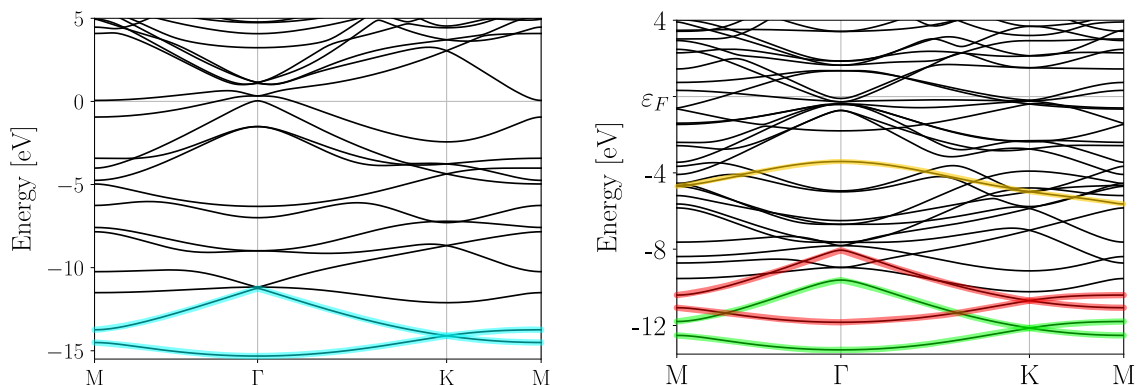
Figure 5.15: Electronic structure of the α'-Monolayer and the α'-Bilayer. Similar states appear in the bilayer and the monolayer (blue, green, red), from which the doubling of states in the bilayer can be understood as bonding and antibonding states of the monolayer (see Fig. 5.14). In orange we highlight the interlayer state α'-Bil.$^{j=16}$, localizing the partial density in the interlayer bond.

partial charge follows a similar distribution for the states in-plane (with the "bonding" and "antibonding" behavior).

Out-of-plane the picture is different. For example, the first out-of-plane state that in the monolayer was slightly localizing the density on top of each atom, is strongly attracted towards the interlayer bonding atom in the bilayer, supporting the covalent picture of the bond [35]. In terms of the electronic structure, these interlayer states appear as distinct states in the band structure. However, contrary to the defect-like states of the monolayers, in the bilayer these states are not low-dispersive.

5.4 Conclusions

In this chapter we performed a detailed analysis of the electronic structure of selected polymorphs. First, we emphasized the resemblance between the electronic structure of flat monolayers in commensurable unit cells. This supports the idea of general features of the electronic structure within the borophene class of materials. For instance, it explains why the *Box* model and self-doping can be used as an approximation to the electronic structure of different polymorphs independently of the specific electronic structure of the polymorphs.

Moreover, our analysis of the electronic structure of polymorphs in commensurable unit cells, and the study of the partial charges, proved the appearance of low-dispersive polymorph-specific states. These show the limitations of the self-doping model. It is worth pointing out that low-dispersive (localized) states are not just a mere curiosity of the electronic structure. In fact, similar flat bands have been the object of research in different fields including quantum Hall physics, superconductivity and photonics [106–108].

Also, we investigated the changes of the electronic structure with respect to buckling of the polymorphs α' and δ_6. As for the creation of defects of the flat monolayers we observed that some states in the buckled structures resemble states from the flat parent structures, but also that upon buckling some degeneracies are broken and some electronic bands shift in energy. Contrary to the creation of vacancies (or addition of interstitial atoms) the polymorph-specific states in the buckled structures do not appear as low-dispersive states in the band structure. Moreover, the changes of the electronic structure upon buckling lead to two situations of particular interest: 1) the case of α' as a semimetal, and 2) the tuning of the Fermi surface of δ_6, relevant for its superconducting properties.

Dielectric properties

In the previous chapter we performed an extensive study of the electronic structure of different polymorphs, and in particular we highlighted their resemblance and the presence of specific signatures like low-dispersive defect-like states that appear due to the creation of point defects in a parent structure. Moreover, we highlighted the fact that buckling of the structures δ_6 and α' can be a parameter to tune the electronic structure which leads to a semimetallic band structure for borophene α'. We also mentioned possible interest of Fermi surfaces for superconductivity. Thus, at this point the importance of the study of the electronic structure as a guideline for different applications is clear.

Many different examples exist in the literature investigating theoretically how and in which situations borophene could be used to tackle a specific problem: we can find it for example in the context of superconductivity [19–23], supercapacitance [24], hydrogen storage [25,26], plasmonics [27–29], and transparent conductors [30,31]. Among these, we remark the optical properties, in particular absorption, for their relatively straightforward connection with the electronic structure. Within this context we highlight the work of Adamska *et. al.* on the polymorphs δ_6 and β_{12}, in their possible application towards transparent conductors [31]. Hereafter we investigate the role of the electronic structure in the optical absorption of the polymorphs presented in Section 1.3.

6.1 Optical absorption

Using the independent-particles approach within KS, we can approximate the optical absorption as the imaginary part of the KS density-density response function (Eq. 2.20). Using this level of approximation, we computed the optical spectra of the polymorphs of Section 1.3, and we present them in Fig. 6.1. The different curves correspond to different components of the dielectric tensor ϵ_M. Our results for δ_6, β_{12} and δ_3 are in good agreement with available results in the literature with the same approximations [30,31,99]. Below, we explain the main features of the absorption spectra, and in particular the origin of "transitionless windows" (energy windows in which absorption spectra vanishes): essentially, these windows are the reason why the polymorphs δ_6 and β_{12} have been proposed as transparent conductors [1].

---

[1]To describe the polymorphs as "good" transparent conductors two conditions must be fulfilled: 1) they must be transparent in the optical regime, and 2) they must be good charge carrier conductors. Here we only focus on the first point, but works on the latter can be found in Ref. [31] for polymorphs δ_6, β_{12}.
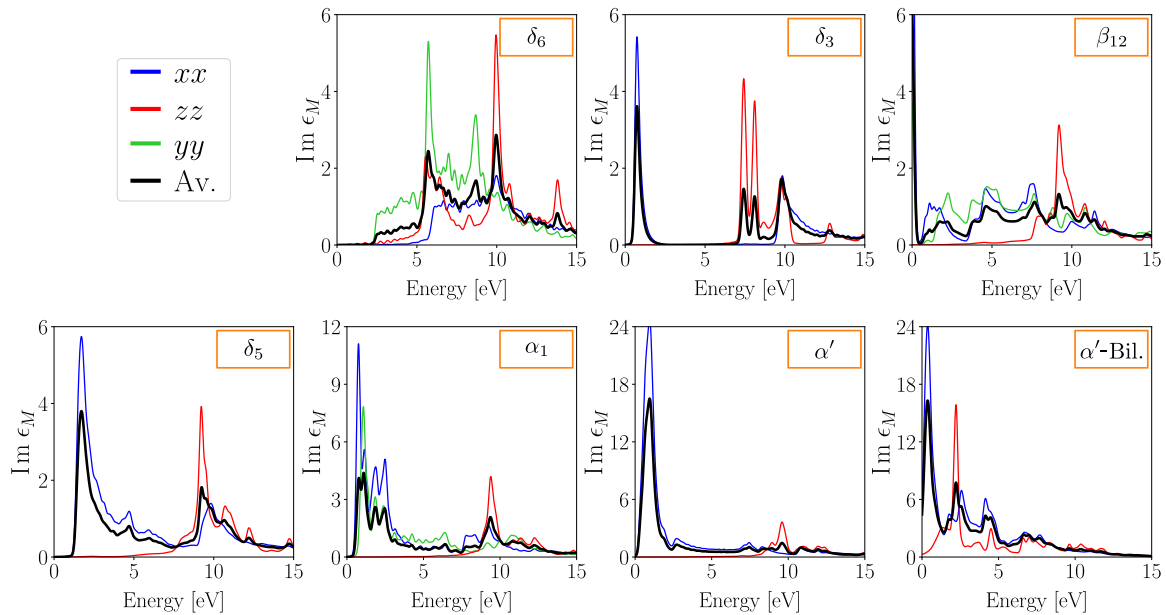
Figure 6.1: Optical absorption of selected borophene polymorphs within the independent particles approximation (IPA): xx, yy and zz describe the change of the induced field due to the electronic transitions paralel to x, y and z, respectively. Av. is the average among the three directions. Moreover, notice that δ_3, δ_5, α' and the α' bilayer have equal diagonal componentsm $(xx) = (yy)$, thus we show only one direction: (xx).

Intraband and interband transitions

Borophene in its multiple polymorphs is a metallic system, as can be seen from the electronic band structures in Fig. 5.1. In optical absorption (Eq. 2.23), where the transitions at vanishing momentum transfer ($\mathbf{q} \to 0$) shape the spectra, transitions around the Fermi level play an important role at vanishing photon energy ($\omega \to 0$), as in principle, they should reflect in the absorption spectra in the form of a very sharp peak at $\omega \to 0$. This is known as the Drude peak [109]. We are not interested in this zone of the spectra which determines the conductivity, but which is notoriously difficult to converge. Thus, we focus only on interband transitions, *i. e.*, the shape of the spectrum for $\omega > 0$.

In fact, Adamska *et al.*, showed that intraband transitions in δ_6 only affect the spectra at low energies ($\omega < 1$ eV) [31]. Analogously, we want to show for our simulations two things: 1) that intraband transitions do not change the absorption spectra besides at $\omega \to 0$: as an example we selected the case of borophene δ_3, and 2) that the sharp peak at $\omega \to 0$ in the β_{12} structure is due to interband transitions. We can understand the latter straightforwardly from the band structure (Fig. 6.2, right): at Γ multiple bands cross the Fermi energy with a $\Delta\omega \sim 0.01$; considering only vertical transitions these could make an absorption peak at $\omega \sim 0.01$, nonetheless, the denominator of the density-density response function (Eq. 2.21) contains a quantity η which acts as a "broadening" of the δ-like transitions in the absorption spectra, thus giving its final shape. Physically such a broadening describes the life time of an electronic transition, but in our picture we use it as an artificial broadening. The effect of broadening can be seen in Fig. 6.2 (left), by comparing the blue and gray curves, with $\eta = 0.01$ and $\eta = 0.001$ eV, respectively.

The intraband transitions can give contributions also at low energies. To show this we performed an explicit computation of Eq. 2.21 with vanishing $\mathbf{q}$ using a "double-grid"
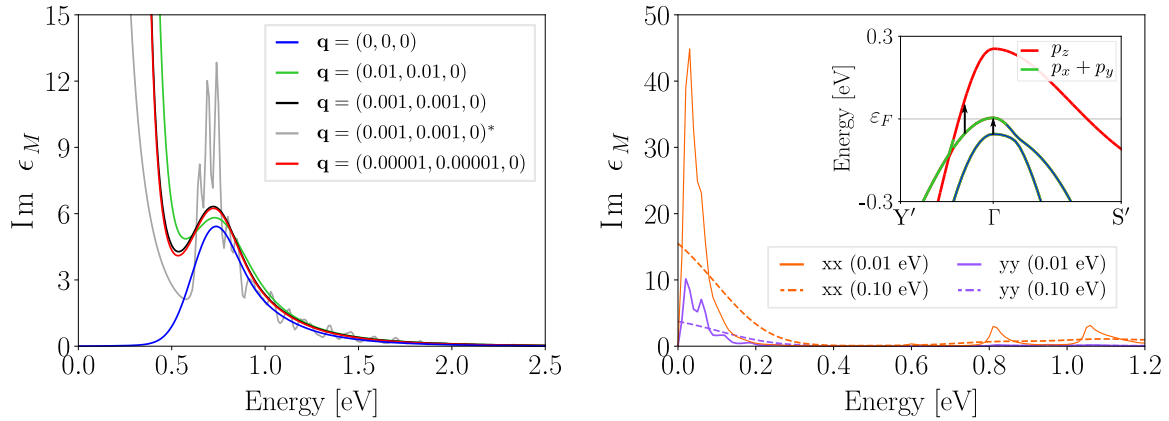
Figure 6.2: Left: low-energy region of the optical spectrum of borophene δ_3 computed with and without explicit evaluation of the transitions at vanishing momentum transfer. The broadening of the spectra is 0.1 eV, except of (*) which broadening is 0.01 eV: the account of interband transitions only affect the optical spectra at $\omega < 0.5$ eV. Right: absorption spectra of borophene β_{12}. The large peak at $\omega \to 0$ eV is due to interband transition at Γ, although it appears in Fig. 6.1 as interband-like due to the broadening of the curve.

method [?][2] for δ_3. Our calculations, plotted in Fig. 6.2, show that the inclusion of transitions at small $\mathbf{q}$ does not affect the optical spectra beyond the addition of the peak at vanishing momentum transfer. Since addition of intraband transitions do not affect the discussion of our results, we proceed with the optical spectra as presented in Fig. 6.1.

A family of electronic transitions

In order to establish some general trends for the different polymorphs, let us focus for a moment on a simple structure: borophene δ_3. In this polymorph we can associate the peaks in its optical absorption spectrum to a minimal set of bands in the electronic structure. For instance, we can recognize five absorption peaks in the range from 0 to 12 eV (Fig. 6.3): 1) at 0.7 eV merely in-plane (xx), 2) 7.4 eV out-of-plane (zz), 3) 8.1 eV out-of-plane, 4) 8.6 eV out-of-plane, and 5) 9.8 eV in-plane and out-of-plane at the beginning of the continuum. Schematically, we can associate these peaks to vertical transitions in the electronic structure of Fig. 6.3[3], and taking into account the hybridization of the states in-plane (s, p_x and p_y), and the negligible hybridization of the out-of-plane states (p_z), we can define six different types of transitions:

- In-plane $p_x + p_y$ to in-plane s: $t(p_\parallel \to s)$.

- Out-of-plane p_z to out-of-plane p_z: $t(p_z \to p_z)$.

- In-plane $s + p_x + p_y$ to in-plane $s + p_x + p_y$: $t(sp_\parallel \to sp_\parallel)$.

- In-plane s-state to out-of-plane p_z: $t(s \to p_z)$.

- In-plane $p_x + p_y$ to out-of-plane p_z: $t(p_\parallel \to p_z)$.

---

[2]With this method we can compute the $\chi(\mathbf{q}, \omega)$ for an arbitrary small $\mathbf{q}$ giving rise to the contribution at $\omega \to 0$ without the need of a large number of $\mathbf{k}$-points in the wave function.

[3]The optical absorption is computed with contributions from the full Brillouin zone (according to the selected $\mathbf{k}$-mesh). The high symmetry path in Fig. 6.3 is representative of these transitions.
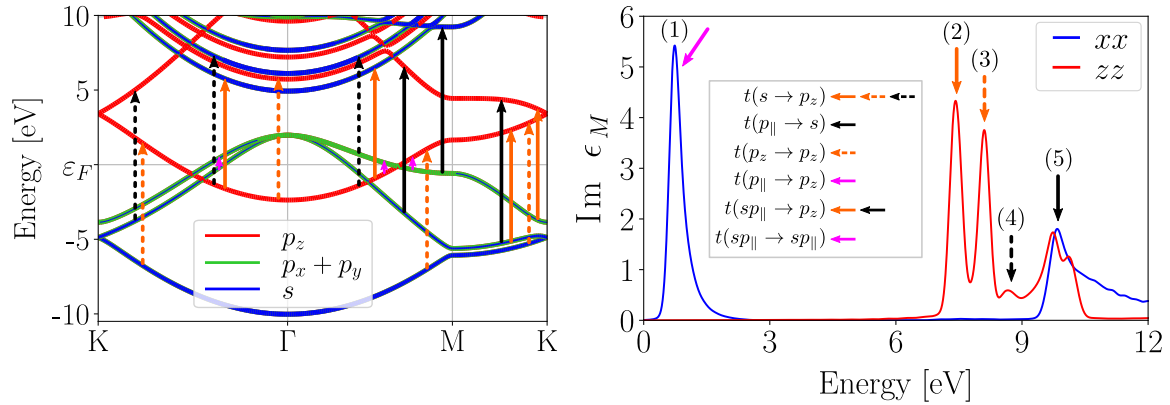
Figure 6.3: Electronic structure of borophene δ_3 projected onto atomic orbital (left), and computed orbital spectra within the IPA (right). The absorption peaks are well-defined, and so are easily associated to vertical transition in the electronic structure (arrows): in-plane absorption peaks appear from in-plane states, while out-of-plane absorption peaks involve transitions from in-plane states to out-of-plane.

- In-plane $s + p_x + p_y$ to out-of-plane p_z: $t(sp_\parallel \to p_z)$.

Moreover, by verifying the energies at which these transitions occur, we can describe the absorption peaks in Fig. 6.3 as a combination of the above transitions as follows:

1) 0.7 eV: $t(sp_\parallel \to sp_\parallel) + t(p_\parallel \to p_z)$

2) 7.4 eV: $t(s \to p_z) + t(sp_\parallel \to p_z)$

3) 8.1 eV: $t(s \to p_z) + t(p_z \to p_z)$

4) 8.6 eV: $t(s \to p_z)$

5) 9.8 eV: $t(sp_\parallel \to p_z) + t(p_\parallel \to s)$

We can use these transitions to explain the in-plane and out-of-plane components of the absorption spectra: for example, the absorption peak at 7.4 eV is visibly only in the (zz) component of the ϵ_M tensor. This is consistent with the analysis in terms of transitions $t(s \to p_z) + t(sp_\parallel \to p_z)$. Sometimes, looking only at the band structure can be misleading. For example, the peak at 0.7 eV is given by the (xx) component of ϵ_M, while energetically, the band structure also suggest that transitions $t(p_\parallel \to p_z)$ contribute. We discuss the importance of the wave functions of the initial and final states of the electronic transitions in the following section.

6.1.1   Borophene as a transparent 2D material: δ_3

Borophene δ_3 shows a feature of technological importance: its absorption spectrum displays an energy window between 1.5 and 7 eV (visible light and near UV) of nearly zero absorption (Fig. 6.4). We refer to it as a transitionless window. This window is much larger than the ones in δ_6 (2.6 eV)[4] and β_{12} (04 eV)[5] [31]. Moreover, δ_3 is among the already synthesized structures [34], and the simplicity of its band structure can help us to understand at the microscopic level how borophene becomes transparent.

There are different reasons for which this polymorph can be transparent within a given energy window: 1) trivially, because there are no conduction and valence states within

---

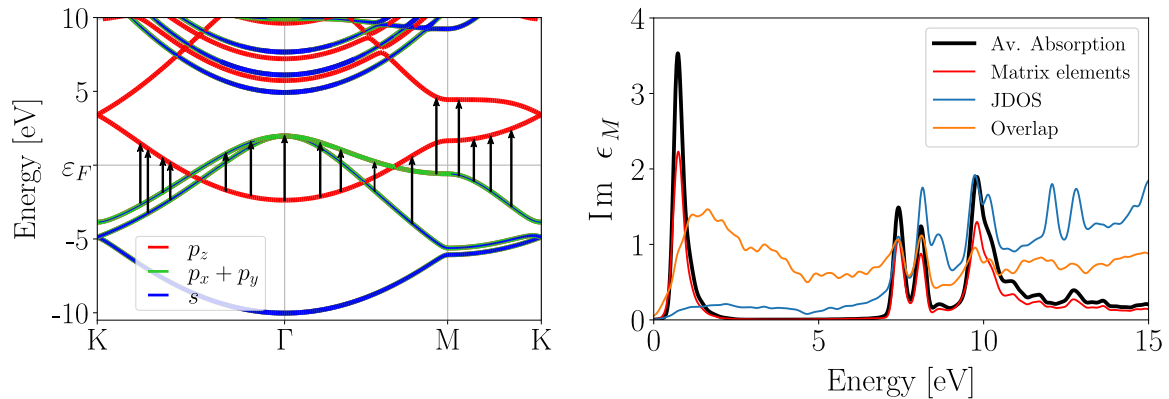[4]Neglecting intraband transitions.
[5]Idem.

Figure 6.4: Vertical transitions within 2 to 6 eV in borophene δ_3 (left), and optical spectra within the IPA (right). The energy window from 1.5 to 7 eV does not show any absorption peak and thus we refer to it as a transitionless window: it does not appear because of a lack of transitions (seen in the JDOS). In fact, it is a feature of the matrix elements, although not due to lack of overlap between the wave functions (overlap calculated with Eq. 6.1).

that energy range that allow for vertical transition (like in a semiconductor within the optical gap), or 2) that the numerator of the polarizability (Eq. 2.20) becomes zero for the transitions within the energy window. To differentiate between these two cases we analyze the joint density of states, JDOS $= -\mathrm{Im}\sum_{nn'}(f_{n'} - f_n)[\omega - (\varepsilon_n - \varepsilon_{n'}) + \mathrm{i}\eta]^{-1}$, defined as the imaginary part of Eq. 2.20 setting the numerator to 1 (i. e., neglecting the contribution of the wave functions and the dipole operator). We plotted the JDOS together with the absorption spectra in Fig. 6.4, which shows that energy differences (between occupied and empty states) are possible at all frequencies.

Thus, the gap in the absorption spectrum is due to the numerator in Eq. 2.20: the matrix elements within the sum over transitions. Moreover, there are two forms in which this numerator can vanish: 1) because of symmetry: due to the operator $[e^{\mathrm{i}\mathbf{q}+\mathbf{G})\cdot\mathbf{r}}]$, or 2) simply because the initial and final wave functions do not overlap. In order to determine the reason we propose a function with the same structure as the polarizability but accounting only for overlap of the wave functions:

$$\mathrm{Overlap}(\mathbf{q}, \omega) = -\mathrm{Im}\left[\sum_{nn'}(f_{n'} - f_n)\frac{\int \mathrm{d}\mathbf{r}\ |\phi^{n'}_{\mathbf{k}-\mathbf{q}}(\mathbf{r})|^2|\phi^n_{\mathbf{k}}(\mathbf{r})|^2}{\omega - (\varepsilon_n - \varepsilon_{n'}) + \mathrm{i}\eta}\right] \qquad (6.1)$$

in the optical regime with $\mathbf{q} \to 0$, Eq. 6.1 has to be compared with the JDOS in order to see the effect of overlap: Eq. 6.1 serves like a weighted JDOS (per transition), and therefore it makes sense only in comparison with another function: the JDOS or the imaginary part of the polarizability. We plotted in Fig. 6.4 the overlap function for δ_3. It reproduces the main peaks of the absorption spectrum, but there is no evidence of the transitionless window. Thus, we can conclude from this analysis that the gap in the absorption spectrum of borophene δ_3 between 1.5 and 7 eV is due to the symmetry of the wave functions in the matrix elements in Eq. 2.20.

The transitionless window is not numerically zero. If we zoom in in this region (see Fig. 6.5, right) we see that the absorption monotonically increases. This increase corresponds to following the in-plane band $(s + p_x + p_y)$ along $\Gamma \to$ K in the band structure (see Fig. 6.5, left panel) for which the s-component becomes larger. Still in the absorption
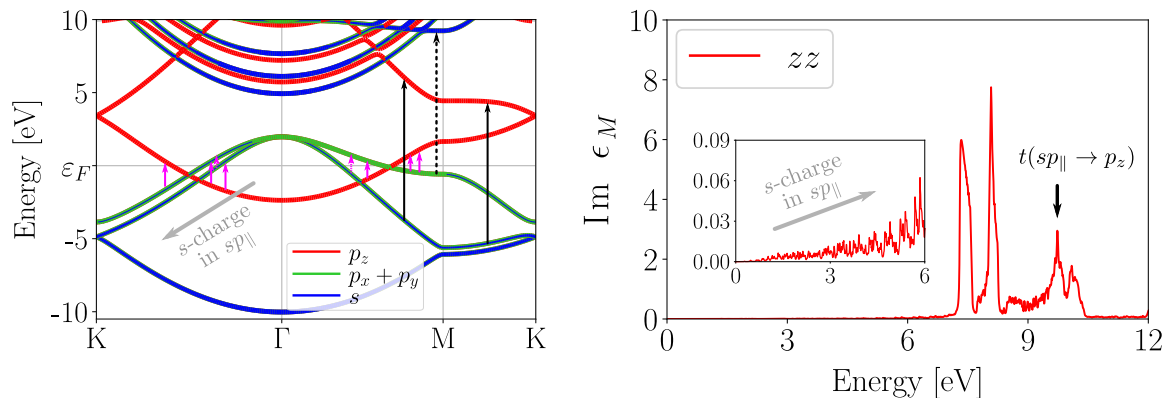
Figure 6.5: Low and high-energy transitions in borophene δ_3: at 9.8 eV the transitions out-of-plane are due to transitions $t(sp_{\parallel} \rightarrow p_z)$, while at low energies (from 0 to 2 eV) the transitions out-of-plane are $t(sp_{\parallel} \rightarrow p_z) + t(p_{\parallel} \rightarrow p_z)$. The latter do not show un in absorption spectrum, thus suggesting that the transitions $t(p_{\parallel} \rightarrow p_z)$ are killed by symmetry. Notice that absorption increases with the hybridization of p states in-plane with s orbitals.

spectrum these contributions are negligible. We now move to analyze the absorption peak at 9.8 eV: both, in-plane and out-of-plane, absorption contributes for this peak. Again by comparing with Fig. 6.3 (left), we associate this peak to transitions $t(p_{\parallel} \rightarrow s)$ near M (Fig. 6.4) and $t(sp_{\parallel} \rightarrow p_z)$ along $\Gamma \rightarrow M \rightarrow K$. In the region from 0 to 2 eV, possible transitions are $t(sp_{\parallel} \rightarrow sp_{\parallel}) + t(sp_{\parallel} \rightarrow p_{\parallel}) + t(p_{\parallel} \rightarrow p_z)$, that lead to the absorption peak in-plane at 0.7 eV but no absorption peak out-of-plane, therefore suggesting a similar situation as for the transitionless window: the transitions $t(p_{\parallel} \rightarrow p_z)$ are either killed by symmetry or overlap.

Electronic transitions in flat monolayers

In a similar approach as for the electronic properties where we analyzed the similarities among the polymorphs, we now turn to to similarities and differences of the optical properties. We can look again at Fig. 6.1: the flat monolayers β_{12}, δ_5, α_1 and even the buckled structure α', show a similar absorption spectra as that of borophene δ_3, namely an in-plane absorption peak below 5 eV and an out-of-plane peak around 10 eV. However, they lose the transitionless window between 1.5 and 7 eV. On the other hand, as it has been pointed out by Adamska *et. al.*, at least β_{12} has its own transitionless window below 0.4 eV [31]. It is evident from Fig. 6.1 that also δ_5 displays a similar behavior (below 1.2 eV), and also α_1, although less pronounced (below 0.5 eV). In order to clarify these common features we perform, as we did for δ_3, a thorough analysis of borophene δ_5 and β_{12}.

Let us start with the peaks out-of-plane: in δ_3 there are two well-defined absorption peaks at 7.4 and 8.1 eV, one weaker and wider at 8.6 eV, and a last one in-plane and out-of-plane at 9.8 eV. In δ_5 we can only recognize a sharp peak at 9.20 eV, and two weaker and wider at 10.8 and 12.28 eV, and in β_{12}, only a well-defined peak at 9.20 eV surrounded by wider and less intense absorption peaks. We can link this difference in the out-of-plane projection of the absorption spectra among polymorphs to the differences in their electronic structure, in particular to the breaking of degeneracies and the appearance of defect-like states; if a rigid model of the electronic structure (self-doping) were valid, the
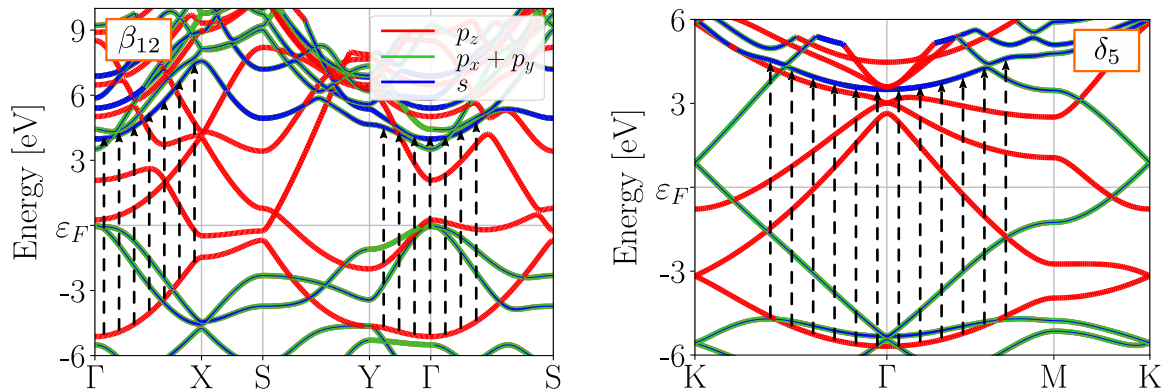
Figure 6.6: Band structure of borophene β_{12} and δ_5: the arrows show the vertical transitions at 9.2 eV, namely $t(s \to p_z)$. These transitions seem to be general for the flat monolayers, and can be understood from the 2D + "particle in a box" model with $j = 2$ and $j = 3$. The *Box* model, however, overestimates the energy difference $|\varepsilon_\perp^{j=3} - \varepsilon_\perp^{j=2}|$.

same out-of-plane peaks should appear at the same photon energy for these high-energy peaks. For simplicity, we focus only on the well-defined peak at around 10 eV, which also seems to be common for α_1 and α'.

We show in Fig. 6.6 the band structure projected onto atomic orbitals for borophene δ_5 and β_{12}: we included the vertical transitions corresponding to 9.20 eV. Despite the difference in shape, this peak is related to the transition $t(p_z \to s)$ and $t(p_z \to sp_\parallel)$: they go from the lowest out-of-plane band to the first unoccupied in-plane band. In the physical interpretation of the 2D HEG + "particle in a Box" model of Section 4.2 this state corresponds to a second replica ($j = 3$).

Next, we investigate the in-plane absorption peak. This appears in δ_5 and β_{12}, but also in α_1 and α'. Energetically in δ_3 this peak at 0.7 eV could be due to transitions $t(sp_\parallel \to sp_\parallel) + t(p_\parallel \to p_z)$, but we later noticed that transitions $t(p_\parallel \to p_z)$ are killed by symmetry, therefore the peak at 0.7 eV must be only due to $t(sp_\parallel \to sp_\parallel)$. These transitions nonetheless seem to be unique of this polymorph, as while electrons are introduced into the system[6], the in-plane bonding states are occupied [45], therefore shifting down with respect to the Fermi energy. The latter has a strong impact on electronic transitions at low energies: we show in Fig. 6.7 that the large absorption peak in-plane in β_{12} (1.5 eV)[7], δ_5 (1.7 eV), α' (0.75 eV)[8], α_1 (0.86 eV) is due to $t(p_z \to p_z)$, but parallel to the plane[9]; this in-plane absorption peak due to out-of-plane transitions is also seen in graphite and graphene due to $\pi \to \pi^*$ transitions [110].

Fig. 6.7, shows that for the flat polymorphs β_{12}, δ_5, and α_1 there is null hybridization of the p_z states, while in α' (buckled), the hybridization is noticeable only near Γ.

---

[6]Following the self-doping idea: 1) other polymorphs can be obtained by adding atoms to δ_3. And 2) the more atoms the more electrons, and thus the Fermi level moves upwads with respect to the rigid electronic structure.

[7]β_{12} has two different absorption peaks in-plane due to its anisotropy and none of them is a sharp peak. To investigate the transitions of the lowest peak we selected the range from 1 to 2 eV which comprises most of the xx-peak and only the beginning of the yy-peak.

[8]We selected the highest peak in-plane, from 0.64 to 1.19 eV.

[9]This means that we investigate the (xx) component of ϵ_M (so with momentum transfer oriented in-plane) but we involve transitions $t(p_z \to p_z)$ from states that are localized above (and below) the boron plane.
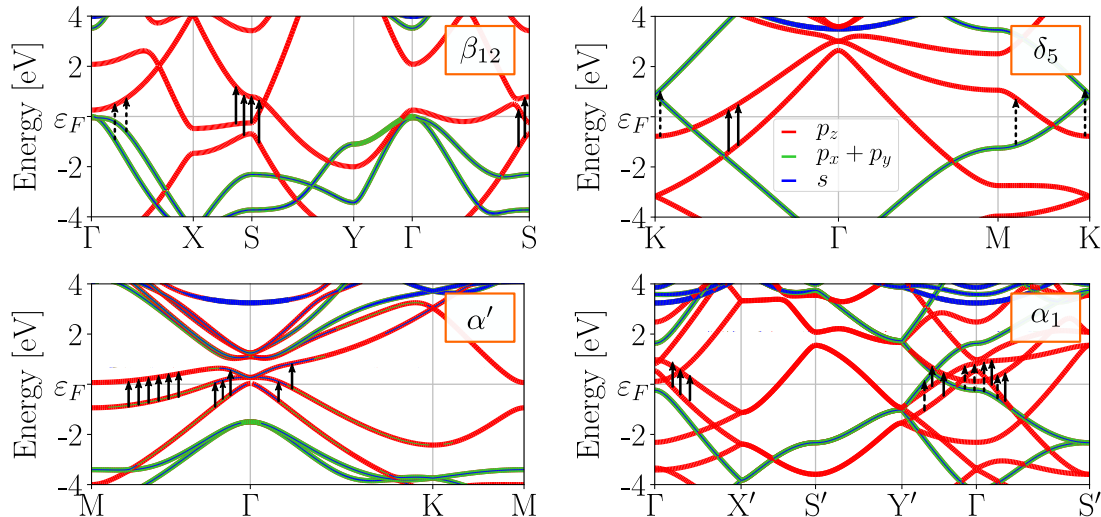
Figure 6.7: Low-energy vertical transition of polymorphs β_{12}, δ_5, α' and α_1: these transitions give raise to the low-energy absorption peaks in Fig. 6.1. Notice that the absorption peaks are "in-plane", but the transitions are $t(p_z \to p_z)$, *i. e.*, parallel to the plane, in contrast with δ_3 which low-energy peak is due to transitions in-plane $t(sp_\parallel \to sp_\parallel)$.

Nonetheless, the charge is predominantly p_z-like and the absorption spectra (Fig. 6.7) only capture the in-plane component. This lack of hybridization plays the main role when it comes to optical absorption, and as we showed earlier, it is responsible for the transparency in borophene δ_3. In fact, other polymorphs show transitionless windows of the same nature as δ_3: β_{12} a small window from 0.3 to 0.6 eV due to $t(p_\parallel \to p_z)$ at Γ, δ_5 from 0 to 1.2 eV due to $t(p_\parallel \to p_z)$ along $M \to K$ and in the vicinity of K along $K \to \Gamma$, and α_1 from 0 to 0.4 from $t(p_\parallel \to p_z)$ at Γ (Fig. 6.7).

Other 2D structures

Among our selection of polymorphs there are two cases we have not discussed so far, and that have absorption spectra (Fig. 6.1) different from those of the flat monolayers: the buckled δ_6 structure, and the α'-Bilayer. The former has been proposed as a transparent conductor because of the large transitionless window from 0 to 2.3 eV [31]. It is interesting to notice that in this polymorph the transitionless window appears mainly because of the lack of vertical transitions within such energy range: we can see this from the joint density of states, and schematically from the band structure in Fig. 6.8: the lowest vertical transition is at 2.5 eV along $\Gamma \to X$, in agreement with the JDOS and the absorption spectra.

Borophene δ_6 is highly anisotropic: it buckles along the y-direction (Fig. 1.4), and this anisotropy is translated into the absorption spectrum being significantly different along xx and yy (Fig. 6.8). Moreover, we can recognize from the projection of the bands onto atomic orbitals that the out-of-plane state now hybridizes with the in-plane states: for example with p_x along $\Gamma \to M$, $S \to Y$ and $\Gamma \to S$, and with p_y around Γ above the Fermi energy (Fig. 6.8). This leads to different types of transitions, and in particular absorption peaks which are both in-plane and out-of-plane. Nonetheless we can still find some similarities between the buckled δ_6 structure and the flat monolayers: for example, the mostly out-of-plane peak at 9.9 eV involves transitions at Γ from a majorly out-of-
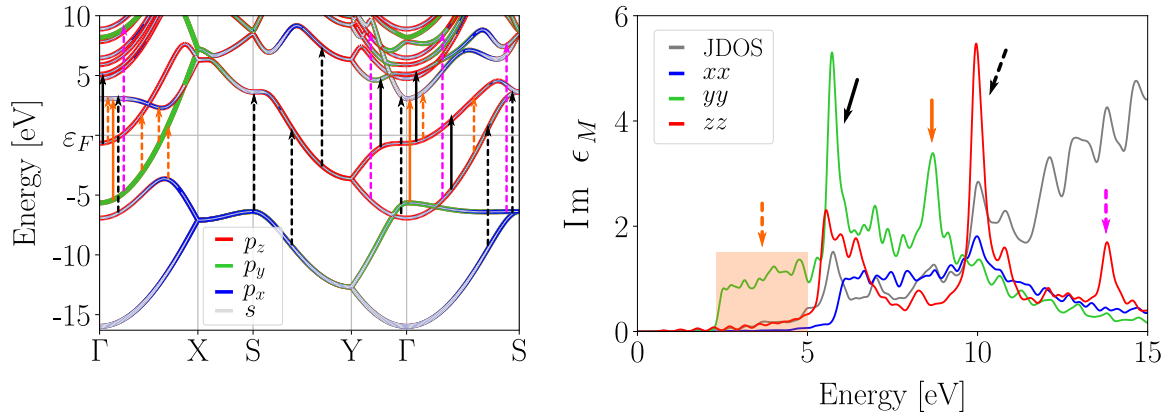
Figure 6.8: Orbital-resolved electronic structure of borophene δ_6 and its absorption spectrum: the arrows in the band structure correspond to the absorption peaks. Notice that this polymorph is strongly anisotropic, and this feature is reflected in the band structure and the absorption spectra: the y direction is the direction along which the structure buckles. Moreover, this polymorph shows a transitionless window from 0 to 2.3 eV, although insted of being due to transitions $t(p_\parallel \to p_z)$ as for the flat monolayers, it is due to the anisotropy of the system. Another difference between δ_6 and the flat polymorphs is the hybridization of the states out-of-plane: noticeable with s along $\Gamma \to X$ below the Fermi energy, with p_x along $S \to Y$ and $\Gamma \to S$ at the Fermi level, and with p_y at Γ above the Fermi energy.

plane state to an in-plane state (of mostly s character) semi-parallel to the valence state. Moreover, the highest peak in-plane (5.7 eV) is due to (mostly) out-of-plane to (mostly) out-of-plane states.

Regarding the occupied bands in δ_6, the hybridization occurs mostly along the x-direction (the non-buckled one): we can see this from the channel-like states out-of-plane seen in the density plots in Section 5.2 (Fig. 5.10). Moreover, notice that the absence of hybridization between p_y and p_z states could, in principle, yield transitionless windows as the ones for the flat polymorphs. We investigate this possibility in Section 7, applied to nesting of the Fermi surface.

We now turn to the α'-Bilayer: we described this polymorph in Section 5.3 essentially as two α' monolayers in bonding and antibonding-like configuration with extra states (defect-like) due to the interlayer bonding atom. Although this picture is adequate for the states investigated in Section 5.3, it is a crude generalization based on the density distribution, and we have already pointed out that the shape of the wave functions has a strong impact on the final shape of the absorption spectra. Thus, it is necessary to look at the orbital-resolved band structure in Figure 6.9 to understand the different contributions: notice the hybridization of the states in-plane and out-of-plane $p_z + s$ and $p_z + p_\parallel$ just below the Fermi level along $\Gamma \to K$, as well as $p_z + s$ at K, and $p_z + p_\parallel$ at Γ above the Fermi energy (Figure 6.9). As it occurs for the buckled δ_6 structure, hybridization yields a mixed in-plane and out-of-plane response.

We can still distinguish at least two well-defined absorption peaks in the bilayer: an in-plane peak at 0.3 eV, and an out-of plane peak at 2.2 eV. The former is due to transitions (mostly) out-of-plane to (mostly) out-of-plane in the vicinity of Γ and K near the Fermi level, while the peak at 2.2 eV (out-of-plane) is mainly due to transitions (mostly) out-of-plane to (mostly) s at K (Fig. 6.9). Thus, besides the hybridization of the states, the absorption peaks in-plane and out-of-plane are of similar nature as those
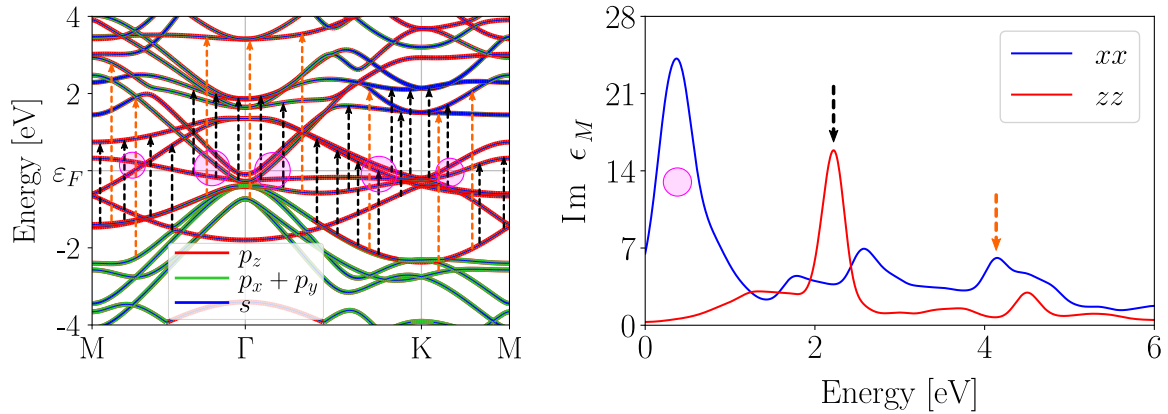
Figure 6.9: Band structure, absorption spectrum and transitions of the α'-Bilayer. Two features stand out for this polymorph with respect to the others: the hybridization of the out-of-plane states with s and $p_x + p_y$ noticeable along $\Gamma \to K$ just below the Fermi level, and the out-of-plane peak shifted towards lower energies with respect to the monolayer: from ≈ 10 eV in α' (Fig. 6.1), to 2.2 eV due to transitions around K.

of the monolayers[10].

6.1.2 Engineering transparent conductors

Among the different polymorphs, δ_3 is in a privileged position: the Fermi level and the electronic structure are such that the transitions occurring from 1.5 to 7 eV are mainly of a single type: $t(p_\parallel \to p_z)$. These transitions are killed by symmetry, yielding a transitionless window. As we have seen, these transitions are not unique of this polymorph (δ_3), in fact similar windows exist for β_{12}, δ_5 and α_1. Moreover, we have seen in Section 5.1, that the electronic structure of different polymorphs share similar features: for instance, δ_3 and β_{12} have a recognizable common band structure (Fig. 5.3), plus the shift of the Fermi energy, the addition of defect-like states, and the breaking of degeneracies. Thus, it is interesting to investigate which of the differences between δ_3 and β_{12} make such different absorption spectra, in particular with respect to the transitionless window.

Self-doping and optical absorption

An obvious point is the position of the Fermi energy: in δ_3 the Fermi level is positioned at a point such that even the low-energy absorption peak is due to transitions $t(sp_\parallel \to sp_\parallel)$, while for the rest of the polymorphs it is due to $t(p_z \to p_z)$. The self-doping picture helps understanding this: the in-plane states get occupied upon the addition of electrons, and thus the transitions $t(sp_\parallel \to sp_\parallel)$ from the bonding states do not appear anymore. From the same shift of the Fermi energy the states out-of-plane get situated around the Fermi level prioritizing transitions $t(p_z \to p_z)$.

---

[10]The shift in energy could be related to the dimensionality: in the 2D HEG + "particle in a box" model of Section 4.2, the discrete jumps in energy out-of-plane are inversely proportional to the box width. In a simplified view, switching from the monolayer to the bilayer would translate as an increment of the box width, and consequently as reduction of the energy differences between $j = 1, 2, 3$, etc., as compared to the monolayer.
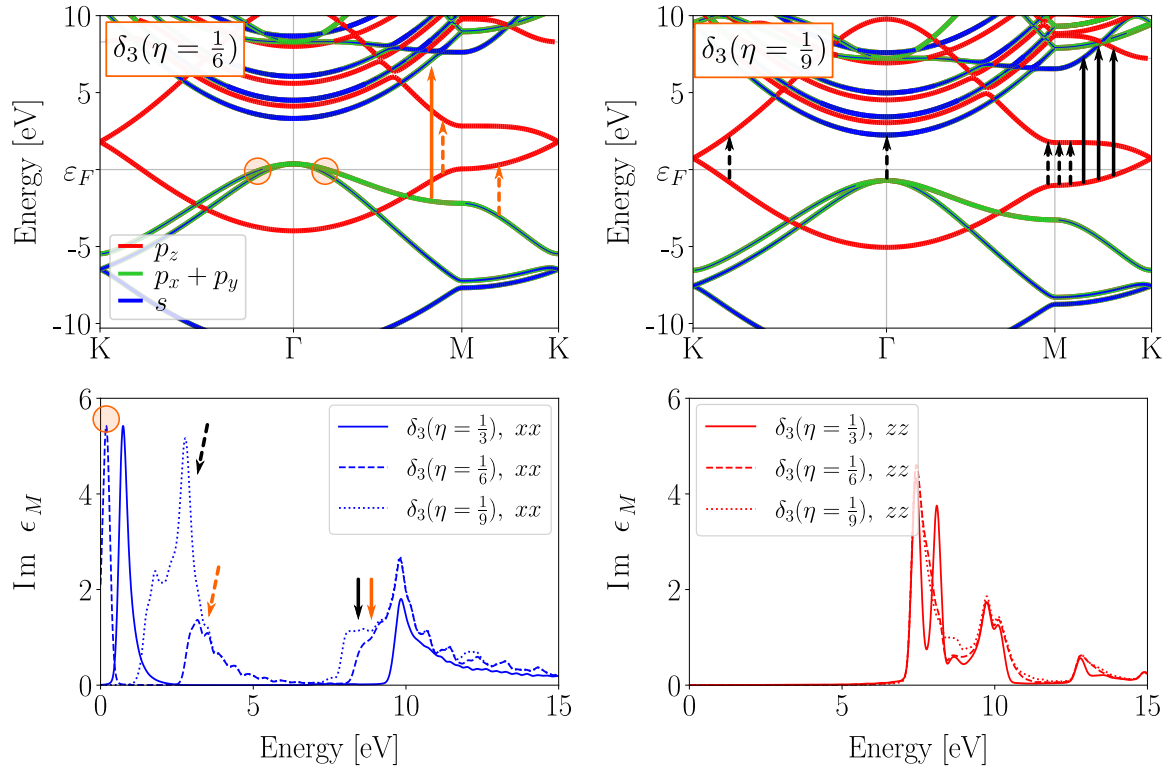
Figure 6.10: Up: Electronic structure of borophene δ_3 electron-doped to $\eta = 1/6$ and $\eta = 1/9$ to simulate the polymorphs β_{12} and α within the self-doping picture. Down: absorption spectra of δ_3 neutral and electron-doped: upon the addition of electrons (shifting upwards the Fermi energy) an absorption peak in-plane appears due to $t(p_z \to p_z)$ transitions as for the actual β_{12} and α (α_1 and α') polymorphs (Fig. 6.7). Moreover, because of the occupation of the states the transitions $t(sp_\parallel \to sp_\parallel)$ vanish. The out-of-plane component of the absorption spectra remains mostly unchanged.

In Figure 6.10 we show the band structure of δ_3 rigidly shifted to match the Fermi energy of the polymorphs β_{12} ($\eta = 1/6$) and α ($\eta = 1/9$)[11]. The simple repositioning of the Fermi energy changes the absorption spectra: it slowly removes the transitions $t(sp_\parallel \to sp_\parallel)$ near Γ, and introduces a wide peak at 3.2 eV for $\delta_3(\eta = 1/6)$, and at 2.8 eV (and a shorter one at 1.8 eV) for $\delta_3(\eta = 1/9)$ mainly due to transitions $t(p_z \to p_z)$ at M. Other differences worth pointing out are: a transitionless window from 0 to 1.8 eV in $\delta_3(\eta = 1/9)$ simply due to lack of transitions in that energy range as for δ_6, and a slight modifications of the absorption peaks in-plane and out-of-plane at high energies due to the filling of the states, in particular the occupation of the band out-of-plane along M $\to$ K (Fig. 6.10).

Of course, with respect to the real β_{12} and α (or α'), more differences exist due to the defect-like states and, in general, the breaking of degeneracies (see Fig. 6.11). Nonetheless this simple example shows how the position of the Fermi level affects the optical properties: for instance, one could trigger absorption within the transitionless window of borophene δ_3 via electron-doping. This is a very powerful conclusion coming from the simple idea of self-doping. Moreover, this make us wonder about the opposite situation: can we hole-dope borophene polymorphs in order to obtain transparency?

---

[11]Keeping the rigid electronic structure of δ_3 we recomputed the Fermi energy with extra electrons according to Eq. 1.3.
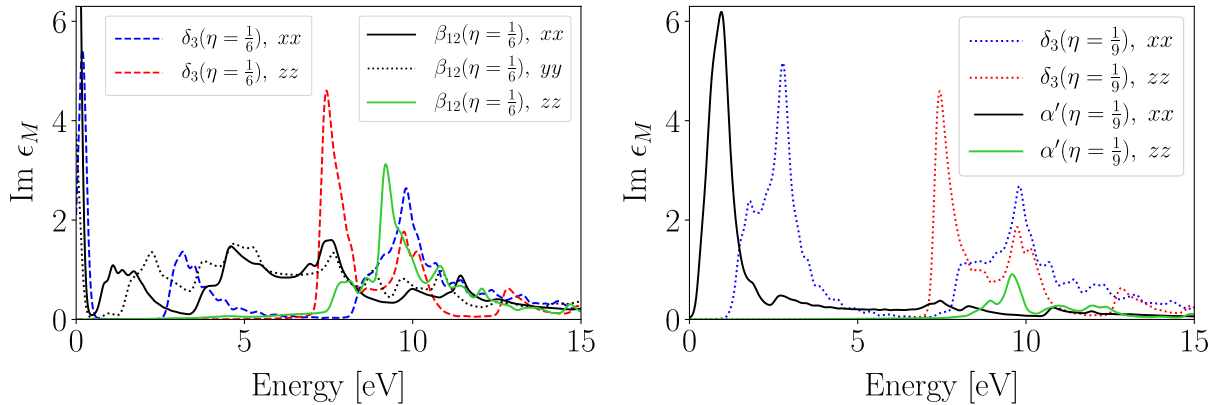
Figure 6.11: Left: absorption spectra of neutral borophene β_{12} and δ_3-electron doped to the same number of electrons per unit unit cell as β_{12} ($\eta = \frac{1}{6}$). Right: δ_3-electron doped to the same number of electrons per unit unit cell as α' ($\eta = \frac{1}{9}$). The spectra for $\alpha'(\eta = \frac{1}{9})$ is scaled by 0.25.
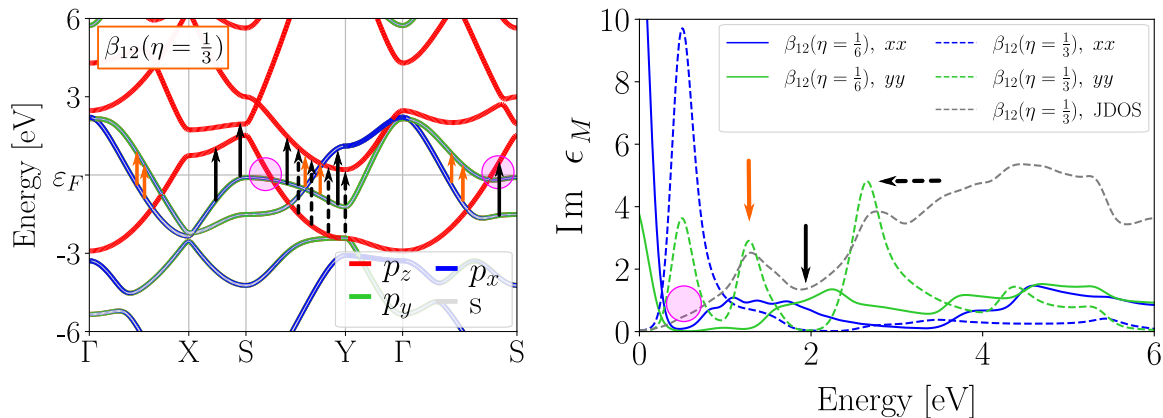
Figure 6.12: Left: electronic structure of borophene β_{12} hole-doped to $\eta = {}^1\!/_3$ to simulate the polymorph δ_3 within the self-dopin picture. Right: absorption spectra of neutral and hole-doped β_{12} with absorption peaks identified within the band structure. A small transitionless window (from 1.8 to 2.2 eV) is opened, nonetheless the characteristic that stands out is the increased absorption upon hole-doping. Moreover, notice that the peak at 2.6 eV is due to transitions $t(p_z \to p_z)$, a feature not present in δ_3.

For this, we selected β_{12}, a polymorph that has already been proposed for transparent conductors [31], and that has been synthesized on a metal substrate [33], and in its free-standing form [36]. Analogously to our study on electron-doping δ_3, we fixed the electronic structure of β_{12} and recomputed to Fermi energy according to the number of electrons in δ_3 ($\eta = {}^1\!/_3$). The obtained absorption spectrum and the shifted orbital-resolved band structure are shown in Figure 6.12. Notice that this polymorph is highly anisotropic (Fig. 1.4), thus we have included separately the projection in-plane as p_x and p_y, and displayed absorption along (xx) and (yy).

We must say that a little transitionless window opened from 1.8 to 2.2 eV: this is accompanied by a decrease of the joint density of states and transitions from states in-plane (mostly of p character) to out-of-plane. However, the most noticeable change is the sudden increase of absorption at 0.5, 1.3 and 2.6 eV (peaks in Fig. 6.12): the peak at 1.3 eV remind us the absorption peak at 0.7 eV in δ_3 due to transitions $t(sp_\parallel \to sp_\parallel)$ (Fig. 6.12), however the peak at 2.6 eV has no equivalent in δ_3: it is due to transitions $t(p_z \to p_z)$, where the p_z state in the conduction band is a defect-like state of the system

Figure 6.13: Left: orbital-resolved electronic structure of borophene β_{12} computed self-consistently with only 12 electrons (3 valence electrons per boron atom, and removing 3). Right: absorption spectrum within the IPA. Notice that the absorption peaks are of similar origin as in Fig. 6.12 (β_{12} rigidly shifted), nonetheless as the out-of-plane st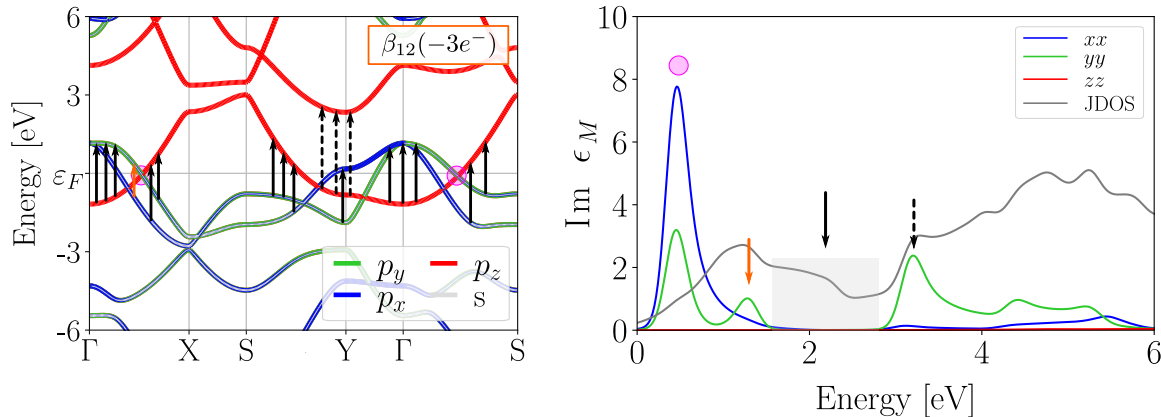ates get closer to the Fermi level as well as the in-plane states, a similar situation to the pristine case of δ_3 occurs: a wide transitionless window due to transitions $t(p_\parallel \to p_z)$.

(see band structure in Fig. 5.3). The appearance of the low energy peak at 0.5 eV is unclear from Fig. 6.12, that suggest transitions from states in-plane (of mostly p-character) to states out-of-plane that, in principle, should be killed by symmetry. It is possible that the origin of this peak is due to the s-character of the band, or that the transitions lie in other **k**-points within the Brillouin zone.

There are different variables determining the absorption spectra of the different polymorphs, and although it is clear that the position of the Fermi energy is one them (Fig. 6.10), it is also clear from Fig. 6.12, that in borophene the polymorph specific states deeply influence the optical response: for instance, it is not straightforward to "infer" optical properties simply guided by the self-doping mechanism. Therefore, the question on whether a given polymorph can become transparent upon hole-doping remains open.

β_{12} as a transparent conductor

As a final test, we want to show how the electronic structure of β_{12} reacts to the equivalent of removing three electrons from the system (simulating the situation $\beta_{12} \xrightarrow{\circ} \delta_3$), this in the spirit of hole-doping the polymorph using an external source; for example an applied electric field as suggested in Ref. [52] for device applications. Contrary to the previous case (self-doping) in which we computed the electronic structure of β_{12} first (charge neutral) and then we repositioned the Fermi energy according to the number of electrons using $\eta = 1/3$, this time we removed the three electrons from the total charge in the unit cell and computed the electronic structure self-consistently. We calculated the optical spectra within the independent particles approximation, as we did in the previous cases (Fig. 6.13). Similarly to the rigidly shifted case of Fig. 6.12 the optical absorption spectrum is mainly composed of three peaks in-plane which can be explained by the repositioning of the Fermi level with respect to the in-plane and out-of-plane states.

The most important change with respect to the rigidly shifted case of Fig. 6.12 is the widening of the transitionless window (1.4 to 3.0 eV in Fig. 6.13): this situation is very similar to δ_3 (Fig. 6.4), in which the large window appears due to transitions $t(p_\parallel \to p_z)$ "killed by symmetry" mostly at Γ. Moreover, it is interesting to point out

that recalculating self-consistently the electronic structure makes the electrons distribute more δ_3-like: shifting upwards the out-of-plane states, hence preferring the population of the in-plane states; this behavior is in agreement with self-doping occurring from π-to-σ upon hole-doping [47]. Lastly, we must remark that the polymorph-specific features of the electronic structure of the different polymorphs completely determine the absorption spectra: for instance, in the hole-doped case of β_{12} (Fig. 6.13) the peak at 3.2 eV does not have an analogous in δ_3, as it is due to transitions $t(p_z \rightarrow p_z)$ which appear because of the presence of a defect-like state out-of-plane.

6.1.3 Conclusions

In this section we performed a detailed analysis of the optical absorption of selected borophene polymorphs within the IPA. In a first part we identified from the electronic structure the origin of the absorption peaks along the in-plane and out of plane directions of the macroscopic dielectric tensor ϵ_M. We showed that a low-energy absorption peak appears in δ_3 due to transitions $t(sp_\parallel \rightarrow sp_\parallel)$, while for the other polymorphs the low-energy peak is due to transitions $t(p_z \rightarrow p_z)$. Moreover, we identified the reason of appearance of transitionless windows in the different polymorphs: 1) in δ_6 because of the shape of the electronic structure, and 2) in δ_3, β_{12}, α_1 and δ_5, because transitions $t(p_\parallel \rightarrow p_z)$ are killed by symmetry.

Moreover, we discussed the possibility of triggering optical absorption in the transitionless window of δ_3 via electron-doping within the self-doping picture. Oppositely, we discussed the option of inducing transparency in β_{12} via hole-doping. For the latter we presented a self-consistent calculation of the electronic structure, and we showed that this situation enhances the opening of the transitionless window with respect to the case of self-doping. We want to highlight that the appearance of the transitionless window and its tuning is directly related to the electronic structure and the fact that the in-plane states do not hybridize with the out-of-plane states. Thus, the transitionless window is not unique for the polymorphs here presented.
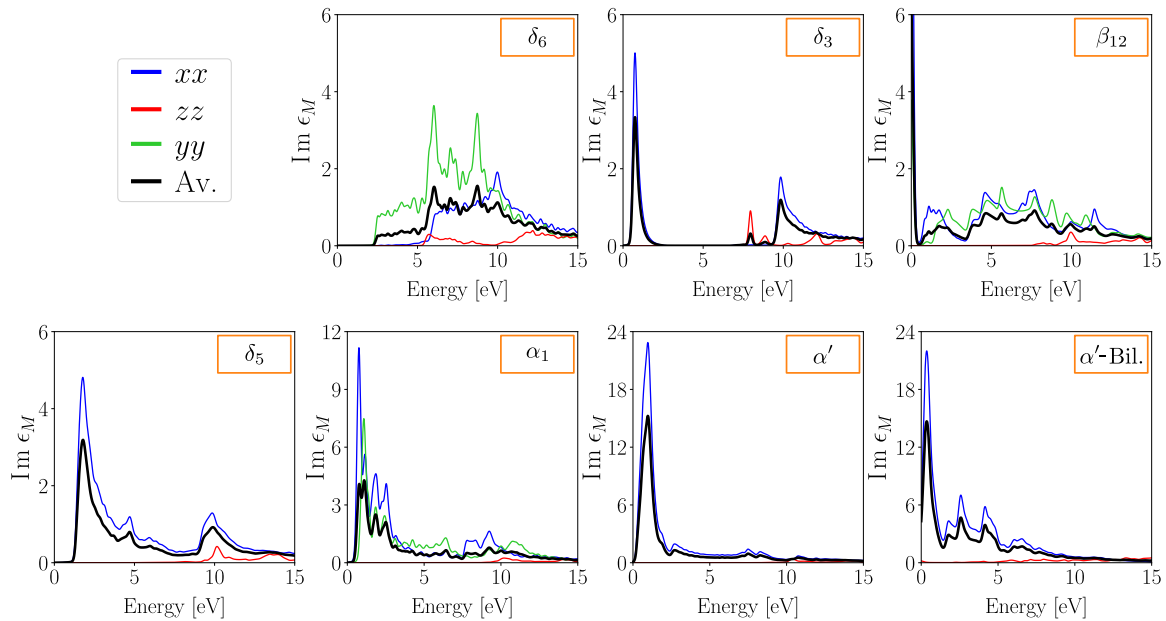
Figure 6.14: Optical absorption of selected borophene polymorphs within the random phase approxima-
tion (RPA): to be compared with Fig. 6.1. The inclusion of crystal local fields supress the absorption
out-of-plane due to the anysotropy in this direction. In-plane, however, the system absorption is unaf-
fected regardless of the different arrangement of the vacancies.

6.2   Measurable quantities

The independent-particle approximation gives a very instructive picture that directly links
the electronic structure with the optical absorption. However, other ingredients can have
an effect on the actual measured quantities, in particular, from Eq. 2.19, the Coulomb
potential and the exchange-correlation kernel to obtain the full response function χ. In 2D
(or layered materials [110]) the Coulomb term can have an important effect out-of-plane
simply due to the inhomogeneity in this direction (vanishing density), thus suppressing
the imaginary part of ϵ_M due to crystal local fields effects (LFE). We computed the
macroscopic dielectric function including LFE within the random phase approximation
(Eq. 2.19 with $f_{xc} = 0$) in the different polymorphs obtaining the aforementioned behavior
(Fig. 6.14). Another aspect to highlight is that regardless of the different arrangement
of the "holes" in the structures, the crystal local fields have negligible effect in-plane
(compare Figs. 6.14 and 6.1).

6.2.1   Absorbance and transmittance

In order to make a link with measurable quantities we computed the reflectance, transmit-
tance, and absorbance as in Eq. 2.27, 2.28 for isotropic 2D systems (see Ref. [88]). Notice,
however, that among the selected polymorphs only δ_3, δ_5, α' and α'-Bilayer are isotropic.
Thus for δ_6, β_{12}, and α_1 we assumed two isotropic sub-systems, one with the in-plane
xx-component, and the second one with the yy-component. Assuming an incident light
beam perpendicular to the plane[12] , we show in Fig. 6.15 the results for absorbance and

---

[12]Under this condition (incident light beam perpendicular to the plane) the absorbance calculated
from Eq. 2.30 is numerically equivalent to $Absorbance = \frac{\omega}{c}\epsilon_2 L$, used for example in Ref. [31]: with ω

transmittance (we have do not show reflectance as it is two orders of magnitude smaller). The computed absorbance for δ_6 and β_{12} are in agreement with the available results by Adamska *et at.*. [31]. We would like to remark once more the case of borophene δ_3 as a transparent metal, with almost zero absorbance within the energy window from 1.3 to 9 eV.

6.2.2 Loss function

Another feature of interest that can be measured experimentally with electron energy loss spectroscopy (EELS), is the loss function (Eq. 2.23). It is proportional to the imaginary part of the inverse macroscopic dielectric function, hence it is illustrative to write it as:

$$\text{Loss function} = \frac{\text{Im } \epsilon_M}{[\text{Re } \epsilon_M]^2 + [\text{Im } \epsilon_M]^2} \tag{6.2}$$

Eq. 6.2 shows the influence of Re ϵ_M on this property (in contrast to optical absorption): peaks in Im ϵ_M are screened. Moreover, the equation shows that peaks in the loss function spectra occur when the denominator $[\text{Re } \epsilon_M]^2 + [\text{Im } \epsilon_M]^2 \to 0$. To exemplify the latter we show in Fig. 6.16 (left upper panel) the calculation of the loss function (Eq. 6.2) for borophene δ_3 with $\mathbf{q} = (0.125, 0, 0)$ without crystal local field effects (NLF). For this polymorph, Fig. 6.16 clearly illustrates the plasmon peak in the loss spectrum, which shows a single peak when Re $\epsilon_M \to 0$. This prototypical behavior is due to the simplicity of the electronic structure: it shows a single peak in Im ϵ_M due to transitions $t(sp_\parallel \to sp_\parallel)$ near the Fermi energy, similarly to the optical spectrum of Fig. 6.5 calculated at $\mathbf{q} \to 0$.

The simple structure of the loss function spectrum does not occur for every polymorph, for instance, we show in Fig. 6.16 (right upper panel) the case of δ_5 with $\mathbf{q} = (0.166, 0, 0)$ (NLF): what immediately stands out is the more complex structure of both real and imaginary part of ϵ_M, and consequently the wide peaks in the loss function. Moreover, notice that around 12 eV there is a second peak in the loss function: in this case both Re ϵ_M and Im ϵ_M are sufficiently small to create a peak in the spectra and thus such peak is also of plasmonic origin, although less striking that in the crossings where Re $\epsilon_M = 0$. It is worth mentioning that the low-loss plasmons are quantities of interest for plasmonic applications. In particular because the interband transitions and the plasmons occur in a slightly different energy range. In this regard, δ_3 appears as a good candidate for 2D plasmonics.

Incorporating the crystal local fields has a strong impact on the dielectric function. While for δ_3 this translates in a small shift of the plasmon frequency towards higher energies, the effect on δ_5 is such that Re ϵ_M does not become vanishingly small (or zero), therefore the structure in the loss function spectra is dominated by the term Im ϵ_M. Hence, closer to absorption. A similar situation occurs for long $\mathbf{q}$'s, where Re $\epsilon_M \to 1$, so that $\lim_{\mathbf{q} \to \infty} \text{Loss function} = \lim_{\mathbf{q} \to \infty} \frac{\text{Im } \epsilon_M}{[\text{Re } \epsilon_M]^2 + [\text{Im } \epsilon_M]^2} \approx \text{Im } \epsilon_M$.

In general the loss function yields information about the dielectric response of the system, and it allows for easy comparison with EELS[13] and IXS[14] experiments [70, 86,

---

the energy of the light beam, c the speed of light, ϵ_2 the imaginary part of the macroscopic dielectric function, and L the out-of-plane length of the simulation box.

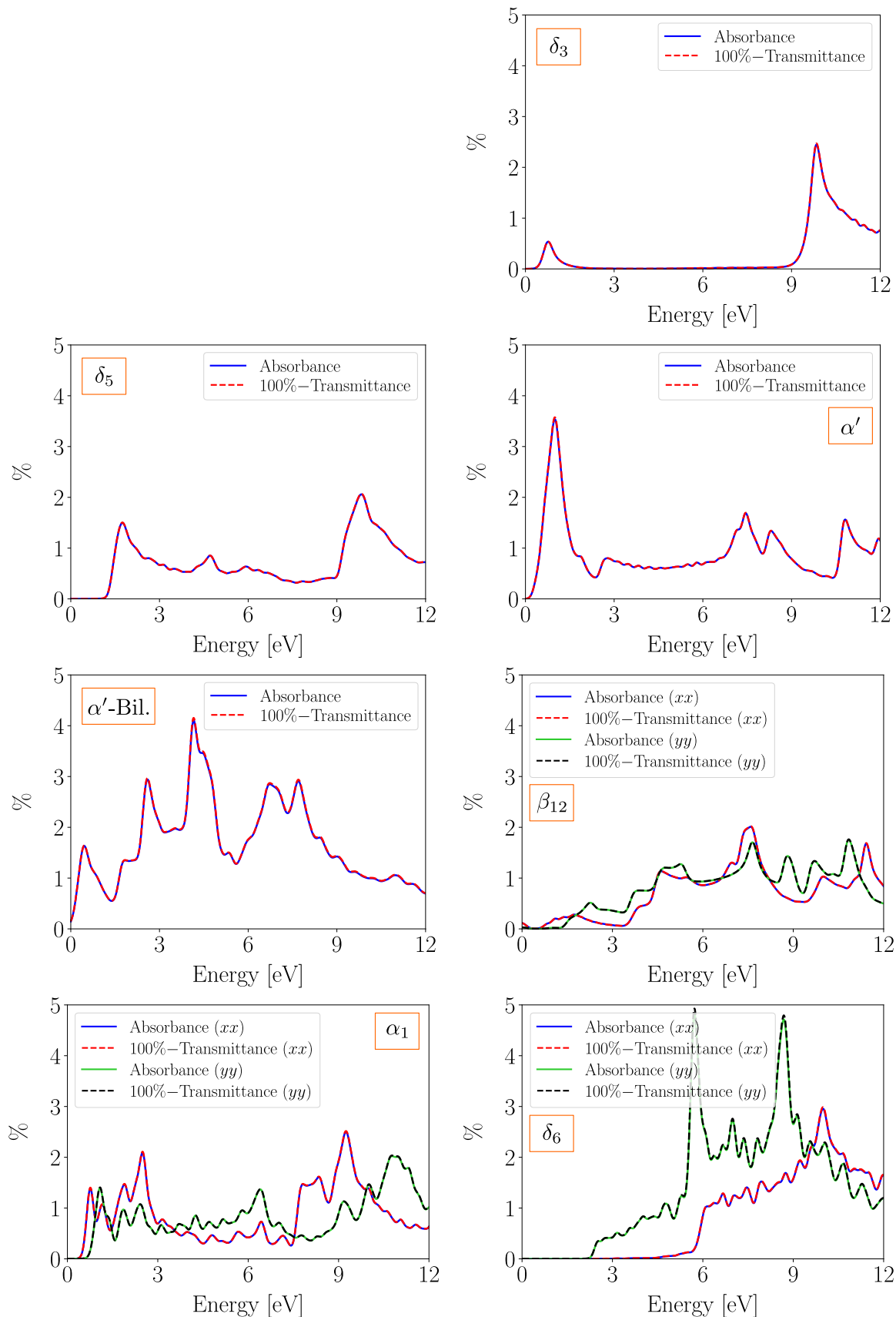[13]Electron energy loss.

[14]Inelastic X-Ray scattering

Figure 6.15: Absorbance and transmittance of selected polymorphs computed with Eq. 2.27 and 2.28 at incident light beam perpendicular to the in-plane directions (x, y). In all cases, the *Absorbance* and $[100\% - Transmittance]$ overlap almost perfectly; in fact the reflectance (Eq. 2.27) is two orders of magnitude smaller, *i. e.*, $< 0.05\%$.
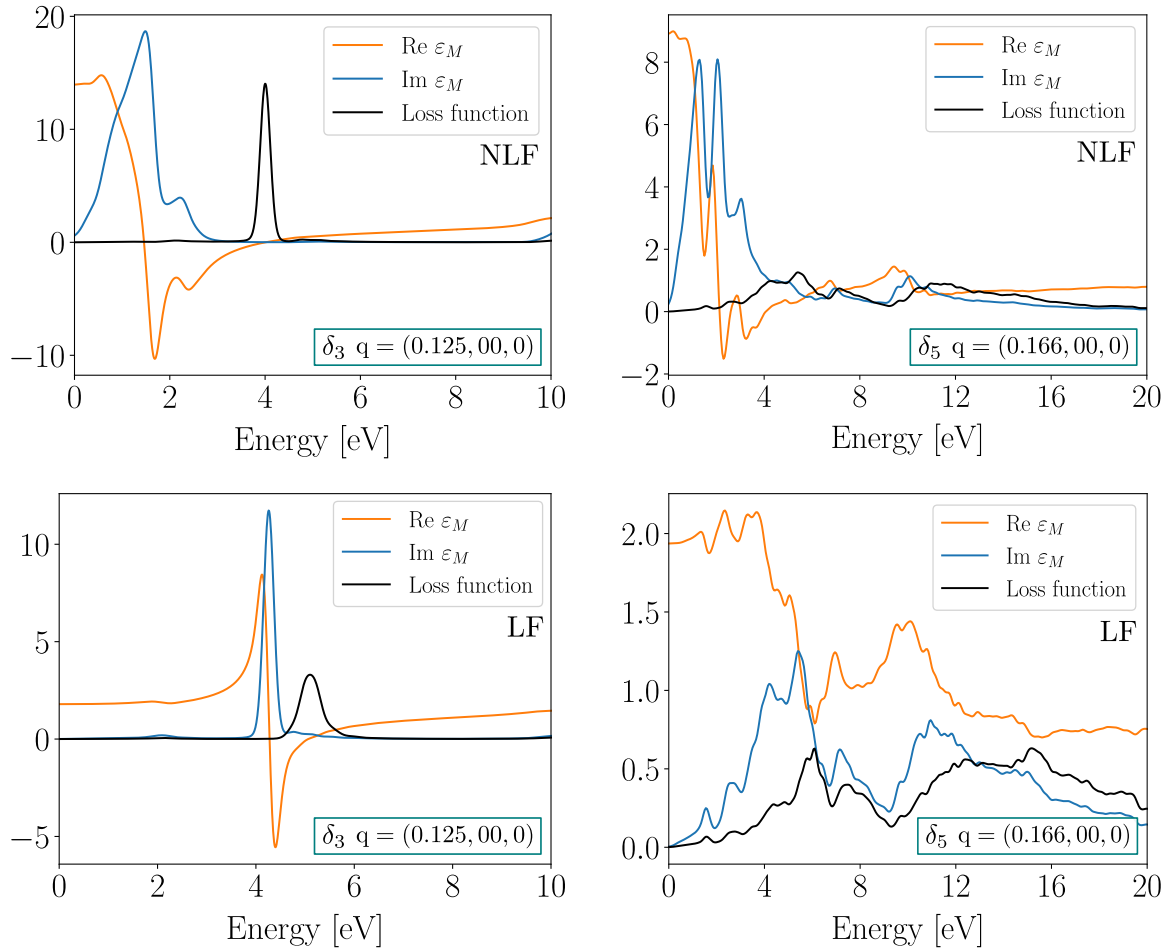
Figure 6.16: Loss function without crystal local fields (upper panels) and with LF (lower panels) of borophene δ_3 (left panels) and δ_5 (right panels). The appearance of the plasmon peak when $[\mathrm{Re}\ \epsilon_M]^2 + [\mathrm{Im}\ \epsilon_M]^2 \to 0$ is clearly identifiable due to the simple electronic structure of δ_3. For δ_5, on the contrary, the plasmon peaks are less defined, nonetheless the structure of the loss function can still be related to the denominator of Eq. 6.2 becoming vanishingly small. Moreover, including local fields has a strong impact of the dielectric response in-plane for finite $\mathbf{q}$'s.

111, 112]. Thus, we report in Fig. 6.17 the Loss function($\mathbf{q}, \omega$) (plasmon dispersion) for selected polymorphs including LF. We stress again the fact that not all the structure in the curves is due to plasmons in the sense of $[\mathrm{Re}\ \epsilon_M]^2 + [\mathrm{Im}\ \epsilon_M]^2 \to 0$. In fact, among the selected polymorphs (and selected $\mathbf{q}$'s) this condition[15] is not satisfied for δ_5, for α' and α'-Bilayer only at $\mathbf{q} = 0$, and for α_1 loosely at $\mathbf{q} = (0.083, 0, 0)$ and $\mathbf{q} = (0, 0.1, 0)$. Only for δ_3 and β_{12} the plasmon seems well-defined for the shorter $\mathbf{q}$'s: we have identified the peaks for which $\mathrm{Re}\ \epsilon_M = 0$ and $\mathrm{Im}\ \epsilon_M \to 0$ with black arrows in Fig. 6.16.

Complementary to Fig. 6.17, we show in Fig. 6.18 the plasmon dispersion of β_{12} along $\Gamma \to \mathrm{X}$ and $\Gamma \to \mathrm{Y}$ as a heat map: these images are constructed from the same data as in Fig. 6.17. There are only 8 $\mathbf{q}$-vectors along each direction, which explains the low resolution. Nonetheless, the dispersion of the plasmons is clear. It is in agreement with the calculations of Ref. [29]. The small differences with respect to the work by Haldar *et. al.* [29], are due to the different scaling, for example the low-energy (< 1 eV) branch

---

[15]For simplification identifying the dispersion of the plasmons we take as reference the "crossing up the zero line" of $\mathrm{Re}\ \epsilon_M$, as pictured for δ_3 in Fig. 6.16.
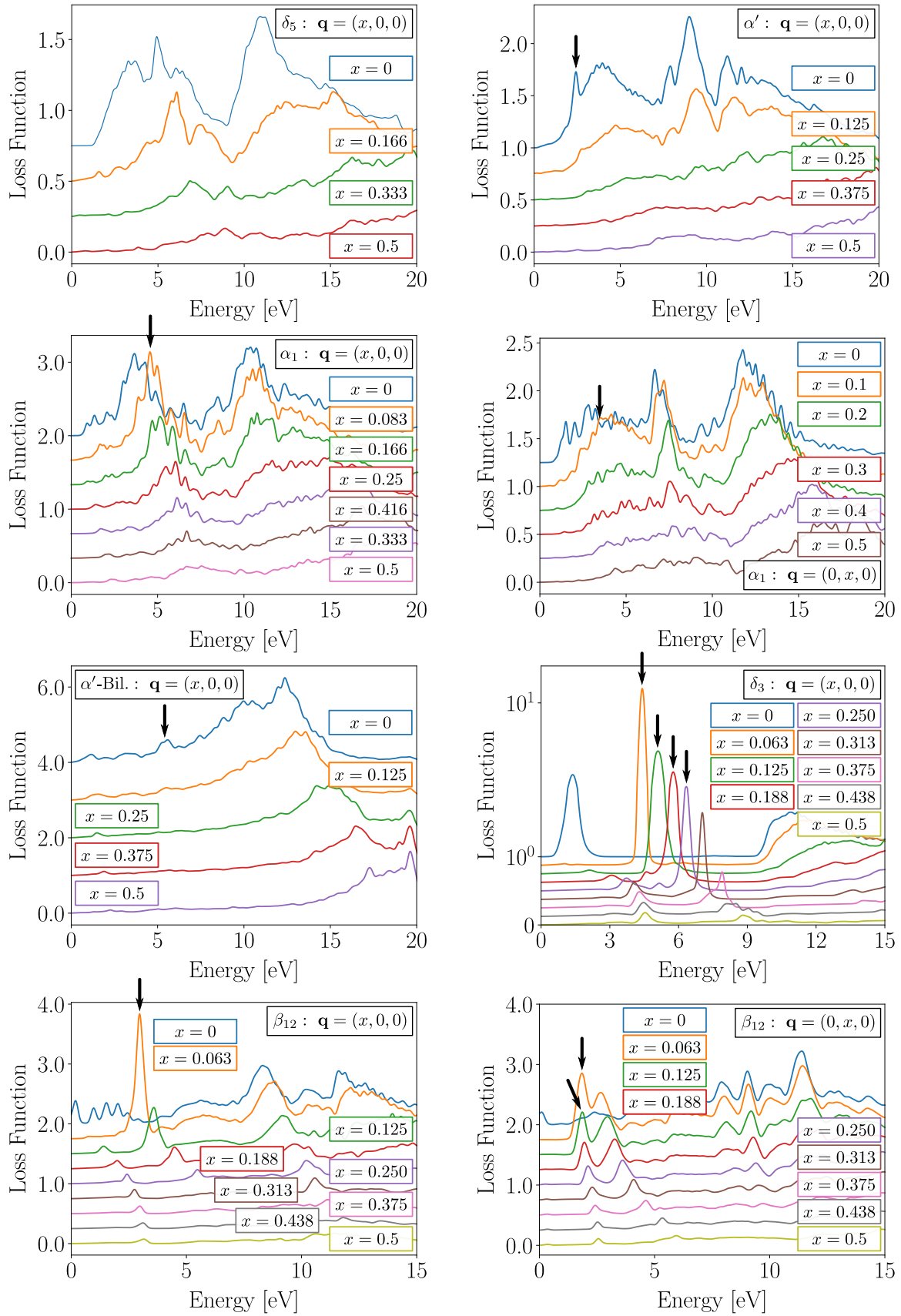
Figure 6.17: Plasmon disperion of selected polymorphs at finite $\mathbf{q}$'s with LF. δ_5, α', α'-Bilayer and δ_3 share the same hexagonal symmetry and we show the dispersion along $\Gamma \to M$. For β_{12} and α_1 with tetragonal symmetry we show two directions: $\Gamma \to X$ and $\Gamma \to Y$. Moreover, the arrows indicate the peaks were $\mathrm{Re}\, \epsilon_M$ crosses up the zero line and $\mathrm{Im}\, \epsilon_M$ becomes small.
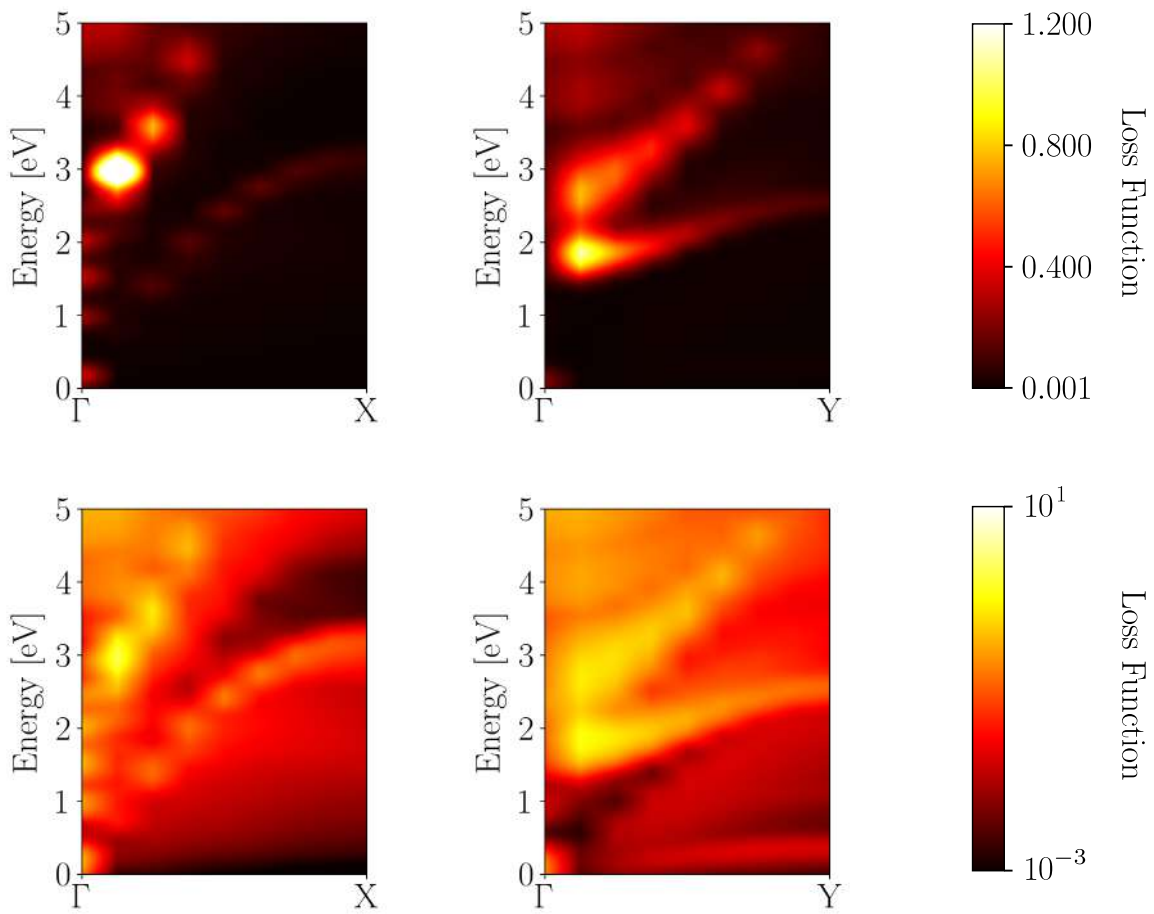
Figure 6.18: Plasmon disperion of β_{12} with local fields: same data as Fig. 6.17 interpolated along $\Gamma \to X$ and $\Gamma \to Y$ in linear (upper panels) and logarithmic scale (lower panels) in agreement with Ref. [29]. The low-energy branch (< 1 eV) along $\Gamma \to Y$ reported in Ref. [29] only appears in the logarithmic scale.

along $\Gamma \to Y$ only appears in the logarithmic scale (Fig. 6.18, lower panels). Moreover, it is probable that this branch is enhanced due to the denser **k**-mesh used in Ref. [29] for the calculation of the loss function: $120 \times 140 \times 1$ for a $2 \times 1 \times 1$ supercell of β_{12} with respect to the unit cell in Fig. 1.4, while for our calculations $64 \times 64 \times 1$.

6.2.3   Conclusions

In this section we showed optical absorption within the random phase approximation. With the addition of crystal local fields the peak in Im ϵ_M out-of-plane vanishes due to the inhomogeneity of the system in this direction. In contrast, the absorption in-plane stays almost unchanged. This is true, regardless of the different arrangements of the vacancies in the atomic structures.

In rder to discuss measurable experimental quantities, we presented absorbance, transmittance and plasmon dispersion of the selected polymorphs. Our results show the potential of the optical properties of borophene δ_3 as a transparent conductor, displaying a large gap in absorbance between 1.3 to 9 eV. Complementary to this, δ_5, α' and α_1 show regions of negligible absorbance although at lower energies (these regions can be tracked to the calculation of Im ϵ_M previously described).

We showed the appearance of well-defined plasmon peaks in α', δ_3 and β_{12} (and loosely in the α'-Bilayer), as well as the plasmon dispersion. These results sum up to the characterization of the dielectric function of these systems, and also, for reference for possible experimental measurements.

Nesting of the Fermi surface

In this chapter we investigate the static response of borophene δ_6. As we mentioned in Section 5, this polymorph has been suggested in different works as a possible super-conductor[1] [19, 23]. However, there is no clear understanding about this behavior. For instance, the critical temperature of borophene δ_6 as a superconductor is evaluated in Refs. [19, 23] in the framework of the McMillan equation, hence on the basis of high electron phonon-coupling constants:

$$\lambda_{\mathbf{q},\nu} \propto \frac{1}{\omega_{\mathbf{q},\nu}^2} \int_{BZ} d\mathbf{k} \sum_{nn'} \delta(\varepsilon_{n\mathbf{k}} - \varepsilon_F)\delta(\varepsilon_{n'\mathbf{k}+\mathbf{q}} - \varepsilon_F)|g_{\mathbf{q},\nu}(\mathbf{k}, n, n')|^2 \qquad (7.1)$$

where $\omega_{\mathbf{q},\nu}$ is the frequency of the phonon, $g_{\mathbf{q},\nu}$ the electron-phonon coupling matrix elements, and the term $\delta(\varepsilon_{i\mathbf{k}} - \varepsilon_F)\delta(\varepsilon_{j\mathbf{k}+\mathbf{q}} - \varepsilon_F)$ describes the topology of the Fermi surface (FS). Thus, as Xiao *et al.*, pointed out [23], the high EPC constants can come from two different sources for a given phonon mode: either from the EPC matrix elements or from the term related to the topology of the FS. In this section we focus on the latter and we refer to it as "nesting of the Fermi surface".

Nesting of the FS is a concept that is usually discussed in the context of charge density waves (CDW) and Kohn anomalies[2] [115–118] [119]. In fact, in borophene δ_6 the discussion about nesting of the FS appears because two Kohn anomalies are observed in its phonon spectrum at momentum transfer[3] $\tilde{\mathbf{q}}_1 = (0.25, 0, 0)$, and $\tilde{\mathbf{q}}_2 = (0.453, 0, 0)$ [19]. Fig. 7.1 shows that indeed, they can be linked to the topology of the FS. The appearance of the Kohn anomalies due to nesting of the FS was suggested by Penev *et al.* [19], and later on investigated in terms of the JDOS (equivalent to the nesting term in Eq. 7.1) by Xiao *et al.*, in Ref. [23].

Here we revisit the problem about the origin of the two Kohn anomalies. Firstly, because in the original work by Walter Kohn about the later-called Kohn anomalies these were described on the basis of screening due to virtual transition at the Fermi surface [119]. Hence, they were linked to the static response of the electronic system, for which the JDOS is only a part of the story. And secondly, because in the possible origin of the Kohn anomalies, if nesting exists, the one at $\tilde{\mathbf{q}}_1$ would occur due to transitions $t(p_z \rightarrow p_z)$, while the second one at $\tilde{\mathbf{q}}_2$ should be due to transitions $t(p_z \rightarrow p_{\parallel})$ (see Fig. 7.2). However, as we have seen earlier the transitions involved in the second case are killed by symmetry in the transitionless window in the optical spectra of the flat monolayers

---

[1]From the evaluation calculation of electron-phonon coupling (EPC) constants, the Eliashberg spectral function and the McMillan equation [66, 113, 114].

[2]"Images of the Fermi surface" in the phonon spectra of metals that appear as sharp dips in the phonon branches.

[3]The tilde in the $\tilde{\mathbf{q}}$ is to refer to the work in Ref. [19]
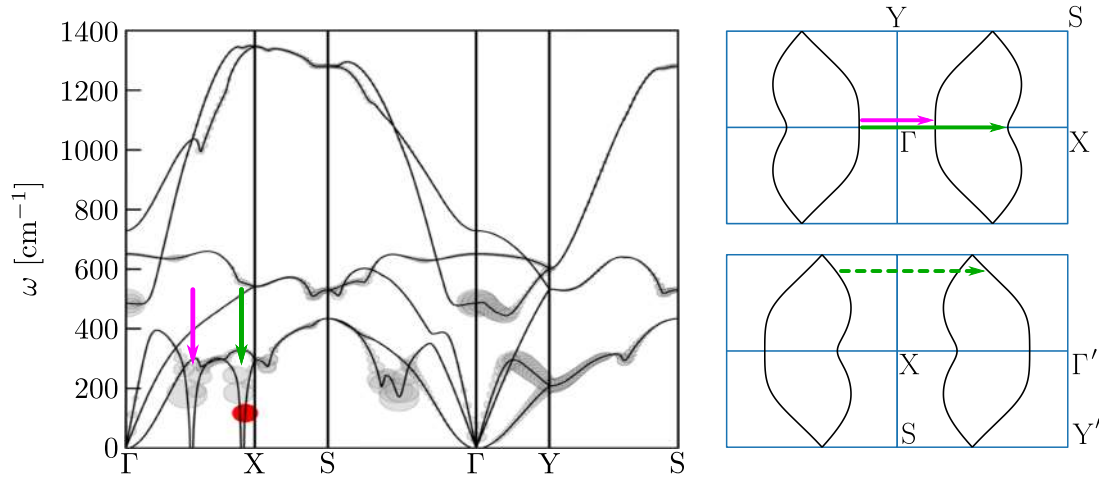
Figure 7.1: Left: phonon spectra of borophene δ_6 calculated by Penev *et al.*, (adapted from Ref. [19]). The gray and red circles come from the original source: they represent the intensity of the electron-phonon coupling constants, but we do not address this information. Right: Fermi surface of borophene δ_6 (calculated in this work). The labels Γ' and Y' refer to the high-symmetry points in a contiguous BZ. The solid arrows point out to the Kohn anomalies reported in Ref. [19] (at $\tilde{\mathbf{q}}_1 = (0.25, 0, 0)$ and $\tilde{\mathbf{q}}_2 = (0.453, 0, 0)$) as well as to the corresponding nesting vector in the FS according to our calculation ($\bar{\mathbf{q}}_1 = (0.223, 0, 0)$ and $\bar{\mathbf{q}}_2 = (0.438, 0, 0)$). The dashed arrow describes nesting for $\mathbf{q} > \bar{\mathbf{q}}_2$.
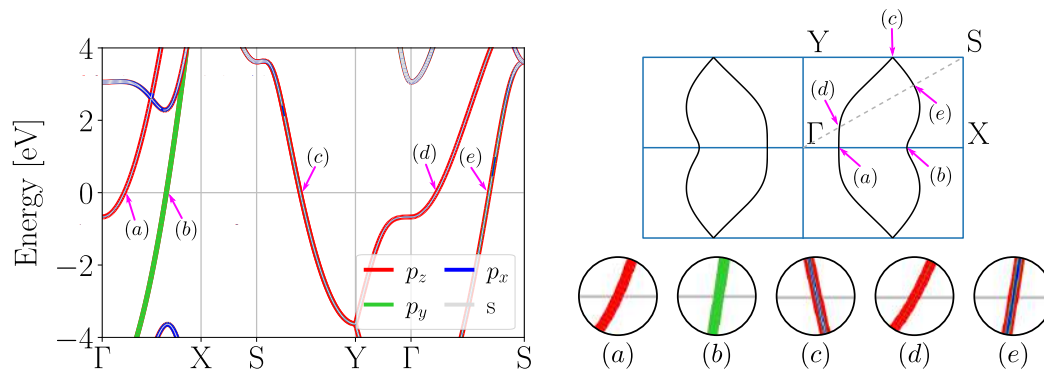
Figure 7.2: Orbital-resolved band structure of borophene δ_6 and Fermi surface. The labels point out to the same points in the band structure and in the Fermi surface. For instance (a) is mainly p_z, (b) p_y, and (e) $p_z + p_x + p_y$.

(Section 6), and it is therefore not clear whether nesting alone will be sufficient to explain the Kohn anomaly.

7.1 The static response

In this work, the nesting vectors measured from the Fermi surface along $\Gamma \to X$ (see Fig. 7.1) are[4]: $\bar{\mathbf{q}}_1 = (0.223, 0, 0)$ and $\bar{\mathbf{q}}_2 = (0.438, 0, 0)$. The closest $\mathbf{q}$-points[5] in our $128 \times 64 \times 1$ mesh are $\mathbf{q}_1 = (0.21875, 0, 0)$ and $\mathbf{q}_2 = (0.4375, 0, 0)$. We computed the static response

---

[4]The bar on top of the $\mathbf{q}$ ($\bar{\mathbf{q}}$) corresponds to the nesting vector measured from our Fermi surface calculation of Fig. 7.1.

[5]The bare $\mathbf{q}$ we use it to refer to the $\mathbf{q}$ points in our calculations closer to those of the nesting vector $\bar{\mathbf{q}}$.

Figure 7.3: Left: Full static response calculation of borophene δ_6 including 50 bands. Right: Static response, JDOS and Overlap calculated only including transitions with energe lower than 0.5 eV. The latter to simulate only the effect at the Fermi surface. The JDOS and overlap function show two peaks near the nesting vectors $\bar{\mathbf{q}}_1$ and $\bar{\mathbf{q}}_2$: at $\mathbf{q}_1 = (0.21875, 0, 0)$ and $\mathbf{q}_2 = (0.4375, 0, 0)$. However, the second peak does not appear in the calculation of the static response. Thus, we conclude that it is killed by the symmetry of the matrix elements.

for this polymorph in the IPA: $[-\mathrm{Re}\ \chi^0(\mathbf{q}, \omega = 0)]$ for $\mathbf{q}$'s inside the IBZ. The result is shown in Fig. 7.3 (left). Essentially, the spectrum is composed by a large peak with maximum at $\mathbf{q}_1$ and an offset (the lowest point is situated at $[-\mathrm{Re}\ \chi^0(\mathbf{q}, 0) = 0.018]$). It seems obvious that the large peak is associated to the nesting vector $\bar{\mathbf{q}}_1$, hence to the quasi-parallel bands in the Fermi surface (Fig. 7.1). Interestingly, there is no trace of the second nesting vector, $\bar{\mathbf{q}}_2$. The question is then whether this is due to the JDOS (as pointed out in Ref. [23]) or from the matrix elements of the electronic transitions.

First, let us mention that the offset of the spectrum comes from the fact that the real part of the polarizability is a sum over all pair of states[6] (nn') in Eq. 7.2 (from Eq. 2.20 with $\omega = \eta = 0$):

$$-\mathrm{Re}\ \chi^0_{\mathbf{G}\mathbf{G}'}(\mathbf{q}, 0) = \sum_{nn'} (f_{n'} - f_n) \frac{\tilde{\rho}_{n'n}(\mathbf{q} + \mathbf{G}) \tilde{\rho}^*_{n'n}(\mathbf{q} + \mathbf{G}')}{(\varepsilon_n - \varepsilon_{n'})} \qquad (7.2)$$

But now, we are interested in the contribution only of the Fermi surface, so we performed a second calculation of the static res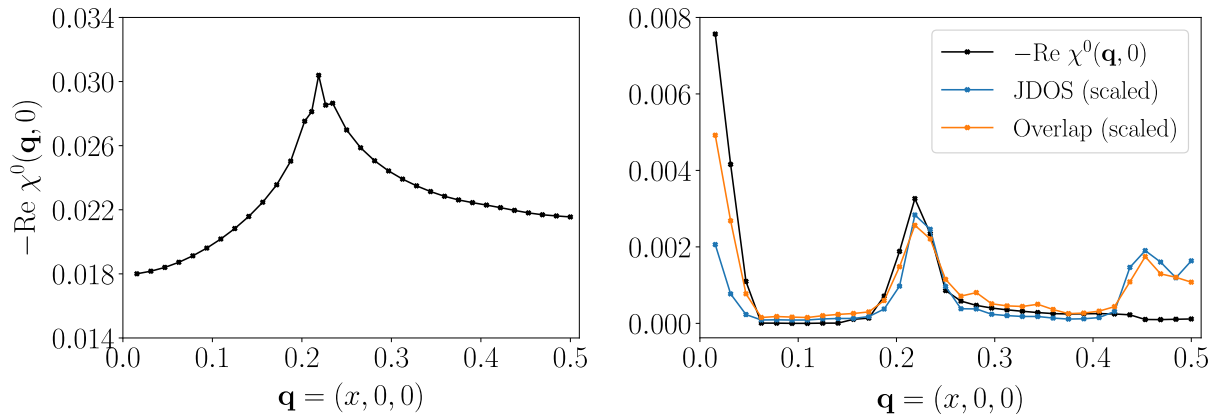ponse only including transition near the Fermi energy: thus, transitions that fulfill the condition $|\varepsilon_n - \varepsilon_{n'}| < 0.5$ eV. The result is shown in Figure 7.3. Notice that accounting only for low-energy transitions still recovers the intense peak at $\mathbf{q}_1$. The sharp peak at smaller $\mathbf{q}$'s is due to the fact that the result in the small $\mathbf{q}$-region is mainly from the low-energy transitions (we elaborate on this in Section 8). Thus, essentially, neglecting higher energy transitions only eliminates the offset due to the multiple (nn') pairs in Eq. 7.2.

With this configuration (only including transitions with $|\varepsilon_n - \varepsilon_{n'}| < 0.5$ eV), we computed the JDOS and the overlap function (Eq. 6.1). The JDOS confirmed nesting of the FS at $\mathbf{q}_2 = (0.4375, 0, 0)$ (also with the larger $\mathbf{q}$'s, see dashed arrow in Fig. 7.1). This is in contrast with Ref. [23] where no peak at $\mathbf{q}_2$ was found in the JDOS. The discrepancy

---

[6]This is a computational reason why the static response is less studied than, for example, optical spectra: it requires to include a large number of empty states to converge the sum in Eq. 7.2. On the other hand, for the computation of nesting of the FS, it is only necessary to know the topology of the FS.

might arise from the fact that the precise $\mathbf{q}$-point needed to observe this behavior: as mentioned in Ref. [19], the second anomaly at $\tilde{\mathbf{q}}_2$ appears in the phonon spectrum at a single point in the $\mathbf{q}$-mesh.

The overlap function confirmed that the transition at $\mathbf{q}_2$ (and larger) are not killed by overlap but from the symmetry of the matrix elements. Thus, these transitions, even at large $\mathbf{q}$, display a similar behavior as the ones in the transitionless windows in the optical spectra of the flat monolayers (Section 6).

Now, making the connection between our calculations and the phonon spectrum calculated in Ref. [19] (Fig. 7.1). Only the first dip at $\tilde{\mathbf{q}}_1$ is a Kohn anomaly in the sense of Ref. [119]. The second one at $\tilde{\mathbf{q}}_2$, must arise from the effect of the electron-phonon coupling matrix elements, as pointed out in Ref. [23]. This situation in which there is a different behavior between the JDOS and the static response is also found in other materials. For instance, in the prototypical example for charge density waves $NbSe_2$ [116], as well as in $TaSe_2$, and $CeTe_3$ [117].

7.1.1   Tuning the static response

We showed in Section 5, that it is possible to tune the Fermi surface of borophene δ_6 based on the buckling height ($\wedge$) and charge doping (rigid shift of the electronic structure). Here we have shown the link between the Fermi surface and the static response. Thus, it is interesting to observe how buckling and charge doping influence the static response, for example for tuning charge density waves in this polymorph. We show in Fig. 7.4 the static response and Fermi surface as a function of buckling and charge doping (rigid shift): notice the displacement of the peak in the static response in agreement with the evolution of the Fermi surface.

The evolution of the intensity of the peaks, however, requires further investigation. There are different factors playing a role: in particular, the curvature of the semi-parallel regions in the FS evolve differently by buckling than by charge-doping. This is more evident in Fig. 5.12: with small buckling the semi-parallel regions in the FS are more rounded than with electron-doping. With high buckling, the semi-parallel regions are flatter than with with hole-doping. This explains the different evolution of the static response between buckling and charge doping. The same evolution also explains why with increasing buckling the peak increases in intensity: the semi-parallel regions flatten and enlarge, and so nesting of the Fermi surface (hence the static response) is enhanced.

For charge doping, however, (Fig. 7.4, right) the evolution of the FS is not obvious (neither from Fig. 5.12). It is probable that that intensity of the peaks is strongly related to the proximity of the $\mathbf{R}$-band (see Fig. 5.9 for label) to the Fermi level. In the case of electron-doping (-0.5 eV), the $\mathbf{R}$-band is situated (at Γ) only 0.17 eV below the Fermi level. For comparison, in $\delta_6(\wedge = 0.7$ Å), the same band (at Γ) is situated 0.38 eV below the Fermi energy.

7.2   Connection with phonon spectra

Phonon spectra (as the one in Fig. 7.1) are usually calculated in the framework of density functional perturbation theory (DFPT) [120]. An important ingredient is the variation of the external potential with respect to atomic displacements. Another formulation of the
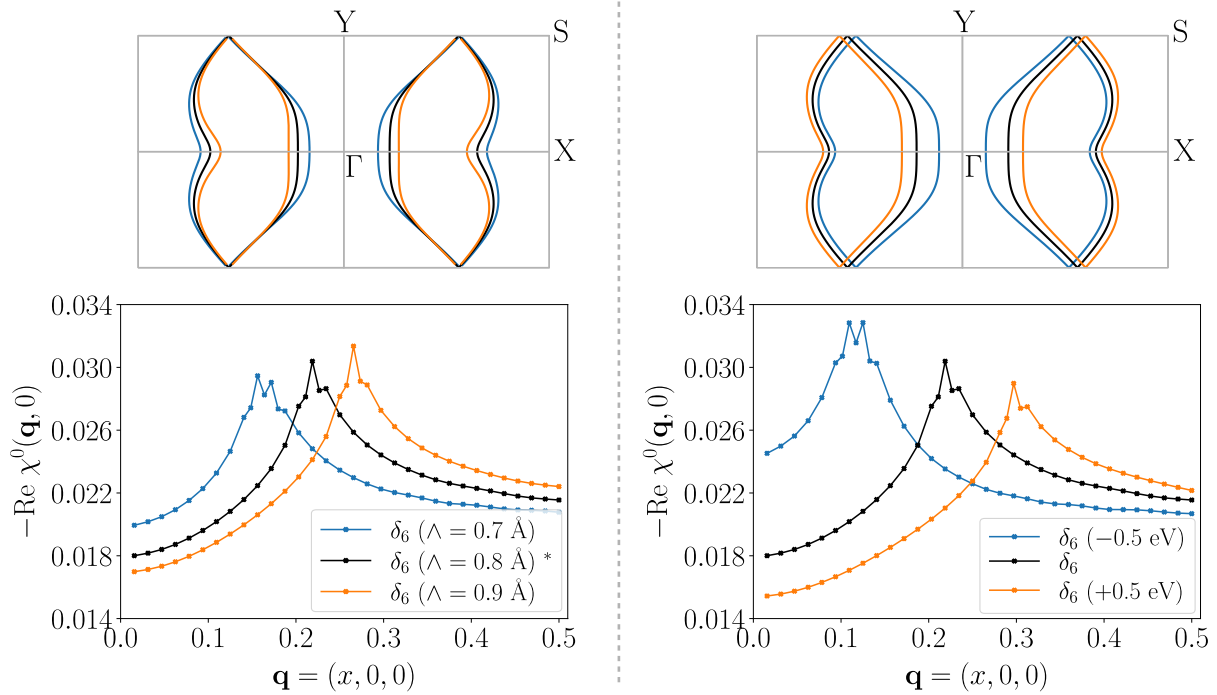
Figure 7.4: Fermi surface and static response evolution as a function of buckling (left) and charge doping (right). The evolution of the electronic structure with these two parameters changes the shape of the Fermi surface (Section 5), which in turn, changes static response.

problem was shown by Pick, Cohen and Martin in 1970 [121]. The authors showed that the phonon modes can be calculated as a function of the static dielectric function:

$$\tilde{C}_{ss'}^{\alpha\beta}(\mathbf{q}) = Z_s Z_{s'} \frac{4\pi e^2}{\Omega} \sum_{\mathbf{G}\mathbf{G}'} \frac{(\mathbf{q}+\mathbf{G})^\alpha (\mathbf{q}+\mathbf{G}')^\beta}{|\mathbf{q}+\mathbf{G}'|^2} \epsilon_{\mathbf{G}\mathbf{G}'}^{-1}(\mathbf{q},0) e^{i(\mathbf{G}\cdot\mathbf{R}_s - \mathbf{G}'\cdot\mathbf{R}_{s'})} \qquad (7.3)$$

where $\tilde{C}_{ss'}^{\alpha\beta}(\mathbf{q})$ describes the interatomic force constants: s (s') are labels for different atoms inside the unit cell, Z_s the charge of atom s, α and β labels for the Cartesian coordinates, and $\mathbf{R}_s$ the position position of the atom s inside the unit cell. The exponential term in Eq. 7.3 ensures the periodicity of the equation in reciprocal space.

Eq. 7.3 is a complicated expression. However, the important point for our discussion is the fact that phonon frequencies can be calculated as a function of the inverse static dielectric function (hence as a function the static response). This means that even the information of the Kohn-like anomaly at $\tilde{\mathbf{q}}_2 = (0.453, 0, 0)$ in Fig. 7.1 should be stored in the full matrix of the static response. In the IPA this is directly determined by: $[-\mathrm{Re}\ \chi_{\mathbf{G}\mathbf{G}'}^0(\mathbf{q},0)]$. So, to highlight this link, we scanned the static response in search of a signature of an anomaly[7] at $\mathbf{q}_2 = (0.4375, 0, 0)$. To simplify the search we only looked through the diagonal terms of the static response: $\mathbf{G} = \mathbf{G}'$. We show in Fig. 7.5 $[-\mathrm{Re}\ \chi_{\mathbf{G}\mathbf{G}}^0(\mathbf{q},0)]$ for $\mathbf{G} = [0,0,14]$ (length: 4.61 Å^{-1}), and $\mathbf{G} = [0,1,9]$ (length: 3.69 Å^{-1}).

Fig. 7.5 shows two cusps at the positions of the nesting vectors $\mathbf{q}_1 = (0.21875, 0, 0)$ and $\mathbf{q}_2 = (0.4375, 0, 0)$. As we have seen before (Fig. 7.3), these do not appear in the static

---

[7]A sharp feature in the curve at $\mathbf{q}_2 = (0.4375, 0, 0)$.
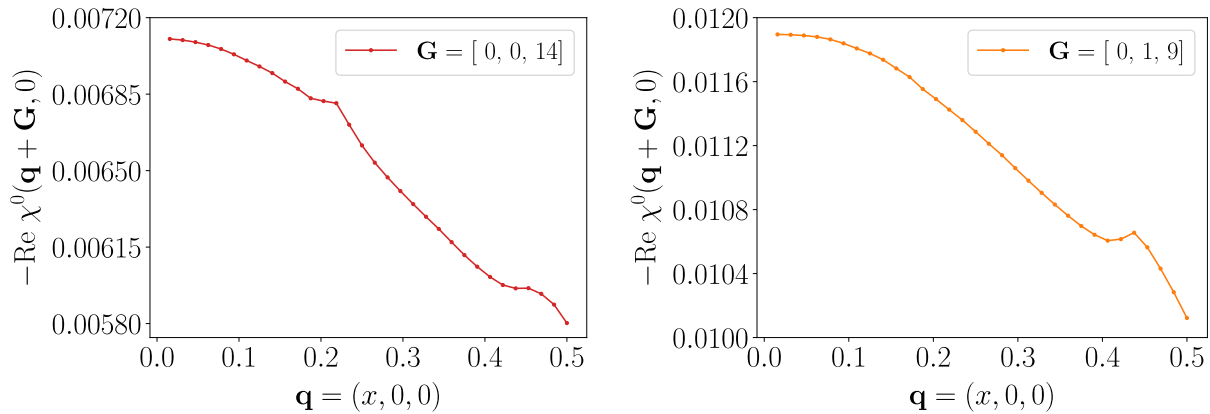
Figure 7.5: Static response of borophene δ_6 with $\mathbf{G} = \mathbf{G}'$. for two different elements of the matrix. These elements of the static response show that the static response contains information about the Kohn anomalies near $\mathbf{q}_1$ and $\mathbf{q}_2$. Thus, even though the anomaly at $\mathbf{q}_2$ does not appear for $\mathbf{G} = \mathbf{G}' = 0$, it might appear from the sum of multiple other elements in Eq. 7.3.

response calculation for $\mathbf{G} = \mathbf{G}' = 0$. From Eq. 7.3, these components (together with all other elements $\mathbf{G}\mathbf{G}'$) sum up and may yield the two anomalies in the phonon spectra of Fig. 7.1. Moreover, notice that even for $\mathbf{G} = [0, 1, 9]$ (Fig. 7.5, right), where the peak at $\mathbf{q}_2 = (0.4375, 0, 0)$ appears more clearly, it is sharp and represented by essentially only one point in the calculation using our $\mathbf{q}$-point grid. Thus, it is not surprising that different references show different phonon frequencies for this Kohn-like anomaly (see for example Refs. [19, 20, 23, 31]). Moreover, as we show in Fig. 7.4 the position of the nesting vectors can significantly shift upon small variations of the electronic structure. Thus, also the small structural variations can complicate the finding of this dip in the phonon spectrum.

7.3 The static response in the long q+G range

The static response gives information about the electronic system that can be used, for example, for the computation of phonons frequencies via Eq. 7.3. Moreover, it is essential for the discussion of the charge density waves, and Kohn anomalies. Thus, together with δ_6 we selected other cases of interest: β_{12} (also suggested as a superconductor) [19], and the simple structures δ_3 and B_T. The Fermi surfaces and the atomic structures used for these calculations are shown in Fig. 7.6. The static response for the different polymorphs parallel to $\Gamma \to X$ and $\Gamma \to Y$ is shown in Fig. 7.7: notice the units in the horizontal axis $(\mathring{A}^{-1})$ used in order to have comparable shapes of the spectra along the two directions, $(\Gamma \to X)$ and $(\Gamma \to Y)$, of the same polymorph. Moreover, we add a vertical line at $\mathbf{G} = [0.5, 0, 0]$ and $[0, 0.5, 0]$ for guiding with the dimension of the BZ.

First, let us point out the overall structure: for all polymorphs (both directions) the static response starts with an offset value. Then, there is a region which contains the information of the Fermi surface: for example in δ_6 this region extends up to $\mathbf{q}+\mathbf{G} = 3 \mathring{A}^{-1}$ along $\Gamma \to X$. After that point there is a second region in which the spectrum starts decaying. This shape is prototypical for the static response. Indeed, for the 2D HEG, there is a flat region followed by a monotonous decay starting at $|2k_F|$ (see Lindhard function in Refs. [115, 122, 123]). Of course, because the Fermi surface is polymorph-
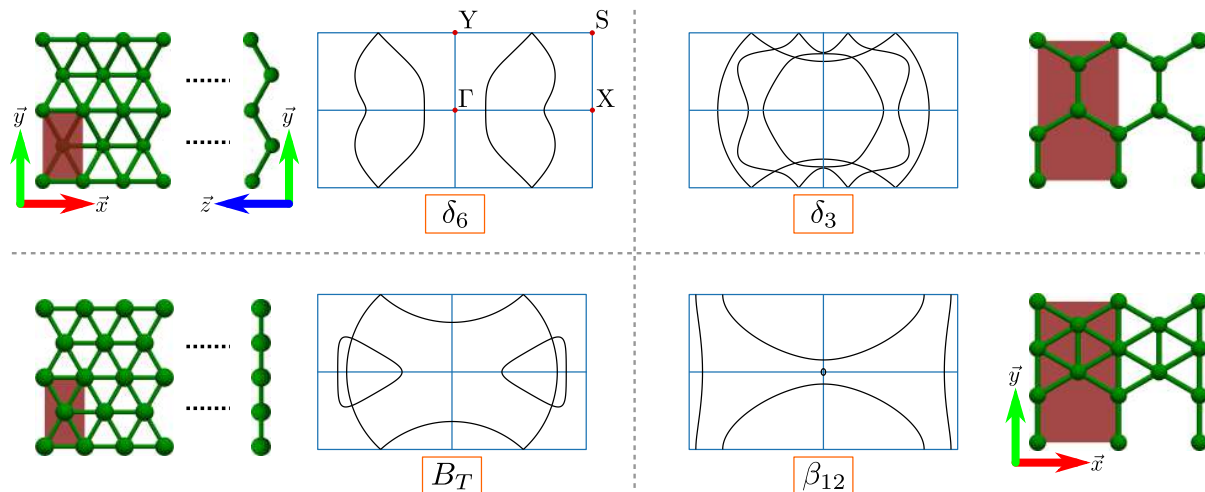
Figure 7.6: Atomic structure and Fermi surface of borophene δ_6, B_T (commensurable with δ_6), β_{12} and δ_3 (commensurable with β_{12})

specific (see Fig. 7.6), the first region is different for each polymorph. Nonetheless, the rest of the structure is the similar[8].

Another aspect worth remarking from Fig. 7.7 is the complexity of the region related to the Fermi surface. While only δ_6 displays an intense well-defined peak within the IBZ, the whole region related to the FS in the other polymorphs is full of ups and downs. As we have seen for δ_6 these peaks might differ from the simpler calculations of the JDOS. Thus, in combination which such calculations, the information of Fig. 7.7 can be used, for example, for the investigation of charge density waves in these systems.

7.4 Conclusions

In this chapter we investigated the appearance of two Kohn anomalies in borophene δ_6. Firstly, we concluded that nesting of the FS occurs for the same vectors as the Kohn anomalies reported in the literature. Then, we concluded that only one of the Kohn anomalies reported in the literature (in our case situated at $\mathbf{q}_1 = (0.21875, 0, 0)$) corresponds to a peak in the diagonal in-plane static response. The second one (in our case at $\mathbf{q}_2 = (0.4375, 0, 0)$) is killed by the symmetry of the matrix elements as in the case of the transitionless windows in Section 6: due to transitions $t(p_z \rightarrow p_\parallel)$. However, adding out-of-plane elements of the static response $[-\mathrm{Re}\,\chi^0_{\mathbf{GG}'}(\mathbf{q}, 0)]$ with $[\mathbf{G}_z = \mathbf{G}'_z \neq 0]$, the two anomalies at $\mathbf{q}_1$ and $\mathbf{q}_2$ can be detected. Indeed, according to the formulation of the dynamical matrix by Pick, Cohen and Martin [121], these components may also lead to imaginary phonon frequencies.

Moreover we showed the effect of buckling and charge doping in the static response of this polymorph (δ_6): essentially changing the intensity and position of the peak at $\mathbf{q}_1$. Lastly, we provided the static response of borophene δ_6, β_{12}, B_T and δ_3: these show a similar background structure. Only a region is modulated by the information of the FS. These results can be used in combination with JDOS calculations to investigate charge density waves in these polymorphs, as well as Kohn anomalies.

---

[8]δ_3 requires further inspection: the shape resembles two HEG with different offsets.
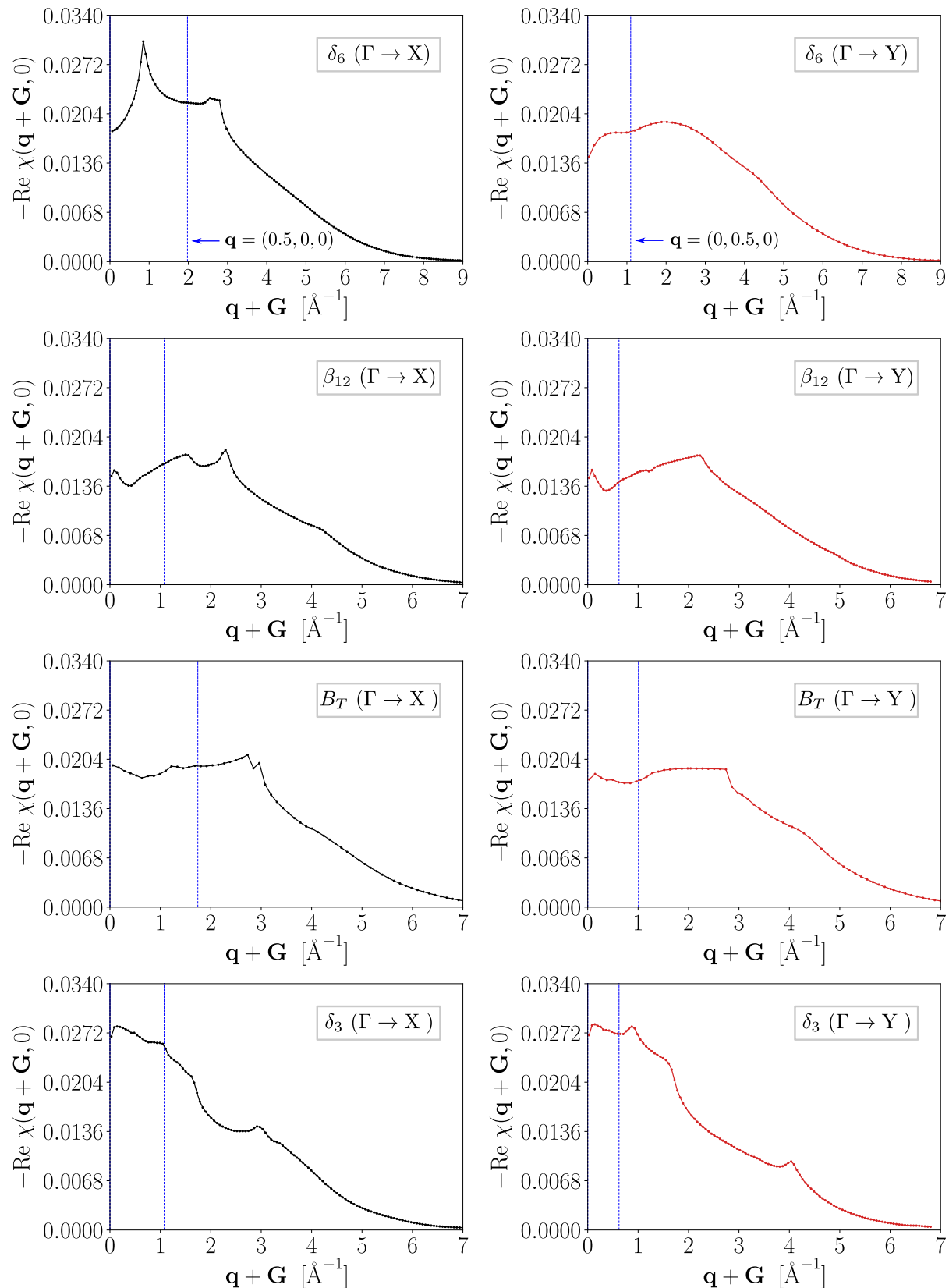
Figure 7.7: Static response calcluculation of borophene δ_6, β_{12}, B_T and δ_3. Left panels: along $(\Gamma \rightarrow X)$, Right panels: along $(\Gamma \rightarrow Y)$. The blue vertical line corresponds to $G = [0.5, 0, 0]$ and $G = [0, 0.5, 0]$, in the left and right panels, respectively. Overall the spectra of the different polymorphs have a similar structure. Only the small $\mathbf{q} + \mathbf{G}$ region is polymoprh specific as it contains the information of the Fermi surface: for example, δ_6 along $\Gamma \rightarrow X$ for $\mathbf{q} + \mathbf{G} < 3$ Å^{-1}. Note: in order to converge the static response in the long $\mathbf{q} + \mathbf{G}$ range we used 300 bands.

Efficient calculation of the static response

Computing the static response, *i. e.*, the real part of the polarizability at $\omega = 0$, is far from a simple task: even though it is evaluated at a single energy, it still requires to perform the whole sum over transitions nn' (Eq. 2.20). To exemplify the complexity of the problem it is more convenient to think about the computation of the polarizability in terms of electronic transitions: these are directly related to the imaginary part of the polarizability in the IPA. The real part is related to the imaginary part via the Kramers-Kronig relations (KK) [124, 125]:

$$\begin{aligned}
\mathrm{Re}\chi(\omega) &= -\frac{1}{\pi} P \int_{-\infty}^{\infty} \mathrm{d}\omega' \frac{\mathrm{Im}\chi(\omega')}{\omega - \omega'} \\
\mathrm{Im}\chi(\omega) &= \frac{1}{\pi} P \int_{-\infty}^{\infty} \mathrm{d}\omega' \frac{\mathrm{Re}\chi(\omega')}{\omega - \omega'}
\end{aligned} \tag{8.1}$$

Thus, in order to obtain the real part, we must integrate Eq. 8.1 over the whole range of energies $[-\infty, +\infty]$. In practice we do not necessarily perform KK to obtain one from the other. Nonetheless, Eq. 8.1 shows that to know a single value $\mathrm{Re}\chi(\omega_0)$ we must know $\mathrm{Im}\chi(\omega)$ over the whole range of frequencies. This translates into converging the calculation with respect to the number of conduction states (empty bands).

From Section 7, it is clear that there are general features among the static response of different polymorphs: for example, the **q**-dependence of the static response has a resemblance with that of of the 2D HEG, namely a semi-flat region for **q** from 0 to a given value (which for the HEG is well-defined at $2|\mathbf{k}_F|$), followed by a monotonous decay. The semi-flat region contains information of the Fermi surface (for example the large peak in borophene δ_6), but seems to be embedded in some general shape common to all polymorphs and which resemble the shape of the Lindhard function for the 2D HEG [122]. This common feature of the static response motivated us to develop an approximated method that does not require the full computation of the response via Eq. 2.20.

In particular, the numerical difficulty resides in computing explicitly Eq. 2.20 with many conduction states. In order to illustrate the problem, let us focus only on the numerator of Eq. 2.20 (the resonant part with $n \equiv c \equiv$ conduction and $n' \equiv v \equiv$ valence), which has the structure NUM $\propto \sum_{vc} \langle v | \hat{\mathcal{O}} | c \rangle \langle c | \hat{\mathcal{O}}^\dagger | v \rangle$, where the sum over all valence and conduction states form a complete basis. Thus we could use the closure (or completeness) relation:

$$\sum_n |n\rangle \langle n| = \sum_v |v\rangle \langle v| + \sum_c |c\rangle \langle c| = 1$$

$$\sum_c |c\rangle \langle c| = 1 - \sum_v |v\rangle \langle v| \tag{8.2}$$

and simplify the numerator to a sum only over valence states: NUM $\propto \sum_v \langle v| \hat{\mathcal{O}} \hat{\mathcal{O}}^* |v\rangle - \sum_{vv'} \langle v| \hat{\mathcal{O}} |v'\rangle \langle v'| \hat{\mathcal{O}}^* |v\rangle$. This is a relevant point for situations in which $N_v << N_c$ (with N_v the number of valence states), hence in the computation of the static response. Eq. 2.20 however, contains also the denominator, which is made of energy differences $(\varepsilon_c - \varepsilon_v)$, so we cannot straightforwardly use the closure relation of Eq. 8.2. In order to use this concept it is necessary to either directly approximate $(\varepsilon_c - \varepsilon_v)$ to a function that does not depend on the valence and conduction states, or to find an equivalent expression for Eq. 2.20 in which we can evaluate the energy difference $(\varepsilon_c - \varepsilon_v)$ differently. For instance, we can use the fact that ε_c and ε_c are eigenvalues of the Hamiltonian $\hat{\mathcal{H}}$, and c and v the corresponding eigenfunctions (see Ref. [126]). Thus, the aim of this Section is to find an expression for (χ^0) [1] at $\omega = 0$ that allows us to relate:

$$\chi^0 \propto \sum_{vc} \frac{\langle v| \hat{\mathcal{O}} |c\rangle \langle c| \hat{\mathcal{O}}^* |v\rangle}{(\varepsilon_c - \varepsilon_v)} \tag{8.3}$$

to terms like

$$\sum_{vc} \langle v| \hat{\mathcal{O}} |c\rangle \langle c| \hat{\mathcal{O}}^* |v\rangle (\varepsilon_c - \varepsilon_v)^m \tag{8.4}$$

In this way, for example for $m = 1$, the expression can be written in terms of the commutator (Ref. [126]):

$$\chi^0 \propto \sum_{vc} \langle v| \hat{\mathcal{O}} |c\rangle \langle c| \hat{\mathcal{O}}^* |v\rangle (\varepsilon_c - \varepsilon_v) \propto \sum_{vc} \langle v| \left[\hat{\mathcal{O}}, \hat{\mathcal{H}}\right] |c\rangle \langle c| \hat{\mathcal{O}}^* |v\rangle \tag{8.5}$$

so that we can apply the closure relation:

$$\chi^0 \propto \sum_v \langle v| \left[\hat{\mathcal{O}}, \hat{\mathcal{H}}\right] \hat{\mathcal{O}}^* |v\rangle - \sum_{vv'} \langle v| \left[\hat{\mathcal{O}}, \hat{\mathcal{H}}\right] |v'\rangle \langle v'| \hat{\mathcal{O}}^* |v\rangle \tag{8.6}$$

In this regard we highlight the work of Berger, *et. al.*, on the so-called "effective energy technique" (EET) [127–129]. In this, the authors developed a method that allows one to write the polarizability as an explicit functional of the one-body reduced density matrix, that can be used in a GW calculation for band gaps where χ^0 is evaluated in the imaginary frequency axis (see Ref. [129]). The present work is inspired by Ref. [129] with the aim to investigate the **q**-dependence of the static response, $[-\text{Re } \chi^0_{\mathbf{GG'}}(\mathbf{q}, \omega = 0)]$. Both, the work of Ref. [129] and the present one are based on Taylor expansions; they are equal at first order, but differ at higher orders.

It is worth pointing out that our interest in the "effective energy technique" for the computation of the static response derived from the expensive calculations performed in

---

[1]We consider only the "resonant" term for simplicity, the antiresonant part has a similar structure and thus it can be easily generalized.

Section 7. However, computing the static polarizability (hence the static dielectric function) is of general interest [130, 131]. For example, the static response yields the interaction kernel of the Bethe-Salpeter equation [132, 133], and it is an important ingredient for *GW* approximations + plasmon pole models [70, 131].

The starting point

For the sake of simplicity we present hereafter the notation that we use all along this Section. We start from the Kohn-Sham polarizability in reciprocal space (Eq. 2.20) that reads:

$$\chi^0_{\mathbf{GG'}}(\mathbf{q},\omega) = \frac{2}{\Omega_{\mathbf{k}}} \sum_{nn',\mathbf{k}} (f_{n',\mathbf{k}-\mathbf{q}} - f_{n,\mathbf{k}}) \frac{\langle n',\mathbf{k}-\mathbf{q}|\, e^{\mathrm{i}(\mathbf{q}+\mathbf{G})\cdot\mathbf{r}}\,|n,\mathbf{k}\rangle\,\langle n,\mathbf{k}|\, e^{-\mathrm{i}(\mathbf{q}+\mathbf{G'})\cdot\mathbf{r'}}\,|n',\mathbf{k}-\mathbf{q}\rangle}{\omega - (\varepsilon_{n,\mathbf{k}} - \varepsilon_{n',\mathbf{k}-\mathbf{q}}) + \mathrm{i}\eta}$$

(8.7)

where $\Omega_{\mathbf{k}} = V_{cell} \cdot N_{\mathbf{k}}$, with V_{cell} the volume of the unit cell and $N_{\mathbf{k}}$ the number of $\mathbf{k}$-points. For simplicity we express the numerator in terms of transition matrix elements $\tilde{\rho}_{n'n}(\mathbf{q}+\mathbf{G}) \equiv \langle n',\mathbf{k}-\mathbf{q}|\, e^{\mathrm{i}(\mathbf{q}+\mathbf{G})\cdot\mathbf{r}}\,|n,\mathbf{k}\rangle$ an we include the normalizing factor $\frac{2}{\Omega_{\mathbf{k}}}$ in the numerator. Thus, Eq. 8.7 in simplified notation becomes (this is the same equation as Eq. 2.20):

$$\chi^0_{\mathbf{GG'}}(\mathbf{q},\omega) = \sum_{nn'} (f_{n'} - f_n) \frac{\tilde{\rho}_{n'n}(\mathbf{q}+\mathbf{G})\tilde{\rho}^*_{n'n}(\mathbf{q}+\mathbf{G'})}{\omega - (\varepsilon_n - \varepsilon_{n'}) + \mathrm{i}\eta}$$

(8.8)

Moreover, because of the presence of the occupation numbers, f_n, we can divide Eq. 8.8 in two pieces: transitions from occupied to empty states for which $(f_{n'} - f_n) > 0$, and which we refer to as "resonant", R:

$$\chi^{0,\mathrm{R}}_{\mathbf{GG'}}(\mathbf{q},\omega) = \sum_{vc} (f_v - f_c) \frac{\tilde{\rho}_{vc}(\mathbf{q}+\mathbf{G})\tilde{\rho}^*_{vc}(\mathbf{q}+\mathbf{G'})}{\omega - (\varepsilon_c - \varepsilon_v) + \mathrm{i}\eta}$$

(8.9)

and transitions for which $(f_{n'} - f_n) < 0$, and which we denote as "antiresonant", AR:

$$\chi^{0,\mathrm{AR}}_{\mathbf{GG'}}(\mathbf{q},\omega) = \sum_{vc} (f_c - f_v) \frac{\tilde{\rho}_{cv}(\mathbf{q}+\mathbf{G})\tilde{\rho}^*_{cv}(\mathbf{q}+\mathbf{G'})}{\omega + (\varepsilon_c - \varepsilon_v) + \mathrm{i}\eta}$$

(8.10)

hence,

$$\chi^0_{\mathbf{GG'}}(\mathbf{q},\omega) = \chi^{0,\mathrm{R}}_{\mathbf{GG'}}(\mathbf{q},\omega) + \chi^{0,\mathrm{AR}}_{\mathbf{GG'}}(\mathbf{q},\omega)$$

(8.11)

Notice that $\tilde{\rho}_{vc}(\mathbf{q}+\mathbf{G}) \neq \tilde{\rho}_{cv}(\mathbf{q}+\mathbf{G})$. Indeed,

$$\tilde{\rho}_{vc}(\mathbf{q}+\mathbf{G}) \equiv \langle v,\mathbf{k}-\mathbf{q}|\, e^{\mathrm{i}(\mathbf{q}+\mathbf{G})\cdot\mathbf{r}}\,|c,\mathbf{k}\rangle$$

(8.12)

$$\tilde{\rho}_{cv}(\mathbf{q}+\mathbf{G}) \equiv \langle c,\mathbf{k}-\mathbf{q}|\, e^{\mathrm{i}(\mathbf{q}+\mathbf{G})\cdot\mathbf{r}}\,|v,\mathbf{k}\rangle$$

(8.13)

In general, the resonant and antiresonant terms of the polarizability do not describe the same transitions, as shown in Fig. 8.1. In order to calculate the response (regardless of the energy) both resonant and antiresonant terms need to be explicitly taken into account.
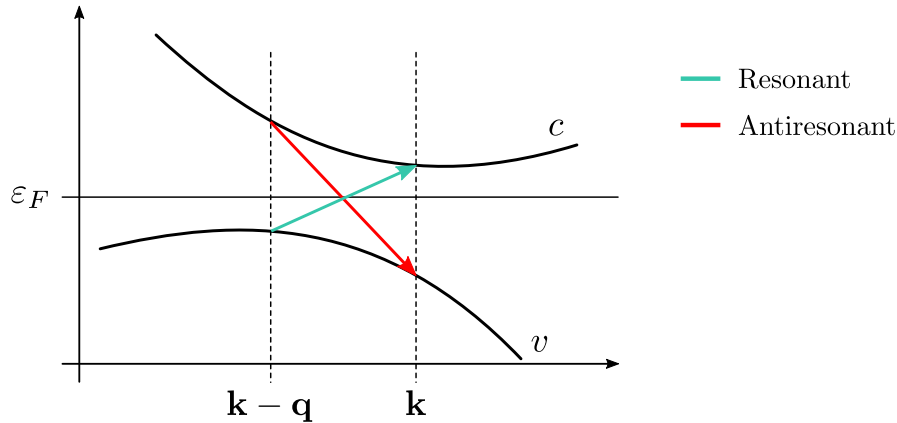
Figure 8.1: Schematic diagram of a resonant and an antiresonant transition in a semiconductor: both transitions share the same $\mathbf{q}$-vector, nonetheless they describe different transitions in the electronic structure.

Nonetheless, both equations have the same structure and, for the sake of simplicity, here we focus on the resonant part only (Eq. 8.9).

In order to deal with metals we have to make another separation of terms in Eq. 8.9: distinguishing between (resonant) transitions from fully occupied to empty states, and transition involving states with fractional occupation numbers[2]:

$$\chi_{\mathbf{GG'}}^{0,\mathrm{R}}(\mathbf{q},\omega) = \sum_{v}^{full}\sum_{c}^{empty} \frac{\tilde{\rho}_{vc}(\mathbf{q}+\mathbf{G})\tilde{\rho}_{vc}^{*}(\mathbf{q}+\mathbf{G'})}{\omega - (\varepsilon_c - \varepsilon_v) + \mathrm{i}\eta} + \sum_{vc}^{frac} \frac{\tilde{\rho}_{vc}(\mathbf{q}+\mathbf{G})\tilde{\rho}_{vc}^{*}(\mathbf{q}+\mathbf{G'})}{\omega - (\varepsilon_c - \varepsilon_v) + \mathrm{i}\eta} \qquad (8.14)$$

the first term in the right side of Eq. 8.14 completely describes resonant transitions in semiconductors, while for metals both terms must be taken into account. We will discuss later the case of metallic systems, for the moment we focus on the simpler case of semiconductors (analogously to Refs. [127–129]): we selected silicon as the prototypical example.

8.1 Taylor expansion

As we mentioned earlier, the aim of this section is to find an expression that allows us to write Eq. 8.14 in a more convenient manner to use the closure relation (Eq. 8.2), so that we can simplify the problem to the sum over only occupied states. For $\omega = 0$ we have:

$$\chi_{\mathbf{GG'}}^{0,\mathrm{R}}(\mathbf{q},0) = \sum_{v}^{full}\sum_{c}^{empty} \frac{\tilde{\rho}_{vc}(\mathbf{q}+\mathbf{G})\tilde{\rho}_{vc}^{*}(\mathbf{q}+\mathbf{G'})}{-(\varepsilon_c - \varepsilon_v)} \qquad (8.15)$$

Notice that we also set $\mathrm{i}\eta = 0$ as this quantity is vanishingly small and in the static limit ($\omega = 0$) of a semiconductor the polarizability is a purely real quantity. Now, as the simplest scenario we propose to add and subtract a constant number δ in the denominator

---

[2]To be precise in the case of metallic systems the transition is continuous. The separation of terms proposed in Eq. 8.14 is simply illustrative to separate semiconducting from metallic cases. We discuss later, in Eq. 8.40, the case of a metallic system.

of Eq. 8.15, with the single condition that $|\frac{\delta - (\varepsilon_c - \varepsilon_v)}{\delta}| \ll 1$. Of course, here there is only one δ and many transition energies $(\varepsilon_c - \varepsilon_v)$. Let us assume for the moment that a δ can be found such that $|\frac{\delta - (\varepsilon_c - \varepsilon_v)}{\delta}|$ is small enough for every combination of v and c. Defining $\theta_{cv} = \delta - (\varepsilon_c - \varepsilon_v)$, Eq. 8.15 becomes:

$$\chi_{\mathbf{GG'}}^{0,\mathrm{R}}(\mathbf{q}, 0) = \sum_{vc} \frac{\tilde{\rho}_{vc}(\mathbf{q} + \mathbf{G})\tilde{\rho}_{vc}^*(\mathbf{q} + \mathbf{G'})}{\theta_{cv} - \delta} \tag{8.16}$$

If $\frac{\theta_{cv}}{\delta}$ is small enough, we can Taylor-expand Eq. 8.16 around $\theta_{cv} = 0$, thus obtaining:

$$\chi_{\mathbf{GG'}}^{0,\mathrm{R}}(\mathbf{q}, 0) = \sum_{m=0}^{\infty} \sum_{vc} \tilde{\rho}_{vc}(\mathbf{q} + \mathbf{G})\tilde{\rho}_{vc}^*(\mathbf{q} + \mathbf{G'}) \left[(-1)^m \frac{(\theta_{cv})^m}{(-\delta)^{m+1}} \right] \tag{8.17}$$

where m is the order of the expansion. Notice from Eq. 8.17 that the denominator does not depend neither on the valence nor on the conduction states, and so we can rewrite Eq. 8.18 in the form:

$$\chi_{\mathbf{GG'}}^{0,\mathrm{R}}(\mathbf{q}, 0) = \sum_{m=0}^{\infty} \frac{(-1)^m}{(-\delta)^{m+1}} \sum_{vc} \tilde{\rho}_{vc}(\mathbf{q} + \mathbf{G})\tilde{\rho}_{vc}^*(\mathbf{q} + \mathbf{G'}) \left[\delta - (\varepsilon_c - \varepsilon_v) \right]^m \tag{8.18}$$

The latter expression is very illustrative of what our goal was: obtaining an expression that does not depend on ε_c or ε_v in the denominator as in Eq. 8.9. Nonetheless, to obtain $\chi_{\mathbf{GG'}}^{0,\mathrm{R}}(\mathbf{q}, 0)$ we must expand to infinite orders, and moreover, define a constant value δ that fulfills the condition $\frac{1}{\delta}|\delta - (\varepsilon_c - \varepsilon_v)| < 1$ for every combination[3] of $(\varepsilon_c - \varepsilon_v)$.

Delimiting the problem

In Eq. 8.16 we introduced δ simply as a mathematical trick to Taylor expand the function in terms of $\frac{\theta_{cv}}{\delta}$, nonetheless this is a very rough approximation: it assumes that all transitions between valence and conduction states have a similar transition energy $\approx \delta$, which, in general, is not the case. For example, we show in Fig. 8.2 the band structure of silicon with 46 conduction bands: the lowest conduction band is situated (in average) at 2.1 eV above the Fermi level, while the highest band at almost 54 eV. In the right panel of Fig. 8.2 we show the static response (resonant) computed brute-force with Eq. 8.15 using different numbers of conduction states, N_c. One can see that many bands are needed to describe $-\mathrm{Re}\chi_{\mathbf{GG}}^{0,\mathrm{R}}(\mathbf{q})$, specially for longer wave vectors. Up to $|\mathbf{q} + \mathbf{G}| \approx 1.5$, $N_c = 46$ yields a good description as compared to a calculation using $N_c = 496$, which in fact is reliable up to $|\mathbf{q} + \mathbf{G}| \approx 3$

Regarding the selection of δ, we propose to define it as an arithmetic average between the smallest and the largest transition energies for $\mathbf{q}$'s within the irreducible Brillouin zone:

$$\delta = \frac{1}{2N_{\mathbf{q}}} \sum_{\mathbf{q} \in \mathrm{IBZ}} \left[(\varepsilon_c - \varepsilon_v)_{\max} + (\varepsilon_c - \varepsilon_v)_{\min} \right] \tag{8.19}$$

---

[3]Regarding the antiresonant part it is easy to see that we can perform an analogous expansion with the only difference that we must define $\delta^{\mathrm{AR}} = -\delta$, thus $\chi_{\mathbf{GG'}}^{0,\mathrm{AR}}(\mathbf{q}, 0)$ takes the same form of Eq. 8.18 with the antiresonant matrix elements.
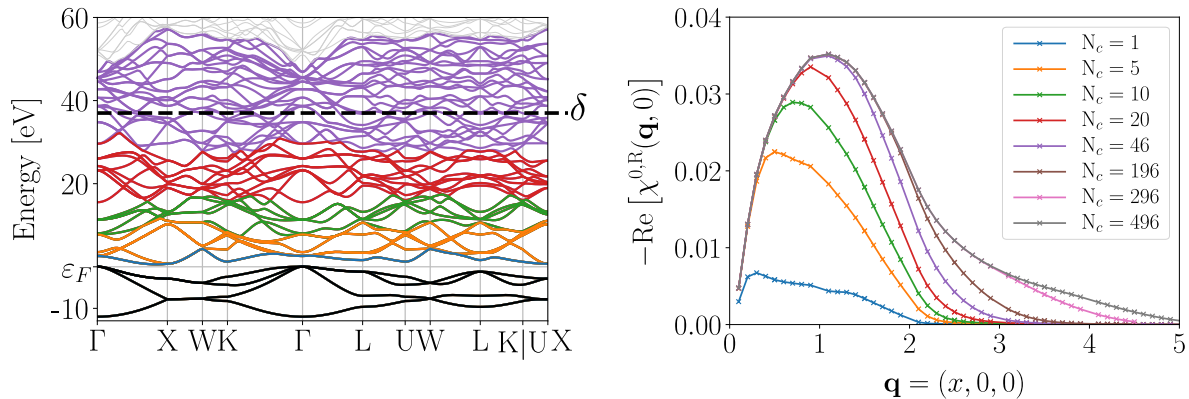
Figure 8.2: Silicon band structure and static response computed from Eq. 8.15: the colors in the two figures correspond to the same number of bands. Notice that at $N_c = 46$ the maximum of the static response is reproduced. For large $\mathbf{q} + \mathbf{G}$'s a larger number of conduction bands is needed. Moreover, in the band structure we have indicated the value of $\delta = 37$ eV: it corresponds to minus the mid value of the valence states plus the mid value of the first 46 conduction states.

Thus, for Si with 50 bands, $\delta = 37$ eV (see Fig. 8.2). In this way, $|\frac{\delta - (\varepsilon_c - \varepsilon_v)}{\delta}| < 1$ for all c, v.

Convergence of the series

First of all we have to study whether the Taylor expansion is at all a viable strategy in practice. In theory we know that Eq. 8.18 is not a converging series for $\frac{1}{\delta}|\delta - (\varepsilon_c - \varepsilon_v)| \geqslant 1$, but here for a given choice of δ some $\{v, c\}$ pairs will make the series to converge very quickly while others will make the convergence difficult. As high orders are straightforward to compute, we tested the convergence numerically: we show in Fig. 8.3 (left panel) $-\mathrm{Re}\chi^{0,\mathrm{R}}_{\mathbf{G}\mathbf{G}'}$ as computed from Eq. 8.18 for $m = 1, 2, \ldots, 10, 12, 14, 16, 18, 20, 60, 80, 100, 200$. Notice that the response calculated from Eq. 8.18 converges slowly towards the benchmark. We show in Fig. 8.3 the difference between the calculations using the Taylor expansion with $m = 60, 80, 100, 200$ and the benchmark with 46 conduction bands: at $m = 200$ we reach the numerical precision of our calculation. Indeed, the result improves significantly in the first 5 orders, but high orders are needed if a precision of less than 1% is required.

The need to account from transition with $[\delta \neq \varepsilon_c - \varepsilon_v]$ is particularly evident for the lower conduction bands: in these, the energy difference $|\varepsilon_c - \varepsilon_v|$ is smaller, and since the real part of Eq. 8.9 evolves as $\sum_{vc} |\varepsilon_c - \varepsilon_v|^{-1}$, these transitions (each) have a higher impact on the shape of the spectra: we can see in Fig. 8.2 (right) how much the spectra improves by adding few conduction states. The fast convergence of the series at long $\mathbf{q}$'s might be due to the choice of δ being well suited for those bands.

Taylor-expanding Eq. 8.15 seems to be a promising direction to approximate the static response of a semiconductor, however it converges very slowly and high-order derivatives are necessary. This problem arises because we are expanding the function around a single effective transition energy δ. There are different manners in which this difficulty could be tackled: for example separating the conduction states into different regions as proposed in Ref. [134], or adding degrees of freedom to δ. In the following section we propose to substitute $(\varepsilon_c - \varepsilon_v)$ in Eq. 8.15 by an unknown function $\Delta(\mathbf{q}, \mathbf{G}, \mathbf{G}')$, in the spirit of the
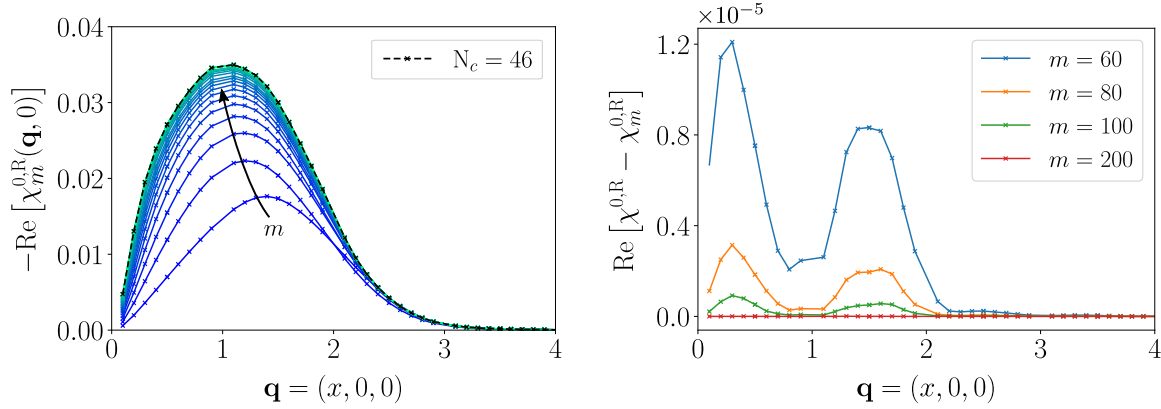
Figure 8.3: Left: static response of silicon computed with Eq. 8.18 (Taylor expansion) at different orders (m): from $m = 0$ (lowest) to $m = 200$ (converged to the full calculation with Eq. 8.15 and $N_c = 46$). Right: difference between the full calculation and the higher-order calculations: at increasing orders the series converges slowly in height and peak position.

EET of Ref. [129].

8.2 Inverting the problem: the Δ function

Now we go back to Eq. 8.15, the original function we want to approximate. We already know that we can expand it as a Taylor series (Eq. 8.18). The resulting function converges for an appropriate selection of the average transition energy, δ and the result depends on the order of the expansion. In order to tackle this problem, as in Ref. [129] we introduce a function $\Delta^{\mathrm{R}} \equiv \Delta^{\mathrm{R}}(\mathbf{q}, \mathbf{G}, \mathbf{G}', \omega = 0)$ that does not depend on the conduction nor on the valence states but that reproduces Eq. 8.15:

$$\tilde{\chi}^{0,\mathrm{R}}_{\mathbf{G}\mathbf{G}'}(\mathbf{q}, 0) = \frac{1}{-\Delta^{\mathrm{R}}} \sum_{v}^{full} \sum_{c}^{empty} \tilde{\rho}_{vc}(\mathbf{q} + \mathbf{G})\tilde{\rho}^*_{vc}(\mathbf{q} + \mathbf{G}') \qquad (8.20)$$

Since the function Δ^{R}, by definition, does not depend on the conduction or valence states we have written it outside the sum. Moreover, notice that Eq. 8.20 yields the exact $\tilde{\chi}^{0,\mathrm{R}}_{\mathbf{G}\mathbf{G}'} = \chi^{0,\mathrm{R}}_{\mathbf{G}\mathbf{G}'}$ for:

$$\Delta^{\mathrm{R},(\mathrm{exact})} = -\frac{\sum_{vc} \tilde{\rho}_{vc}(\mathbf{q} + \mathbf{G})\tilde{\rho}^*_{vc}(\mathbf{q} + \mathbf{G}')}{\chi^{0,\mathrm{R}}_{\mathbf{G}\mathbf{G}'}(\mathbf{q}, 0)} \qquad (8.21)$$

Of course, the difficulty resides in finding the function Δ^{R}. To find a reasonable approximation, we Taylor-expand also $\tilde{\chi}^{0,\mathrm{R}}_{\mathbf{G}\mathbf{G}'}$ in Eq. 8.20, which yields:

$$\tilde{\chi}^{0,\mathrm{R}}_{\mathbf{G}\mathbf{G}'}(\mathbf{q}, 0) = \sum_{m=0}^{\infty} \frac{(-1)^m (\delta - \Delta^{\mathrm{R}})^m}{(-\delta)^{m+1}} \sum_{vc} \tilde{\rho}_{vc}(\mathbf{q} + \mathbf{G})\tilde{\rho}^*_{vc}(\mathbf{q} + \mathbf{G}') \qquad (8.22)$$

We now suppose that a Δ that well-reproduces some m^{th}-order approximation will also well-reproduce the whole series. This is us a prescription for Δ^{R} at m-th order: $\Delta^{\mathrm{R},(m)}$. Let us look at the first-order approximation, $\Delta^{\mathrm{R},(1)}$. In order to simplify the notation we call $\mathrm{M}^{\mathrm{R}}_{vc} \equiv \tilde{\rho}_{vc}(\mathbf{q} + \mathbf{G})\tilde{\rho}^*_{vc}(\mathbf{q} + \mathbf{G}')$ and $\varepsilon_{cv} \equiv (\varepsilon_c - \varepsilon_v)$. By Taylor-expanding $\tilde{\chi}^{0,\mathrm{R}}_{\mathbf{G}\mathbf{G}'}$

and $\chi^{0,\mathrm{R}}_{\mathbf{GG}'}$ around $[\delta - \varepsilon_{cv}] = 0$ and $[\Delta^{\mathrm{R},(1)} - \varepsilon_{cv}] = 0$, respectively, imposing equality and solving for $\Delta^{\mathrm{R},(1)}$:

$$
\sum_{vc} \frac{\mathrm{M}^{\mathrm{R}}_{vc}}{-\delta} - \sum_{vc} \frac{\mathrm{M}^{\mathrm{R}}_{vc}\,[\delta - \varepsilon_{cv}]}{(-\delta)^2} = \sum_{vc} \frac{\mathrm{M}^{\mathrm{R}}_{vc}}{-\delta} - \sum_{vc} \frac{\mathrm{M}^{\mathrm{R}}_{vc}\,[\delta - \Delta^{\mathrm{R},(1)}]}{(-\delta)^2}
$$

$$
\frac{1}{(-\delta)^2} \sum_{vc} \mathrm{M}^{\mathrm{R}}_{vc}\,[\delta - \varepsilon_{cv}] = \frac{[\delta - \Delta^{\mathrm{R},(1)}]}{(-\delta)^2} \sum_{vc} \mathrm{M}^{\mathrm{R}}_{vc}
$$

$$
\delta \sum_{vc} \mathrm{M}^{\mathrm{R}}_{vc} - \sum_{vc} \mathrm{M}^{\mathrm{R}}_{vc}\varepsilon_{cv} = \delta \sum_{vc} \mathrm{M}^{\mathrm{R}}_{vc} - \Delta^{\mathrm{R},(1)} \sum_{vc} \mathrm{M}^{\mathrm{R}}_{vc}
$$

$$
\sum_{vc} \mathrm{M}^{\mathrm{R}}_{vc}\varepsilon_{cv} = \Delta^{\mathrm{R},(1)} \sum_{vc} \mathrm{M}^{\mathrm{R}}_{vc} \tag{8.23}
$$

This yields an expression for Δ^{R} to first order which depends on the matrix elements and the energy difference $(\varepsilon_c - \varepsilon_v)$, the latter in the numerator:

$$
\Delta^{\mathrm{R},(1)} = \frac{\sum_{vc} \mathrm{M}^{\mathrm{R}}_{vc}\varepsilon_{cv}}{\sum_{vc} \mathrm{M}^{\mathrm{R}}_{vc}} \tag{8.24}
$$

We can do the same to second order, $\Delta^{\mathrm{R},(2)}$:

$$
\sum_{vc} \left[\frac{\mathrm{M}^{\mathrm{R}}_{vc}}{-\delta} - \frac{\mathrm{M}^{\mathrm{R}}_{vc}\,[\delta - \varepsilon_{cv}]}{(-\delta)^2} + \frac{\mathrm{M}^{\mathrm{R}}_{vc}\,[\delta - \varepsilon_{cv}]^2}{(-\delta)^3} \right] = \sum_{vc} \left[\frac{\mathrm{M}^{\mathrm{R}}_{vc}}{-\delta} - \frac{\mathrm{M}^{\mathrm{R}}_{vc}\,[\delta - \Delta^{\mathrm{R},(2)}]}{(-\delta)^2} + \frac{\mathrm{M}^{\mathrm{R}}_{vc}\,[\delta - \Delta^{\mathrm{R},(2)}]^2}{(-\delta)^3} \right]
$$

$$
\sum_{vc} \left[\frac{\mathrm{M}^{\mathrm{R}}_{vc}\,[\delta - \varepsilon_{cv}]}{(-\delta)^2} - \frac{\mathrm{M}^{\mathrm{R}}_{vc}\,[\delta - \varepsilon_{cv}]^2}{(-\delta)^3} \right] = \sum_{vc} \left[\frac{\mathrm{M}^{\mathrm{R}}_{vc}\,[\delta - \Delta^{\mathrm{R},(2)}]}{(-\delta)^2} - \frac{\mathrm{M}^{\mathrm{R}}_{vc}\,[\delta - \Delta^{\mathrm{R},(2)}]^2}{(-\delta)^3} \right]
$$

$$
\sum_{vc} \mathrm{M}^{\mathrm{R}}_{vc} \left[\delta - \varepsilon_{cv} - \frac{[\delta - \varepsilon_{cv}]^2}{-\delta} \right] = \left[\delta - \Delta^{\mathrm{R},(2)} - \frac{[\delta - \Delta^{\mathrm{R},(2)}]^2}{-\delta} \right] \sum_{vc} \mathrm{M}^{\mathrm{R}}_{vc}
$$

$$
\sum_{vc} \mathrm{M}^{\mathrm{R}}_{vc} \left[\varepsilon_{cv} + \frac{[\delta - \varepsilon_{cv}]^2}{-\delta} \right] = \left[\Delta^{\mathrm{R},(2)} + \frac{[\delta - \Delta^{\mathrm{R},(2)}]^2}{-\delta} \right] \sum_{vc} \mathrm{M}^{\mathrm{R}}_{vc}
$$

$$
\frac{1}{-\delta} \sum_{vc} \mathrm{M}^{\mathrm{R}}_{vc} \left[\varepsilon_{cv}(-3\delta) + \delta^2 + \varepsilon_{cv}^2 \right] = \frac{1}{-\delta} \left[\Delta^{\mathrm{R},(2)}(-3\delta) + \delta^2 + \left(\Delta^{\mathrm{R},(2)}\right)^2 \right] \sum_{vc} \mathrm{M}^{\mathrm{R}}_{vc}
$$

$$
\sum_{vc} \mathrm{M}^{\mathrm{R}}_{vc} \left[\varepsilon_{cv}(-3\delta) + \varepsilon_{cv}^2 \right] = \left[\Delta^{\mathrm{R},(2)}(-3\delta) + \left(\Delta^{\mathrm{R},(2)}\right)^2 \right] \sum_{vc} \mathrm{M}^{\mathrm{R}}_{vc} \tag{8.25}
$$

At each order the problem gets more complicated; for the second order approximation we have to to solve a second order equation:

$$
\left(\Delta^{\mathrm{R},(2)}\right)^2 + (-3\delta)\Delta^{\mathrm{R},(2)} - \frac{(-3\delta)\sum_{vc} \mathrm{M}^{\mathrm{R}}_{vc}\varepsilon_{cv} + \sum_{cv} \mathrm{M}^{\mathrm{R}}_{vc}\varepsilon_{cv}^2}{\sum_{vc} \mathrm{M}^{\mathrm{R}}_{vc}} = 0 \tag{8.26}
$$

Solving for $\Delta^{\mathrm{R},(2)}$ we obtain:

$$
\Delta^{\mathrm{R},(2)} = \pm \frac{1}{2} \sqrt{ \frac{4 \sum_{vc} \mathrm{M}^{\mathrm{R}}_{vc}\,[\varepsilon_{cv}^2 - 3\delta\varepsilon_{cv}]}{\sum_{vc} \mathrm{M}^{\mathrm{R}}_{vc}} + (3\delta)^2 } + \frac{3\delta}{2} \tag{8.27}
$$

In general, finding an expression for $\Delta^{\mathrm{R},(m)}$ is reduced to finding the roots of a polynomial of order m. This is not trivial and adds another layer in the problem: the interpretation of the different solutions. For instance $\Delta^{\mathrm{R},(2)}$ in Eq. 8.27 has two different solutions; in order to understand which of them fulfills the initial conditions $\left|\frac{\delta - \varepsilon_{cv}}{\delta}\right| < 1$ and $\left|\frac{\delta - \Delta^{\mathrm{R}}}{\delta}\right| < 1$ let us simplify Eq. 8.27 to a single-transition scenario. In this case we should find $\Delta = \varepsilon_{cv}$ if $\delta = \varepsilon_{cv}$ is chosen. The quadratic equation yields:

$$
\begin{aligned}
\Delta_{single,\pm}^{\mathrm{R},(2)} &= \pm \frac{1}{2} \sqrt{\frac{4 \mathrm{M}_{vc}^{\mathrm{R}} \left[\varepsilon_{cv}^2 - 3\delta\varepsilon_{cv}\right]}{\mathrm{M}_{vc}^{\mathrm{R}}} + (3\delta)^2} + \frac{3\delta}{2} \\
&= \pm \frac{1}{2} \sqrt{4\left[\varepsilon_{cv}^2 - 3\delta\varepsilon_{cv}\right] + (3\delta)^2} + \frac{3\delta}{2} \\
&= \pm \frac{1}{2} \sqrt{\left[2\varepsilon_{cv} - 3\delta\right]^2} + \frac{3\delta}{2} \\
&= \pm \frac{1}{2} |2\varepsilon_{cv} - 3\delta| + \frac{3\delta}{2}
\end{aligned}
\tag{8.28}
$$

For $\delta = \varepsilon_{cv}$, $\Delta_{single,+}^{\mathrm{R},(2)} = 2\varepsilon_{cv}$, while $\Delta_{single,-}^{\mathrm{R},(2)} = \varepsilon_{cv}$. Thus, the better and also more physical solution corresponds to the negative root of Eq. 8.27:

$$
\Delta^{\mathrm{R},(2)} = -\frac{1}{2} \sqrt{\frac{4 \sum_{vc} \mathrm{M}_{vc}^{\mathrm{R}} \left[\varepsilon_{cv}^2 - 3\delta\varepsilon_{cv}\right]}{\sum_{vc} \mathrm{M}_{vc}^{\mathrm{R}}} + (3\delta)^2} + \frac{3\delta}{2}
\tag{8.29}
$$

Different series

In order to avoid solving high order equations we can rewrite Eq. 8.15 in a different manner. In particular, using the equality $\frac{1}{1-x} = 1 + x\left(\frac{1}{1-x}\right)$ we can obtain an exact expression for Eq. 8.15 expanded as a polynomial:

$$
\begin{aligned}
\chi_{\mathbf{G}\mathbf{G}'}^{0,\mathrm{R}}(\mathbf{q}, 0) &= \sum_{cv} \frac{\mathrm{M}_{vc}^{\mathrm{R}}}{(-\delta) - (\varepsilon_{cv} - \delta)} = \sum_{cv} \frac{\mathrm{M}_{vc}^{\mathrm{R}}}{(-\delta)} \frac{1}{1 - \left(\frac{\varepsilon_{cv} - \delta}{-\delta}\right)} \\
&= \sum_{cv} \frac{\mathrm{M}_{vc}^{\mathrm{R}}}{(-\delta)} + \sum_{cv} \frac{\mathrm{M}_{vc}^{\mathrm{R}}}{(-\delta)} \left(\frac{\varepsilon_{cv} - \delta}{-\delta}\right) \left(\frac{1}{1 - \left(\frac{\varepsilon_{cv} - \delta}{-\delta}\right)}\right) \\
&= \sum_{cv} \frac{\mathrm{M}_{vc}^{\mathrm{R}}}{(-\delta)} + \sum_{cv} \frac{\mathrm{M}_{vc}^{\mathrm{R}}}{(-\delta)} \left(\frac{\varepsilon_{cv} - \delta}{-\delta}\right) + \sum_{cv} \frac{\mathrm{M}_{vc}^{\mathrm{R}}}{(-\delta)} \left(\frac{\varepsilon_{cv} - \delta}{-\delta}\right)^2 \left(\frac{1}{1 - \left(\frac{\varepsilon_{cv} - \delta}{-\delta}\right)}\right)
\end{aligned}
\tag{8.30}
$$

This series can be continued, neglecting $\frac{\varepsilon_{cv} - \delta}{-\delta}$ in the last term bring us back to the Taylor expansion. Instead, here the idea is to directly approximate the lastcontribution. The hope is that a low-order expansion will be sufficient, since a factor $\left(\frac{\varepsilon_{cv} - \delta}{-\delta}\right)^2$ is already present. Taylor-expanding to first order only the very last term of Eq. 8.30 we obtain:

$$
\sum_{cv} \frac{\mathrm{M}_{vc}^{\mathrm{R}}}{(-\delta)} \left(\frac{\varepsilon_{cv} - \delta}{-\delta}\right)^2 \left(\frac{1}{1 - \left(\frac{\varepsilon_{cv} - \delta}{-\delta}\right)}\right) \approx \sum_{cv} \frac{\mathrm{M}_{vc}^{\mathrm{R}}}{(-\delta)} \left(\frac{\varepsilon_{cv} - \delta}{-\delta}\right)^2 \left(1 + \frac{\varepsilon_{cv} - \delta}{-\delta}\right)
\tag{8.31}
$$

Notice that this is first-order expansion of a second-order term in the polynomial of Eq. 8.30 and thus it acts as third-order correction for the full polynomial. In order to differentiate it from a straightforward 3rd-order expansion analogous to Eq. 8.29, which would yield a 3rd-order equation, we denote it as $\tilde{\Delta}^{\mathrm{R},(3)}$. The derivation is:

$$
\sum_{cv} \frac{\mathrm{M}_{vc}^{\mathrm{R}}}{(-\delta)} \left(\frac{\varepsilon_{cv} - \delta}{-\delta} \right)^2 \left(1 + \frac{\varepsilon_{cv} - \delta}{-\delta} \right) = \sum_{cv} \frac{\mathrm{M}_{vc}^{\mathrm{R}}}{(-\delta)} \left(\frac{\varepsilon_{cv} - \delta}{-\delta} \right)^2 \left(1 + \frac{\tilde{\Delta}^{\mathrm{R},(3)} - \delta}{-\delta} \right)
$$

$$
\sum_{cv} \mathrm{M}_{vc}^{\mathrm{R}} \left(\varepsilon_{cv} - \delta \right)^2 \left[(-\delta) + (\varepsilon_{cv} - \delta) \right] = \sum_{cv} \mathrm{M}_{vc}^{\mathrm{R}} \left(\varepsilon_{cv} - \delta \right)^2 \left[(-\delta) + (\tilde{\Delta}^{\mathrm{R},(3)} - \delta) \right] \quad (8.32)
$$

$$
\sum_{cv} \mathrm{M}_{vc}^{\mathrm{R}} \left(\varepsilon_{cv} - \delta \right)^3 = \sum_{cv} \mathrm{M}_{vc}^{\mathrm{R}} \left(\varepsilon_{cv} - \delta \right)^2 \left(\tilde{\Delta}^{\mathrm{R},(3)} - \delta \right)
$$

Therefore[4]:

$$
\tilde{\Delta}^{\mathrm{R},(3)} = \delta + \frac{\sum_{cv} \mathrm{M}_{vc}^{\mathrm{R}} \left(\varepsilon_{cv} - \delta \right)^3}{\sum_{cv} \mathrm{M}_{vc}^{\mathrm{R}} \left(\varepsilon_{cv} - \delta \right)^2} \tag{8.33}
$$

It is convenient to remark that $\tilde{\Delta}^{\mathrm{R},(3)}$ enters only in the very last term of Eq. 8.30, so we can simplify Eq. 8.30 for $\tilde{\chi}_{\mathbf{GG}'}^{0,\mathrm{R}}(\mathbf{q}, 0)$ with $\tilde{\Delta}^{\mathrm{R},(3)}$ as:

$$
\begin{aligned}
\tilde{\chi}_{\mathbf{GG}'}^{0,\mathrm{R}}(\mathbf{q}, 0) &= -\frac{1}{\delta} \sum_{cv} \mathrm{M}_{vc}^{\mathrm{R}} \left[1 - \frac{\varepsilon_{cv} - \delta}{\delta} + \frac{(\varepsilon_{cv} - \delta)^2}{\delta \, \tilde{\Delta}^{\mathrm{R},(3)}} \right] \\
&= \frac{1}{\delta^2} \sum_{cv} \mathrm{M}_{vc}^{\mathrm{R}} \left[\varepsilon_{cv} - \frac{(\varepsilon_{cv} - \delta)^2}{\tilde{\Delta}^{\mathrm{R},(3)}} \right]
\end{aligned} \tag{8.34}
$$

Taylor series vs the Δ function

Summarizing the previous section we obtained three equations: Eq. 8.24 and Eq. 8.29 for $\Delta^{\mathrm{R},(m)}$ for $m = 1$ and 2, respectively, and Eq. 8.33 for $\tilde{\Delta}^{\mathrm{R},(3)}$. Now we will test numerically these approximations and compare them with the simple Taylor expansion of the static response (Eq. 8.18). Thus, we calculated $\Delta^{\mathrm{R},(1)}$ and $\Delta^{\mathrm{R},(1)}(\delta = 37 \text{ eV})$, and $\tilde{\Delta}^{\mathrm{R},(3)}(\delta = 37 \text{ eV})$ and plugged them in Equations 8.20 and 8.34 to obtain the approximated static response, $\tilde{\chi}_{\mathbf{GG}'}^{0,\mathrm{R}}(\mathbf{q}, 0)$: the results are shown in Fig. 8.4.

Let us start by pointing out the convergence of the curves with respect to the full calculation using Eq. 8.15 with $\mathrm{N}_c = 46$. At short $\mathbf{q}$'s ($\mathbf{q} < (0.5, 0, 0)$) using the Δ function (any order) gives a better approximation to the full calculation than only the Taylor expansion at similar order: this is particularly evident at the shortest $\mathbf{q} = (0.1, 0, 0)$ where the curves calculated with Δ almost overlap with the full calculation. The relative errors at $\mathbf{q} = (0.1, 0, 0)$ with respect to the exact result is $\sim 14\%$ by using $\Delta^{\mathrm{R},(1)}$, $\sim 11\%$ with $\Delta^{\mathrm{R},(2)}$ and $\sim 7\%$ with $\tilde{\Delta}^{\mathrm{R},(3)}$, while for the Taylor series the relative error is as high as $\sim 60\%$ with $m = 3$. We will come back later to this good approximation of the static response at the shorter $\mathbf{q}$'s. For the moment let us emphasize that using the Δ^{R} function seems a promising way to approximate the static response of a semiconductor.

---

[4]Analogously, following Equations 8.30, 8.31, 8.32 we can obtain $\tilde{\Delta}^{\mathrm{R}}$ to different orders: we can see from Eq. 8.32 that we can generalize it for the m-th order as $\tilde{\Delta}^{\mathrm{R},(m)} = \delta + \frac{\sum_{cv} \mathrm{M}_{vc}^{\mathrm{R}}(\varepsilon_{cv} - \delta)^m}{\sum_{cv} \mathrm{M}_{vc}^{\mathrm{R}}(\varepsilon_{cv} - \delta)^{m-1}}$.
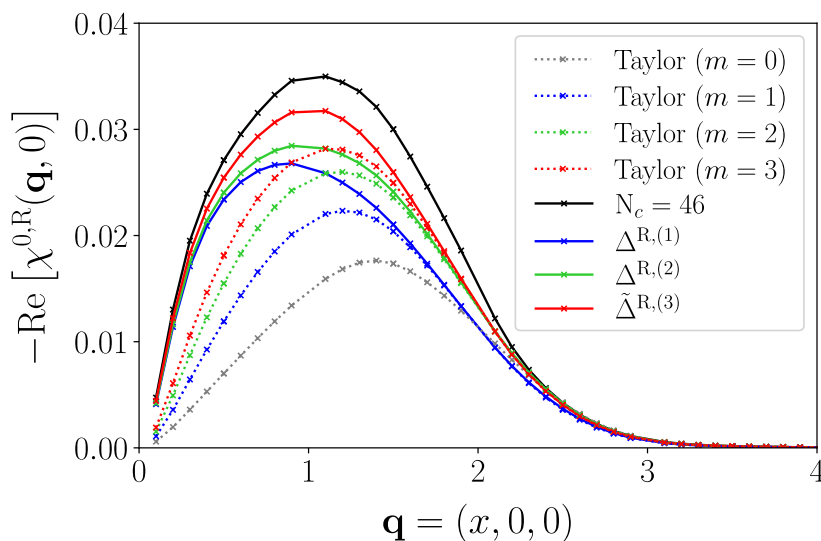
Figure 8.4: Static response of Si approximated with the Δ-method: $\Delta^{\mathrm{R},(1)}$ (Eq. 8.24), $\Delta^{\mathrm{R},(2)}$ (Eq. 8.29) and $\tilde{\Delta}^{\mathrm{R},(3)}$ (Eq. 8.33), and with the Taylor expansion (Eq. 8.18) at similar orders. Using Δ yields a closer result to the exact one than Taylor expansion: even at the lowest order (1), the response at the small $\mathbf{q} = (0.1, 0, 0)$ is converged, and in general the performance of using Δ is better order-by-order, for the same computational cost.

Another point worth remarking is regarding $\Delta^{\mathrm{R},(1)}$: it gives a good approximation for short and long $\mathbf{q}$'s without the need of a parameter as the "average transition energy", δ. This is not a minor point, taking δ to be the arithmetic average of transition energies may not be the optimal choice. The final goal is to use the closure relation to account for all conduction states, thus having a converging function that does not depend on defining a converging transition energy is crucial for the implementation. In the search of improved parameter-free approximations, we could think of using $\Delta^{\mathrm{R},(1)}$ in the place of δ: both behave as an average transition energy, but while δ is just an arithmetic average (constant), $\Delta^{\mathrm{R},(1)}$ has the same degrees of freedom as $\tilde{\chi}^{0,\mathrm{R}}_{\mathbf{GG}'}$. Hence, by construction, it is an average with information of the system, in particular with the information of the matrix elements. We will explore this in Section 8.3, but first, let us get more insight concerning Δ.

8.2.1   How does Δ look like?

The exact Δ^{R} is an effective energy which is a function of $\mathbf{q}$, $\mathbf{G}$ and $\mathbf{G}'$ with one-to-one correspondence with $\chi^{0,\mathrm{R}}_{\mathbf{GG}'}$. Now we want to investigate how this function behaves. For reference, from the equality $\chi^{0,\mathrm{R}}_{\mathbf{GG}'} = \tilde{\chi}^{0,\mathrm{R}}_{\mathbf{GG}'}$ with $\tilde{\chi}^{0,\mathrm{R}}_{\mathbf{GG}'}$ obtained from Eq. 8.20 we can write an expression for the exact Δ^{R} (see Eq. 8.21), and similarly for $\tilde{\Delta}^{\mathrm{R},(3)}$ from Eq. 8.34:

$$\tilde{\Delta}^{\mathrm{R},(3)}_{\mathrm{exact}} = - \left[\sum_{vc} \mathrm{M}^{\mathrm{R}}_{vc} (\varepsilon_{cv} - \delta)^2 \right] \left[\delta^2 \chi^{0,\mathrm{R}}_{\mathbf{GG}'}(\mathbf{q}, 0) - \sum_{vc} \mathrm{M}^{\mathrm{R}}_{vc} \varepsilon_{cv} \right]^{-1} \quad (8.35)$$

Notice that in contrast with $\Delta^{\mathrm{R},(\mathrm{exact})}$ (Eq. 8.21), $\tilde{\Delta}^{\mathrm{R},(3)}_{\mathrm{exact}}$ depends on the on the choice of δ (Eq. 8.35). We have plotted in Fig. 8.5 the different approximations with the exact Δ^{R}
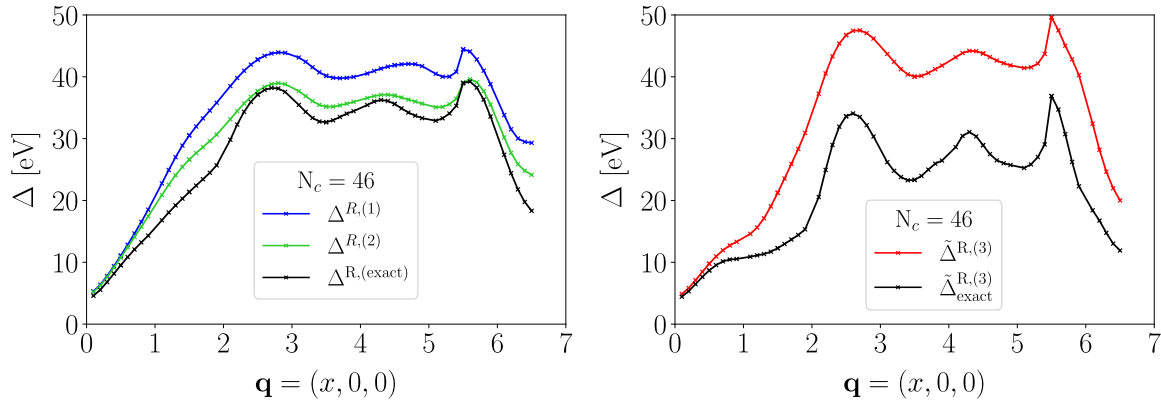
Figure 8.5: Left: Δ^{R} as a function of $\mathbf{q}+\mathbf{G}$: exact (Eq. 8.21) and first and second-order approximations (Eq. 8.24 and 8.29, respectively). Right: $\tilde{\Delta}^{\mathrm{R},(3)}_{\mathrm{exact}}$ (Eq. 8.35) and approximated (Eq. 8.33) with $\delta = 37$ eV. Despite the complexity of the curves, the different approximations for Δ^{R} manage to follow the exact results. Moreover, there is a clear improvement between the first and second order approximations in the left panel.

functions for Si with $N_{\mathrm{c}} = 46$ and using $\delta = 37$ eV.

Regardless of the complexity of the curves there is a clear resemblance between the approximated functions and the exact ones. Moreover, there is a noticeable improvement between the first and second order of Δ^{R} (Fig. 8.5, left panel), which is more evident at the longer $\mathbf{q}$'s (between $\mathbf{q} = (3,0,0)$ and $(6,0,0)$). Still, major differences can be observed between $\mathbf{q} = (0.1,0,0)$ and $(2,0,0)$. These were already expected from the differences in the static response (Fig. 8.4). On the other side $\tilde{\Delta}^{\mathrm{R},(3)}$ shows the major difference with respect to the exact function (Fig. 8.5, right panel): this does not result astonishing at the level of the Δ^{R} function given that $\tilde{\Delta}^{\mathrm{R},(3)}$ is obtained from a first-order approximation (Eq. 8.32). Nonetheless, the closer values to the full calculation of the static response (Fig. 8.4) are due to the fact that $\tilde{\Delta}^{\mathrm{R},(3)}$ is used to approximate a smaller part of the function (only the very last term of Eq. 8.34).

At this stage, what results surprising is the complexity of the curves at long $\mathbf{q}$'s, especially given the simple evolution of the static response in this region. See for example Fig. 8.4 with $N_{\mathrm{c}} = 46$, after $\mathbf{q} = (1,0,0)$ the curve starts decaying and the details observed in $\Delta^{\mathrm{R},(\mathrm{exact})}$ do not seem to appear. In this region the static response is not converged anymore with respect to the number of bands (Fig. 8.2, right panel). Thus, the Δ^{R} function seems very sensible to the information in the matrix elements $\mathrm{M}^{\mathrm{R}}_{vc}$. In order to verify the latter, we computed $\Delta^{\mathrm{R},(\mathrm{exact})}$ with $N_{\mathrm{c}} = 496$ (500 bands): we show the comparison with $\Delta^{\mathrm{R},(\mathrm{exact})}_{50\ \mathrm{bands}}$ in Fig. 8.6.

For the shorter $\mathbf{q}$'s $(\mathbf{q} < (1,0,0))$ $\Delta^{\mathrm{R},(\mathrm{exact})}_{50\ \mathrm{bands}}$ is numerically equivalent to $\Delta^{\mathrm{R},(\mathrm{exact})}_{500\ \mathrm{bands}}$ (expected from the convergence of the static response in Fig. 8.2), however at longer $\mathbf{q}$'s there is an enormous discrepancy between the two functions. In the static response of Fig. 8.2 this difference gets masked, because for long $\mathbf{q}$'s the static response decays to zero. Moreover, it is interesting to notice that at $\mathbf{q}$'s approximately between $\mathbf{q} = (2,0,0)$ and $(4,0,0)$ $\Delta^{\mathrm{R},(\mathrm{exact})}$ evolves similar to the energy of a plane wave, $\propto \frac{1}{2}|\mathbf{q}+\mathbf{G}|^2$, in agreement with the 0th term in the original development of the effective energy technique by Berger *et al* [127–129]. In fact, from Fig. 8.6 (left panel) we can differentiate among two different regions for $\Delta^{\mathrm{R},(\mathrm{exact})}$: essentially linear for $\mathbf{q} < (2,0,0)$ and quadratic for longer $\mathbf{q}$'s.
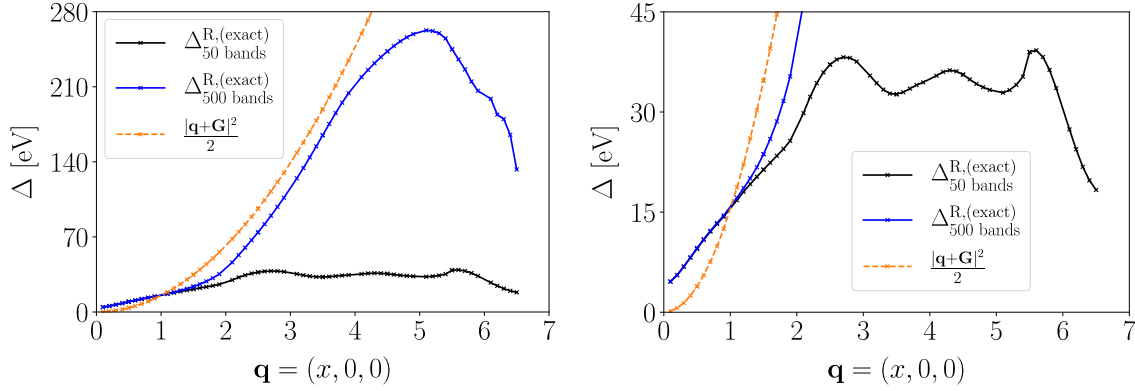
Figure 8.6: $\Delta^{\mathrm{R,(exact)}}$ for 50 and 500 bands ($\mathrm{N}_c = 46$ and 496, respectively) calculated with Eq. 8.21. The right panel is a zoom on the left panel. Only for short $\mathbf{q}$'s the curves coincide, after $\mathbf{q} = (1,0,0)$ there is a huge discrepancy among the two functions. This difference is associate to $\Delta^{\mathrm{R,(exact)}}_{50\text{ bands}}$ not being converged for long $\mathbf{q}$. This behavior is already present in the static response calculations of Fig. 8.2.

8.3   The challenge of many conduction states

Ideally we want to find a unique approximation to compute the static response as a function of $\mathbf{q}$ and we have already seen that using the Δ^{R} function promises a good path for development. However we have seen that the exact Δ^{R} function strongly depends on the number of bands, and so to obtain a clearer perspective of the function we now turn to the calculation of the static response (full and approximated) with 500 bands. In the approach with the average transition energy δ, this imposes a major complication, as now δ must account for transitions up to ~ 300 eV. Using 500 bands in total ($\mathrm{N}_c = 496$) the arithmetic average for the effective transition energy yields $\delta = 158$ eV. Nevertheless, given the long range of energies it is interesting to show how $\Delta^{\mathrm{R,(2)}}$ and $\tilde{\Delta}^{\mathrm{R,(3)}}$ change with respect to this parameter. We show in Fig. 8.7 both functions for selected values of δ.

As in the case of 50 bands (Figs. 8.4 and 8.5), we notice an improvement in the static response calculated using $\Delta^{\mathrm{R,(2)}}$ and $\tilde{\Delta}^{\mathrm{R,(3)}}$ with $\delta = 150$ eV, with respect to $\Delta^{\mathrm{R,(1)}}$ (parameter-free). However in this case it is much less pronounced. In fact, using $\Delta^{\mathrm{R,(2)}}$ there is no much benefit with respect to $\Delta^{\mathrm{R,(1)}}$: overall it describes the same curve and, as $\Delta^{\mathrm{R,(1)}}$, it fails to describe the region between $(0.5,0,0)$ and $(3,0,0)$ (Fig. 8.7, upper right panel). Moreover, when δ becomes too small[5] (see $\delta = 37$) the function suddenly diverges. We can understand this behavior from Eq. 8.29 as the competition between the negative term (the square root) and the positive term $\frac{3}{2}\delta$: when $\varepsilon_{cv}^2 = 3\delta\varepsilon_{cv}$, $\Delta^{\mathrm{R,(2)}} = 0$ hence Eq. 8.20 diverges. The latter gives us an exact constraint for the selection of δ:

$$\delta > \frac{1}{3}\varepsilon_{cv} \tag{8.36}$$

In Fig. 8.7 the constraint of Eq. 8.36 is evidently violated at around $\mathbf{q} \approx (2.5,0,0)$ for $\delta = 37$ eV. Nonetheless, it is interesting to notice that previous to the divergence $\tilde{\chi}^{\mathrm{R,0}}_{\mathbf{GG'}}$ with $\Delta^{\mathrm{R,(2)}}$ gets closer to full calculation ($\chi^{\mathrm{R,0}}_{500\text{ bands}}$ in Fig. 8.7). This is clear at $\mathbf{q} \approx (1,0,0)$, as the value of $\tilde{\chi}^{\mathrm{R,0}}_{\mathbf{GG'}}$ calculated with $\Delta^{\mathrm{R,(2)}}(\delta = 37$ eV$)$ lies in the middle between the approximations with the other values of δ and the exact curve, although $\delta =$

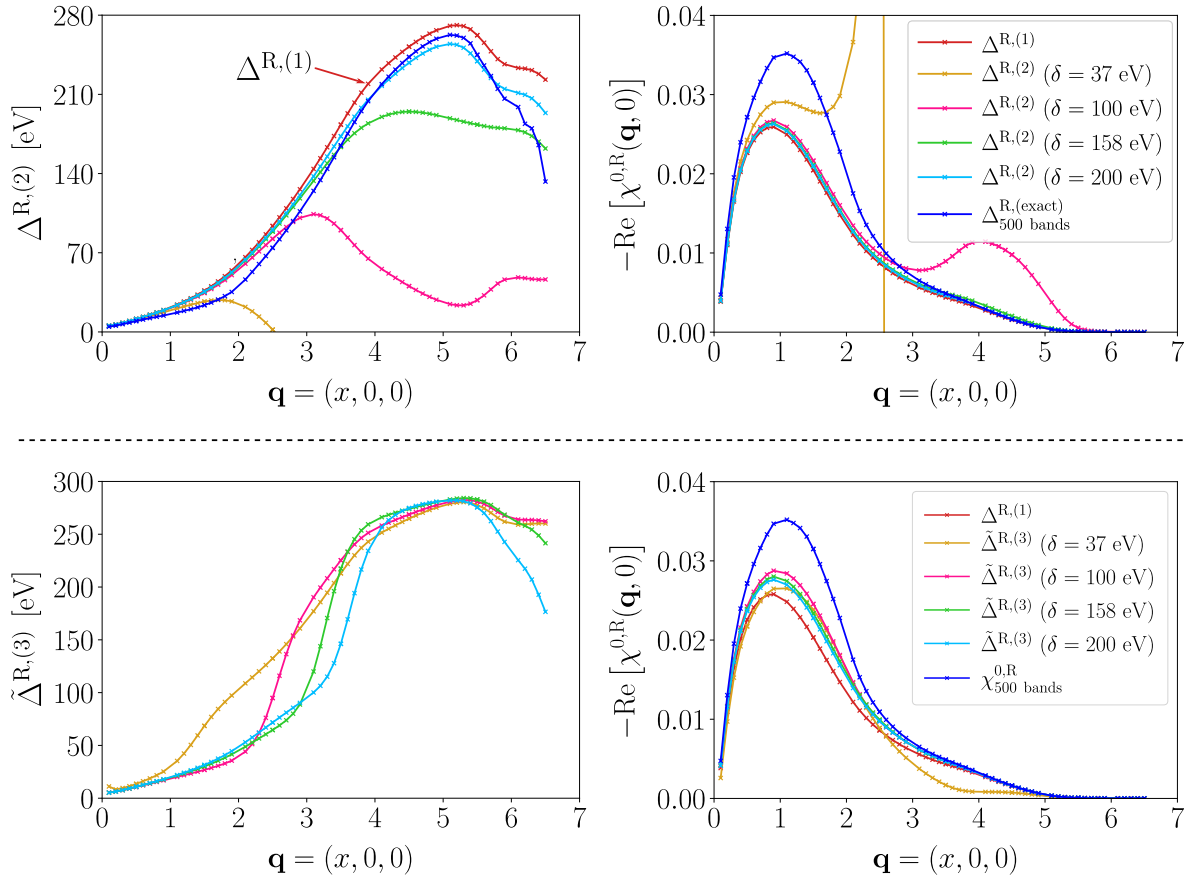[5] For instance with respect to the average transition energy $\delta = 158$ eV.

Figure 8.7: Upper panels: $\Delta^{R,(2)}$ (left) and static response (right) calculated with Eqs. 8.29 and 8.20, respectively with different δ values. Lower panels: $\tilde{\Delta}^{R,(3)}$ (left) and static response (right) with different δ values, caculated with Eq. 8.33 and Eq. 8.34, respectively. We included the static response calculated with $\Delta^{R,(1)}$ (Eq. 8.24) for comparison as well as the exact result. Both, $\Delta^{R,(2)}$ and $\tilde{\Delta}^{R,(3)}$ strongly vary with the average transition energy δ. In the case of $\Delta^{R,(2)}$ this dependence provokes the divergence of the static response when $\varepsilon_{cv}^2 = 3\delta\varepsilon_{cv}$.

37 eV is small with respect to the average transition energy of 158 eV. This observation suggests the need of including the **q**-dependence of the static response in different regions; for example using a small δ to approximate the shorter **q**'s and a larger one for the larger **q**'s. Notice that this is analogous to our comment about splitting $\Delta^{R,(exact)}$ for the two different regions (linear and quadratic) observed in the exact curve in Fig. 8.6.

$\tilde{\Delta}^{R,(3)}$ also shows significant changes with different δ values (Fig. 8.7, lower panels), for instance in the range between $(1, 0, 0)$ and $(4, 0, 0)$. However these differences are not as large as for $\Delta^{R,(2)}$ and they are even less pronounced in the static response (Fig. 8.7, lower right panel). Again, this is because $\tilde{\Delta}^{R,(3)}$ only approximates a small part in the polynomial of Eq. 8.30. From now on we focus only on $\Delta^{R,(2)}$ as it gives a clearer connection between the Δ^R function and the static response via Eq. 8.20.

8.3.1 $\Delta^{R,(2)}$ parameter-free

We commented previously about the possibility of using $\Delta^{R,(2)}$ splitting the study of the static response in two different regions. However we still need to develop a method to do it consistently. To this aim we first propose to use $\delta = \Delta^{R,(1)}$ in $\Delta^{R,(2)}$. Based on the
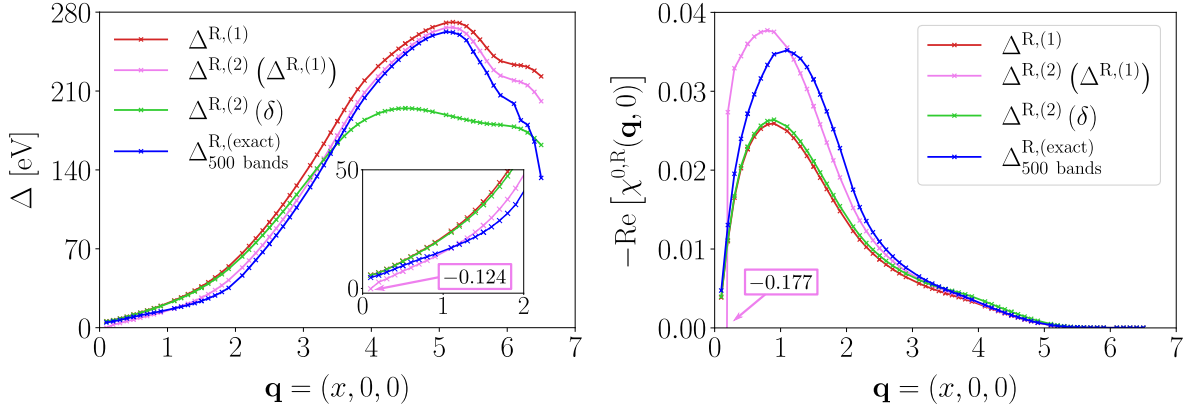
Figure 8.8: Δ^{R} function (left) and static response (right), caluclated with different approximations. Here we emphasize the result of using $\Delta^{\mathrm{R},(1)}$ as the effective transition energy in $\Delta^{\mathrm{R},(2)}$ (see Eq. 8.37). This approximation yields the closest result to the exact one for the longer $\mathbf{q}$'s. In the shorter $\mathbf{q}$ region, where $\Delta^{\mathrm{R,exact}}$ behaves linearly (from $\mathbf{q} = (0.1,0,0)$ to $\sim (1.5,0,0)$), $\Delta^{\mathrm{R},(1)}$ fails to describe the effective transition energy as it becomes too small. The latter is evident in the initial point ($\mathbf{q} = (0.1,0,0)$), where $\Delta^{\mathrm{R},(2)}(\Delta^{\mathrm{R},(1)})$ becomes negative and so, the static response as well.

idea that $\Delta^{\mathrm{R},(1)}$ is also an effective average transition but with information of the matrix elements (Eq. 8.24). Substituting $\delta = \Delta^{\mathrm{R},(1)}$ in Eq. 8.29 we obtain:

$$\Delta^{\mathrm{R},(2)}\left(\Delta^{\mathrm{R},(1)}\right) = -\frac{1}{2}\sqrt{\frac{4\sum_{vc}\mathrm{M}_{vc}^{\mathrm{R}}\left[\varepsilon_{cv}^2 - 3\Delta^{\mathrm{R},(1)}\varepsilon_{cv}\right]}{\sum_{vc}\mathrm{M}_{vc}^{\mathrm{R}}} + (3\Delta^{\mathrm{R},(1)})^2} + \frac{3\Delta^{\mathrm{R},(1)}}{2} \qquad (8.37)$$

We computed $\Delta^{\mathrm{R},(2)}\left(\Delta^{\mathrm{R},(1)}\right)$ and the static response by plugging Eq. 8.37 in Eq. 8.20: we show both curves in Fig. 8.8. First, notice that compared to $\Delta^{\mathrm{R},(1)}$ and $\Delta^{\mathrm{R},(2)}(\delta = 158 \text{ eV})$, $\Delta^{\mathrm{R},(2)}\left(\Delta^{\mathrm{R},(1)}\right)$ overall yields a better approximation to $\Delta^{\mathrm{R},(\text{exact})}$. This is an outstanding result: Eq. 8.37 is parameter-free as $\Delta^{\mathrm{R},(1)}$ is also parameter-free, and it yields the best approximation for the static response here discussed. In particular, notice from Fig. 8.8 that the best approximation to the exact curve using Eq. 8.37 corresponds to the region in which $\Delta^{\mathrm{R},(\text{exact})}$ behaves quadratically: $\mathbf{q} > (2,0,0)$.

It is in the linear regime, for $\mathbf{q} < 1.5$, where $\Delta^{\mathrm{R},(2)}\left(\Delta^{\mathrm{R},(1)}\right)$ fails to describe the exact curve. For instance, at $\mathbf{q} = (0.1,0,0)$ (the shortest one in Fig. 8.8) $\Delta^{\mathrm{R},(2)}\left(\Delta^{\mathrm{R},(1)}\right)$ becomes negative. This occurs because for the shorter $\mathbf{q}$'s $\Delta^{\mathrm{R},(1)}$ becomes too small such that the condition of Eq. 8.36 is violated.

Eq. 8.37 gives a promising method to approximate the parabolic region of the static response. As we have seen however, for the linear region $\Delta^{\mathrm{R},(1)}$ becomes too small to be used in $\Delta^{\mathrm{R},(2)}$. For this, we propose to use Eq. 8.29 with a constant value for δ. The motivation is the fact that for small $\mathbf{q}$ the energy region in which the electronic transitions are more important to shape the static response is quite limited. Look back to Fig. 8.2 (right panel): with only the first 10 conduction bands (14 bands in total) the converged result is reproduced up to $\mathbf{q} = (0.5,0,0)$, and only 36 more bands are enough to reproduce the maximum of the curve of the static response. Thus, it is evident that the lower energy transitions are more important for the short $\mathbf{q}$'s, and therefore, for the linear regime in $\Delta^{\mathrm{R},(\text{exact})}$. We show in Fig. 8.9 $\Delta^{\mathrm{R},(2)}(\delta)$ evaluated with different small values of δ, as well as the static response. Clearly using a small δ value helps to accelerate
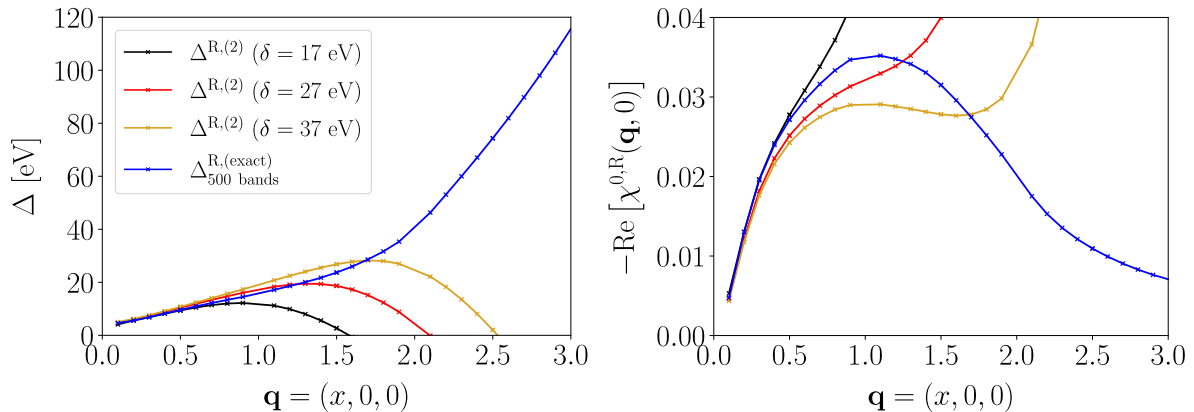
Figure 8.9: Left: $\Delta^{R,(2)}$ with different small δ values. Right: static reponse calculated with $\Delta^{R,(2)}(\delta)$. For the latter only the points before the divergence are shown. The exact Δ^R shows two different regimes: linear in the shorter $\mathbf{q}$'s and quadratric for the longer values. Here we propose to approximate the linear regime with a constant effective transition energy, find a good approximation for the shorter $\mathbf{q}$'s. Of course as the selected δ value is too small compared to the transitions in the whole spectrum, $\Delta^{R,(2)}$ becomes negative and $\mathbf{q}$ diverges at a given (long) $\mathbf{q}$. Ideally, the second region of the static response can be treated differently, for instance with Eq. 8.37.

the convergence of $\Delta^{R,(2)}$ for the shorter $\mathbf{q}$'s. Eventually, for longer $\mathbf{q}$'s $\Delta^{R,(2)} = 0$, so the static response diverges (Fig. 8.9). As we propose, the two regions of $\Delta^{R,(exact)}$ need to be treated separately: for the linear region δ needs to be optimized, while for the parabolic region the choice of $\Delta^{R,(2)} \left(\Delta^{R,(1)} \right)$ gives a good approximation to the exact result.

8.4 Adding explicitly few conduction states

A point of numerical interest is to separate Eq. 8.15 into two different groups of transitions: for example, if we were interested in only N_c conduction bands (with $N_c = c_1 + c_2$), we could separate them into two different groups: a first one accounting for the lower conduction bands (up to c_1), and the second one for the remaining states (from $c_1 + 1$ to c_2). Thus, we could compute the first set of low energy transition explicitly and approximate only the second part of the sum (this is referred to in Ref. [129] as the "simplified EET"):

$$\chi^{0,R}_{\mathbf{GG'}}(\mathbf{q},0) = \sum_v^{all} \sum_{c=1}^{c_1} \frac{\tilde{\rho}_{vc}(\mathbf{q}+\mathbf{G})\tilde{\rho}^*_{vc}(\mathbf{q}+\mathbf{G'})}{-(\varepsilon_c - \varepsilon_v)} + \sum_v^{all} \sum_{c=c_1+1}^{c_2} \frac{\tilde{\rho}_{vc}(\mathbf{q}+\mathbf{G})\tilde{\rho}^*_{vc}(\mathbf{q}+\mathbf{G'})}{-\Delta^R} \quad (8.38)$$

We show in Fig. 8.10 the evolution of the static response taking low-energy transitions into account explicitly according to Eq. 8.38: $c_1 = 0$ is the usual case that we presented in Fig. 8.4, approximating all transitions. It is interesting to notice that taking explicitly into account 10 conduction bands (and treating the rest with $\Delta^{R,(1)}$) the spectrum almost matches the full calculation with $N_c = 46$ (which at short $\mathbf{q}$'s is already converged, see Fig. 8.2). Moreover, this separation of terms does not interfere with the closure relation of Eq. 8.2: we only need to redefine it using $\sum_c |c\rangle \langle c| = \sum_{c_1} |c_1\rangle \langle c_1| + \sum_{c_2} |c_2\rangle \langle c_2|$, thus analogously to Eq. 8.2, the closure relation in the simplified EET becomes:

$$\sum_{c_2} |c_2\rangle \langle c_2| = 1 - \sum_{c_1} |c_1\rangle \langle c_1| - \sum_v |v\rangle \langle v| \quad (8.39)$$
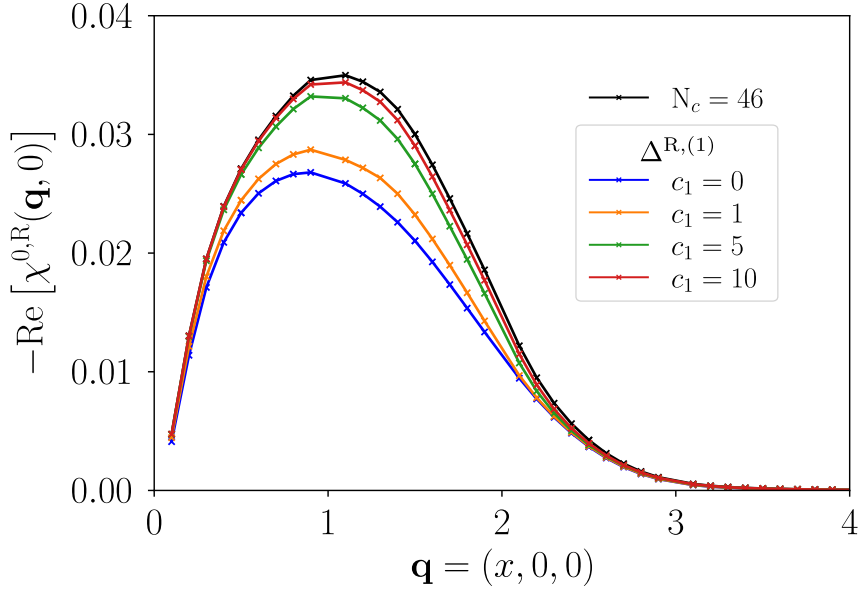
Figure 8.10: Static response calculated with $\Delta^{\mathrm{R},(1)}$ within the "simplified EET" picture of Eq. 8.38. $c_1 = 0$ corresponds to the case in which the contibution of all bands is approximated within $\Delta^{\mathrm{R},(1)}$, and $c_1 = 1$ to calculating explicitly the transitions between the valence states and lowest unoccupied state. Notice that considering a very small number of empty states clearly yields a better of the static response. For instance, taking into account 10 conduction states almost reproduce the full calculation with $\mathrm{N}_c = 46$.

8.4.1   Metallic systems: borophene δ_6

The main material of interest in this thesis is borophene, which is metallic. We therefore have to extend our approach to metallic systems. The structure of the polarizability is a simple sum over transitions, and we have separated it three times so far: resonant + antiresonant transitions (Eq. 8.10), states with fractional + integer occupation numbers (Eq. 8.16), and low and high energy transitions (Eq. 8.38). Among these, we can realize that the latter two are very similar, thus, we could apply a procedure analogous to Eq. 8.38 to treat metallic systems adding few conduction states.

We must remark that there must be a modification: in metals the transition between "occupied" and "empty" states is continuous and so, it is difficult to define what is occupied and empty in the same sense as for a semiconductor; in this regard the most natural choice seems to be defining the separation of the sum based on an energy threshold, E:

$$
\tilde{\chi}^{0,\mathrm{R}}_{\mathbf{G}\mathbf{G}'}(\mathbf{q},0) = \sum_{vc \ \forall \ |\varepsilon_c - \varepsilon_v| \leq E} \frac{(f_v - f_c)\tilde{\rho}_{vc}(\mathbf{q}+\mathbf{G})\tilde{\rho}^*_{vc}(\mathbf{q}+\mathbf{G}')}{-(\varepsilon_c - \varepsilon_v)} \\
+ \sum_{vc \ \forall \ |\varepsilon_c - \varepsilon_v| > E} \frac{(f_v - f_c)\tilde{\rho}_{vc}(\mathbf{q}+\mathbf{G})\tilde{\rho}^*_{vc}(\mathbf{q}+\mathbf{G}')}{-\Delta^{\mathrm{R}}}
\tag{8.40}
$$

For example, with Δ^{R} to first order as in Eq. 8.24:

$$
\Delta^{\mathrm{R},(1)} = \frac{\sum_{vc \ \forall \ |\varepsilon_c - \varepsilon_v| > E} (f_v - f_c)\tilde{\rho}_{vc}(\mathbf{q}+\mathbf{G})\tilde{\rho}^*_{vc}(\mathbf{q}+\mathbf{G}')(\varepsilon_c - \varepsilon_v)}{\sum_{vc \ \forall \ |\varepsilon_c - \varepsilon_v| > E} (f_v - f_c)\tilde{\rho}_{vc}(\mathbf{q}+\mathbf{G})\tilde{\rho}^*_{vc}(\mathbf{q}+\mathbf{G}')}
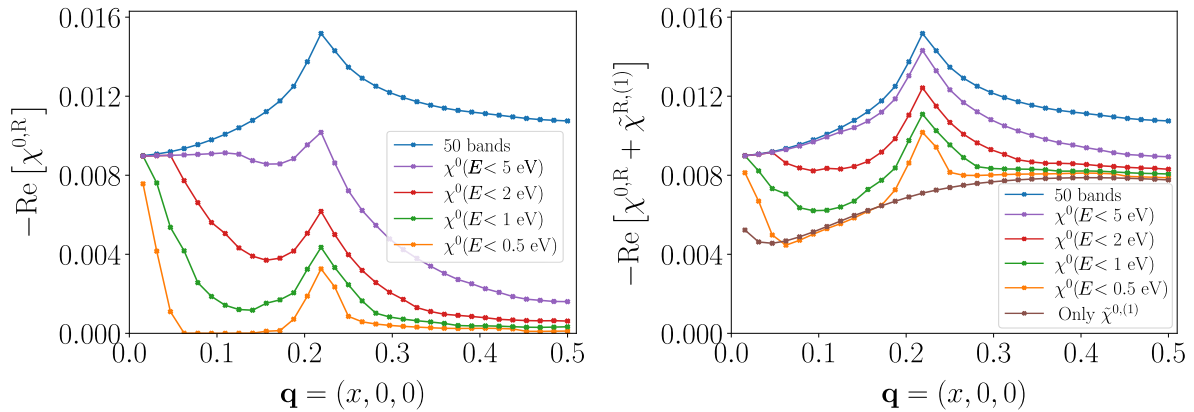\tag{8.41}
$$

Figure 8.11: Static response of borophene δ_6. Left: full calculation including only low energy transitions (Eq. 8.9). Right: mixed calculation with Eq. 8.40 adding the "background" structure with $\Delta^{R,(1)}$ up to 50 bands: the largest energy transition considering explicitly the 50 bands (blue curve) has a maximum transition energy of 58 eV. Notice that, for metallic systems (as borophene δ_6) the "image" of the Fermi surface needs to be explicitly taken into account, this leads to a necessary convergence of the energy window in which the transitions need to be taken explicitly: for instance with 5 eV the mixed approach leads to a similar curve as the full calculation with 50 bands.

We show in Fig. 8.11 the static response of borophene δ_6 computed with this method (Eq. 8.40) at the level of $\Delta^{R,(1)}$ with Eq. 8.41. Let us first look at the left panel. When only transitions around the Fermi level are taken into account $\chi^{R,0}$ shows the peak characteristic for nesting above $\mathbf{q} = (0.2, 0, 0)$ but the background on which this peak lies is completely absent. It emerges gradually when more bands are taken into account. Instead, the right panel of Fig. 8.11 shows that this background can be to an extent reproduced by $\Delta^{R,(1)}$.

Similarly to the case of semiconductors (Si for instance), the approximation for static response of the metallic case can be improved at selected with Δ^R at higher orders. We plotted in Fig. 8.12 (left) the static response of borophene δ_6 evaluated at $E = 0$, at the level of $\Delta^{R,(1)}$ (Eq. 8.41) and $\Delta^{R,(2)}$ and $\Delta^{R,(2)} \left(\Delta^{R,(1)} \right)$, the latter two analogous to Eqs. 8.29 and 8.37 for metallic systems[6]. Of course, the approximation for metals suffers from the same caveats as for the semiconductors: in particular notice the divergence of the static response at around $\mathbf{q} = (0.1, 0, 0)$ using $\Delta^{R,(2)} \left(\Delta^{R,(1)} \right)$. It is evident from Fig. 8.12 (right) that $\Delta^{R,(1)}$ becomes very small, and therefore $\Delta^{R,(2)} \left(\Delta^{R,(1)} \right)$ becomes negative. For an efficient calculation one can now combine the use of an energy window as in Fig. 8.11 with the use of $\Delta^{R,(2)}$ as in Fig. 8.12 (or higher order), this reproduces with good precision both the background and the nesting peak.

8.5 Conclusions

Let us summarize and highlight the conclusions developed in this chapter. We investigated different approximations for the evolution of the static response with the momentum transfer. First, we showed that it is possible to approximate it via Taylor expansion although it requires higher orders to yield results with high precision. Then, we devel-

---

[6]The only difference with respect to Eqs. 8.29 and 8.37 is the occupation numbers and definition of the energy window E.
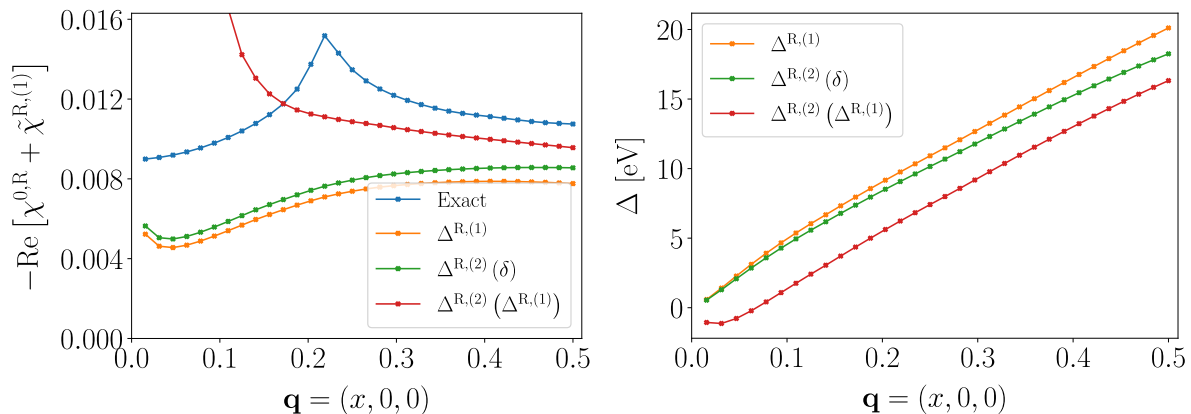
Figure 8.12: Left: static response of borophene δ_6 calculated with the full sum over transitions ("Exact": Eq. 8.14) and with different Δ^{R}'s: $\Delta^{R,(1)}$ as in Eq. 8.41, $\Delta^{R,(2)}$ as in Eq. 8.29 (for metallic systems, *i. e.*, including the fractional occupation numbers as in Eq. 8.41) and $\Delta^{R,(2)}\left(\Delta^{R,(1)}\right)$ as Eq. 8.37 (for metallic systems). In all cases $E = 0$, and $\delta = 29$ eV (calculated from Eq. 8.19 for 50 bands) only relevant for $\Delta^{R,(2)}$. Right: Δ^{R}'s functions.

oped different approximations to the static response in the spirit of the effective energy technique [129], by obtaining different functions (Δ^{R} and $\tilde{\Delta}^{R,(3)}$). These approximations perform much better than the simple Taylor expansion, in particular at the very small and large $\mathbf{q}$'s even at the lowest order $\Delta^{R,(1)}$.

We showed that $\Delta^{R,(1)}$, by construction parameter-free, already gives a good approximation for the static response even simulating a very large number of conduction bands. The higher-order approximations $\Delta^{R,(2)}$ and $\tilde{\Delta}^{R,(3)}$, do not necessarily perform better, as both depend on an effective transition energy. Nonetheless we showed that we can improve the approximation given by $\Delta^{R,(2)}$ by setting the average transition energy δ to $\Delta^{R,(1)}$. In the latter case $\Delta^{R,(2)}$ becomes parameter-free and displays the best performance towards the static response among the approximations studied in this work (for the quadratic regime of $\Delta^{R,(\text{exact})}$ $\mathbf{q}$'s). We also showed that it is possible to extend these approximations to metallic systems and, as a proof of concept, we presented the approximated static response for borophene δ_6.

We showed that in numerical calculations, the approximated static response calculations for semiconductors can be significantly improved by taking few conduction states explicitly into account, in the spirit of the simplified EET [129]. In a similar idea for metallic systems, the explicit inclusion of low-energy transitions not only helps the convergence but it also allows one to add explicit information of the Fermi surface: as we showed in Section 7 this information is crucial for the discussion of Kohn anomalies, charge density waves and phonons in metals.

8.6   Outlook

The closure relation

As the final goal, we are interested in applying the closure relation to avoid the sum over many conduction bands for the calculation of the static response. Only by doing so, the approximation will lead to numerically efficient calculations. Moreover, as we will see,

interesting expressions are obtained. The approximate expression for the function Δ^{R} (and $\tilde{\Delta}^{\mathrm{R}}$), Eqs. 8.24, 8.29 and 8.33, together with the one for $\tilde{\chi}^{\mathrm{R}}_{\mathbf{GG'}}$ (Eq. 8.20), contain the matrix elements $\mathrm{M}^{\mathrm{R}}_{vc}$ in either the numerator or denominator but in a form in which, in principle, we can apply the closure relation of Eq. 8.2: in general, the matrix elements appear in Equations 8.24, 8.29, 8.33 and 8.20 as:

$$\sum_{vc} \tilde{\rho}_{vc}(\mathbf{q}+\mathbf{G}) \tilde{\rho}^*_{vc}(\mathbf{q}+\mathbf{G'}) (\varepsilon_c - \varepsilon_v)^w \tag{8.42}$$

We deal later with the term $(\varepsilon_c - \varepsilon_v)^\omega$, for now we want to show the numerical implementation of the closure relation as it will make this concept clear. For instance, in explicit form Eq. 8.42 with $w = 0$ reads:

$$\sum_{vc} \langle v, \mathbf{k}-\mathbf{q}|\, e^{i(\mathbf{q}+\mathbf{G})\cdot\mathbf{r}} \,|c, \mathbf{k}\rangle \langle c, \mathbf{k}|\, e^{-i(\mathbf{q}+\mathbf{G'})\cdot\mathbf{r'}} \,|v, \mathbf{k}-\mathbf{q}\rangle \tag{8.43}$$

and upon the application of the closure relation (Eq. 8.2) it becomes (with v' being a valence state at $\mathbf{k}-\mathbf{q}$):

$$\sum_{v} \langle v, \mathbf{k}-\mathbf{q}|\, e^{i(\mathbf{G}-\mathbf{G'})\cdot\mathbf{r}} \,|v, \mathbf{k}-\mathbf{q}\rangle$$
$$-\sum_{vv'} \langle v, \mathbf{k}-\mathbf{q}|\, e^{i(\mathbf{q}+\mathbf{G})\cdot\mathbf{r}} \,|v', \mathbf{k}\rangle \langle v', \mathbf{k}|\, e^{-i(\mathbf{q}+\mathbf{G'})\cdot\mathbf{r'}} \,|v, \mathbf{k}-\mathbf{q}\rangle \tag{8.44}$$

This rewriting represents a huge reduction of computational time. For instance, in order to compute the matrix elements as in Eq. 8.9 we have to perform a large sum over valence and conduction states, and for example, in the static response calculation of Fig. 8.2 it is clear that using $N_c = 46$ (or even 196) is not enough to converge the spectrum at long $\mathbf{q}$'s. On the contrary, using Eq. 8.44 to compute the matrix elements requires only from the occupied states, but accounts also for all empty states. In order to illustrate this we have plotted the matrix elements as computed using Eq. 8.43 with different number of conduction bands (up to $N_c = 496$) and using the closure relation according to Eq. 8.44 with only valence states: the results are shown in Fig. 8.13.

The results at small $\mathbf{q}$'s up to $\mathbf{q} \approx (3, 0, 0)$ evaluated with Eq. 8.43 are converged with $N_c = 496$ bands and equal to that using the closure relation (Eq. 8.44). At larger $\mathbf{q}$'s the matrix elements computed with the closure relation stay almost constant while Eq. 8.43 shows a decay, simply because more bands are required to be complete. Nonetheless it is also evident from the evolution of the curves from $N_c = 46$ to 496 that the curves tend towards the same constant value, thus confirming numerically the possibility of, and the need for, using the closure relation (Eq. 8.44) to compute the matrix elements of the polarizability.

The missing pieces

Let us go back to Eq. 8.42, as it is the main ingredient in the polarizability $\tilde{\chi}^{\mathrm{R}}_{\mathbf{GG'}}(\mathbf{q}, 0)$ (Eq. 8.20) and in the different expressions for Δ. In the latter in particular we remark the appearance of the term $(\varepsilon_c - \varepsilon_v)^w$ which does not let us use the closure relation straightforwardly. Thus, we propose to rewrite Eq. 8.42 with $w = 1$ using the electronic
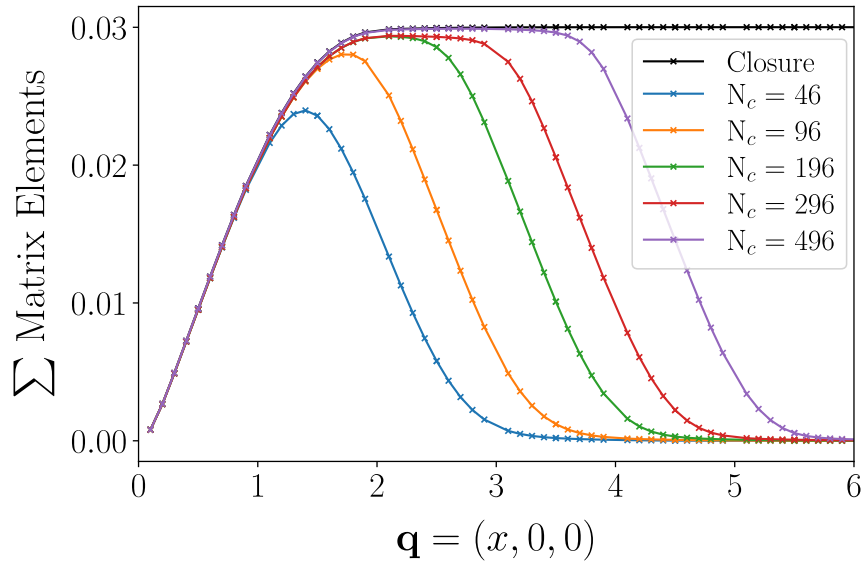
Figure 8.13: Matrix elements (M_{vc}^{R}) computed with different conduction states (Eq. 8.43), and using the closure relation (Eq. 8.44). The closure relation correctly reproduces the calculation with a large number of conduction states at a much lower computational price: for instance the full calcualtion with $N_c = 496$ diverges from the constant value of the matrix elements at large $\mathbf{q}$'s, while using the closure relation with only 4 bands shows this evolution.

Hamiltonian $\hat{\mathscr{H}}$, such that $\hat{\mathscr{H}} |n\rangle = \varepsilon_n |n\rangle$, and hence rewrite $(\varepsilon_c - \varepsilon_v)$ as a commutator, as shown in Eqs. 8.5 and 8.6, and used for example in Ref. [126].

To simplify the notation we refer to Eq. 8.42 with $w = 1$ as Ω^{R}, and to avoid confusion we remind the reader that the matrix elements contain the information of the $\mathbf{k}$ (and $\mathbf{k} - \mathbf{q}$) vectors; the closure relation is only applied to the valence and conduction states (Eq. 8.44). We start by using $\hat{\mathscr{H}} |c\rangle = \varepsilon_c |c\rangle$, and $\langle v| \hat{\mathscr{H}} = \varepsilon_v \langle c|$ to obtain the commutator:

$$
\begin{aligned}
\Omega^{\mathrm{R}} &= \sum_{vc} \langle v| e^{\mathrm{i}(\mathbf{q}+\mathbf{G})\cdot\mathbf{r}} |c\rangle \langle c| e^{-\mathrm{i}(\mathbf{q}+\mathbf{G}')\cdot\mathbf{r}'} |v\rangle \, (\varepsilon_c - \varepsilon_v) \\
&= \sum_{vc} \langle v| e^{\mathrm{i}(\mathbf{q}+\mathbf{G})\cdot\mathbf{r}} |c\rangle \langle c| e^{-\mathrm{i}(\mathbf{q}+\mathbf{G}')\cdot\mathbf{r}'} |v\rangle \, \varepsilon_c - \sum_{vc} \langle v| e^{\mathrm{i}(\mathbf{q}+\mathbf{G})\cdot\mathbf{r}} |c\rangle \langle c| e^{-\mathrm{i}(\mathbf{q}+\mathbf{G}')\cdot\mathbf{r}'} |v\rangle \, \varepsilon_v \\
&= \sum_{vc} \langle v| e^{\mathrm{i}(\mathbf{q}+\mathbf{G})\cdot\mathbf{r}} \hat{\mathscr{H}} |c\rangle \langle c| e^{-\mathrm{i}(\mathbf{q}+\mathbf{G}')\cdot\mathbf{r}'} |v\rangle - \sum_{vc} \langle v| \hat{\mathscr{H}} e^{\mathrm{i}(\mathbf{q}+\mathbf{G})\cdot\mathbf{r}} |c\rangle \langle c| e^{-\mathrm{i}(\mathbf{q}+\mathbf{G}')\cdot\mathbf{r}'} |v\rangle \\
&= \sum_{vc} \langle v| e^{\mathrm{i}(\mathbf{q}+\mathbf{G})\cdot\mathbf{r}} \hat{\mathscr{H}} - \hat{\mathscr{H}} e^{\mathrm{i}(\mathbf{q}+\mathbf{G})\cdot\mathbf{r}} |c\rangle \langle c| e^{-\mathrm{i}(\mathbf{q}+\mathbf{G}')\cdot\mathbf{r}'} |v\rangle \\
&= \sum_{vc} \langle v| \left[e^{\mathrm{i}(\mathbf{q}+\mathbf{G})\cdot\mathbf{r}}, \hat{\mathscr{H}} \right] |c\rangle \langle c| e^{-\mathrm{i}(\mathbf{q}+\mathbf{G}')\cdot\mathbf{r}'} |v\rangle
\end{aligned}
\tag{8.45}
$$

Note that we made an arbitrary choice: we introduced the Hamiltonian in the integral centered in $\mathbf{r}$, but we could have selected to add the Hamiltonian in the integral in $\mathbf{r}'$, and obtain:

$$
\Omega^{\mathrm{R}} = \sum_{vc} \langle v| e^{\mathrm{i}(\mathbf{q}+\mathbf{G})\cdot\mathbf{r}} |c\rangle \langle c| \left[\hat{\mathscr{H}}, e^{-\mathrm{i}(\mathbf{q}+\mathbf{G}')\cdot\mathbf{r}'} \right] |v\rangle
\tag{8.46}
$$

Using the fact that $|v\rangle$ and $|c\rangle$ are eigenfunctions of $\hat{\mathscr{H}}$, Eqs. 8.45 and 8.46 must be equivalent[7] (the parallel development shown in this Section for the commutator in Eq. 8.46 can be found in Appendix IV).

Evaluation of the Hamiltonian

Now, we evaluate the electronic Hamiltonian $\hat{\mathscr{H}} = -\frac{\nabla^2}{2} + \hat{\mathscr{V}}$, thus, Eq. 8.45 becomes:

$$
\begin{aligned}
\Omega^{\mathrm{R}} &= \sum_{vc} \langle v| \left[e^{\mathrm{i}(\mathbf{q}+\mathbf{G})\cdot\mathbf{r}}, \hat{\mathscr{H}} \right] |c\rangle \langle c| \, e^{-\mathrm{i}(\mathbf{q}+\mathbf{G}')\cdot\mathbf{r}'} |v\rangle \\
&= \sum_{vc} \langle v| \left[e^{\mathrm{i}(\mathbf{q}+\mathbf{G})\cdot\mathbf{r}}, -\frac{\nabla^2}{2} \right] |c\rangle \, \tilde{\rho}_{vc}^* + \sum_{vc} \langle v| \left[e^{\mathrm{i}(\mathbf{q}+\mathbf{G})\cdot\mathbf{r}}, \hat{\mathscr{V}} \right] |c\rangle \, \tilde{\rho}_{vc}^*
\end{aligned}
\tag{8.47}
$$

The second line shows two terms, one with the kinetic part, and another one with the static potential. To simplify the development we separate these two pieces:

$$
\Omega^{\mathrm{R}} \equiv \Omega_{\nabla}^{\mathrm{R}} + \Omega_{\hat{\mathscr{V}}}^{\mathrm{R}}
\tag{8.48}
$$

and we focus initially on the kinetic part $\Omega_{\nabla}^{\mathrm{R}}$. Hereafter we show the evaluation of the second-order derivative ∇^2:

$$
\begin{aligned}
\Omega_{\nabla}^{\mathrm{R}} &= -\frac{1}{2} \sum_{vc} \langle v| \left[e^{\mathrm{i}(\mathbf{q}+\mathbf{G})\cdot\mathbf{r}}, \nabla^2 \right] |c\rangle \, \tilde{\rho}_{vc}^* \\
&= -\frac{1}{2} \sum_{vc} \left[\langle v| \, e^{\mathrm{i}(\mathbf{q}+\mathbf{G})\cdot\mathbf{r}} \nabla^2 |c\rangle - \langle v| \, \nabla^2 e^{\mathrm{i}(\mathbf{q}+\mathbf{G})\cdot\mathbf{r}} |c\rangle \right] \tilde{\rho}_{vc}^* \\
&= -\frac{1}{2} \sum_{vc} \left[\langle v| \, e^{\mathrm{i}(\mathbf{q}+\mathbf{G})\cdot\mathbf{r}} \nabla^2 |c\rangle - \langle v| \, \nabla e^{\mathrm{i}(\mathbf{q}+\mathbf{G})\cdot\mathbf{r}} \nabla |c\rangle - \mathrm{i}(\mathbf{q}+\mathbf{G}) \langle v| \, \nabla e^{\mathrm{i}(\mathbf{q}+\mathbf{G})\cdot\mathbf{r}} |c\rangle \right] \tilde{\rho}_{vc}^* \\
&= -\frac{1}{2} \sum_{vc} \left[\langle v| \, e^{\mathrm{i}(\mathbf{q}+\mathbf{G})\cdot\mathbf{r}} \nabla^2 |c\rangle - \langle v| \, e^{\mathrm{i}(\mathbf{q}+\mathbf{G})\cdot\mathbf{r}} \nabla^2 |c\rangle - \mathrm{i}(\mathbf{q}+\mathbf{G}) \langle v| \, e^{\mathrm{i}(\mathbf{q}+\mathbf{G})\cdot\mathbf{r}} \nabla |c\rangle \right] \tilde{\rho}_{vc}^* \\
&\quad + \frac{1}{2} \sum_{vc} \left[\mathrm{i}(\mathbf{q}+\mathbf{G}) \langle v| \, e^{\mathrm{i}(\mathbf{q}+\mathbf{G})\cdot\mathbf{r}} \nabla |c\rangle - (\mathbf{q}+\mathbf{G})^2 \langle v| \, e^{\mathrm{i}(\mathbf{q}+\mathbf{G})\cdot\mathbf{r}} |c\rangle \right] \tilde{\rho}_{vc}^* \\
&= -\frac{(\mathbf{q}+\mathbf{G})^2}{2} \sum_{vc} \langle v| \, e^{\mathrm{i}(\mathbf{q}+\mathbf{G})\cdot\mathbf{r}} |c\rangle \, \tilde{\rho}_{vc}^* + \mathrm{i}(\mathbf{q}+\mathbf{G}) \sum_{vc} \langle v| \, e^{\mathrm{i}(\mathbf{q}+\mathbf{G})\cdot\mathbf{r}} \nabla |c\rangle \, \tilde{\rho}_{vc}^*
\end{aligned}
\tag{8.49}
$$

Grouping terms we arrive to:

$$
\Omega_{\nabla}^{\mathrm{R}} = -\frac{(\mathbf{q}+\mathbf{G})^2}{2} \sum_{vc} \langle v| \, e^{\mathrm{i}(\mathbf{q}+\mathbf{G})\cdot\mathbf{r}} |c\rangle \, \tilde{\rho}_{vc}^* + \mathrm{i}(\mathbf{q}+\mathbf{G}) \sum_{vc} \langle v| \, e^{\mathrm{i}(\mathbf{q}+\mathbf{G})\cdot\mathbf{r}} \nabla |c\rangle \, \tilde{\rho}_{vc}^*
\tag{8.50}
$$

Explicitly, Eq. 8.50 reads:

---

[7]The same situation was found in Ref. [129], where the asymmetry in $\mathbf{G}$, $\mathbf{G}'$ is addressed by defining $\Omega'^{,\mathrm{R}} = \frac{1}{2} \left[\Omega^{\mathrm{R}} + h.\,c. \right]$ with $h.\,c.$ being the Hermitian conjugate of Ω^{R}.

$$\Omega_\nabla^{\mathrm{R}} = -\frac{(\mathbf{q}+\mathbf{G})^2}{2} \sum_{vc} \langle v| \, e^{\mathrm{i}(\mathbf{q}+\mathbf{G})\cdot\mathbf{r}} \, |c\rangle \, \langle c| \, e^{-\mathrm{i}(\mathbf{q}+\mathbf{G}')\cdot\mathbf{r}'} \, |v\rangle$$
$$+\mathrm{i}(\mathbf{q}+\mathbf{G}) \sum_{vc} \langle v| \, e^{\mathrm{i}(\mathbf{q}+\mathbf{G})\cdot\mathbf{r}} \nabla \, |c\rangle \, \langle c| \, e^{-\mathrm{i}(\mathbf{q}+\mathbf{G}')\cdot\mathbf{r}'} \, |v\rangle \tag{8.51}$$

Eq. 8.51 shows that the original goal of this chapter is reached: an equation that does not depend on $(\varepsilon_c - \varepsilon_v)$, and to which we can apply the closure relation (Eq. 8.2) on the sum over conduction states[8]:

$$\Omega_\nabla^{\mathrm{R}} = -\frac{(\mathbf{q}+\mathbf{G})^2}{2} \left[\sum_v \langle v| \, e^{\mathrm{i}(\mathbf{G}-\mathbf{G}')\cdot\mathbf{r}} \, |v\rangle - \sum_{vv'} \langle v| \, e^{\mathrm{i}(\mathbf{q}+\mathbf{G})\cdot\mathbf{r}} \, |v'\rangle \, \langle v'| \, e^{-\mathrm{i}(\mathbf{q}+\mathbf{G}')\cdot\mathbf{r}'} \, |v\rangle \right]$$
$$+\mathrm{i}(\mathbf{q}+\mathbf{G}) \left[\sum_v \langle v| \, e^{\mathrm{i}(\mathbf{q}+\mathbf{G})\cdot\mathbf{r}} \nabla e^{-\mathrm{i}(\mathbf{q}+\mathbf{G}')\cdot\mathbf{r}} \, |v\rangle - \sum_{vv'} \langle v| \, e^{\mathrm{i}(\mathbf{q}+\mathbf{G})\cdot\mathbf{r}} \nabla \, |v'\rangle \, \langle v'| \, e^{-\mathrm{i}(\mathbf{q}+\mathbf{G}')\cdot\mathbf{r}'} \, |v\rangle \right] \tag{8.52}$$

evaluating the derivative in the second term of Eq. 8.52:

$$\Omega_\nabla^{\mathrm{R}} = -\frac{(\mathbf{q}+\mathbf{G})^2}{2} \left[\sum_v \langle v| \, e^{\mathrm{i}(\mathbf{G}-\mathbf{G}')\cdot\mathbf{r}} \, |v\rangle - \sum_{vv'} \langle v| \, e^{\mathrm{i}(\mathbf{q}+\mathbf{G})\cdot\mathbf{r}} \, |v'\rangle \, \langle v'| \, e^{-\mathrm{i}(\mathbf{q}+\mathbf{G}')\cdot\mathbf{r}'} \, |v\rangle \right]$$
$$+\mathrm{i}(\mathbf{q}+\mathbf{G}) \sum_v \langle v| \, e^{\mathrm{i}(\mathbf{G}-\mathbf{G}')\cdot\mathbf{r}} \nabla \, |v\rangle + (\mathbf{q}+\mathbf{G})(\mathbf{q}+\mathbf{G}') \sum_v \langle v| \, e^{\mathrm{i}(\mathbf{G}-\mathbf{G}')\cdot\mathbf{r}} \, |v\rangle \tag{8.53}$$
$$-\mathrm{i}(\mathbf{q}+\mathbf{G}) \sum_{vv'} \langle v| \, e^{\mathrm{i}(\mathbf{q}+\mathbf{G})\cdot\mathbf{r}} \nabla \, |v'\rangle \, \langle v'| \, e^{-\mathrm{i}(\mathbf{q}+\mathbf{G}')\cdot\mathbf{r}'} \, |v\rangle$$

Eq. 8.53 contains different elements: First, $\tilde{\rho}_{vv'}(\mathbf{q}+\mathbf{G})$ and $\tilde{\rho}_{vv'}^*(\mathbf{q}+\mathbf{G}')$. Their structure resemble the matrix elements of $\chi_{\mathbf{G}\mathbf{G}'}^{0,\mathrm{R}}$ (Eq. 8.9). Second, a new density-like term $\tilde{\rho}_{vv}(\mathbf{G}-\mathbf{G}')$, and third, two more quantities which involve the derivative of the wave functions $|v, \mathbf{k}-\mathbf{q}\rangle$ and $|v', \mathbf{k}\rangle$. Due to a similar use of the commutator, these terms can also be found in Eq. 13, 14 and 16 of Ref. [129] in terms of the independent-particle one-body reduced density matrix. Indeed, we can write Eq. 8.53 as:

$$\Omega_\nabla^{\mathrm{R}} = -\frac{(\mathbf{q}+\mathbf{G})^2}{2} \left[\int \mathrm{d}\mathbf{r} \, e^{\mathrm{i}(\mathbf{G}-\mathbf{G}')\cdot\mathbf{r}} \rho(\mathbf{r}) - \int \mathrm{d}\mathbf{r}\mathrm{d}\mathbf{r}' \, e^{\mathrm{i}(\mathbf{q}+\mathbf{G})\cdot\mathbf{r}} e^{-\mathrm{i}(\mathbf{q}+\mathbf{G}')\cdot\mathbf{r}'} |\rho(\mathbf{r},\mathbf{r}')|^2 \right]$$
$$+\mathrm{i}(\mathbf{q}+\mathbf{G}) \int \mathrm{d}\mathbf{r} \, e^{\mathrm{i}(\mathbf{G}-\mathbf{G}')\mathbf{r}} \left(\nabla_{\mathbf{r}'} \rho(\mathbf{r}',\mathbf{r}) \right)_{\mathbf{r}'\to\mathbf{r}}$$
$$-\mathrm{i}(\mathbf{q}+\mathbf{G}) \int\int \mathrm{d}\mathbf{r} \, \mathrm{d}\mathbf{r}' \, e^{\mathrm{i}(\mathbf{q}+\mathbf{G})\mathbf{r}} e^{\mathrm{i}(\mathbf{q}+\mathbf{G}')\mathbf{r}'} \rho(\mathbf{r}',\mathbf{r}) \, \nabla_{\mathbf{r}} \rho(\mathbf{r}',\mathbf{r}) \tag{8.54}$$
$$+(\mathbf{q}+\mathbf{G})(\mathbf{q}+\mathbf{G}') \int \mathrm{d}\mathbf{r} \, e^{\mathrm{i}(\mathbf{G}-\mathbf{G}')\cdot\mathbf{r}} \rho(\mathbf{r})$$

Regarding the static potential $\hat{\mathcal{V}}_l$, we can assume a potential of the form $\hat{\mathcal{V}} = \hat{\mathcal{V}}_l + \hat{\mathcal{V}}_{nl}$ (local and non-local):

---

[8]The "1" in the closure relation is translates as $\delta(\mathbf{r}-\mathbf{r}')$ within the integral.

$$\Omega_{\hat{\mathscr{V}}}^{\mathrm{R}} = \sum_{vc} \langle v| \left[e^{\mathrm{i}(\mathbf{q}+\mathbf{G})\cdot\mathbf{r}}, \hat{\mathscr{V}} \right] |c\rangle \, \tilde{\rho}_{vc}^{*}$$

$$= \sum_{vc} \langle v| \left[e^{\mathrm{i}(\mathbf{q}+\mathbf{G})\cdot\mathbf{r}}, \hat{\mathscr{V}}_{l} \right] |c\rangle \, \tilde{\rho}_{vc}^{*} + \sum_{vc} \langle v| \left[e^{\mathrm{i}(\mathbf{q}+\mathbf{G})\cdot\mathbf{r}}, \hat{\mathscr{V}}_{nl} \right] |c\rangle \, \tilde{\rho}_{vc}^{*} \tag{8.55}$$

The operator $\left[e^{\mathrm{i}(\mathbf{q}+\mathbf{G})\cdot\mathbf{r}} \right]$ is a local potential, *i. e.*, it is a diagonal matrix. Therefore commutes with $\hat{\mathscr{V}}_{l}$: $\left[e^{\mathrm{i}(\mathbf{q}+\mathbf{G})\cdot\mathbf{r}}, \hat{\mathscr{V}}_{l} \right] = 0$. Thus, for local potentials, $\Delta^{\mathrm{R},(1)}$ is obtained by simply dividing Eq. 8.54 by Eq. 8.44. In terms of the one-body reduced density matrix we obtain:

$$\Delta_{l}^{\mathrm{R},(1)} = -\frac{(\mathbf{q}+\mathbf{G})^2}{2}$$

$$+\mathrm{i}(\mathbf{q}+\mathbf{G}) \frac{\int \mathrm{d}\mathbf{r}\, e^{\mathrm{i}(\mathbf{G}-\mathbf{G}')\mathbf{r}} \left(\nabla_{\mathbf{r}'} \rho(\mathbf{r}',\mathbf{r}) \right)_{\mathbf{r}'\to\mathbf{r}} - \int\int \mathrm{d}\mathbf{r}\,\mathrm{d}\mathbf{r}'\, e^{\mathrm{i}(\mathbf{q}+\mathbf{G})\mathbf{r}}\, e^{\mathrm{i}(\mathbf{q}+\mathbf{G}')\mathbf{r}'}\rho(\mathbf{r}',\mathbf{r})\, \nabla_{\mathbf{r}}\rho(\mathbf{r}',\mathbf{r})}{\left[\int \mathrm{d}\mathbf{r}\, e^{\mathrm{i}(\mathbf{G}-\mathbf{G}')\cdot\mathbf{r}}\rho(\mathbf{r}) - \int \mathrm{d}\mathbf{r}\mathrm{d}\mathbf{r}'\, e^{\mathrm{i}(\mathbf{q}+\mathbf{G})\cdot\mathbf{r}}e^{-\mathrm{i}(\mathbf{q}+\mathbf{G}')\cdot\mathbf{r}'}|\rho(\mathbf{r},\mathbf{r}')|^2 \right]}$$

$$+(\mathbf{q}+\mathbf{G})(\mathbf{q}+\mathbf{G}') \frac{\int \mathrm{d}\mathbf{r}\, e^{\mathrm{i}(\mathbf{G}-\mathbf{G}')\cdot\mathbf{r}}\rho(\mathbf{r})}{\left[\int \mathrm{d}\mathbf{r}\, e^{\mathrm{i}(\mathbf{G}-\mathbf{G}')\cdot\mathbf{r}}\rho(\mathbf{r}) - \int \mathrm{d}\mathbf{r}\mathrm{d}\mathbf{r}'\, e^{\mathrm{i}(\mathbf{q}+\mathbf{G})\cdot\mathbf{r}}e^{-\mathrm{i}(\mathbf{q}+\mathbf{G}')\cdot\mathbf{r}'}|\rho(\mathbf{r},\mathbf{r}')|^2 \right]} \tag{8.56}$$

This equation (Eq. 8.56) is similar to the one obtained by Berger *et al*, in Ref. [129] (Eq. 21). The main difference comes from the evaluation of the commutator in $\mathbf{r}'$ in Ref. [129] (and the symmetrization). Moreover, as explained in Ref. [128], Eq. 8.56 can be generalized for non-local potentials by evaluating explicitly the commutator with the non-local part (the last term in Eq. 8.55), such that $\Delta^{\mathrm{R},(1)} = \Delta_{l}^{\mathrm{R},(1)} + \Delta_{nl}^{\mathrm{R},(1)}$ (an explicit expression for $\Delta^{\mathrm{R},(1)}$ can be found in Appendix IV).

Finally, let us point out the structure of Eq. 8.56, in particular the prefactors in the first and last term: $[-\frac{1}{2}(\mathbf{q}+\mathbf{G})]$ and $[+(\mathbf{q}+\mathbf{G})(\mathbf{q}+\mathbf{G}')]$. In the case of a diagonal matrix, $\mathbf{G} = \mathbf{G}'$ these terms together evolve $\propto [\frac{1}{2}(\mathbf{q}+\mathbf{G})]$ (weighted by the one-body reduced density matrix elements in the last term of Eq. 8.56). This is interesting because we can relate it to the energy of a plane wave in the long $\mathbf{q}$ range as we pointed out in Fig. 8.6. Clearly from Fig. 8.6 the term $[\frac{1}{2}(\mathbf{q}+\mathbf{G})]$ is dominant between $\mathbf{q} = (2,0,0)$ and $(3.5,0,0)$ for the calculation with 500 bands. We can also see that the matrix elements play an important role in shaping $\Delta^{\mathrm{R,(exact)}}$, or in the case of Eq. 8.56: the linear term in $[\mathbf{q}+\mathbf{G}]$ and all the one-body reduced density matrix ingredients.

Summary

In this last part, a proof of concept, we applied the closure relation to the matrix elements of silicon, and we showed that with only the valence states (4 in Si) we can account for the contribution of up to 500 bands (496 empty states). This shows that writing the static response as a function of the one-body reduced density matrix is a promising and efficient way to calculate the evolution of the static response for semiconductors as a function of wavevector. Thus we developed $\Delta^{\mathrm{R},(1)}$ as a function of the independent-particle one-body reduced density matrix.

It is worth mentioning that there are different research directions that can be continued from our development of the approximation of the static response: For instance, 1) the

expression and calculation of the static response of a semiconductor (Si for example), completely as a function of the one-body reduced density matrix. 2) The development of a precise method for $\Delta^{\mathrm{R},(2)}\left(\Delta^{\mathrm{R},(1)}\right)$, parameter-free, in particular for the shorter $\mathbf{q}$'s when $\Delta^{\mathrm{R},(1)}$ becomes small and thus $\Delta^{\mathrm{R},(2)}\left(\Delta^{\mathrm{R},(1)}\right)$ diverges. And 3) the in-depth investigation of $\tilde{\Delta}^{\mathrm{R},(3)}$, for example, parameter-free with $\delta = \Delta^{\mathrm{R},(1)}$.

Code availability

All the calculations in this section (except the Si band structure of Fig. 8.2) were obtained with the DP code [135]. All the approximations, from the simple Taylor expansion to $\Delta^{\mathrm{R},(1)}$, $\Delta^{\mathrm{R},(2)}$ and $\tilde{\Delta}^{\mathrm{R},(3)}$, $\tilde{\chi}^{0,\mathrm{R}}_{\mathbf{GG}'}$ and the closure relation for the matrix elements were implemented in the DP code [135] in the framework of this thesis within `creation_chi0_accel_Delta.F90` .

Overview of the density response

From the beginning of this project the aim was to investigate how the atomic structure affects the response of the material to a given perturbation. For instance, section 6 was centered around the idea of investigating the dielectric properties of the different polymorphs, showing a clear connection between the electronic structure and, for example, optical absorption. In this section we show, as a proof of concept, the computation of the induced density (Eq. 2.15) in real space and time calculated from the SRden code.

9.1 The SRden code

Upon a time-dependent external perturbation of a medium, a borophene polymorph for example, the latter "reacts" in some way according to the perturbation: for instance, when light is sent to the sample it interacts with the medium and promotes electrons from the valence to the occupied states, leading to a difference between the incoming and outgoing beams, and yielding, for example, the absorbance spectra as shown in Section. 6.2. This process gives information of the sample which can be linked directly to its electronic structure, nonetheless it still remains very complicated to determine what is the actual response of the system to the external perturbation. In linear response (Section 2.2) this takes the name of the induced density, $\delta n(\mathbf{r}, t)$ (Eq. 2.15), which in reciprocal space reads:

$$\delta n(\mathbf{r}, t) = \int d\mathbf{q} \int d\omega \sum_{\mathbf{G}, \mathbf{G}'} e^{i((\mathbf{q}+\mathbf{G})\cdot\mathbf{r}-\omega t)} \chi_{\mathbf{G}\mathbf{G}'}(\mathbf{q}, \omega) V_{\mathbf{G}'}^{ext}(\mathbf{q}, \omega) \qquad (9.1)$$

Eq. 9.1 is very simple, and only two ingredients are needed: 1) the polarizability which contains the information of the electronic system, and 2) the external perturbation. These two pieces are independent of each other, thus for a system of interest one could calculate the polarizability only once, store it, and use it for different external potentials. Moreover in Eq. 9.1 $V_{\mathbf{G}'}^{ext}(\mathbf{q}, \omega)$ dictates which parts of the polarizability are "activated": for example, in the simple case of a plane wave-like perturbation with $\mathbf{q} = \mathbf{q}_0$, and $\omega = \omega_0$, Eq. 9.1 is reduced to only the sum over $\mathbf{G}\mathbf{G}'$, thus $\delta n(\mathbf{r}, t)$ can be completely determined with $\chi_{\mathbf{G}\mathbf{G}'}(\mathbf{q}_0, \omega_0)$. Inverting this idea, the effect of an external potential can be simulated by selected values of $\chi_{\mathbf{G}\mathbf{G}'}(\mathbf{q}, \omega)$. This simple equation is used in the SRden code to compute the density response from Eq. 9.1 (details on this tool can be found in Ref. [136] and Appendix IV).

The external potential

We are interesting in visualizing what is the effect of the atomic structure in the induced density. For this, it is convenient to consider a δ-like perturbation in real space and time, such that after the initial[1] "kick" the induced density can evolve freely without any significant effect due to the external potential. In this case $V^{ext}(\mathbf{r}, t)$ is modeled as:

$$V^{ext}(\mathbf{r}, t) = \frac{1}{(2\pi)^4} \sum_{\mathbf{G}} \int d\omega \int d\mathbf{q}\ e^{i(\mathbf{q}+\mathbf{G})\cdot\mathbf{r}+i\omega t} \tag{9.2}$$

which translates in having to know $\chi_{\mathbf{G}\mathbf{G}'}(\mathbf{q}, \omega)$ for an *a priori*, infinite set of $\mathbf{G}$'s, $\mathbf{q}$'s and ω's to localize the external perturbation. This is of course not a viable process and the number of ingredients to compute Eq. 9.1 needs to be delimited within a finite range, hence compromising the localization. For illustration, we show in Fig. 9.1 $V^{ext}(\mathbf{r}, t)$ for a minimal set of ω, $\Delta\omega$, $\mathbf{G}$'s and $\mathbf{q}$'s calculated for borophene δ_3[2].

The first challenge in these calculations is to determine the "convergence" of the localization. One can define it based on a given phenomenon that wants to observe: for example, solving Eq. 9.1 with a given potential yields the evolution of the density, and as we mentioned earlier, we want the external potential to be sufficiently localized in space and time such that after the initial "kick" it does not contribute anymore to the induced density. Another relevant parameter to determine localization in-space can be with respect to the dimension of the unit cell: in this regard notice from Fig. 9.1 that using 250 $\mathbf{G}$-vectors localizes the maximum within 2 Å, while the lattice parameters of δ_3 are $a = b = 2.91$ Å. It is clear that, with respect to the unit cell, the localization of the potential with $\mathbf{G}$ vectors is "unconverged". Again, this depends on the phenomenon to be observed: while the perturbation of Fig. 9.1 does not allow to the details within the unit cell it can show the overall evolution of the density after the perturbation.

The challenges to localize this perturbation using this methodology are not minor. To-date, $\chi_{\mathbf{G}\mathbf{G}'}(\mathbf{q}, \omega)$ is computed as in Eq. 2.20, and the induced density with Eq. 9.1. Thus, obtaining a sufficiently well localized perturbation (in space and time) requires a huge amount of calculations. For instance, from the best parameters of Fig. 9.1: $\Delta\omega = 0.05$ eV, $\omega_{max} = 30$ eV, a $8 \times 8 \times 1$ $\mathbf{q}$-mesh (24 $\mathbf{q}$-points after reducing by symmetry), and 250 $\mathbf{G}$-vectors: 24 independent calculations of Eq. 2.20, with at 600 frequencies for the $\chi_{\mathbf{G}\mathbf{G}'}$ matrices with dimensions 250×250, and which depend implicitly on the sum over $\mathbf{k}$-points[3]. Without much gain between 100 and 200 $\mathbf{G}$-vectors, and limited in computational memory to larger matrix dimensions, we explored the induced density of this polymorph with only 100 $\mathbf{G}$'s.

---

[1] $\delta n(\mathbf{r}, t)$ calculated from Eq. 9.1 yields a periodic perturbation. The "replicas" need to be sufficiently separated such that nor the external potential nor the induced density from each of them overlaps with the neighboring ones. Within this condition we refer to the "initial kick" to any of the periodic perturbations in space and time.

[2] The external potential does not depend on the system but it is constructed from the information in $\chi_{\mathbf{G}\mathbf{G}'}(\mathbf{q}, \omega)$ of the system.

[3] For the induced-density calculations we used the same $\mathbf{k}$-mesh as for the optical absorption and loss function of Section 6.2: $32 \times 32 \times 1$ $\mathbf{k}$.
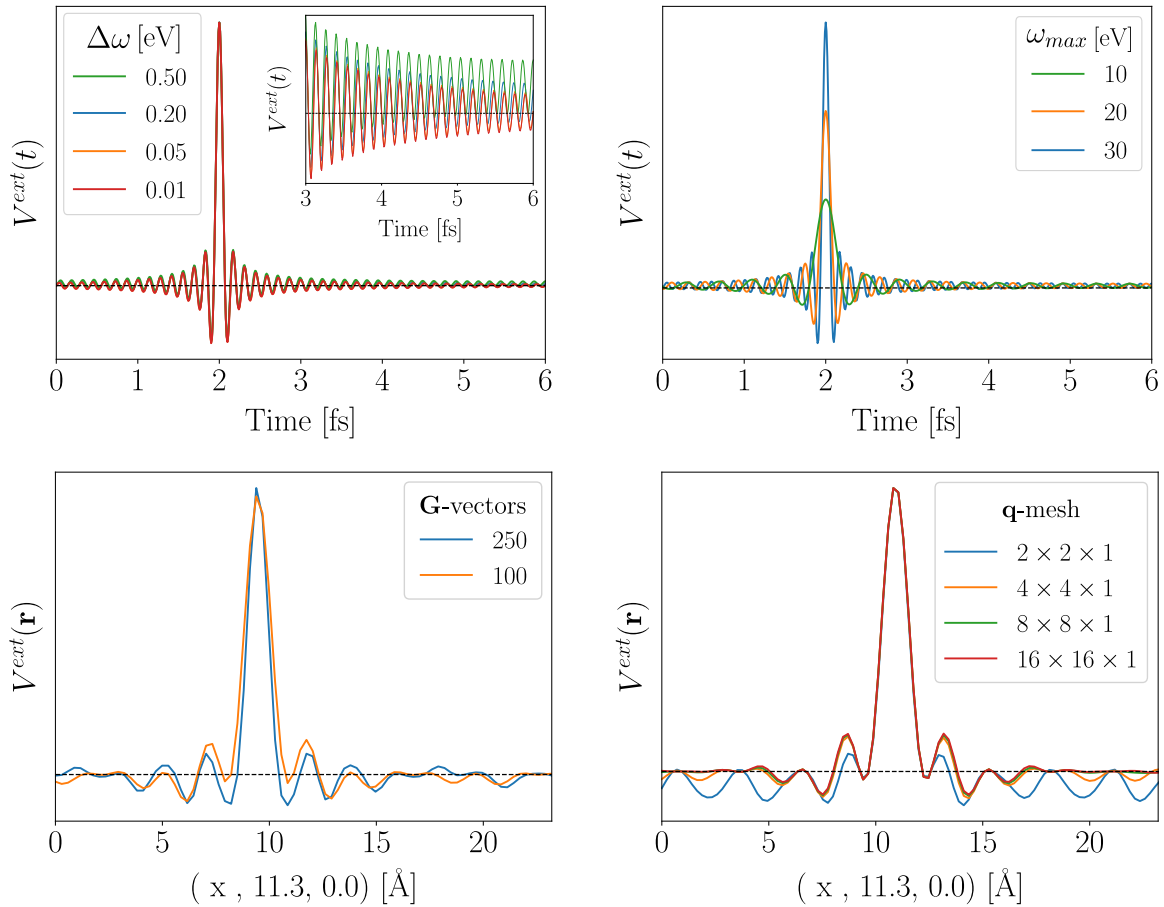
Figure 9.1: Localization of the external potential in space and time (Eq. 9.2) with different parameters: $\Delta\omega$ the frequency step for the sum over frequencies (upper left), ω_{max} the upper limit in frequencies (upper right), number of **G**-vectors for the localization in space (lower left) and **q**-mesh (lower right). From this, we can get the "best" parameters as $\Delta\omega = 0.05$ eV, $\omega = 30$ eV, $8 \times 8 \times 1$ **q**-mesh and 250 **G**-vectors. The localization in space with the **G**-vectors clearly is not as sharp as with the frequencies: this is the major problem in the calculations of the induced density, as increasing the **G**-vectors leads to very memory-intensive calculations.

The induced density

The second challenge on the induced density calculations is the interpretation of the results: Eq. 9.1 describes the overlap between the transitions and the perturbation, such that the higher the overlap the higher the presence of such transitions in the induced density. The evolution in time is given by the transitions "reacting" out-of-phase with respect to each other (see phase factor in Eq. 9.1) and summing up. How this occurs however, is not trivial, nor how the atomic structure affects the overall evolution of the induced density. To illustrate the complexity of the problem we show in Fig. 9.2 the snapshots of the density evolution in borophene δ_3 to the external potential determined with Eq. 9.1 using $\Delta\omega = 0.5$ eV, $\omega = 30$ eV, 100 **G**-vectors and a $8 \times 8 \times 1$ **q**-mesh calculated within the independent particles approximation. The animation of the induced density corresponding to Fig. 9.2 can be found in Ref. [137], and similar calculations for β_{12} and α_1 using SRden in Refs. [138, 139].

Overall the induced density in Fig. 9.2 and Refs. [137–139] has the expected behavior:
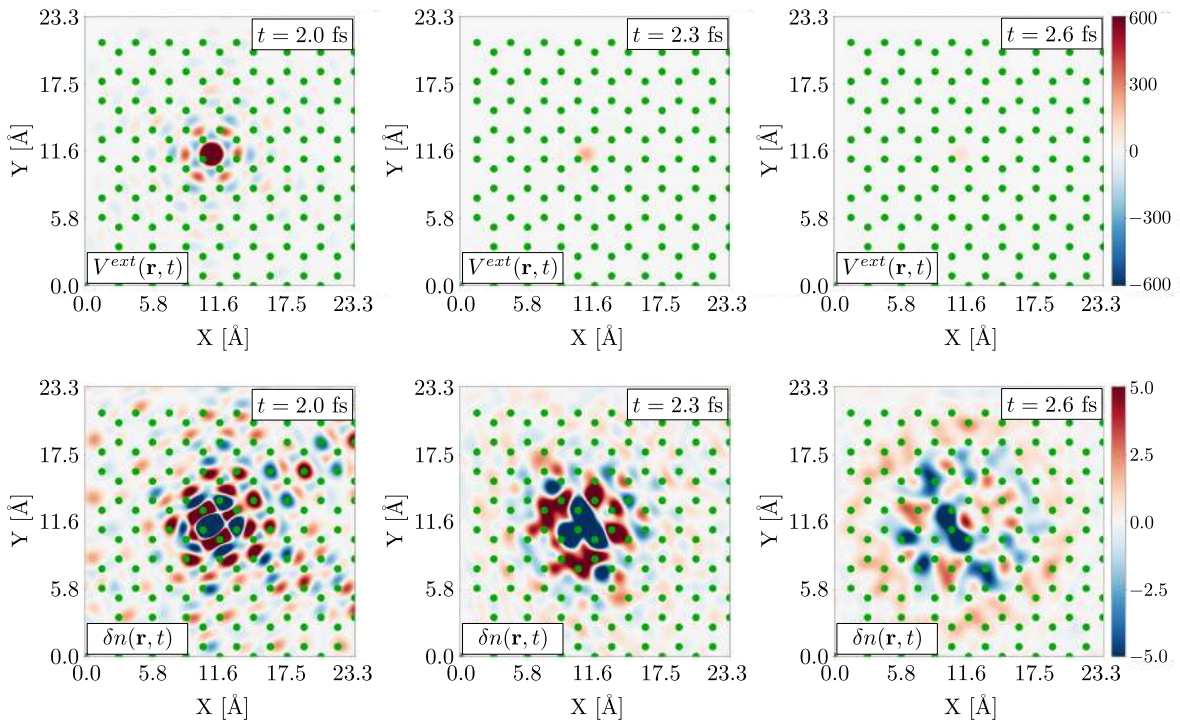
Figure 9.2: Snapshots of the external potential and the induced density in borophene δ_3 t the perturbation time (2 fs), and 0.3 and 0.6 fs later (atomic positions shown in green): upon the initial kick the induced density evolves moving further from the perturbation center following the structure of the polymorph. The corresponding animation can be found in Ref. [137].

it follows the initial perturbation with its maximum of intensity at the same point in space, and it occurs at a slightly later time. After that, the density seems to evolve independently of the external potential moving away from the perturbation center. It is worth highlighting that the induced density does not evolve trivially as concentric waves, in fact it seems to evolve along the bonds of the structure. Thus, it is interesting to investigate how the atomic structure influences this evolution: a natural step forward would be to use the gained knowledge about the similarities of the electronic structure and the defect-like states in the multiple polymorphs. A second step, the computation of the induced density with other approximations for χ in Eq. 9.1: for example χ^{RPA} with and without local fields to study the evolution of the plasmon along the structure.

9.2   Outlook

The visualization of the induced density as from Eq. 9.1, is a simple and qualitative way that can be used to study charge propagation: it requires from two simple ingredients, and moreover the main one, $\chi_{\mathbf{GG'}}(\mathbf{q}, \omega)$, that contains the information of the electronic system, can be stored and reused for any perturbation. However, as we presented above the methodology to-date presents some limitations, in particular the expensive calculations that need to be done in order localize the perturbation in space and time.

Therefore, it is almost compulsory to develop efficient methods for either the calculation of $\chi_{\mathbf{GG'}}(\mathbf{q}, \omega)$, such as the method in Section 8 for the static response, but also for
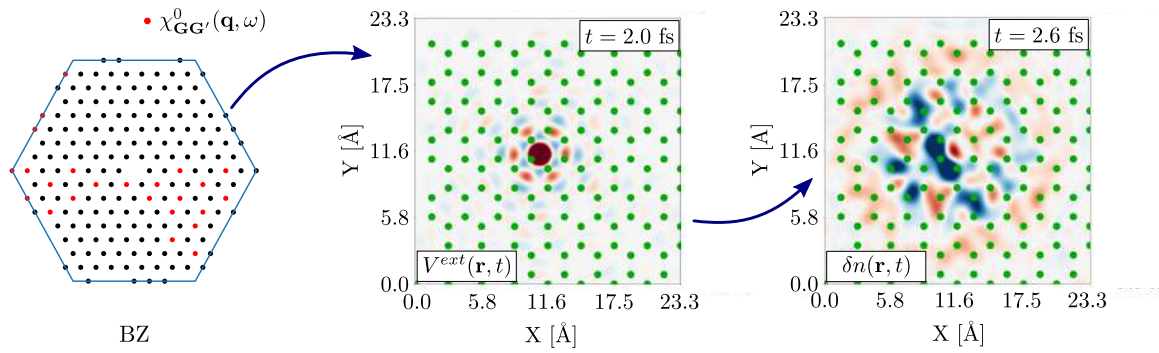
Figure 9.3: $8 \times 8 \times 1$ **q**-mesh represented within the BZ (left), external potential at the moment of the perturbation (center), and induced density 0.6 fs after the perturbation (right). Each red point in the **q**-mesh (24 in total) represents a calculation of $\chi^0_{\mathbf{GG}'}$ needed to build $V^{ext}(\mathbf{r}, t)$ localized in space (and time). By symmetry, the 24 calculations unfold into 192 (black points), yielding the "circular" localization of the external potential.

the induced density. For example, solving Eq. 9.1 in real space for localized perturbation could alleviate the problem of localizing the potential based on the large sum over the reciprocal lattice vectors, although at the expense of possibly large supercell calculations. Moreover, as we highlighted previously, there is also the need for understanding the physics behind the evolution of $\delta n(\mathbf{r}, t)$: the apparently simple behavior of the induced density shown in Fig. 9.2 and Ref. [137] seeming to evolve along the bonds is the result of all available transitions with energies between 0 and 30 eV, and 24 **q**-vectors all mixing in time with different phase factors (see Fig. 9.3).

Part III

Conclusions

Conclusions and outlook

Conclusions

The goal of this project was to study borophene as a prototypical class of 2D materials. In particular, the aim was to distinguish the properties which are general for all borophene structures from those which are polymorph-specific. To this aim we employed simple models that describe the general features of the electronic structure: the 2D HEG + "particle in a box", and the self-doping of parent structures. Moreover, upon further inspection of the electronic structure, we described polymorph-specific states: these defect-like states appear in a parent borophene electronic structure, are low-dispersive, and show the break down of simple approximations such as self-doping. We applied our understanding of the general and polymorph-specific features of the electronic structure of borophene to the characterization of the dielectric properties of this class of materials: optical absorption, loss function and the static response. Moreover, using our results from the static response, we linked the description of the electronic problem to structural instabilities.

The phonon dynamical matrix can be formulated explicitly in terms of the inverse dielectric function. This historical expression is usually not used in ab-initio calculations since it is computationally expensive. However, it is interesting for analysis. This was one of our motivations to complement our study by developing a new method that allows to approximate the static response in an efficient manner, only as a function of the one-body reduced density matrix. Below we summarize the outcomes of this project:

In order to describe the relation between atomic structure and the electronic response, we first studied the relation between the atomic structure and the electronic structure. Thus, for a set of selected polymorphs including flat monolayers (B_T, δ_3, α_1, δ_5, β_{12}), buckled monolayers (δ_6, α') and a bilayer (α'-Bilayer), we performed a detailed study of their electronic structure. Our study pointed out to similar electronic band structures among different polymorphs. Moreover, we observed that the electronic band structures of these polymorphs had a resemblance with the 2D homogeneous electron gas. Thus, we developed a simple model based on the 2D HEG and the "particle in a box" problem from quantum mechanics, to describe borophene polymorphs as a confined gas of electrons. This "*Box*" model gives a qualitative description of the electronic structure provided that one knows simple parameters from ab-initio calculations.

We identified the appearance of polymorph-specific states that break the self-doping picture. We refer to these states, related to the rigid electronic structure, as defect-like states. Indeed, the defect-like states are low-dispersive, and our analysis of the partial density showed that the partial charge is localized around polymorph-specific features of the atomic structure. Moreover, we showed that the atomic displacements out-of-plane have an important effect in tuning the electronic structure breaking degeneracies and inducing important changes in the occupation of specific bands. Thus, we proved that

buckling can be used as a tuning parameter to change and induce exotic properties into the polymorphs, such as semimetallicity in α' and nesting of the Fermi surface in δ_6.

Then, we performed a detailed study of the optical properties of the selected polymorphs. We identified general features: low-energy in-plane absorption peaks (~ 1 eV), and high-energy (~ 10 eV) out-of-plane absorption peaks. Nonetheless the study of the optical properties put in evidence the importance of the defect-like states: besides the low- and high-energy peaks, the spectrum in-between is different for every polymorph. Moreover, we identified the appearance of transitionless windows due to specific transitions $t(p_\| \rightarrow p_z)$ being killed by the symmetry of the wave functions in the density-density response. Thus, these windows have a well-defined nature. We proved theoretically the these windows can be modulated to induce transparency in borophene under charge-doping conditions. Together with our fundamental studies of the dielectric properties, we also presented calculated quantities like EELS and absorbance that can be used for comparison to experimental results, and that may be important for applications.

With our calculations of the static response we illustrated the link between the electronic system and structural instabilities: we showed that we can find signatures of anomalies in the static polarizability at the points of Kohn anomalies reported in the literature. The static response is a computationally expensive quantity and it is rarely reported although it can be of use for the discussion of Kohn anomalies and charge density waves. Thus, we reported the static response of borophene δ_6, δ_3, β_{12} and the model system B_T.

Following the last point, we developed an approximation to compute the static response in a more efficient manner without the need of conduction states, hence reducing significantly the computational cost for the evaluation of this quantity. Our approximation is parameter-free and it can be written in terms of the independent-particle one-body reduced density matrix. Moreover, upon the addition of few conduction states the result is significantly improved. The numerical implementation allows us to calculate the static response also for metallic systems and to include explicitly the polymorph-specific information of the Fermi surface.

Outlook

This project can continue in different directions: First, in borophene with the investigation of more complex structures, such as, the borophene α_1 with a large hole. This structure is essentially a single polymorph with variable vacancy ratio, and therefore, a single polymorph with tunable properties.

Another interesting aspect worth investigating is the link between the static response and the phonon frequencies, and in particular how the elements of the static dielectric function sum up to yield the phonon spectra. This can be done, for example, in combination with the method developed in this work for evaluating efficiently the static response.

Moreover, regarding the efficient calculation of the static response, the implementation of the full expression of the static response as a functional of the single-particle one-body reduced density matrix in the ab-initio code remains to be completed and made freely available. Moreover, the approximation has to be improved in linear regime of small $\mathbf{q}$'s.

Lastly, the charge density dynamics are still an open question. A first take on this subject, from the developments in this work, could be to focus on the static response. Already at this level we could gain some understanding about the role of the atomic and electronic structure in the response of the density, or in other words, how the general

and the defect-like states of the borophene polymorphs change the picture of the density response. Our formulation of the static response in terms of the single-particle one-body reduced density matrix may open the way to interpret the density response by establishing a direct link to the structure of the material.

Part IV

Appendices

Appendix A

Borophene electronic structures

B_T

We have built this structure based on the bond distances of δ_6 (1.68 and 1.80 Å). We noticed that although the choice has a strong impact on the band width of the electronic structure of B_T (Fig. 9.4), the overall shape of the individual bands is maintained, as well as their crossings of the Fermi energy. For its comparison with other polymorphs, we chose the B_T structure with 1.68 Å bond distance.
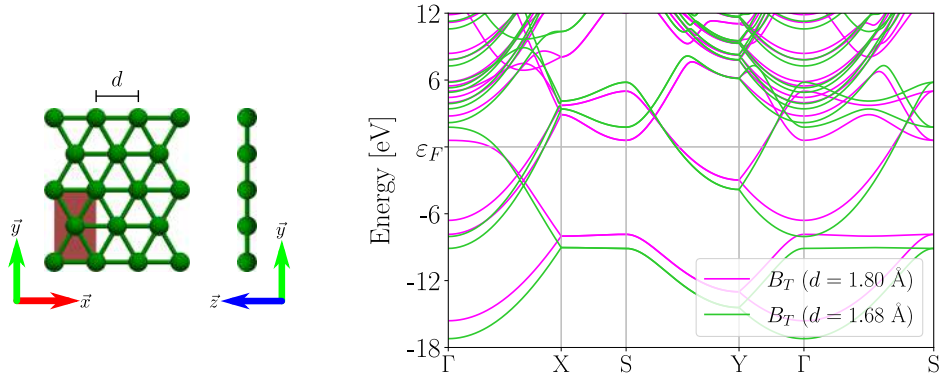

Figure 9.4: Electronic band structure of the model system B_T with two different bond distances. Besides a slight change of band width, the electronic bands mantain their shape and crossing of the Fermi energy.

α'

In terms of formation energy and electronic stability one of the most investigated structures is the planar α polymorph [14, 15, 45, 57]. This was, however, found to be unstable and it was predicted to show a slight distortion out-of-plane. The resulting polymorph was called α' [16]. The unit cell of this polymorph has symmetry *P-3m1*, with 8 atoms at the positions *6g* and *2d*. In this case, the atomic positions and lattice parameters were optimized in the present work, and the lattice parameters were found to be: $a = b = 5.058$ Å, with the off-plane displacement of the two atoms by ±0.085 Å. The optimized structure is in contrast with Refs. [16, 59]. In Ref. [16], $a = 5.046$ and $b = 5.044$ Å (DFT-PBE) with buckling distance of ±0.17 Å (atomic positions optimized with PBE0 on top of the PBE-optimized lattice parameter structure), while in Ref. [59] $a = b = 5.10$ Å with the off-plane displacement of ±0.14 Å (DFT-PBE).
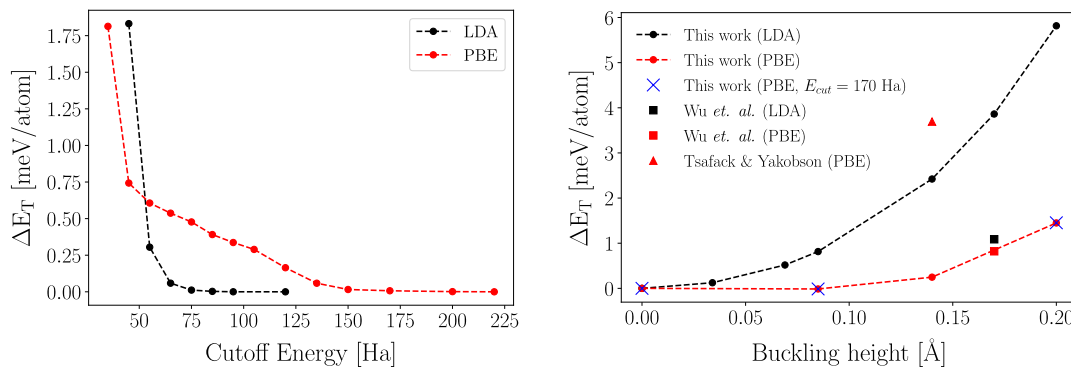
Figure 9.5: (Left) Cutoff energy convergence of α' ($\wedge = 0.085$ Å) with LDA and PBE: with $E_{cut} = 75$ Ha the total energy per atom is converged within 15 μeV/atom within the LDA, while for PBE only under 0.5 meV/atom. With $E_{cut} = 170$ Ha the convergence with PBE is achieved under 10 μeV/atom. (Right) Potential energy surface of α' with buckling: within the LDA the lowest energy configuration is the flat α structure. Using PBE the lowest energy configuration was α' ($\wedge = 0.085$ Å), only 13 μeV/atom lower than its flat counterpart.

In view of the difference between our calculated atomic structure and those of Refs. [16, 59], we explored the potential energy surface (PES) at difference buckling heights ($\wedge$). We maintained the optimized lattice parameters fixed ($a = b = 5.058$ Å) as well as the atomic positions, except for the two "buckling" atoms (at positions $2d$) which we displaced off-plane by the same distance in opposite directions (the coordinates in-plane for these atoms are also maintained). We observed that, within the LDA, the lowest energy configuration belongs to the flat α structure, and from $\wedge = 0.00$ Å to $\wedge = 0.20$ Å the PES evolves smoothly increasing its total energy (E_T) as the buckling height is increased (Fig. 9.5). Using PBE, the lowest-energy configuration was found to be $\wedge = 0.085$ Å, as expected from the structural optimization.

In the exploration of the PES (Fig. 9.5) we included the computed energies obtained from approximated structures to those of Wu *et. al.*, ($a = 5.046$, $b = 5.044$, $\wedge = 0.17$ Å) [16], and Tsafack and Yakobson ($a = b = 5.10$, $\wedge = 0.14$ Å) [59][4]. The structure from Tsafack and Yakobson (Ref. [59]) lead to the highest energies in both, DFT-LDA and PBE, presumably do to the longer lattice parameters ($a = b = 5.10$). The structure from Wu *et. al.*, [16], follows the same trend with respect to buckling as our calculations using PBE. Surprisingly, within the LDA, the change of lattice parameters from $a = b = 5.058$ Å to $a = 5.046$, $b = 5.044$ lowers the energy by ≈ 2.8 meV/atom with respect to our structure with $\wedge = 0.17$ Å.

Using the PBE exchange-correlation functional the differences in energies with respect to the flat configuration are, in general, smaller than within the LDA. However, we must bring attention to the numerical difficulties using this functional (Fig. 9.5): while $E_{cut} = 75$ Ha converges the LDA-calculated total energy within 15 μeV/atom, for PBE the convergence is in the order of 1 meV/atom. This is a very important difference concerning the PES, as the structures with $\wedge = 0.00$, 0.085 and 0.14, as well as the one from Wu *et. al.* (Ref. [16]) lie within this window. Increasing the cutoff energy for the PBE calculation gives a very slow evolution of E_T, which prevents us (in terms of CPU time and memory)

---

[4]To approximate the structures from Refs. [16, 59] we used the same reduced coordinates (relative to the lattice parameters) as found through our structural relaxation, changing $\wedge$ to their reported values.
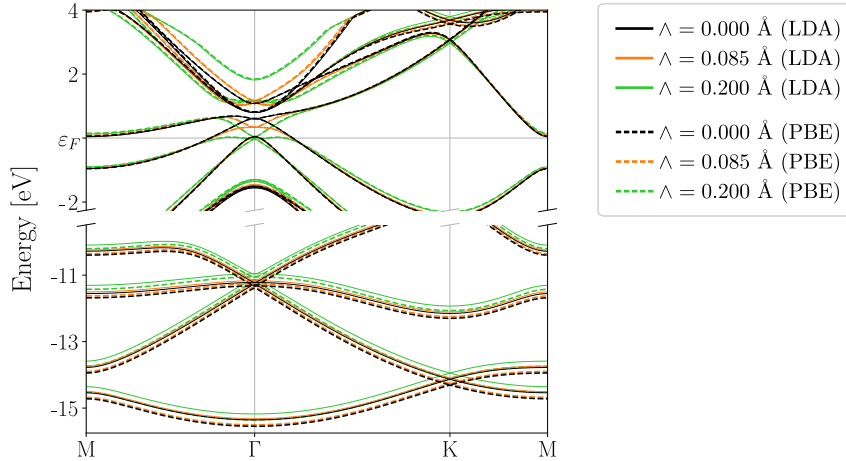
Figure 9.6: Electronic band structure of α' calculated at different buckling heights with the LDA and PBE. Overall, the characteristics of the band spectra for the different buckling configurations are maintained by using both functionals. The major changes occur upon buckling at Γ and near the Fermi energy.

from a more stringent calculation during the structural relaxation. In view of this, we delimited the problem to only the buckling height, we computed the total energy of α ($\wedge = 0.000$ Å), and α' with $\wedge = 0.085$ Å and 0.200 with $E_{cut} = 170$ Ha (converging E_T within 10 μeV/atom). We found minimal differences among the computed energies with $E_{cut} = 70$ Ha, and, in particular, we highlight that the lowest energy configuration was α' ($\wedge = 0.085$ Å), ~ 13 μeV/atom lower than α ($\wedge = 0.000$ Å).

The flatness of the PES imposes a challenge in the search for the "true" ground state of this polymorph. And we must remark that, among the computed configurations, different minima were found using different functionals: α ($\wedge = 0.000$ Å) within the LDA, α' ($\wedge = 0.085$ Å) using PBE, and not to forget the structure from Wu *et. al.*, ($a = 5.046$, $b = 5.044$, $\wedge = 0.170$ Å) using PBE + PBE0. In order to circumvent this problem we computed the KS band structure for different buckling heights using the LDA and PBE, and we observed that regardless of the difference in the evolution of the total energy using these functionals, the computed electronic bands showed minimal differences. So as the difficulty of finding the true minimum in the PES do not influence the discussion of our results based primarily on the electronic structure, we continue it using our own optimized atomic structure (buckling height = 0.085 Å).

Appendix B

Building $\tilde{\rho}$ via Fourier transform.

A basic Equation along this work is the one-particle polarizability, χ^0, in reciprocal space (Eq. 2.20) with ingredients $\tilde{\rho}_{n'n}(\mathbf{q}+\mathbf{G}) \equiv \langle n', \mathbf{k}' | e^{i(\mathbf{q}+\mathbf{G})\cdot\mathbf{r}} | n, \mathbf{k} \rangle$. It is worth showing how these quantities are built, in particular for the relation between $\mathbf{k}$ and $\mathbf{k}'$. In real space, expanded in plane waves, the wave functions $\phi_{\mathbf{k}}^n(\mathbf{r})$ and $\phi_{\mathbf{k}'}^{n'*}(\mathbf{r})$ read:

$$\psi_{\mathbf{k}}^n(\mathbf{r}) = u_{\mathbf{k}}^n(\mathbf{r})e^{i\mathbf{k}\cdot\mathbf{r}} = \sum_{\tilde{\mathbf{G}}} C_{\mathbf{k}}^n(\tilde{\mathbf{G}})e^{i\mathbf{k}\cdot\mathbf{r}}e^{i\tilde{\mathbf{G}}\cdot\mathbf{r}} \tag{9.3}$$

$$\phi_{\mathbf{k}'}^{n'*}(\mathbf{r}) = u_{\mathbf{k}'}^{n'*}(\mathbf{r})e^{-i\mathbf{k}'\cdot\mathbf{r}} = \sum_{\tilde{\tilde{\mathbf{G}}}} C_{\mathbf{k}'}^{n'*}(\tilde{\tilde{\mathbf{G}}})e^{-i\mathbf{k}'\cdot\mathbf{r}}e^{-i\tilde{\tilde{\mathbf{G}}}\cdot\mathbf{r}} \tag{9.4}$$

And from the product of the wave functions we can obtain $\tilde{\rho}_{n'n}(\mathbf{r})$ in real space:

$$\begin{aligned}
\tilde{\rho}_{n'n}(\mathbf{r}) = \phi_{\mathbf{k}'}^{n'*}(\mathbf{r})\phi_{\mathbf{k}}^n(\mathbf{r}) &= \sum_{\tilde{\tilde{\mathbf{G}}}} C_{\mathbf{k}'}^{n'*}(\tilde{\tilde{\mathbf{G}}})e^{-i\mathbf{k}'\cdot\mathbf{r}}e^{-i\tilde{\tilde{\mathbf{G}}}\cdot\mathbf{r}} \sum_{\tilde{\mathbf{G}}} C_{\mathbf{k}}^n(\tilde{\mathbf{G}})e^{i\mathbf{k}\cdot\mathbf{r}}e^{i\tilde{\mathbf{G}}\cdot\mathbf{r}} \\
&= \sum_{\tilde{\tilde{\mathbf{G}}}} C_{\mathbf{k}'}^{n'*}(\tilde{\tilde{\mathbf{G}}}) \sum_{\tilde{\mathbf{G}}} C_{\mathbf{k}}^n(\tilde{\mathbf{G}})e^{-i\mathbf{k}'\cdot\mathbf{r}}e^{-i\tilde{\tilde{\mathbf{G}}}\cdot\mathbf{r}}e^{i\mathbf{k}\cdot\mathbf{r}}e^{i\tilde{\mathbf{G}}\cdot\mathbf{r}} \\
&= \sum_{\tilde{\tilde{\mathbf{G}}}} C_{\mathbf{k}'}^{n'*}(\tilde{\tilde{\mathbf{G}}}) \sum_{\tilde{\mathbf{G}}} C_{\mathbf{k}}^n(\tilde{\mathbf{G}})e^{i(\mathbf{k}-\mathbf{k}')\cdot\mathbf{r}}e^{i(\tilde{\mathbf{G}}-\tilde{\tilde{\mathbf{G}}})\cdot\mathbf{r}}
\end{aligned} \tag{9.5}$$

And perform the Fourier transform to obtain $\tilde{\rho}_{n'n}(\mathbf{q}+\mathbf{G})$, *i. e.*, in reciprocal space:

$$\begin{aligned}
\tilde{\rho}_{n'n}(\mathbf{q}+\mathbf{G}) &= \sum_{\tilde{\tilde{\mathbf{G}}}} C_{\mathbf{k}'}^{n'*}(\tilde{\tilde{\mathbf{G}}}) \sum_{\tilde{\mathbf{G}}} C_{\mathbf{k}}^n(\tilde{\mathbf{G}}) \int d\mathbf{r} \, e^{i(\mathbf{k}-\mathbf{k}')\cdot\mathbf{r}}e^{i(\tilde{\mathbf{G}}-\tilde{\tilde{\mathbf{G}}})\cdot\mathbf{r}}e^{-i(\mathbf{q}+\mathbf{G})} \\
&= \sum_{\tilde{\tilde{\mathbf{G}}}} C_{\mathbf{k}'}^{n'*}(\tilde{\tilde{\mathbf{G}}}) \sum_{\tilde{\mathbf{G}}} C_{\mathbf{k}}^n(\tilde{\mathbf{G}})\delta(\mathbf{k}-\mathbf{k}'-\mathbf{q})\delta(\tilde{\mathbf{G}}-\tilde{\tilde{\mathbf{G}}}-\mathbf{G})
\end{aligned} \tag{9.6}$$

The latter yields a relation between $\mathbf{k}$ and $\mathbf{k}'$ such that the product of the wave function does not need to be done over all $\mathbf{k}$ and $\mathbf{k}'$, but only over $\mathbf{k}$ and $\mathbf{k}' = \mathbf{k} - \mathbf{q}$. Thus, Eq. 9.5 simplifies to:

$$\tilde{\rho}_{n'n}(\mathbf{r}) = \sum_{\tilde{\tilde{\mathbf{G}}}} C_{\mathbf{k}-\mathbf{q}}^{n'*}(\tilde{\tilde{\mathbf{G}}}) \sum_{\tilde{\mathbf{G}}} C_{\mathbf{k}}^n(\tilde{\mathbf{G}})e^{i\mathbf{q}\cdot\mathbf{r}}e^{i(\tilde{\mathbf{G}}-\tilde{\tilde{\mathbf{G}}})\cdot\mathbf{r}} = u_{\mathbf{k}-\mathbf{q}}^{n'*}(\mathbf{r})u_{\mathbf{k}}^n(\mathbf{r})e^{i\mathbf{q}\cdot\mathbf{r}} \tag{9.7}$$

Eq. 9.7 is convenient for illustrative purposes because, for example, the DP code [135] used in this work, is the "ingredient" that builds prior to the Fourier transform[5]:

$$\tilde{\rho}_{n'n}(\mathbf{q} + \mathbf{G}) = \int d\mathbf{r} \; u_{\mathbf{k}-\mathbf{q}}^{n'*}(\mathbf{r})u_{\mathbf{k}}^{n}(\mathbf{r})e^{-i\mathbf{G}\cdot\mathbf{r}} \tag{9.8}$$

It is important to notice that even though the construction of Eq. 9.8 is a very optimized process, the Fourier transform needs to be performed at every single transition. Therefore, the computational time for evaluating Eq. 2.20 easily increases with the number of bands and $\mathbf{k}$-points. The effect of the latter is evident on metallic systems which require from dense $\mathbf{k}$-meshes, and the effect of the number of bands in calculations that necessarily require from a large number of conduction states, for example in the computation of the static response.

---

[5]To be precise it only builds the product between the coefficients as the exponential vanishes upon the Fourier transform (Eq. 9.8).

Appendix C

Evaluation of the commutator in r'

In Section 8 we evaluated Eq. 8.42 with $w = 1$ using the commutator centered in **r**:

$$\Omega^{\mathrm{R}} = \sum_{vc} \langle v | \left[e^{\mathrm{i}(\mathbf{q}+\mathbf{G})\cdot\mathbf{r}}, \hat{\mathscr{H}} \right] | c \rangle \langle c | e^{-\mathrm{i}(\mathbf{q}+\mathbf{G}')\cdot\mathbf{r}'} | v \rangle \tag{9.9}$$

equivalently we could have evaluated it in $\mathbf{r}'$ yielding Eq. 8.46 (here repeated):

$$\Omega^{\mathrm{R}} = \sum_{vc} \langle v | e^{\mathrm{i}(\mathbf{q}+\mathbf{G})\cdot\mathbf{r}} | c \rangle \langle c | \left[\hat{\mathscr{H}}, e^{-\mathrm{i}(\mathbf{q}+\mathbf{G}')\cdot\mathbf{r}'} \right] | v \rangle \tag{9.10}$$

Upon the evaluation of the kinetic part of the Hamiltonian $\left(-\frac{\nabla^2}{2} \right)$ Eq. 9.10 yields a term with $(\mathbf{q}+\mathbf{G}')$, analogously to Eq. 8.50 with $(\mathbf{q}+\mathbf{G})$:

$$\Omega_\nabla^{\mathrm{R}} = -\frac{1}{2} \sum_{vc} \tilde{\rho}_{vc} \langle c | \left[\nabla^2, e^{-\mathrm{i}(\mathbf{q}+\mathbf{G}')\cdot\mathbf{r}'} \right] | v \rangle$$

$$= -\frac{1}{2} \sum_{vc} \tilde{\rho}_{vc} \left[\langle c | \nabla^2 e^{-\mathrm{i}(\mathbf{q}+\mathbf{G}')\cdot\mathbf{r}'} | v \rangle - \langle c | e^{-\mathrm{i}(\mathbf{q}+\mathbf{G}')\cdot\mathbf{r}'} \nabla^2 | v \rangle \right]$$

$$= -\frac{1}{2} \sum_{vc} \tilde{\rho}_{vc} \left[\langle c | \nabla e^{-\mathrm{i}(\mathbf{q}+\mathbf{G}')\cdot\mathbf{r}'} \nabla | v \rangle - \mathrm{i}(\mathbf{q}+\mathbf{G}') \langle c | \nabla e^{-\mathrm{i}(\mathbf{q}+\mathbf{G}')\cdot\mathbf{r}'} | v \rangle - \langle c | e^{-\mathrm{i}(\mathbf{q}+\mathbf{G}')\cdot\mathbf{r}'} \nabla^2 | v \rangle \right]$$

$$= -\frac{1}{2} \sum_{vc} \tilde{\rho}_{vc} \left[\langle c | e^{-\mathrm{i}(\mathbf{q}+\mathbf{G}')\cdot\mathbf{r}'} \nabla^2 | v \rangle - \mathrm{i}(\mathbf{q}+\mathbf{G}') \langle c | e^{-\mathrm{i}(\mathbf{q}+\mathbf{G}')\cdot\mathbf{r}'} \nabla | v \rangle - \langle c | e^{-\mathrm{i}(\mathbf{q}+\mathbf{G}')\cdot\mathbf{r}'} \nabla^2 | v \rangle \right]$$

$$+ \frac{\mathrm{i}}{2}(\mathbf{q}+\mathbf{G}') \sum_{vc} \tilde{\rho}_{vc} \langle c | \nabla e^{-\mathrm{i}(\mathbf{q}+\mathbf{G}')\cdot\mathbf{r}'} | v \rangle$$

$$= -\frac{1}{2} \sum_{vc} \tilde{\rho}_{vc} \left[\langle c | e^{-\mathrm{i}(\mathbf{q}+\mathbf{G}')\cdot\mathbf{r}'} \nabla^2 | v \rangle - \mathrm{i}(\mathbf{q}+\mathbf{G}') \langle c | e^{-\mathrm{i}(\mathbf{q}+\mathbf{G}')\cdot\mathbf{r}'} \nabla | v \rangle - \langle c | e^{-\mathrm{i}(\mathbf{q}+\mathbf{G}')\cdot\mathbf{r}'} \nabla^2 | v \rangle \right]$$

$$+ \frac{\mathrm{i}}{2}(\mathbf{q}+\mathbf{G}') \sum_{vc} \tilde{\rho}_{vc} \left[\langle c | e^{-\mathrm{i}(\mathbf{q}+\mathbf{G}')\cdot\mathbf{r}'} \nabla | v \rangle - \mathrm{i}(\mathbf{q}+\mathbf{G}') \langle c | e^{-\mathrm{i}(\mathbf{q}+\mathbf{G}')\mathbf{r}'} | v \rangle \right]$$

$$\Omega_\nabla^{\mathrm{R}} = \frac{(\mathbf{q}+\mathbf{G}')^2}{2} \sum_{vc} \tilde{\rho}_{vc} \langle c | e^{-\mathrm{i}(\mathbf{q}+\mathbf{G}')\cdot\mathbf{r}'} | v \rangle + \mathrm{i}(\mathbf{q}+\mathbf{G}') \sum_{vc} \tilde{\rho}_{vc} \langle c | e^{-\mathrm{i}(\mathbf{q}+\mathbf{G}')\cdot\mathbf{r}'} \nabla | v \rangle \tag{9.11}$$

And also, analogously to Eq. 8.53, apply the closure relation (Eq. 8.2) and obtain an expression which only depends on the valence states:

$$\Omega_\nabla^{\mathrm{R}} = \frac{(\mathbf{q}+\mathbf{G}')^2}{2} \sum_{vc} \langle v | \, e^{\mathrm{i}(\mathbf{q}+\mathbf{G})\cdot\mathbf{r}} \, |c\rangle \, \langle c| \, e^{-\mathrm{i}(\mathbf{q}+\mathbf{G}')\cdot\mathbf{r}'} \, |v\rangle$$

$$+\mathrm{i}(\mathbf{q}+\mathbf{G}') \sum_{vc} \langle v| \, e^{\mathrm{i}(\mathbf{q}+\mathbf{G})\cdot\mathbf{r}} \, |c\rangle \, \langle c| \, e^{-\mathrm{i}(\mathbf{q}+\mathbf{G}')\cdot\mathbf{r}'} \nabla \, |v\rangle$$

$$= \frac{(\mathbf{q}+\mathbf{G}')^2}{2} \left[\sum_v \langle v| \, e^{\mathrm{i}(\mathbf{G}-\mathbf{G}')\cdot\mathbf{r}} \, |v\rangle - \sum_{vv'} \langle v| \, e^{\mathrm{i}(\mathbf{q}+\mathbf{G})\cdot\mathbf{r}} \, |v'\rangle \, \langle v'| \, e^{-\mathrm{i}(\mathbf{q}+\mathbf{G}')\cdot\mathbf{r}'} \, |v\rangle \right] \qquad (9.12)$$

$$+\mathrm{i}(\mathbf{q}+\mathbf{G}') \left[\sum_v \langle v| \, e^{\mathrm{i}(\mathbf{G}-\mathbf{G}')\cdot\mathbf{r}} \nabla \, |v\rangle - \sum_{vv'} \langle v| \, e^{\mathrm{i}(\mathbf{q}+\mathbf{G})\cdot\mathbf{r}} \, |v'\rangle \, \langle v'| \, e^{-\mathrm{i}(\mathbf{q}+\mathbf{G}')\cdot\mathbf{r}'} \nabla \, |v\rangle \right]$$

Upon the evaluation of the derivative:

$$\Omega_\nabla^{\mathrm{R}} = \frac{(\mathbf{q}+\mathbf{G}')^2}{2} \left[\sum_v \langle v| \, e^{\mathrm{i}(\mathbf{G}-\mathbf{G}')\cdot\mathbf{r}} \, |v\rangle - \sum_{vv'} \langle v| \, e^{\mathrm{i}(\mathbf{q}+\mathbf{G})\cdot\mathbf{r}} \, |v'\rangle \, \langle v'| \, e^{-\mathrm{i}(\mathbf{q}+\mathbf{G}')\cdot\mathbf{r}'} \, |v\rangle \right]$$

$$-\mathbf{k}(\mathbf{q}+\mathbf{G}') \sum_v \langle v| \, e^{\mathrm{i}(\mathbf{G}-\mathbf{G}')\cdot\mathbf{r}} \, |v\rangle - (\mathbf{q}+\mathbf{G}') \sum_v \langle v| \, e^{\mathrm{i}(\mathbf{G}-\mathbf{G}')\cdot\mathbf{r}} \, |v_{\tilde{\mathbf{G}}}\rangle$$

$$+\mathbf{k}(\mathbf{q}+\mathbf{G}') \sum_{vv'} \langle v| \, e^{\mathrm{i}(\mathbf{q}+\mathbf{G})\cdot\mathbf{r}} \, |v'\rangle \, \langle v'| \, e^{-\mathrm{i}(\mathbf{q}+\mathbf{G}')\cdot\mathbf{r}'} \, |v\rangle \qquad (9.13)$$

$$+(\mathbf{q}+\mathbf{G}') \sum_{vv'} \langle v| \, e^{\mathrm{i}(\mathbf{q}+\mathbf{G})\cdot\mathbf{r}} \, |v'\rangle \, \langle v'| \, e^{-\mathrm{i}(\mathbf{q}+\mathbf{G}')\cdot\mathbf{r}'} \, |v_{\tilde{\mathbf{G}}}\rangle$$

and lastly from time-reversal symmetry:

$$\Omega_\nabla^{\mathrm{R}} = \frac{(\mathbf{q}+\mathbf{G}')^2}{2} \left[\sum_v \langle v| \, e^{\mathrm{i}(\mathbf{G}-\mathbf{G}')\cdot\mathbf{r}} \, |v\rangle - \sum_{vv'} \langle v| \, e^{\mathrm{i}(\mathbf{q}+\mathbf{G})\cdot\mathbf{r}} \, |v'\rangle \, \langle v'| \, e^{-\mathrm{i}(\mathbf{q}+\mathbf{G}')\cdot\mathbf{r}'} \, |v\rangle \right]$$

$$-(\mathbf{q}+\mathbf{G}') \sum_v \langle v| \, e^{\mathrm{i}(\mathbf{G}-\mathbf{G}')\cdot\mathbf{r}} \, |v_{\tilde{\mathbf{G}}}\rangle + (\mathbf{q}+\mathbf{G}') \sum_{vv'} \langle v| \, e^{\mathrm{i}(\mathbf{q}+\mathbf{G})\cdot\mathbf{r}} \, |v'\rangle \, \langle v'| \, e^{-\mathrm{i}(\mathbf{q}+\mathbf{G}')\cdot\mathbf{r}'} \, |v_{\tilde{\mathbf{G}}}\rangle$$

$$(9.14)$$

It is worth pointing out that in Ref. [129] it was the commutator in $\mathbf{r}'$ that Berger *et al.*, evaluated. Thus, Eq. 9.14 is similar to Eq. 14 and 16 of Ref. [129] for local potentials, and without the symmetrization with the Hermitian conjugate.

Appendix D

Explicit evaluation of $\Delta^{\mathrm{R},(1)}$

In Section 8 we showed the

At this point it is convenient to focus only on the terms with the derivatives. Thus, assuming a plane waves basis set, the wave function of a state $|n, \mathbf{k}\rangle$ reads:

$$\psi_{\mathbf{k}}^n(\mathbf{r}) = \sum_{\tilde{\mathbf{G}}} C_{\mathbf{k}}^n(\tilde{\mathbf{G}}) e^{\mathrm{i}(\mathbf{k}+\tilde{\mathbf{G}})\cdot\mathbf{r}} \tag{9.15}$$

and its derivative:

$$\nabla \psi_{\mathbf{k}}^n(\mathbf{r}) = \mathrm{i}\mathbf{k} \sum_{\tilde{\mathbf{G}}} C_{\mathbf{k}}^n(\tilde{\mathbf{G}}) e^{\mathrm{i}(\mathbf{k}+\tilde{\mathbf{G}})\cdot\mathbf{r}} + \mathrm{i} \sum_{\tilde{\mathbf{G}}} C_{\mathbf{k}}^n(\tilde{\mathbf{G}}) \cdot \tilde{\mathbf{G}} e^{\mathrm{i}(\mathbf{k}+\tilde{\mathbf{G}})\cdot\mathbf{r}} \tag{9.16}$$

notice that, because of the derivative, the imaginary number comes down as a multiplying factor. Moreover, in the derivatives of Eq. 8.53 there is also an i multiplying, thus it is convenient to group these terms. In order to simplify the notation we write:

$$\mathrm{i}\nabla |n, \mathbf{k}\rangle = -\mathbf{k} |n, \mathbf{k}\rangle - |n_{\tilde{\mathbf{G}}}, \mathbf{k}\rangle \tag{9.17}$$

where $|n_{\tilde{\mathbf{G}}}, \mathbf{k}\rangle \equiv \sum_{\tilde{\mathbf{G}}} C_{\mathbf{k}}^n(\tilde{\mathbf{G}}) \cdot \tilde{\mathbf{G}} e^{\mathrm{i}(\mathbf{k}+\tilde{\mathbf{G}})\cdot\mathbf{r}}$. We now rewrite Eq. 8.53 evaluating the derivative as in Eq. 9.17:

$$
\begin{aligned}
\Omega_{\nabla}^{\mathrm{R}} = & -\frac{(\mathbf{q}+\mathbf{G})^2}{2} \left[\sum_v \langle v| e^{\mathrm{i}(\mathbf{G}-\mathbf{G}')\cdot\mathbf{r}} |v\rangle - \sum_{vv'} \langle v| e^{\mathrm{i}(\mathbf{q}+\mathbf{G})\cdot\mathbf{r}} |v'\rangle \langle v'| e^{-\mathrm{i}(\mathbf{q}+\mathbf{G}')\cdot\mathbf{r}'} |v\rangle \right] \\
& -\mathbf{k}'(\mathbf{q}+\mathbf{G}) \sum_v \langle v| e^{\mathrm{i}(\mathbf{G}-\mathbf{G}')\cdot\mathbf{r}} |v\rangle - (\mathbf{q}+\mathbf{G}) \sum_v \langle v| e^{\mathrm{i}(\mathbf{G}-\mathbf{G}')\cdot\mathbf{r}} |v_{\tilde{\mathbf{G}}}\rangle \\
& +(\mathbf{q}+\mathbf{G})(\mathbf{q}+\mathbf{G}') \sum_v \langle v| e^{\mathrm{i}(\mathbf{G}-\mathbf{G}')\cdot\mathbf{r}} |v\rangle \\
& +\mathbf{k}(\mathbf{q}+\mathbf{G}) \sum_{vv'} \langle v| e^{\mathrm{i}(\mathbf{q}+\mathbf{G})\cdot\mathbf{r}} |v'\rangle \langle v'| e^{-\mathrm{i}(\mathbf{q}+\mathbf{G}')\cdot\mathbf{r}'} |v\rangle \\
& +(\mathbf{q}+\mathbf{G}) \sum_{vv'} \langle v| e^{\mathrm{i}(\mathbf{q}+\mathbf{G})\cdot\mathbf{r}} |v'_{\tilde{\mathbf{G}}}\rangle \langle v'| e^{-\mathrm{i}(\mathbf{q}+\mathbf{G}')\cdot\mathbf{r}'} |v\rangle
\end{aligned}
\tag{9.18}
$$

and we can make a further simplification assuming time-reversal symmetry, meaning that $\psi_{\mathbf{k}}^n(\mathbf{r}) = \psi_{-\mathbf{k}}^{n*}(\mathbf{r})$. Thus, if for every $(+\mathbf{k})$ there is a $(-\mathbf{k})$, the term mutiplied by $\mathbf{k}$ (or $\mathbf{k}'$) does not contribute to the final sum. Thus, Eq. 9.18 simplifies to:

116

$$\Omega_\nabla^R = -\frac{(\mathbf{q}+\mathbf{G})^2}{2}\left[\sum_v \langle v| e^{i(\mathbf{G}-\mathbf{G}')\cdot\mathbf{r}} |v\rangle - \sum_{vv'} \langle v| e^{i(\mathbf{q}+\mathbf{G})\cdot\mathbf{r}} |v'\rangle \langle v'| e^{-i(\mathbf{q}+\mathbf{G}')\cdot\mathbf{r}'} |v\rangle\right]$$

$$-(\mathbf{q}+\mathbf{G})\sum_v \langle v| e^{i(\mathbf{G}-\mathbf{G}')\cdot\mathbf{r}} |v_{\tilde{\mathbf{G}}}\rangle + (\mathbf{q}+\mathbf{G})(\mathbf{q}+\mathbf{G}')\sum_v \langle v| e^{i(\mathbf{G}-\mathbf{G}')\cdot\mathbf{r}} |v\rangle \quad (9.19)$$

$$+(\mathbf{q}+\mathbf{G})\sum_{vv'} \langle v| e^{i(\mathbf{q}+\mathbf{G})\cdot\mathbf{r}} |v'_{\tilde{\mathbf{G}}}\rangle \langle v'| e^{-i(\mathbf{q}+\mathbf{G}')\cdot\mathbf{r}'} |v\rangle$$

Eq. 9.19 is the final expression for Ω_∇^R as it cannot be further simplified, now we must add it to Eq. 8.48: $\Omega^R = \Omega_\nabla^R + \Omega_{\hat{\mathcal{V}}}^R$, from where we need to evaluate the commutator with the potential $\hat{\mathcal{V}}$. For this we assume a separable potential of the form $\hat{\mathcal{V}} = \hat{\mathcal{V}}_l + \hat{\mathcal{V}}_{nl}$ (local and non-local):

$$\Omega_{\hat{\mathcal{V}}}^R = \sum_{vc} \langle v| \left[e^{i(\mathbf{q}+\mathbf{G})\cdot\mathbf{r}}, \hat{\mathcal{V}}\right] |c\rangle \tilde{\rho}_{vc}^*$$

$$= \sum_{vc} \langle v| \left[e^{i(\mathbf{q}+\mathbf{G})\cdot\mathbf{r}}, \hat{\mathcal{V}}_l\right] |c\rangle \tilde{\rho}_{vc}^* + \sum_{vc} \langle v| \left[e^{i(\mathbf{q}+\mathbf{G})\cdot\mathbf{r}}, \hat{\mathcal{V}}_{nl}\right] |c\rangle \tilde{\rho}_{vc}^* \quad (9.20)$$

Notice that the dipole operator $\left[e^{i(\mathbf{q}+\mathbf{G})\cdot\mathbf{r}}\right]$ is a local potential, *i. e.*, is a diagonal matrix, and therefore commutes with $\hat{\mathcal{V}}_l$: $\left[e^{i(\mathbf{q}+\mathbf{G})\cdot\mathbf{r}}, \hat{\mathcal{V}}_l\right] = 0$. On the other hand the non-local part necessarily needs to be evaluated:

$$\Omega_{\hat{\mathcal{V}}}^R = \Omega_{\hat{\mathcal{V}}_{nl}}^R = \sum_{vc} \langle v| \left[e^{i(\mathbf{q}+\mathbf{G})\cdot\mathbf{r}}, \hat{\mathcal{V}}\right] |c\rangle \tilde{\rho}_{vc}^* = \sum_{vc} \langle v| \left[e^{i(\mathbf{q}+\mathbf{G})\cdot\mathbf{r}}, \hat{\mathcal{V}}_{nl}\right] |c\rangle \langle c| e^{-i(\mathbf{q}+\mathbf{G}')\cdot\mathbf{r}'} |v\rangle$$

$$(9.21)$$

and upon the application of the closure relation (Eq. 8.2) becomes:

$$= \sum_v \langle v| \left[e^{i(\mathbf{q}+\mathbf{G})\cdot\mathbf{r}}, \hat{\mathcal{V}}_{nl}\right] e^{-i(\mathbf{q}+\mathbf{G}')\cdot\mathbf{r}} |v\rangle - \sum_{vv'} \langle v| \left[e^{i(\mathbf{q}+\mathbf{G})\cdot\mathbf{r}}, \hat{\mathcal{V}}_{nl}\right] |v'\rangle \langle v'| e^{-i(\mathbf{q}+\mathbf{G}')\cdot\mathbf{r}'} |v\rangle$$

$$(9.22)$$

Moreover, simply to give a consistent (explicit) expression with Eq. 9.19, we can expand the commutator of Eq. 9.22 in its different terms:

$$= \sum_v \langle v| e^{i(\mathbf{q}+\mathbf{G})\cdot\mathbf{r}} \hat{\mathcal{V}}_{nl} e^{-i(\mathbf{q}+\mathbf{G}')\cdot\mathbf{r}} |v\rangle - \sum_v \langle v| \hat{\mathcal{V}}_{nl} e^{i(\mathbf{G}-\mathbf{G}')\cdot\mathbf{r}} |v\rangle$$

$$-\sum_{vv'} \langle v| e^{i(\mathbf{q}+\mathbf{G})\cdot\mathbf{r}} \hat{\mathcal{V}}_{nl} |v'\rangle \langle v'| e^{-i(\mathbf{q}+\mathbf{G}')\cdot\mathbf{r}'} |v\rangle + \sum_{vv'} \langle v| \hat{\mathcal{V}}_{nl} e^{i(\mathbf{q}+\mathbf{G})\cdot\mathbf{r}} |v'\rangle \langle v'| e^{-i(\mathbf{q}+\mathbf{G}')\cdot\mathbf{r}'} |v\rangle$$

$$(9.23)$$

and finally give an explicit expression for Ω^R, as an explicit functional of the one-body density matrix with $\Omega^R = \Omega_\nabla^R + \Omega_{\hat{\mathcal{V}}}^R = \Omega_\nabla^R + \Omega_{\hat{\mathcal{V}}_{nl}}^R$:

$$\Omega^{\mathrm{R}} = -\frac{(\mathbf{q}+\mathbf{G})^2}{2}\left[\sum_v \langle v|\, e^{\mathrm{i}(\mathbf{G}-\mathbf{G}')\cdot\mathbf{r}}\,|v\rangle - \sum_{vv'}\langle v|\, e^{\mathrm{i}(\mathbf{q}+\mathbf{G})\cdot\mathbf{r}}\,|v'\rangle\,\langle v'|\, e^{-\mathrm{i}(\mathbf{q}+\mathbf{G}')\cdot\mathbf{r}'}\,|v\rangle\right]$$
$$-(\mathbf{q}+\mathbf{G})\sum_v \langle v|\, e^{\mathrm{i}(\mathbf{G}-\mathbf{G}')\cdot\mathbf{r}}\,|v_{\tilde{\mathbf{G}}}\rangle + (\mathbf{q}+\mathbf{G})(\mathbf{q}+\mathbf{G}')\sum_v \langle v|\, e^{\mathrm{i}(\mathbf{G}-\mathbf{G}')\cdot\mathbf{r}}\,|v\rangle$$
$$+(\mathbf{q}+\mathbf{G})\sum_{vv'}\langle v|\, e^{i(\mathbf{q}+\mathbf{G})\cdot\mathbf{r}}\,|v'_{\tilde{\mathbf{G}}}\rangle\,\langle v'|\, e^{-\mathrm{i}(\mathbf{q}+\mathbf{G}')\cdot\mathbf{r}'}\,|v\rangle$$
$$+\sum_v \langle v|\, e^{i(\mathbf{q}+\mathbf{G})\cdot\mathbf{r}}\,\hat{\mathscr{V}}_{nl}\,e^{-\mathrm{i}(\mathbf{q}+\mathbf{G}')\cdot\mathbf{r}'}\,|v\rangle - \sum_v \langle v|\,\hat{\mathscr{V}}_{nl}\,e^{i(\mathbf{G}-\mathbf{G}')\cdot\mathbf{r}}\,|v\rangle$$
$$-\sum_{vv'}\langle v|\, e^{i(\mathbf{q}+\mathbf{G})\cdot\mathbf{r}}\,\hat{\mathscr{V}}_{nl}\,|v'\rangle\,\langle v'|\, e^{-\mathrm{i}(\mathbf{q}+\mathbf{G}')\cdot\mathbf{r}'}\,|v\rangle + \sum_{vv'}\langle v|\,\hat{\mathscr{V}}_{nl}\,e^{i(\mathbf{q}+\mathbf{G})\cdot\mathbf{r}}\,|v'\rangle\,\langle v'|\, e^{-\mathrm{i}(\mathbf{q}+\mathbf{G}')\cdot\mathbf{r}'}\,|v\rangle$$

$$(9.24)$$

After the long derivation it is necessary to remind the reader that $\Omega^{\mathrm{R}} \equiv \sum_{vc}\tilde{\rho}_{vc}(\mathbf{q}+\mathbf{G})\tilde{\rho}^*_{vc}(\mathbf{q}+\mathbf{G}')(\varepsilon_c - \varepsilon_v)$, and that with the application of the closure relation it accounts for all conduction states. Thus, Eq. 9.24 let us write Eq. 8.24 $\left(\Delta^{\mathrm{R},(1)}\right)$ explicitly, we must simply divide Eq. 9.24 over Eq. 8.44:

$$\Delta^{\mathrm{R},(1)} = -\frac{(\mathbf{q}+\mathbf{G})^2}{2}$$
$$+\frac{(\mathbf{q}+\mathbf{G})(\mathbf{q}+\mathbf{G}')\sum_v \langle v|\, e^{\mathrm{i}(\mathbf{G}-\mathbf{G}')\cdot\mathbf{r}}\,|v\rangle}{\sum_v \langle v|\, e^{\mathrm{i}(\mathbf{G}-\mathbf{G}')\cdot\mathbf{r}}\,|v\rangle - \sum_{vv'}\langle v|\, e^{\mathrm{i}(\mathbf{q}+\mathbf{G})\cdot\mathbf{r}}\,|v'\rangle\,\langle v'|\, e^{-\mathrm{i}(\mathbf{q}+\mathbf{G}')\cdot\mathbf{r}'}\,|v\rangle}$$
$$-(\mathbf{q}+\mathbf{G})\frac{\sum_v \langle v|\, e^{\mathrm{i}(\mathbf{G}-\mathbf{G}')\cdot\mathbf{r}}\,|v_{\tilde{\mathbf{G}}}\rangle - \sum_{vv'}\langle v|\, e^{\mathrm{i}(\mathbf{q}+\mathbf{G})\cdot\mathbf{r}}\,|v'_{\tilde{\mathbf{G}}}\rangle\,\langle v'|\, e^{-\mathrm{i}(\mathbf{q}+\mathbf{G}')\cdot\mathbf{r}'}\,|v\rangle}{\sum_v \langle v|\, e^{\mathrm{i}(\mathbf{G}-\mathbf{G}')\cdot\mathbf{r}}\,|v\rangle - \sum_{vv'}\langle v|\, e^{\mathrm{i}(\mathbf{q}+\mathbf{G})\cdot\mathbf{r}}\,|v'\rangle\,\langle v'|\, e^{-\mathrm{i}(\mathbf{q}+\mathbf{G}')\cdot\mathbf{r}'}\,|v\rangle}$$
$$+\frac{\sum_v \langle v|\, e^{i(\mathbf{q}+\mathbf{G})\cdot\mathbf{r}}\,\hat{\mathscr{V}}_{nl}\,e^{-\mathrm{i}(\mathbf{q}+\mathbf{G}')\cdot\mathbf{r}'}\,|v\rangle - \sum_v \langle v|\,\hat{\mathscr{V}}_{nl}\,e^{i(\mathbf{G}-\mathbf{G}')\cdot\mathbf{r}}\,|v\rangle}{\sum_v \langle v|\, e^{\mathrm{i}(\mathbf{G}-\mathbf{G}')\cdot\mathbf{r}}\,|v\rangle - \sum_{vv'}\langle v|\, e^{\mathrm{i}(\mathbf{q}+\mathbf{G})\cdot\mathbf{r}}\,|v'\rangle\,\langle v'|\, e^{-\mathrm{i}(\mathbf{q}+\mathbf{G}')\cdot\mathbf{r}'}\,|v\rangle}$$
$$-\frac{\sum_{vv'}\langle v|\, e^{i(\mathbf{q}+\mathbf{G})\cdot\mathbf{r}}\,\hat{\mathscr{V}}_{nl}\,|v'\rangle\,\langle v'|\, e^{-\mathrm{i}(\mathbf{q}+\mathbf{G}')\cdot\mathbf{r}'}\,|v\rangle - \sum_{vv'}\langle v|\,\hat{\mathscr{V}}_{nl}\,e^{i(\mathbf{q}+\mathbf{G})\cdot\mathbf{r}}\,|v'\rangle\,\langle v'|\, e^{-\mathrm{i}(\mathbf{q}+\mathbf{G}')\cdot\mathbf{r}'}\,|v\rangle}{\sum_v \langle v|\, e^{\mathrm{i}(\mathbf{G}-\mathbf{G}')\cdot\mathbf{r}}\,|v\rangle - \sum_{vv'}\langle v|\, e^{\mathrm{i}(\mathbf{q}+\mathbf{G})\cdot\mathbf{r}}\,|v'\rangle\,\langle v'|\, e^{-\mathrm{i}(\mathbf{q}+\mathbf{G}')\cdot\mathbf{r}'}\,|v\rangle}$$

$$(9.25)$$

and to complete the approximation, plug it in Eq. 8.20, where the closure relation must be also applied:

$$\tilde{\chi}^{0,\mathrm{R}}_{\mathbf{G}\mathbf{G}'}(\mathbf{q},0) = \frac{\sum_v \langle v|\, e^{\mathrm{i}(\mathbf{G}-\mathbf{G}')\cdot\mathbf{r}}\,|v\rangle - \sum_{vv'}\langle v|\, e^{\mathrm{i}(\mathbf{q}+\mathbf{G})\cdot\mathbf{r}}\,|v'\rangle\,\langle v'|\, e^{-\mathrm{i}(\mathbf{q}+\mathbf{G}')\cdot\mathbf{r}'}\,|v\rangle}{-\Delta^{\mathrm{R}}} \qquad (9.26)$$

We must conclude this section by commenting on the fact that, although the implementation of Eqs. 9.25 and 9.26 is not trivial, the operations to build the different pieces are the same as for the polarizability (Eq. 8.7): mostly the Fourier transforms to build $\tilde{\rho}_{vv'}(\mathbf{q}+\mathbf{G})$ and $\tilde{\rho}_{vv}(\mathbf{G}-\mathbf{G}')$, plus the integrals with the non-local potential, nonetheless these two terms can be evaluated efficiently using fast Fourier transforms, and pseudopotentials of the type Kleinman-Bylander [92, 128, 140].

Appendix F

The SRden code is a tool written in Python (2.7) to compute the evolution of the induced density in space and time, which uses the polarizability files from DP [98] and Exc [141]. This code has been part of a continuous development by Igor Reshetnyak, Ralf Hambach, Giulia Pegolotti, Arnaud Lorin, Vitaly Gorelov and Muhammed Gunes. The main details on how to use the code, definitions of the input variables and a typical input file can be found in Ref. [136]. Along this work some changes were done in the code which are worth mentioning: the inclusion of the variable

```
write_tden = <True/False> # (boolean)
```

and the deprecation of `t_plot` and `r_ind` to plot immediately after the calculation. Now, with `write_tden = True`, SRden generates a NetCDF4 file with the induced density and the potential. A typical output file `<root>_TDEN.nc4` has the structure:

```
netcdf My_file_TDEN {
dimensions:
    space_dim = 3 ;
    one_dim = 1 ;
    perturbation_type_len = 14 ;
    list_of_energies_len = 61 ;
    list_of_qvectors_input_file_len = 24 ;
    total_list_of_qvectors_len = 193 ;
    total_list_of_gvectors_len = 99 ;
    atoms_in_unit_cell = 2 ;
    atoms_in_box = 144 ;
    time = 601 ;
    mesh_points = 1000000 ;
variables:
    char perturbation_type(perturbation_type_len) ;
    float perturbation_position(one_dim, space_dim) ;
     perturbation_position:units = "Reduced coordinates" ;
    float perturbation_time(one_dim) ;
     perturbation_time:units = "fs" ;
    float list_of_energies(one_dim, list_of_energies_len) ;
     list_of_energies:units = "eV" ;
    float list_of_qvectors_input_file(list_of_qvectors_input_file_len, space_dim) ;
     list_of_qvectors_input_file:units = "Reduced coordinates" ;
```

```
        float total_list_of_qvectors(total_list_of_qvectors_len, space_dim) ;
          total_list_of_qvectors:units = "Reduced coordinates" ;
        int npwmat(one_dim) ;
        int total_list_of_gvectors(total_list_of_gvectors_len, space_dim) ;
        float lattice_parameters_rprimd(space_dim, space_dim) ;
          lattice_parameters_rprimd:units = "Angstroms" ;
        float box_size_orthogonal(one_dim, space_dim) ;
          box_size_orthogonal:units = "Angstroms" ;
        int number_of_atoms_in_cell(one_dim) ;
          number_of_atoms_in_cell:units = "natom" ;
        int atoms_in_cell_type(atoms_in_unit_cell) ;
          atoms_in_cell_type:units = "znucl" ;
        float atoms_in_cell_positions(atoms_in_unit_cell, space_dim) ;
          atoms_in_cell_positions:units = "Angstroms" ;
        int number_of_atoms_in_box(one_dim) ;
          number_of_atoms_in_box:units = "natom" ;
        int atoms_in_box_type(atoms_in_box) ;
          atoms_in_box_type:units = "znucl" ;
        float atoms_in_box_positions(atoms_in_box, space_dim) ;
          atoms_in_box_positions:units = "Angstroms" ;
        float time(time) ;
          time:units = "fs" ;
        float mesh_points(mesh_points, space_dim) ;
          mesh_points:units = "Angstroms" ;
        int number_of_mesh_points_XYZ(one_dim, space_dim) ;
        float induced_density(time, mesh_points) ;
          induced_density:units = "units" ;
        float external_potential(time, mesh_points) ;
          external_potential:units = "units" ;
// global attributes:
        :file_creation_date = "11-03-2022 09:28:22" ;
        :SRden_version_date = "15-12-2021" ;
        :chi_elements_in_SRden = "full" ;
        :chi_type_from_dp = "chi0" ;
}
```

where the names of the variables are self-explanatory. The NetCDF format allows for easy manipulation of the data. Moreover, the capabilities of SRden to produce the density plots, snapshots, and .xsf files with the density were migrated (and more analysis were implemented) to an external tool called `SRden_output.py` which requires the output file from SRden `<root>_TDEN.nc4`. This tool runs with the following instruction:

```
SRden_output.py -i <input_for_graphical_tool>.py -d <root>_TDEN.nc4
```

And a typical input file for the graphical tool is shown below:

```
# Input file for visualization

save_figures     = False   # Save figure in pdf/png
plot_figures     = True    # Show figure after running
write_pOd_0D     = False   # Write <.dat> with potential and density
                           # at a point r in space.
write_pOd_1D     = False   # Write <.dat>  '' '' ''
                           # along a line in space.
write_pOd_norm   = False # Write  <.dat> with the norm of potential
                           # and density
plot_tot_2D      = False   # Plot a 2D cut with the total potential
plot_pot_2D      = False   # '' ''  '' external potential
plot_den_2D      = False   # '' '' '' induced density
plot_tot_1D      = False  # Plot along a line the total potential
plot_pot_1D      = False # '' '' '' external potential
plot_den_1D      = False  # '' '' '' induced density
plot_tot_0D      = False   # Plot at a point r in space he total potential
plot_pot_0D      = False   # '' '' ''  external potential
plot_den_0D      = False   # '' '' '' induced density
plot_norm_tot    = False   # Plot the norm of the total potential
plot_norm_pot    = True # '' '' '' external potential
plot_norm_den    = True # '' '' '' induced density
integration_rad  = False # Integrate the norm of the total/external potential
                           # and density within a radius
                           # [in Angstrom]. If False =
                           # integrate over all space.
plot_atoms       = False   # Plot atoms 2D figures and videos.
xsf_file         = False   # Generate .xsf with the density at a given time
make_movie_1_tot = False  # Make animation in space and time of the total potential
make_movie_1_pot = False  # '' '' '' external potential
make_movie_1_den = False  # '' '' '' induced density
make_movie_2       = False  # Make movie with external potential and induced
                           # density side-to-side
impose_normalization = True   # Normalize potential/density to the maximum
                           # value in file
print_header       = True   # Print the information in <root> TDEN.nc4
                           # (formatted)

# Output root name ------------------
save_image_as = 'png'     # Format to save the images of the plots.

# Time ----------------------------
plot_at_time = 3.40       # Time to plot 0D/1D/2D [in fs]
xsf_at_time = [0]         # Array in fs
```

```
# For movie -------------------------
interpolation = 'spline16'  # Interpolation type

time_range = False            # False (all times in TDEN file),
                              # Or [min_fs,max_fs] for a time period
                              # Or [fs_1, fs_2, ...]: more than two elements
                              # in the array select specific points in time.
fps_movie = 10                # fps for the density animation
scale_colorbar_tot = 1     # Scale colorbar (Does not work on single frames)
scale_colorbar_pot = 1     #
scale_colorbar_den = 1
force_cbmax_tot = False # Force colorbar values (overwrites the value
                             # set for scale_colorbar_* to 1)
force_cbmax_pot = False # For a first run it is recommended to
                             # set these variables to False.
force_cbmax_den = False

# For cut_1D -----------------------
plot_line_type  = 'X'     # Cut type: X, Y, Z
plot_at_distance_line = [0.00,0.00] # In AA. [Y,Z] if X. [X,Z] if Y. [X,Y] if Z

# For cut_2D -----------------------
plot_at_distance_from_origin = 0   # Needs to be in AA
plot_cut_type = 'XY'               # Cut type: XY, XZ, YZ

# For pOd at r ---------------------
plot_at_r = [[10.24, 10.40,  0.00]]
```

Résumé

Comprendre les propriétés des matériaux par la théorie et les calculs implique deux aspects qui nécessitent des efforts théoriques : la description générale d'une propriété donnée d'une part, et les considérations spécifiques aux matériaux d'autre part. Bien entendu, en fonction de la propriété et du matériau que l'on souhaite examiner, différentes descriptions pour le même objet peuvent être pertinentes. Dans la présente thèse, nous nous intéressons à la description d'une classe de matériaux qui est atomiquement mince. Cela suggère que la description la plus pertinente se situe au niveau atomique. Ici, nous nous concentrons sur le borophène : cela se réfère à une famille de matériaux bidimensionnels (2D) expérimentaux et théoriques constitués d'une seule espèce atomique : le bore. Le borophène est particulièrement fascinant en raison de sa capacité à former plusieurs structures polymorphes, chacune ayant des propriétés électroniques uniques. Ainsi, parmi les multiples polymorphes qui ont été prédits et synthétisés, la seule différence réside dans l'arrangement atomique des atomes. Cependant, différents polymorphes présentent des propriétés différentes.

La question la plus évidente est alors : comment la structure atomique affecte-t-elle les propriétés du borophène? C'est la question fondamentale de notre travail. Nous y répondons en distinguant les propriétés communes à tous les matériaux de celles spécifiques aux polymorphes. Nous réalisons cette étude en deux étapes : d'abord, déterminer comment la structure atomique affecte la structure électronique, puis déterminer comment la structure électronique affecte les propriétés. En particulier, nous nous concentrons sur les propriétés diélectriques : celles-ci ont un lien clair avec le système électronique et peuvent également être reliées aux mesures expérimentales. En explorant ces propriétés, nous espérons offrir des perspectives nouvelles pour le développement de dispositifs électroniques avancés.

Dans ce travail, nous traitons principalement de deux concepts : la structure électronique des différents polymorphes de borophène et la polarisabilité électronique. Cette dernière est construite à partir de la structure électronique. Avec la structure électronique, nous explorons et répondons à différentes questions 1) qu'est-ce qui est commun dans la structure électronique des différents polymorphes de borophène?, 2) qu'est-ce qui est différent?, et 3) comment peut-on ajuster la structure électronique de certains polymorphes? Ces questions sont essentielles pour comprendre les mécanismes sous-jacents qui dictent les propriétés de ces matériaux fascinants.

De plus, avec la polarisabilité (et la structure électronique), nous caractérisons principalement l'absorption optique. Dans notre discussion, un sujet central est le borophène en tant que conducteur transparent. Ainsi, les principales questions à cet égard sont : 1) comment le borophène devient-il transparent?, et 2) comment pouvons-nous ajuster la transparence de ce matériau? Nous discutons de règles théoriques simples qui peuvent

être utiles pour concevoir le borophène en tant que conducteur transparent. En outre, nous explorons les applications potentielles de ce matériau dans des domaines tels que l'électronique flexible et les dispositifs optoélectroniques.

Enfin, nous abordons un dernier point concernant la réponse statique. Nous la discutons dans le contexte du repliement de la surface de Fermi, ce qui est, par exemple, intéressant pour les applications de supraconductivité, ainsi que pour comprendre les instabilités structurelles. Nous soulignons ici la possibilité d'utiliser la polarisabilité électronique pour discuter des instabilités structurelles, allant au-delà d'une simple recherche de repliement de la surface de Fermi. La réponse statique, bien qu'elle soit largement utilisée dans différents contextes, par exemple comme ingrédient dans la théorie de la perturbation à plusieurs corps, est une quantité computationnellement exigeante. Dans ce travail, nous développons une méthode qui nous permet d'approximer la réponse statique de manière efficace : en tant que fonctionnelle explicite de la matrice de densité réduite à une particule. Cette approche innovante ouvre de nouvelles voies pour l'étude des propriétés des matériaux à l'échelle atomique, rendant les simulations plus accessibles et plus précises.

Bibliography

[1] E. Pomerantseva and Y. Gogotsi, "Two-dimensional heterostructures for energy storage," *Nature Energy*, vol. 2, no. 7, p. 17089, Jun 2017. [Online]. Available: https://doi.org/10.1038/nenergy.2017.89

[2] P. Raghavan, J.-H. Ahn, and M. Shelke, "The role of 2d material families in energy harvesting: An editorial overview," *Journal of Materials Research*, Sep 2022. [Online]. Available: https://doi.org/10.1557/s43578-022-00721-z

[3] X. Liu and M. C. Hersam, "2d materials for quantum information science," *Nature Reviews Materials*, vol. 4, no. 10, pp. 669–684, Oct 2019. [Online]. Available: https://doi.org/10.1038/s41578-019-0136-x

[4] J. R. Schaibley, H. Yu, G. Clark, P. Rivera, J. S. Ross, K. L. Seyler, W. Yao, and X. Xu, "Valleytronics in 2d materials," *Nature Reviews Materials*, vol. 1, no. 11, p. 16055, Aug 2016. [Online]. Available: https://doi.org/10.1038/natrevmats.2016.55

[5] Y. Liu, N. O. Weiss, X. Duan, H.-C. Cheng, Y. Huang, and X. Duan, "Van der waals heterostructures and devices," *Nature Reviews Materials*, vol. 1, no. 9, p. 16042, Jul 2016. [Online]. Available: https://doi.org/10.1038/natrevmats.2016.42

[6] M. Chhowalla, D. Jena, and H. Zhang, "Two-dimensional semiconductors for transistors," *Nature Reviews Materials*, vol. 1, no. 11, p. 16052, Aug 2016. [Online]. Available: https://doi.org/10.1038/natrevmats.2016.52

[7] A. Majed, M. Kothakonda, F. Wang, E. N. Tseng, K. Prenger, X. Zhang, P. O. Å. Persson, J. Wei, J. Sun, and M. Naguib, "Transition metal carbo-chalcogenide "tmcc:" a new family of 2d materials," *Advanced Materials*, vol. 34, no. 26, p. 2200574, Jul 2022. [Online]. Available: https://doi.org/10.1002/adma.202200574

[8] A. G. Ricciardulli, S. Yang, J. H. Smet, and M. Saliba, "Emerging perovskite monolayers," *Nature Materials*, vol. 20, no. 10, pp. 1325–1336, Oct 2021. [Online]. Available: https://doi.org/10.1038/s41563-021-01029-9

[9] S. Manzeli, D. Ovchinnikov, D. Pasquier, O. V. Yazyev, and A. Kis, "2d transition metal dichalcogenides," *Nature Reviews Materials*, vol. 2, no. 8, p. 17033, Jun 2017. [Online]. Available: https://doi.org/10.1038/natrevmats.2017.33

[10] K. S. Novoselov, V. I. Falko, L. Colombo, P. R. Gellert, M. G. Schwab, and K. Kim, "A roadmap for graphene," *Nature*, vol. 490, no. 7419, pp. 192–200, Oct 2012. [Online]. Available: https://doi.org/10.1038/nature11458

[11] J. Nilsson, A. H. Castro Neto, F. Guinea, and N. M. R. Peres, "Electronic properties of bilayer and multilayer graphene," *Phys. Rev. B*, vol. 78, p. 045405, Jul 2008. [Online]. Available: https://link.aps.org/doi/10.1103/PhysRevB.78.045405

[12] A. Nimbalkar and H. Kim, "Opportunities and challenges in twisted bilayer graphene: A review," *Nano-Micro Letters*, vol. 12, no. 1, p. 126, Jun 2020. [Online]. Available: https://doi.org/10.1007/s40820-020-00464-8

[13] Z. A. Piazza, H.-S. Hu, W.-L. Li, Y.-F. Zhao, J. Li, and L.-S. Wang, "Planar hexagonal b36 as a potential basis for extended single-atom layer boron sheets," *Nature Communications*, vol. 5, no. 1, p. 3113, Jan 2014. [Online]. Available: https://doi.org/10.1038/ncomms4113

[14] E. S. Penev, S. Bhowmick, A. Sadrzadeh, and B. I. Yakobson, "Polymorphism of two-dimensional boron," *Nano Letters*, vol. 12, no. 5, pp. 2441–2445, May 2012. [Online]. Available: https://doi.org/10.1021/nl3004754

[15] H. Tang and S. Ismail-Beigi, "First-principles study of boron sheets and nanotubes," *Phys. Rev. B*, vol. 82, p. 115412, Sep 2010. [Online]. Available: https://link.aps.org/doi/10.1103/PhysRevB.82.115412

[16] X. Wu, J. Dai, Y. Zhao, Z. Zhuo, J. Yang, and X. C. Zeng, "Two-dimensional boron monolayer sheets," *ACS Nano*, vol. 6, pp. 7443–7453, 2012. [Online]. Available: https://doi.org/10.1021/nn302696v

[17] X. Yu, L. Li, X.-W. Xu, and C.-C. Tang, "Prediction of two-dimensional boron sheets by particle swarm optimization algorithm," *The Journal of Physical Chemistry C*, vol. 116, no. 37, pp. 20 075–20 079, Sep 2012. [Online]. Available: https://doi.org/10.1021/jp305545z

[18] W.-c. Yi, W. Liu, J. Botana, L. Zhao, Z. Liu, J.-y. Liu, and M.-s. Miao, "Honeycomb boron allotropes with dirac cones: A true analogue to graphene," *The Journal of Physical Chemistry Letters*, vol. 8, no. 12, pp. 2647–2653, Jun 2017. [Online]. Available: https://doi.org/10.1021/acs.jpclett.7b00891

[19] E. S. Penev, A. Kutana, and B. I. Yakobson, "Can two-dimensional boron superconduct?" *Nano Letters*, vol. 16, no. 4, pp. 2522–2526, Apr 2016. [Online]. Available: https://doi.org/10.1021/acs.nanolett.6b00070

[20] G. Li, Y. Zhao, S. Zeng, M. Zulfiqar, and J. Ni, "Strain effect on the superconductivity in borophenes," *The Journal of Physical Chemistry C*, vol. 122, no. 29, pp. 16 916–16 924, Jul 2018. [Online]. Available: https://doi.org/10.1021/acs.jpcc.8b03108

[21] Y. Zhao, S. Zeng, C. Lian, Z. Dai, S. Meng, and J. Ni, "Multigap anisotropic superconductivity in borophenes," *Phys. Rev. B*, vol. 98, p. 134514, Oct 2018. [Online]. Available: https://link.aps.org/doi/10.1103/PhysRevB.98.134514

[22] Y. Zhao, S. Zeng, and J. Ni, "Phonon-mediated superconductivity in borophenes," *Applied Physics Letters*, vol. 108, no. 24, p. 242601, 06 2016. [Online]. Available: https://doi.org/10.1063/1.4953775

[23] R. C. Xiao, D. F. Shao, W. J. Lu, H. Y. Lv, J. Y. Li, and Y. P. Sun, "Enhanced superconductivity by strain and carrier-doping in borophene: A first principles prediction," *Applied Physics Letters*, vol. 109, no. 12, p. 122604, 09 2016. [Online]. Available: https://doi.org/10.1063/1.4963179

[24] Z.-L. Lv, H.-L. Cui, H. Wang, and X.-H. Li, "Can borophenes with dirac cone be promising electrodes for supercapacitors," *Applied Surface Science*, vol. 562, p. 150154, Oct 2021. [Online]. Available: https://doi.org/10.1016/j.apsusc.2021.150154

[25] S. Haldar, S. Mukherjee, and C. V. Singh, "Hydrogen storage in li, na and ca decorated and defective borophene: a first principles study," *RSC Advances*, vol. 8, no. 37, pp. 20 748–20 757, 2018. [Online]. Available: https://doi.org/10.1039/C7RA12512G

[26] S. Er, G. A. de Wijs, and G. Brocks, "Dft study of planar boron sheets: A new template for hydrogen storage," *The Journal of Physical Chemistry C*, vol. 113, no. 43, pp. 18 962–18 967, Oct 2009. [Online]. Available: https://doi.org/10.1021/jp9077079

[27] C. Lian, S.-Q. Hu, J. Zhang, C. Cheng, Z. Yuan, S. Gao, and S. Meng, "Integrated plasmonics: Broadband dirac plasmons in borophene," *Phys. Rev. Lett.*, vol. 125, p. 116802, Sep 2020. [Online]. Available: https://link.aps.org/doi/10.1103/PhysRevLett.125.116802

[28] Y. Huang, S. N. Shirodkar, and B. I. Yakobson, "Two-dimensional boron polymorphs for visible range plasmonics: A first-principles exploration," *Journal of the American Chemical Society*, vol. 139, no. 47, pp. 17 181–17 185, Nov 2017. [Online]. Available: https://doi.org/10.1021/jacs.7b10329

[29] A. Haldar, C. L. Cortes, P. Darancet, and S. Sharifzadeh, "Microscopic theory of plasmons in substrate-supported borophene," *Nano Letters*, vol. 20, no. 5, pp. 2986–2992, May 2020. [Online]. Available: https://doi.org/10.1021/acs.nanolett.9b04789

[30] L. Adamska and S. Sharifzadeh, "Fine-tuning the optoelectronic properties of freestanding borophene by strain," *ACS Omega*, vol. 2, no. 11, pp. 8290–8299, Nov 2017. [Online]. Available: https://doi.org/10.1021/acsomega.7b01232

[31] L. Adamska, S. Sadasivam, J. J. Foley IV, P. Darancet, and S. Sharifzadeh, "First-principles investigation of borophene as a monolayer transparent conductor," *The Journal of Physical Chemistry C*, vol. 122, no. 7, pp. 4037–4045, Feb 2018. [Online]. Available: https://doi.org/10.1021/acs.jpcc.7b10197

[32] A. J. Mannix, X.-F. Zhou, B. Kiraly, J. D. Wood, D. Alducin, B. D. Myers, X. Liu, B. L. Fisher, U. Santiago, J. R. Guest, M. J. Yacaman, A. Ponce, A. R. Oganov, M. C. Hersam, and N. P. Guisinger, "Synthesis of borophenes: Anisotropic, two-dimensional boron polymorphs," *Science*, vol. 350, no. 6267, pp. 1513–1516, 2015. [Online]. Available: https://www.science.org/doi/abs/10.1126/science.aad1080

[33] B. Feng, J. Zhang, Q. Zhong, W. Li, S. Li, H. Li, P. Cheng, S. Meng, L. Chen, and K. Wu, "Experimental realization of two-dimensional boron sheets," *Nature Chemistry*, vol. 8, no. 6, pp. 563–568, Jun 2016. [Online]. Available: https://doi.org/10.1038/nchem.2491

[34] W. Li, L. Kong, C. Chen, J. Gou, S. Sheng, W. Zhang, H. Li, L. Chen, P. Cheng, and K. Wu, "Experimental realization of honeycomb borophene," *Science Bulletin*, vol. 63, no. 5, pp. 282–286, 2018. [Online]. Available: https://www.sciencedirect.com/science/article/pii/S2095927318300707

[35] X. Liu, Q. Li, Q. Ruan, M. S. Rahn, B. I. Yakobson, and M. C. Hersam, "Borophene synthesis beyond the single-atomic-layer limit," *Nature Materials*, vol. 21, no. 1, pp. 35–40, Jan 2022. [Online]. Available: https://doi.org/10.1038/s41563-021-01084-2

[36] P. Ranjan, T. K. Sahu, R. Bhushan, S. S. Yamijala, D. J. Late, P. Kumar, and A. Vinu, "Freestanding borophene and its hybrids," *Advanced Materials*, vol. 31, no. 27, p. 1900353, 2019. [Online]. Available: https://onlinelibrary.wiley.com/doi/abs/10.1002/adma.201900353

[37] X. Liu, Z. Zhang, L. Wang, B. I. Yakobson, and M. C. Hersam, "Intermixing and periodic self-assembly of borophene line defects," *Nature Materials*, vol. 17, no. 9, pp. 783–788, Sep 2018. [Online]. Available: https://doi.org/10.1038/s41563-018-0134-1

[38] L. Liu, Z. Zhang, X. Liu, X. Xuan, B. I. Yakobson, M. C. Hersam, and W. Guo, "Borophene concentric superlattices via self-assembly of twin boundaries," *Nano Letters*, vol. 20, no. 2, pp. 1315–1321, 2020, pMID: 31951420. [Online]. Available: https://doi.org/10.1021/acs.nanolett.9b04798

[39] C. Chen, H. Lv, P. Zhang, Z. Zhuo, Y. Wang, C. Ma, W. Li, X. Wang, B. Feng, P. Cheng, X. Wu, K. Wu, and L. Chen, "Synthesis of bilayer borophene," *Nature Chemistry*, vol. 14, no. 1, pp. 25–31, Jan 2022. [Online]. Available: https://doi.org/10.1038/s41557-021-00813-z

[40] Q. Li, V. S. C. Kolluru, M. S. Rahn, E. Schwenker, S. Li, R. G. Hennig, P. Darancet, M. K. Y. Chan, and M. C. Hersam, "Synthesis of borophane polymorphs through hydrogenation of borophene," *Science*, vol. 371, no. 6534, pp. 1143–1148, 2021. [Online]. Available: https://www.science.org/doi/abs/10.1126/science.abg1874

[41] C. Zhong, X. Li, and P. Yu, "Strain-tunable dirac semimetal phase transition and emergent superconductivity in a borophane," *Communications Physics*, vol. 7, no. 1, p. 38, Jan 2024. [Online]. Available: https://doi.org/10.1038/s42005-024-01523-x

[42] M. Yu, Z. Zhang, and W. Guo, "Structures, mechanics, and electronics of borophanes," *The Journal of Physical Chemistry C*, vol. 125, no. 41, pp. 22 917–22 928, Oct 2021. [Online]. Available: https://doi.org/10.1021/acs.jpcc.1c07275

[43] Z. Wang, T.-Y. Lü, H.-Q. Wang, Y. P. Feng, and J.-C. Zheng, "New crystal structure prediction of fully hydrogenated borophene by first principles calculations," *Scientific Reports*, vol. 7, no. 1, p. 609, Apr 2017. [Online]. Available: https://doi.org/10.1038/s41598-017-00667-x

[44] Y. Xu, P. Zhang, X. Xuan, M. Xue, Z. Zhang, W. Guo, and B. I. Yakobson, "Borophane polymorphs," *The Journal of Physical Chemistry Letters*, vol. 13, no. 4, pp. 1107–1113, Feb 2022. [Online]. Available: https://doi.org/10.1021/acs.jpclett.1c03827

[45] H. Tang and S. Ismail-Beigi, "Novel precursors for boron nanotubes: The competition of two-center and three-center bonding in boron sheets," *Phys. Rev. Lett.*, vol. 99, p. 115501, Sep 2007. [Online]. Available: https://link.aps.org/doi/10.1103/PhysRevLett.99.115501

[46] ——, "Self-doping in boron sheets from first principles: A route to structural design of metal boride nanostructures," *Phys. Rev. B*, vol. 80, p. 134113, Oct 2009. [Online]. Available: https://link.aps.org/doi/10.1103/PhysRevB.80.134113

[47] L. Qiu, X. Zhang, X. Kong, I. Mitchell, T. Yan, S. Y. Kim, B. I. Yakobson, and F. Ding, "Theory of sigma bond resonance in flat boron materials," *Nature Communications*, vol. 14, no. 1, p. 1804, Mar 2023. [Online]. Available: https://doi.org/10.1038/s41467-023-37442-8

[48] Y. Wang, Y. Park, L. Qiu, I. Mitchell, and F. Ding, "Borophene with large holes," *The Journal of Physical Chemistry Letters*, vol. 11, no. 15, pp. 6235–6241, 2020, pMID: 32640798. [Online]. Available: https://doi.org/10.1021/acs.jpclett.0c01359

[49] Y. Park, Y. Wang, V. Gladkikh, D. Hedman, X. Kong, and F. Ding, "High temperature phases of borophene: borophene glass and liquid," *Nanoscale Horiz.*, vol. 8, pp. 353–360, 2023. [Online]. Available: http://dx.doi.org/10.1039/D2NH00518B

[50] K. C. Lau and R. Pandey, "Thermodynamic stability of novel boron sheet configurations," *The Journal of Physical Chemistry B*, vol. 112, no. 33, pp. 10 217–10 220, Aug 2008. [Online]. Available: https://doi.org/10.1021/jp8052357

[51] L. Zhu, B. Zhao, T. Zhang, G. Chen, and S. A. Yang, "How is honeycomb borophene stabilized on al(111)?" *The Journal of Physical Chemistry C*, vol. 123, no. 23, pp. 14 858–14 864, Jun 2019. [Online]. Available: https://doi.org/10.1021/acs.jpcc.9b03447

[52] Z. Zhang, S. N. Shirodkar, Y. Yang, and B. I. Yakobson, "Gate-voltage control of borophene structure formation," *Angewandte Chemie International Edition*, vol. 56, no. 48, pp. 15 421–15 426, 2017. [Online]. Available: https://onlinelibrary.wiley.com/doi/abs/10.1002/anie.201705459

[53] K. C. Lau and R. Pandey, "Stability and electronic properties of atomistically-engineered 2d boron sheets," *The Journal of Physical Chemistry C*, vol. 111, no. 7, pp. 2906–2912, Feb 2007. [Online]. Available: https://doi.org/10.1021/jp066719w

[54] J. P. Perdew and Y. Wang, "Accurate and simple analytic representation of the electron-gas correlation energy," *Phys. Rev. B*, vol. 45, pp. 13 244–13 249, Jun 1992. [Online]. Available: https://link.aps.org/doi/10.1103/PhysRevB.45.13244

[55] B. Feng, J. Zhang, R.-Y. Liu, T. Iimori, C. Lian, H. Li, L. Chen, K. Wu, S. Meng, F. Komori, and I. Matsuda, "Direct evidence of metallic bands in a monolayer boron sheet," *Phys. Rev. B*, vol. 94, p. 041408, Jul 2016. [Online]. Available: https://link.aps.org/doi/10.1103/PhysRevB.94.041408

[56] C. Adamo and V. Barone, "Toward reliable density functional methods without adjustable parameters: The PBE0 model," *The Journal of Chemical Physics*, vol. 110, no. 13, pp. 6158–6170, 04 1999. [Online]. Available: https://doi.org/10.1063/1.478522

[57] X. Yang, Y. Ding, and J. Ni, "Ab initio prediction of stable boron sheets and boron nanotubes: Structure, stability, and electronic properties," *Phys. Rev. B*, vol. 77, p. 041402, Jan 2008. [Online]. Available: https://link.aps.org/doi/10.1103/PhysRevB.77.041402

[58] J. P. Perdew, K. Burke, and M. Ernzerhof, "Generalized gradient approximation made simple," *Phys. Rev. Lett.*, vol. 77, pp. 3865–3868, Oct 1996. [Online]. Available: https://link.aps.org/doi/10.1103/PhysRevLett.77.3865

[59] T. Tsafack and B. I. Yakobson, "Thermomechanical analysis of two-dimensional boron monolayers," *Phys. Rev. B*, vol. 93, p. 165434, Apr 2016. [Online]. Available: https://link.aps.org/doi/10.1103/PhysRevB.93.165434

[60] M. H. Evans, J. D. Joannopoulos, and S. T. Pantelides, "Electronic and mechanical properties of planar and tubular boron structures," *Phys. Rev. B*, vol. 72, p. 045434, Jul 2005. [Online]. Available: https://link.aps.org/doi/10.1103/PhysRevB.72.045434

[61] S. M. Mozvashi, M. R. Givi, and M. B. Tagani, "The effects of substrate and stacking in bilayer borophene," *Scientific Reports*, vol. 12, no. 1, p. 13661, Aug 2022. [Online]. Available: https://doi.org/10.1038/s41598-022-18076-0

[62] X.-F. Zhou, X. Dong, A. R. Oganov, Q. Zhu, Y. Tian, and H.-T. Wang, "Semimetallic two-dimensional boron allotrope with massless dirac fermions," *Phys. Rev. Lett.*, vol. 112, p. 085502, Feb 2014. [Online]. Available: https://link.aps.org/doi/10.1103/PhysRevLett.112.085502

[63] Q. Gao, Q. Yan, Z. Hu, and L. Chen, "Bilayer kagome borophene with multiple van hove singularities," 2023.

[64] M. Born and R. Oppenheimer, "Zur quantentheorie der molekeln," *Annalen der Physik*, vol. 389, no. 20, pp. 457–484, 1927. [Online]. Available: https://onlinelibrary.wiley.com/doi/abs/10.1002/andp.19273892002

[65] J. Kohanoff, *Electronic Structure Calculations for Solids and Molecules: Theory and Computational Methods*. Cambridge: Cambridge University Press, 2006. [Online]. Available: https://www.cambridge.org/core/product/0C0AF2B01A380912FC13816A9A0C350F

[66] A. B. Migdal, "Interaction between electrons and the lattice vibrations in a normal metal," *Soviet Physics JETP*, vol. 34, no. 6, 6 1958. [Online]. Available: http://jetp.ras.ru/cgi-bin/e/index/e/7/6/p996?a=list

[67] E. Kaxiras, *Atomic and Electronic Structure of Solids*. Cambridge: Cambridge University Press, 2003. [Online]. Available: https://www.cambridge.org/core/product/1B7E5043BE2B6D12C749AB9A1E913295

[68] E. Madelung, "Das elektrische feld in systemen von regelmäßig angeordneten punktladungen," *Physikalische Zeitschrift*, vol. 19, pp. 524–533, 1919.

[69] P. Hohenberg and W. Kohn, "Inhomogeneous electron gas," *Phys. Rev.*, vol. 136, pp. B864–B871, Nov 1964. [Online]. Available: https://link.aps.org/doi/10.1103/PhysRev.136.B864

[70] D. M. Ceperley, R. M. Martin, and L. Reining, *Interacting Electrons: Theory and Computational Approaches*. Cambridge: Cambridge University Press, 2016. [Online]. Available: https://www.cambridge.org/core/product/4317C43D0531C900920E83DD4632CFE9

[71] D. R. Hartree, "The wave mechanics of an atom with a non-coulomb central field. part i. theory and methods," *Mathematical Proceedings of the Cambridge Philosophical Society*, vol. 24, no. 1, pp. 89–110, 1928. [Online]. Available: https://www.cambridge.org/core/product/C9417AC1CEC84B934C1EA4C4B8401FEF

[72] V. Fock, "Näherungsmethode zur lösung des quantenmechanischen mehrkörperproblems," *Zeitschrift für Physik*, vol. 61, no. 1, pp. 126–148, Jan 1930. [Online]. Available: https://doi.org/10.1007/BF01340294

[73] L. Hedin, "New method for calculating the one-particle green's function with application to the electron-gas problem," *Phys. Rev.*, vol. 139, pp. A796–A823, Aug 1965. [Online]. Available: https://link.aps.org/doi/10.1103/PhysRev.139.A796

[74] J. C. Slater, "Note on hartree's method," *Phys. Rev.*, vol. 35, pp. 210–211, Jan 1930. [Online]. Available: https://link.aps.org/doi/10.1103/PhysRev.35.210.2

[75] R. G. Parr and Y. Weitao, "Density-functional theory of atoms and molecules," Jan 1995. [Online]. Available: https://doi.org/10.1093/oso/9780195092769.001.0001

[76] W. Kohn and L. J. Sham, "Self-consistent equations including exchange and correlation effects," *Phys. Rev.*, vol. 140, pp. A1133–A1138, Nov 1965. [Online]. Available: https://link.aps.org/doi/10.1103/PhysRev.140.A1133

[77] D. M. Ceperley and B. J. Alder, "Ground state of the electron gas by a stochastic method," *Phys. Rev. Lett.*, vol. 45, pp. 566–569, Aug 1980. [Online]. Available: https://link.aps.org/doi/10.1103/PhysRevLett.45.566

[78] C. G. Broyden, "A class of methods for solving nonlinear simultaneous equations," *Mathematics of Computation*, vol. 19, pp. 577–593, 1965. [Online]. Available: https://api.semanticscholar.org/CorpusID:2802972

[79] P. Pulay, "Convergence acceleration of iterative sequences. the case of scf iteration," *Chemical Physics Letters*, vol. 73, no. 2, pp. 393–398, Jul 1980. [Online]. Available: https://www.sciencedirect.com/science/article/pii/0009261480803964

[80] R. Car and M. Parrinello, "Unified approach for molecular dynamics and density-functional theory," *Phys. Rev. Lett.*, vol. 55, pp. 2471–2474, Nov 1985. [Online]. Available: https://link.aps.org/doi/10.1103/PhysRevLett.55.2471

[81] S. Botti, A. Schindlmayr, R. D. Sole, and L. Reining, "Time-dependent density-functional theory for extended systems," *Reports on Progress in Physics*, vol. 70, no. 3, p. 357, feb 2007. [Online]. Available: https://dx.doi.org/10.1088/0034-4885/70/3/R02

[82] S. L. Adler, "Quantum theory of the dielectric constant in real solids," *Phys. Rev.*, vol. 126, pp. 413–420, Apr 1962. [Online]. Available: https://link.aps.org/doi/10.1103/PhysRev.126.413

[83] N. Wiser, "Dielectric constant with local field effects included," *Phys. Rev.*, vol. 129, pp. 62–69, Jan 1963. [Online]. Available: https://link.aps.org/doi/10.1103/PhysRev.129.62

[84] G. Onida, L. Reining, and A. Rubio, "Electronic excitations: density-functional versus many-body green's-function approaches," *Rev. Mod. Phys.*, vol. 74, pp. 601–659, Jun 2002. [Online]. Available: https://link.aps.org/doi/10.1103/RevModPhys.74.601

[85] F. Sottile, F. Bruneval, A. G. Marinopoulos, L. K. Dash, S. Botti, V. Olevano, N. Vast, A. Rubio, and L. Reining, "Tddft from molecules to solids: The role of long-range interactions," *International Journal of Quantum Chemistry*, vol. 102, no. 5, pp. 684–701, 2005. [Online]. Available: https://onlinelibrary.wiley.com/doi/abs/10.1002/qua.20486

[86] A. G. Marinopoulos, L. Reining, V. Olevano, A. Rubio, T. Pichler, X. Liu, M. Knupfer, and J. Fink, "Anisotropy and interplane interactions in the dielectric response of graphite," *Phys. Rev. Lett.*, vol. 89, p. 076402, Jul 2002. [Online]. Available: https://link.aps.org/doi/10.1103/PhysRevLett.89.076402

[87] N. Tancogne-Dejean, C. Giorgetti, and V. Véniard, "Optical properties of surfaces with supercell ab initio calculations: Local-field effects," *Phys. Rev. B*, vol. 92, p. 245308, Dec 2015. [Online]. Available: https://link.aps.org/doi/10.1103/PhysRevB.92.245308

[88] S. Mazzei and C. Giorgetti, "Optical response of two-dimensional systems: Insights from classical electromagnetism to *abinitio* calculations," *Phys. Rev. B*, vol. 106, p. 035431, Jul 2022. [Online]. Available: https://link.aps.org/doi/10.1103/PhysRevB.106.035431

[89] L. Yang, J. Deslippe, C.-H. Park, M. L. Cohen, and S. G. Louie, "Excitonic effects on the optical response of graphene and bilayer graphene," *Phys. Rev. Lett.*, vol. 103, p. 186802, Oct 2009. [Online]. Available: https://link.aps.org/doi/10.1103/PhysRevLett.103.186802

[90] S. Mazzei and C. Giorgetti, "Optical properties of quasi-two-dimensional objects from time-dependent density functional theory: Longitudinal versus transverse dielectric functions," *Phys. Rev. B*, vol. 107, p. 165412, Apr 2023. [Online]. Available: https://link.aps.org/doi/10.1103/PhysRevB.107.165412

[91] X. Gonze, B. Amadon, G. Antonius, F. Arnardi, L. Baguet, J.-M. Beuken, J. Bieder, F. Bottin, J. Bouchet, E. Bousquet, N. Brouwer, F. Bruneval, G. Brunin, T. Cavignac, J.-B. Charraud, W. Chen, M. Côté, S. Cottenier, J. Denier, G. Geneste, P. Ghosez, M. Giantomassi, Y. Gillet, O. Gingras, D. R. Hamann, G. Hautier, X. He, N. Helbig, N. Holzwarth, Y. Jia, F. Jollet, W. Lafargue-Dit-Hauret, K. Lejaeghere, M. A. Marques, A. Martin, C. Martins, H. P. Miranda, F. Naccarato, K. Persson, G. Petretto, V. Planes, Y. Pouillon, S. Prokhorenko, F. Ricci, G.-M. Rignanese, A. H. Romero, M. M. Schmitt, M. Torrent, M. J. van Setten, B. Van Troeye, M. J. Verstraete, G. Zérah, and J. W. Zwanziger, "The abinitproject: Impact, environment and recent developments," *Computer Physics Communications*, vol. 248, p. 107042, 2020. [Online]. Available: https://www.sciencedirect.com/science/article/pii/S0010465519303741

[92] D. R. Hamann, "Optimized norm-conserving vanderbilt pseudopotentials," *Phys. Rev. B*, vol. 88, p. 085117, Aug 2013. [Online]. Available: https://link.aps.org/doi/10.1103/PhysRevB.88.085117

[93] H. T. Stokes and D. M. Hatch, "FINDSYM: program for identifying the space-group symmetry of a crystal," *Journal of Applied Crystallography*, vol. 38, no. 1, pp. 237–238, Feb 2005. [Online]. Available: https://doi.org/10.1107/S0021889804031528

[94] H. T. Stokes, D. M. Hatch, and B. J. Campbell. Findsym, isotropy software suite. [Online]. Available: https://iso.byu.edu

[95] C. Hartwigsen, S. Goedecker, and J. Hutter, "Relativistic separable dual-space gaussian pseudopotentials from h to rn," *Phys. Rev. B*, vol. 58, pp. 3641–3662, Aug 1998. [Online]. Available: https://link.aps.org/doi/10.1103/PhysRevB.58.3641

[96] H. J. Monkhorst and J. D. Pack, "Special points for brillouin-zone integrations," *Phys. Rev. B*, vol. 13, pp. 5188–5192, Jun 1976. [Online]. Available: https://link.aps.org/doi/10.1103/PhysRevB.13.5188

[97] E. Runge and E. K. U. Gross, "Density-functional theory for time-dependent systems," *Phys. Rev. Lett.*, vol. 52, pp. 997–1000, Mar 1984. [Online]. Available: https://link.aps.org/doi/10.1103/PhysRevLett.52.997

[98] F. Sottile, L. Reining, and V. Olevano. The dp code. [Online]. Available: https://etsf.polytechnique.fr/software/Ab_Initio/

[99] L. Zhu and T. Zhang, "Optimized tight binding parameters for single layer honeycomb borophene," *Solid State Communications*, vol. 282, pp. 50–54, 2018. [Online]. Available: https://www.sciencedirect.com/science/article/pii/S0038109818304149

[100] B. Peng, H. Zhang, H. Shao, Y. Xu, R. Zhang, and H. Zhu, "The electronic, optical, and thermodynamic properties of borophene from first-principles calculations," *J. Mater. Chem. C*, vol. 4, pp. 3592–3598, 2016. [Online]. Available: http://dx.doi.org/10.1039/C6TC00115G

[101] P. Menz, H. Hanafi, J. Imbrock, and C. Denz, "Noncontractible loop states from a partially flat band in a photonic borophene lattice," *Nanophotonics*, vol. 12, no. 17, pp. 3409–3415, 2023. [Online]. Available: https://doi.org/10.1515/nanoph-2023-0222

[102] P. Narang, C. A. C. Garcia, and C. Felser, "The topology of electronic band structures," *Nature Materials*, vol. 20, no. 3, pp. 293–300, Mar 2021. [Online]. Available: https://doi.org/10.1038/s41563-020-00820-4

[103] D. S. Sanchez, I. Belopolski, T. A. Cochran, X. Xu, J.-X. Yin, G. Chang, W. Xie, K. Manna, V. Süß, C.-Y. Huang, N. Alidoust, D. Multer, S. S. Zhang, N. Shumiya, X. Wang, G.-Q. Wang, T.-R. Chang, C. Felser, S.-Y. Xu, S. Jia, H. Lin, and M. Z. Hasan, "Topological chiral crystals with helicoid-arc quantum states," *Nature*, vol. 567, no. 7749, pp. 500–505, Mar 2019. [Online]. Available: https://doi.org/10.1038/s41586-019-1037-2

[104] F. Ma, Y. Jiao, G. Gao, Y. Gu, A. Bilic, Z. Chen, and A. Du, "Graphene-like two-dimensional ionic boron with double dirac cones at ambient condition," *Nano Letters*, vol. 16, no. 5, pp. 3022–3028, May 2016. [Online]. Available: https://doi.org/10.1021/acs.nanolett.5b05292

[105] S. Baroni, S. de Gironcoli, A. Dal Corso, and P. Giannozzi, "Phonons and related crystal properties from density-functional perturbation theory," *Rev. Mod. Phys.*, vol. 73, pp. 515–562, Jul 2001. [Online]. Available: https://link.aps.org/doi/10.1103/RevModPhys.73.515

[106] P. M. Neves, J. P. Wakefield, S. Fang, H. Nguyen, L. Ye, and J. G. Checkelsky, "Crystal net catalog of model flat band materials," 2023.

[107] N. Lazarides and G. P. Tsironis, "Compact localized states in engineered flat-band pt metamaterials," *Scientific Reports*, vol. 9, no. 1, p. 4904, Mar 2019. [Online]. Available: https://doi.org/10.1038/s41598-019-41155-8

[108] A. A. Daniel Leykam and S. Flach, "Artificial flat band systems: from lattice models to experiments," *Advances in Physics: X*, vol. 3, no. 1, p. 1473052, 2018. [Online]. Available: https://doi.org/10.1080/23746149.2018.1473052

[109] P. Drude, "Zur elektronentheorie der metalle," *Annalen der Physik*, vol. 306, no. 3, pp. 566–613, 1900. [Online]. Available: https://onlinelibrary.wiley.com/doi/abs/10.1002/andp.19003060312

[110] A. G. Marinopoulos, L. Reining, A. Rubio, and V. Olevano, "Ab initio study of the optical absorption and wave-vector-dependent dielectric response of graphite," *Phys. Rev. B*, vol. 69, p. 245419, Jun 2004. [Online]. Available: https://link.aps.org/doi/10.1103/PhysRevB.69.245419

[111] H.-C. Weissker, J. Serrano, S. Huotari, E. Luppi, M. Cazzaniga, F. Bruneval, F. Sottile, G. Monaco, V. Olevano, and L. Reining, "Dynamic structure factor and dielectric function of silicon for finite momentum transfer: Inelastic x-ray scattering experiments and ab initio calculations," *Phys. Rev. B*, vol. 81, p. 085104, Feb 2010. [Online]. Available: https://link.aps.org/doi/10.1103/PhysRevB.81.085104

[112] W. Schulke, "Electron dynamics by inelastic x-ray scattering," 2007. [Online]. Available: https://api.semanticscholar.org/CorpusID:118858965

[113] G. M. Éliashberg, "Interactions between electrons and lattice vibrations in a superconductor," *Journal of Experimental and Theoretical Physics*, 1960. [Online]. Available: https://api.semanticscholar.org/CorpusID:119782170

[114] W. L. McMillan, "Transition temperature of strong-coupled superconductors," *Phys. Rev.*, vol. 167, pp. 331–344, Mar 1968. [Online]. Available: https://link.aps.org/doi/10.1103/PhysRev.167.331

[115] J. Z. Xuetao Zhu, Jiandong Guo and E. W. Plummer, "Misconceptions associated with the origin of charge density waves," *Advances in Physics: X*, vol. 2, no. 3, pp. 622–640, 2017. [Online]. Available: https://doi.org/10.1080/23746149.2017.1343098

[116] M. D. Johannes, I. I. Mazin, and C. A. Howells, "Fermi-surface nesting and the origin of the charge-density wave in Nbse$_2$," *Phys. Rev. B*, vol. 73, p. 205102, May 2006. [Online]. Available: https://link.aps.org/doi/10.1103/PhysRevB.73.205102

[117] M. D. Johannes and I. I. Mazin, "Fermi surface nesting and the origin of charge density waves in metals," *Phys. Rev. B*, vol. 77, p. 165135, Apr 2008. [Online]. Available: https://link.aps.org/doi/10.1103/PhysRevB.77.165135

[118] X. Zhu, Y. Cao, J. Zhang, E. W. Plummer, and J. Guo, "Classification of charge density waves based on their nature," *Proceedings of the National Academy of Sciences*, vol. 112, no. 8, pp. 2367–2371, 2015. [Online]. Available: https://www.pnas.org/doi/abs/10.1073/pnas.1424791112

[119] W. Kohn, "Image of the fermi surface in the vibration spectrum of a metal," *Phys. Rev. Lett.*, vol. 2, pp. 393–394, May 1959. [Online]. Available: https://link.aps.org/doi/10.1103/PhysRevLett.2.393

[120] S. Baroni, P. Giannozzi, and A. Testa, "Green's-function approach to linear response in solids," *Phys. Rev. Lett.*, vol. 58, pp. 1861–1864, May 1987. [Online]. Available: https://link.aps.org/doi/10.1103/PhysRevLett.58.1861

[121] R. M. Pick, M. H. Cohen, and R. M. Martin, "Microscopic theory of force constants in the adiabatic approximation," *Phys. Rev. B*, vol. 1, pp. 910–920, Jan 1970. [Online]. Available: https://link.aps.org/doi/10.1103/PhysRevB.1.910

[122] G. Giuliani and G. Vignale, *Quantum Theory of the Electron Liquid*. Cambridge University Press, 2005.

[123] G. Gruner, *Density waves in solids*. CRC press, 2018.

[124] R. de L. Kronig, "On the theory of dispersion of x-rays," *J. Opt. Soc. Am.*, vol. 12, no. 6, pp. 547–557, Jun 1926. [Online]. Available: https://opg.optica.org/abstract.cfm?URI=josa-12-6-547

[125] H. A. Kramers, "La diffusion de la lumiere par les atomes," in *Atti Cong. Intern. Fisica (Transactions of Volta Centenary Congress) Como*, vol. 2, 1927, pp. 545–557.

[126] F. Bechstedt, R. Del Sole, G. Cappellini, and L. Reining, "An efficient method for calculating quasiparticle energies in semiconductors," *Solid State Communications*, vol. 84, no. 7, pp. 765–770, 1992. [Online]. Available: https://www.sciencedirect.com/science/article/pii/003810989290476P

[127] J. A. Berger, L. Reining, and F. Sottile, "Ab initio calculations of electronic excitations: Collapsing spectral sums," *Phys. Rev. B*, vol. 82, p. 041103, Jul 2010. [Online]. Available: https://link.aps.org/doi/10.1103/PhysRevB.82.041103

[128] ——, "Efficient gw calculations for sno_2, zno, and rubrene: The effective-energy technique," *Phys. Rev. B*, vol. 85, p. 085126, Feb 2012. [Online]. Available: https://link.aps.org/doi/10.1103/PhysRevB.85.085126

[129] ——, "Efficient calculation of the polarizability: a simplified effective-energy technique," *The European Physical Journal B*, vol. 85, no. 9, p. 326, Sep 2012. [Online]. Available: https://doi.org/10.1140/epjb/e2012-30237-5

[130] R. W. Godby, M. Schlüter, and L. J. Sham, "Trends in self-energy operators and their corresponding exchange-correlation potentials," *Phys. Rev. B*, vol. 36, pp. 6497–6500, Oct 1987. [Online]. Available: https://link.aps.org/doi/10.1103/PhysRevB.36.6497

[131] M. S. Hybertsen and S. G. Louie, "Electron correlation in semiconductors and insulators: Band gaps and quasiparticle energies," *Phys. Rev. B*, vol. 34, pp. 5390–5413, Oct 1986. [Online]. Available: https://link.aps.org/doi/10.1103/PhysRevB.34.5390

[132] E. Salpeter and H. A. Bethe, "A relativistic equation for bound state problems," *Physical Review*, vol. 84, pp. 1232–1242, 1951. [Online]. Available: https://api.semanticscholar.org/CorpusID:124439487

[133] G. Strinati, "Application of the green's functions method to the study of the optical properties of semiconductors," *La Rivista del Nuovo Cimento (1978-1999)*, vol. 11, no. 12, pp. 1–86, Dec 1988. [Online]. Available: https://doi.org/10.1007/BF02725962

[134] T. Miyake and F. Aryasetiawan, "Efficient algorithm for calculating noninteracting frequency-dependent linear response functions," *Phys. Rev. B*, vol. 61, pp. 7172–7175, Mar 2000. [Online]. Available: https://link.aps.org/doi/10.1103/PhysRevB.61.7172

[135] F. Sottile, L. Reining, and V. Olevano. The dp code. [Online]. Available: https://etsf.polytechnique.fr/software/Ab_Initio/

[136] A. Lorin, "Electronic properties of silver chloride: influence of excitons on the charge dynamics," Ph.D. dissertation, Instit Polytechnique de Paris, 2020.

[137] A. T. Osorio Delgadillo. d3 polymorph density animation. [Online]. Available: https://youtu.be/MMp8jJtTtDk

[138] ——. b12 polymorph density animation. [Online]. Available: https://youtu.be/I1g_JDw_UPA

[139] ——. a1 polymorph density animation. [Online]. Available: https://youtu.be/_k_1LC0G4fU

[140] L. Kleinman and D. M. Bylander, "Efficacious form for model pseudopotentials," *Phys. Rev. Lett.*, vol. 48, pp. 1425–1428, May 1982. [Online]. Available: https://link.aps.org/doi/10.1103/PhysRevLett.48.1425

[141] F. Sottile, L. Reining, and V. Olevano. The exc code. [Online]. Available: https://etsf.polytechnique.fr/software/Ab_Initio/

Titre : Réponse de la densité de charge des polymorphes 2D : le borophène comme cas prototypique.

Mots clés : borophène, plasmonique, polarisabilité

Résumé : L'objectif de cette thèse est d'élucider la dynamique de charge dans les matériaux bidimensionnels présentant des structures atomiques complexes. À cette fin, le borophène a été choisi comme matériau prototypique présentant de nombreux allotropes, permettant ainsi d'étudier directement l'influence de la structure atomique sur les propriétés électroniques. Parmi les multiples allotropes, j'ai identifié huit structures d'importance théorique et expérimentale, et j'ai calculé leur structure de bande électronique. Ensuite, j'ai utilisé les caractéristiques communes de la structure électronique des différents polymorphes pour les relier à une structure parente commune, et j'ai construit un modèle théorique basé sur un gaz d'électrons tridimensionnel confiné et homogène. Ce modèle explique plusieurs résultats pour la structure électronique des différents polymorphes étudiés dans ce travail.

La structure électronique des différents polymorphes a montré des caractéristiques communes entre différents allotropes, mais elle a également révélé des différences sous la forme de bandes faiblement dispersives. Ces bandes plates se manifestent comme une signature de la structure atomique spécifique. Nous les appelons des états de type défaut qui apparaissent suite à la création de défauts ponctuels dans une structure atomique commune du borophène. De plus, j'ai étudié l'effet du bombement sur la structure électronique et montré que nous pouvons utiliser ce paramètre pour ajuster les propriétés électroniques du matériau, influençant potentiellement la semi-métallicité et même la supraconductivité.

L'étude de la structure électronique a également révélé le potentiel de cette classe de matériaux à être utilisée comme conducteur transparent. J'ai décrit le mécanisme selon lequel certaines transitions électroniques n'apparaissent pas dans les spectres d'absorption en raison de la symétrie : la position de l'énergie de Fermi dans la structure de bande est un paramètre important pour déterminer les propriétés optiques du borophène, et les positions relatives des états p dans le plan et hors du plan jouent également un rôle important autour du niveau de Fermi. J'ai donc décrit le repliement de la surface de Fermi en me basant sur les informations des transitions électroniques. L'étude du repliement de la surface de Fermi a été complétée par le calcul de la réponse linéaire statique, ce qui m'a permis de dévoiler la nature de deux anomalies de Kohn apparaissant dans le borophène δ_6.

Le calcul des fonctions de réponse est très coûteux en termes de calculs. J'ai abordé ce problème en développant une méthode approximative qui nous permet d'exprimer la réponse statique en tant que fonction explicite de la matrice de densité. Cela présente un intérêt à la fois fondamental et pratique, car c'est l'un des rares exemples de fonctionnelles explicites de la matrice de densité pour les observables, et cela conduit à un gain d'ordre de grandeur en temps de calcul.

Title : Charge density response of 2D polymorphs : borophene as a prototypical case.

Keywords : borophene, plasmonics, polarizability

Abstract : The aim of this thesis is to elucidate the charge dynamics in 2D materials with complex atomic structures. To this end, borophene was chosen as a prototypical material that exhibits numerous allotropes, such that the influence of the atomic structure on the electronic properties can be investigated directly. Among the multiple allotropes I identified eight structures of theoretical and experimental relevance and computed their electronic band structure. I then used the shared characteristics of the electronic structure of the different polymorphs to relate them to a common parent structure, and I built a theoretical model based on a confined three-dimensional homogeneous electron gas. This model explain several findings for the electronic structure of the different polymorphs studied in this work. The electronic structure of the different polymorphs showed common features among different allotropes, but it also showed differences in the form of weakly-dispersive bands. These flat bands show up as a signature of the specific atomic structure. We refer to them as defect-like states that appear from the creation of point defects in a common borophene atomic structure. Moreover, I investigated the effect of buckling on the electronic structure and showed that we can use this parameter to tune electronic properties of the material such that semi-metallicity and eventually even superconductivity might be impacted. The study of the electronic structure also showed the potential of this class of materials to be used as a transparent conductor. I described the mechanism for which certain electronic transitions do not appear in the absorption spectra by symmetry : the position of the Fermi energy in the band structure is an important parameter to determine the optical properties of borophene, and the relative positions of p-states in-plane and out-of-plane plays also an important role around the Fermi level. I therefore described nesting of the Fermi surface based on the information of the electronic transitions. The study of the nesting of the Fermi surface was complemented with the computation of the static linear response, which allowed me to we unravel the nature of two Kohn anomalies appearing in borophene δ_6 . The calculation of the response functions is computationally very expensive. I addressed this problem by developing an approximated method that allows us to write the static response as an explicit functional of the density matrix. This is of both fundamental and practical interest since it is one of the few examples of explicit density matrix functionals for observables, and since it leads to an order of magnitude gain in computer time.